

Impact of eruption dynamics and gas–aerosol interaction on the early stage evolution of volcanic plumes

Zur Erlangung des akademischen Grades einer
DOKTORIN DER NATURWISSENSCHAFTEN (Dr. rer. nat.)
von der KIT-Fakultät für Physik des
Karlsruher Instituts für Technologie (KIT)

genehmigte

DISSERTATION

von

M. Sc. Julia Rebecca Bruckert
aus Lüdenscheid

Tag der mündlichen Prüfung:	21.04.2023
Referentin:	Prof. Dr. Corinna Hoose
Korreferent:	Prof. Dr. Christian von Savigny

Abstract

Explosive volcanic eruptions emit particles and gases into the atmosphere, which can influence the Earth's climate by disturbing the radiation budget. The strength of the impact on the radiation budget primarily depends on the amount of sulfate aerosols produced from the volcanic sulfur dioxide (SO₂) emissions. However, plume processes that influence the formation of sulfate particles are not yet fully understood. Most modeling approaches assume highly simplified volcanic emissions and neglect plume dynamics and gas–ash interactions. This leads to a gap between the source conditions during the emission and the atmospheric dispersion with impacts on weather and climate.

This thesis investigates the emissions and the interaction of volcanic ash and chemical species during the early plume evolution in the atmosphere. Therefore, the ICON-ART (ICOsahedral Nonhydrostatic model – Aerosol and Reactive Trace gases) modeling system is coupled with the one-dimensional volcanic plume model FPlume to calculate the eruption source parameters (ESPs) online. Two recent volcanic eruptions are simulated and validated against available observations to study physical and chemical processes in the early stage of volcanic plumes: the 2019 Raikoke and the 2021 La Soufrière eruption. The emissions of both eruptions are characterized by multiple eruption phases, which need to be resolved in order to link the complex eruption dynamics to volcanic plume dispersion forecasts.

The modeled ash and SO₂ dispersion after the Raikoke eruption is compared with satellite retrievals. Results of numerical experiments confirm that resolving the eruption phases significantly improves the ash burden and dispersion of the plume in the first two days. Further improvements are achieved by calculating the mass eruption rate with FPlume instead of commonly used empirical relationships.

In the next step, modeled aerosol aging following the La Soufrière eruption is validated with observations from the Multiangle Imaging SpectroRadiometer (MISR) Research Aerosol (RA) algorithm and the Cloud–Aerosol Lidar with Orthogonal Polarization (CALIOP) instrument directly for the first time. The aerosol aging modeled with ICON-ART is in very good agreement with observations from MISR RA near the emission source and with CALIOP at larger distances to the volcano. The simulation shows that particle aging occurs faster in the troposphere than in the stratosphere due to the availability of water vapor and hydroxyl radicals. Nevertheless, a layer of coated ash appears at the plume top due to faster oxidation of SO₂ and lofting by aerosol–radiation interaction.

Simulations with a complex chemistry mechanism including aqueous-phase chemistry for coated aerosols and SO₂ adsorption on fresh ash are conducted to investigate the fate of volcanic SO₂ in the early stage of the plume. The results suggest that aqueous-phase chemistry plays a negligible role. However, adsorption of SO₂ accelerates ash aging, which increases the aerosol liquid water content (ALWC) due to a

higher hygroscopicity of the particles. Whether this increase in ALWC can enhance the role of aqueous reactions beyond the early stage needs to be evaluated in further studies.

This thesis links the ESPs and in-plume aerosol dynamical processes and chemistry to the dispersion of early volcanic plumes. Considering the influence of these factors in models can enhance our understanding of plume effects on weather and clouds and the impacts on climate after large volcanic eruptions.

Zusammenfassung

Explosive Vulkanausbrüche emittieren Partikel und Gase in die Atmosphäre, welche das Klima der Erde beeinflussen können, indem sie den Strahlungshaushalt stören. Die Stärke des Einflusses auf den Strahlungshaushalt hängt in erster Linie von der Menge der Sulfataerosole ab, die durch die Emissionen von vulkanischem Schwefeldioxid (SO_2) entstehen. Die Fahrenprozesse, die die Bildung von Sulfatpartikeln beeinflussen, sind jedoch noch nicht vollständig verstanden. Die meisten Modellierungsansätze gehen von stark vereinfachten vulkanischen Emissionen aus und vernachlässigen die Fahndynamik und Gas-Asche-Wechselwirkungen. Dies führt zu einer Lücke zwischen den Quellbedingungen während der Emission und der Ausbreitung in der Atmosphäre mit Auswirkungen auf Wetter und Klima.

Diese Arbeit untersucht die Emissionen und die Wechselwirkung von Vulkanasche und chemischen Stoffen in der frühen Fahrenentwicklung in der Atmosphäre. Dazu wird das ICON-ART (ICOsahedral Non-hydrostatic model – Aerosols and Reaktive Trace gases) Modellsystem mit dem eindimensionalen Vulkanfahnenmodell FPlume gekoppelt um die Parameter der Eruptionsquellen (ESPs) online zu berechnen. Zur Untersuchung der physikalischen und chemischen Prozesse in der Anfangsphase von Vulkanfahnen werden zwei aktuelle Vulkanausbrüche simuliert und anhand verfügbarer Beobachtungen validiert: die Eruption des Raikoke im Jahr 2019 und die des La Soufrière im Jahr 2021. Die Emissionen beider Eruptionen sind durch mehrere Eruptionsphasen gekennzeichnet, die aufgelöst werden müssen um die komplexe Eruptionsdynamik mit Vorhersagen zur Ausbreitung der Vulkanfahne zu verknüpfen.

Die modellierte Asche- und SO_2 -Ausbreitung nach dem Ausbruch des Raikoke wird mit Satellitenmessungen verglichen. Die Ergebnisse der numerischen Experimente bestätigen, dass die Auflösung der Eruptionsphasen die Aschemasse und die Ausbreitung der Aschefahne in den ersten beiden Tagen deutlich verbessert. Weitere Verbesserungen werden durch die Berechnung der Masseneruptionsrate mit FPlume anstelle der üblicherweise verwendeten empirischen Gleichungen erzielt.

Im nächsten Schritt wird die modellierte Aerosolalterung nach dem Ausbruch des La Soufrière direkt mit Beobachtungen des Multiangle Imaging SpectroRadiometer (MISR) Research Aerosol (RA) Algorithmus und des Cloud-Aerosol Lidar with Orthogonal Polarization (CALIOP) Instruments validiert. Die mit ICON-ART modellierte Aerosolalterung ist in sehr guter Übereinstimmung mit den Beobachtungen von MISR RA in der Nähe der Emissionsquelle und mit CALIOP in größeren Distanzen zum Vulkan. Die Simulation zeigt, dass die Partikelalterung in der Troposphäre aufgrund der Verfügbarkeit von Wasserdampf und Hydroxyl-Radikalen schneller erfolgt als in der Stratosphäre. Allerdings tritt eine Schicht gealterter Asche an der Oberkante der Fahne wegen der schnelleren Oxidation von SO_2 und Anhebung durch Aerosol-Strahlungs-Wechselwirkung auf.

Simulationen mit einem komplexen chemischen Mechanismus einschließlich der Chemie der Flüssigphase auf gealterten Aerosolen und SO_2 -Adsorption an frischer Asche werden durchgeführt, um das Abbauverhalten von vulkanischem SO_2 in der Anfangsphase der Fahne zu untersuchen. Die Ergebnisse deuten darauf hin, dass die Flüssigphase in der frühen Phase der Vulkanfahne eine vernachlässigbare Rolle spielt. Die Adsorption von SO_2 beschleunigt jedoch die Alterung der Asche, wodurch sich der Flüssigwassergehalt des Aerosols (ALWC) aufgrund einer höheren Hygroskopizität der Partikel erhöht. Ob dieser Anstieg des ALWC die Rolle der Reaktionen in der Flüssigphase über das Anfangsstadium hinaus verstärken kann, muss in weiteren Studien untersucht werden.

Diese Arbeit stellt eine Verbindung der ESPs und den aerosoldynamischen und chemischen Prozessen zu der Ausbreitung der frühen Vulkanfahne her. Die Berücksichtigung des Einflusses dieser Faktoren in Modellen kann unser Verständnis der Auswirkungen von Vulkanfahnen auf das Wetter und die Wolken sowie der Auswirkungen auf das Klima nach großen Vulkanausbrüchen verbessern.

Contents

Abstract	i
Zusammenfassung	iii
1 Introduction	1
1.1 Eruption source parameters	3
1.2 Aerosol dynamics and aerosol–radiation interaction	4
1.3 Volcanic plume chemistry	5
1.4 Research questions and outline	8
2 Volcanic ejection	9
2.1 Volcanic eruptions from the volcanological perspective	9
2.2 Plume dynamics of explosive volcanic eruptions	11
2.3 Atmospheric chemistry	13
2.3.1 Gas-phase chemistry	13
2.3.2 Dissolution of gases in water	16
2.3.3 Aqueous-phase chemistry	17
2.3.4 Adsorption and heterogeneous chemistry	19
2.4 Atmospheric aerosols	20
2.4.1 Aerosol dynamical processes	20
2.4.2 Radiative properties of aerosols	21
3 ICON-ART modeling system	25
3.1 ICON model	25
3.2 ART submodule	26
3.2.1 Aerosol tracers	27
3.2.2 Gas-phase tracers	29
3.3 Emissions from volcanic eruptions with FPlume	29
3.4 Aerosol dynamic processes	32
3.4.1 Gas–particle partitioning with ISORROPIA II	32
3.4.2 Nucleation	33
3.4.3 Condensation	33

3.4.4	Coagulation	35
3.4.5	Aerosol–radiation interaction	37
3.5	Gas-phase chemistry	39
3.5.1	Simplified OH-chemistry	40
3.5.2	Chemistry mechanism with MECCA	41
3.6	Aqueous-phase chemistry and adsorption	41
4	Simulated cases, observational data, and validation techniques	43
4.1	Simulated cases	43
4.1.1	2019 Raikoke eruption	43
4.1.2	2021 La Soufrière eruption	43
4.1.3	Model configurations	44
4.2	Observational volcanic input	45
4.3	Separation of the volcanic plume from the background	46
4.4	Himawari-8 ash and SO ₂ loading	46
4.5	BCO	47
4.6	MISR	48
4.7	CALIPSO	49
5	Plume dynamics and lofting after the 2019 Raikoke eruption	51
5.1	Validation of mass loading	53
5.2	Validation of dispersion using SAL	56
5.3	Vertical separation of SO ₂ and ash plumes	57
6	Aerosol aging in model and observations after the 2021 La Soufrière eruption	63
6.1	Vertical distribution of ash near the volcanic source	64
6.2	Plume dispersion	66
6.3	Proximal aging of the aerosols	67
6.3.1	Plume height validation	68
6.3.2	Aerosol properties	70
6.4	Distal aging of the aerosols	72
6.4.1	Validation along satellite track	72
6.4.2	Temporal average	74
7	Sulfur chemistry in explosive volcanic eruptions	77
7.1	Chemical fate of volcanic SO ₂	78
7.1.1	Aqueous-phase chemistry on aged aerosols	79
7.1.2	SO ₂ adsorption on ash	82

7.1.3 Discussion	83
7.2 Impacts of sulfur emissions on atmospheric chemistry	85
8 Conclusions	89
8.1 Outlook	91
A FPlume input parameters	93
B Chemistry mechanism of Chapter 7	97
C Additional figures	105
D Symbols and acronyms	123
E Bibliography	131
F List of figures	147
G List of tables	149

1. Introduction

In Europe and North America, the year 1816 is often described as the year without summer. In that year, reduced temperatures and increased precipitation over Western Europe as well as frost and snow in northern New England and Canada led to crop failures. This resulted in famines, diseases, and social distress on large parts of the Northern Hemisphere (e.g., Stommel and Stommel, 1979; Stothers, 1984; Luterbacher and Pfister, 2015). Nowadays, we know that sulfate aerosols in the stratosphere produced from sulfur dioxide (SO_2) emissions by the eruption of the Tambora volcano in 1815 increased the scattering of sunlight. This reduced surface temperatures (e.g., Robock, 2000; Schurer et al., 2019) and affected atmospheric dynamics (Schurer et al., 2019). The eruption took place on the island of Sumbawa in Indonesia (Stothers, 1984) and was among the most explosive eruptions in the recorded history (Stothers, 1984).

The example of the Tambora eruption demonstrated how volcanic eruptions affect human life even at global scales by changing surface weather and climate. However, the impacts of volcanic eruptions on weather and climate are more complex and not yet fully understood. This increases uncertainties of climate predictions following volcanic eruptions.

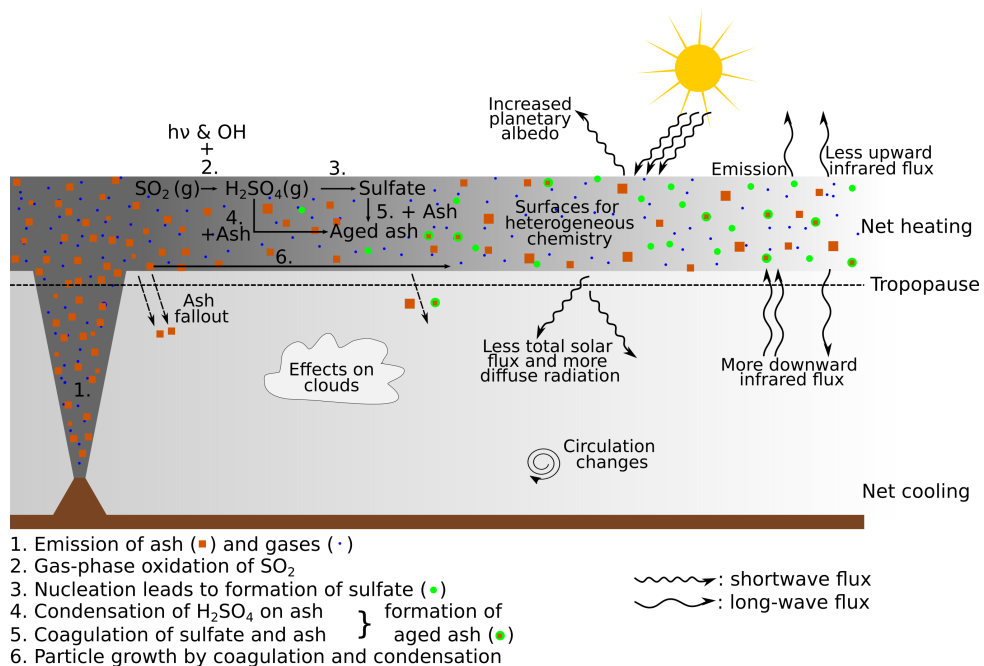


Figure 1.1.: Schematic illustration of important processes in volcanic plumes and the impact on the atmosphere. The lengths are not to scale.

Figure 1.1 summarizes the most important processes happening in volcanic plumes and the effects on the atmosphere. Explosive volcanic eruptions emit solid particles, also called tephra, and gases such as water vapor, sulfur-containing gases, and halogens into the Earth's atmosphere. In the atmosphere, volcanic compounds are dispersed and undergo various transition processes. The emitted gases are involved in chemical reactions and the formation of secondary volcanic aerosols such as sulfate particles from emitted SO_2 . Volcanic ash particles, defined as tephra with a diameter <2 mm (Rose and Durant, 2009), are affected by particle aging. Both volcanic ash and sulfate particles can drift away several thousand kilometers from the eruption point when emitted into the lower stratosphere or higher. Volcanic ash can remain airborne for up to a few months before being removed by sedimentation (e.g., Robock, 2000; Niemeier et al., 2009; Jensen et al., 2018). Sulfate aerosols can stay in the atmosphere even up to two years and are then removed by the residual stratospheric meridional circulation (Robock, 2000).

By scattering and absorbing shortwave (SW) and long-wave (LW) radiation, volcanic aerosols modify the Earth's radiation budget, which affects surface temperatures and atmospheric dynamics for up to two to three years (e.g., Robock, 2000; Marshall et al., 2022, and references therein). Additionally, volcanic aerosols provide surfaces for stratospheric heterogeneous chemistry, which destroys ozone (O_3) in the stratosphere (Solomon et al., 1996; Solomon, 1999). On shorter time scales and more regionally constrained, volcanic aerosols can serve as cloud condensation nuclei (CCN) or ice nucleating particles (IN) and influence the formation and appearance of clouds (e.g., Twomey, 1974; Malavelle et al., 2017; Haghghatnasab et al., 2022). Furthermore, the dispersion of ash particles matters for aviation safety (Casadevall, 1994), regional public health (Horwell and Baxter, 2006), and local environment and infrastructure (e.g., Spence et al., 2005; Stewart et al., 2006; Wardman et al., 2012). Therefore, the interest in both modeling the plume dispersion within the first days after the eruption and the prediction of climate impacts is large.

In most weather and climate models, the dispersion of the erupted material is entirely decoupled from the physical and chemical development of eruption plumes. The main physical and chemical processes in volcanic eruption plumes include cooling and dilution due to interaction with the atmosphere, aggregation, cloud microphysics, gas-phase chemistry, gas-aerosol partitioning, and aerosol chemistry and dynamics. These processes modify the amount of gases in the plume and the physiochemical properties of ash particles (e.g., hygroscopicity, radiative properties, cloud formation characteristics). Thus, the decoupling of volcanological processes from dispersion and climate models leads to a huge gap. This gap causes uncertainties in the forecast of the short-term dispersion, in simulations of volcanic effects on clouds, and in the prediction of modeled climate impacts of volcanic eruptions (e.g., Timmreck, 2012; von Savigny et al., 2020).

In this thesis, I aim to link the processes occurring in the first hours and days after volcanic eruptions to the further plume development, which becomes relevant when predicting the climate impact of volcanic eruptions. In the following, I present the existing literature on modeling volcanic eruptions in general and the role of aerosols and chemistry in (volcanic) plumes. Throughout this thesis, I use the term

'plume' or 'volcanic plume' to describe the part of the volcanic material dispersed in the atmosphere as commonly used in the meteorology instead of 'volcanic cloud' to maintain a clear distinction from the meteorological clouds.

1.1. Eruption source parameters¹

Forecasting the dispersion of volcanic aerosols in the atmosphere relies on the representation of the source and sink parameters as well as related processes. It has been shown that eruption source parameters (ESPs) such as the mass eruption rate (MER), the initial plume height, the emission profile, and the duration of the eruption can strongly influence the quality of the forecast of the spatial distribution of the volcanogenic gases and particles (e.g., Scollo et al., 2008; Harvey et al., 2018). The plume height can be estimated instantaneously by visual, radar, and lidar based or satellite observations. Until a few hours after the onset of a volcanic eruption when such plume height observations become available, the MER usually remains uncertain. Estimates of the MER include empirical parametrizations based on plume height (e.g., Mastin et al., 2009) partially corrected by wind effects (e.g., Degruyter and Bonadonna, 2012; Woodhouse et al., 2013) or are derived with one-dimensional (1-D) volcanic plume rise models (e.g., Folch et al., 2016). Further uncertainties arise from the choice of the emission profile (e.g., de Leeuw et al., 2021), i.e., the vertical distribution of mass. Different approaches exist to parameterize the emission profile, e.g., idealized profiles (Stuefer et al., 2012), plume-theory-based profiles (Marti et al., 2017), Gaussian-shaped profiles derived from backward trajectory modeling (Rieger et al., 2015), constant profiles (e.g., Beckett et al., 2020; Muser et al., 2020), or more complex ones derived from the observations (e.g., de Leeuw et al., 2021).

However, in all parametrizations of the ESPs the volcanic plume dispersion remains decoupled from unresolved volcanic eruption dynamics including also the influence of the atmosphere on the emission height. This accounts for large uncertainties in modeling studies at regional to global scales (Textor et al., 2005; Timmreck, 2012; von Savigny et al., 2020). Marti et al. (2017) overcame this issue by coupling the NMMB-MONARCH-ASH transport model (Nonhydrostatic Multiscale Model on the B-grid – Multiscale Online Nonhydrostatic Atmosphere Chemistry model – ASH) with the 1-D plume model FPlume, which calculates the MER and the mass distribution in the column online. Another example is the study by Collini et al. (2013), who combined the WRF/ARW (Weather Research and Forecasting Model / Advanced Research WRF) forecast system with FALL-3D and highlighted a good agreement in ash transport simulations with satellite observations for the Cordon Caulle eruption 2011. Plu et al. (2021) simulated the 2010 Eyjafjallajökull eruption with the MOCAGE model (Modèle de Chimie Atmosphérique de Grande Echelle) and hourly changing MERs from FPlume. They highlighted more

¹This section is adapted from: Bruckert, J., G. A. Hoshyaripour, Á. Horváth, L. O. Muser, F. J. Prata, C. Hoose, and B. Vogel, 2022: Online treatment of eruption dynamics improves the volcanic ash and SO₂ dispersion forecast: case of the 2019 Raikoke eruption. *Atmospheric Chemistry and Physics*, **22** (5), 3535–3552, doi:10.5194/acp-22-3535-2022.

concentrated ash concentrations in the horizontal and vertical scale, which more realistically represents the horizontal dispersion compared to parameterized MERs.

Only ash particles smaller than $32\ \mu\text{m}$ (hereafter referred to as very fine ash) are relevant for long-range transport in the atmosphere (Rose and Durant, 2009). Nevertheless, the amount of very fine ash emitted by a volcanic eruption is uncertain and depends on different parameters such as the strength and height of an eruption (Gouhier et al., 2019), the composition of magma (Rose and Durant, 2009), and the availability of water (e.g., van Eaton et al., 2012; Prata et al., 2017). Gouhier et al. (2019) analyzed data of past volcanic eruptions with respect to the fraction of very fine ash in the whole mass erupted. They found that strong volcanic eruptions are less efficient in emitting very fine ash into the atmosphere possibly due to higher sedimentation within the plume. Most forecast models assume a fixed value for the fraction of very fine ash between 1% (e.g., Muser et al., 2020) and 5% (e.g., Webster et al., 2012; Beckett et al., 2020) regardless of the strength of the eruption and lava composition.

1.2. Aerosol dynamics and aerosol–radiation interaction²

Aerosols are removed from the atmosphere by sedimentation as well as wet and dry deposition. Sedimentation of particles describes the removal due to gravity, and it depends on their shape, size, and density (Seinfeld and Pandis, 2006). Further aerosol dynamic processes include nucleation and coagulation as well as condensation, evaporation, and sublimation of gases on or from aerosols. These processes generate new particles and modify the size and composition of existing particles (particle aging) and, thus, their optical properties and lifetime in the atmosphere (Riemer et al., 2003; Seinfeld and Pandis, 2006; Eriksson et al., 2017). Kahn and Limbacher (2012), Scollo et al. (2012), and Flower and Kahn (2020) investigated particle aging by applying the Multiangle Imaging Spectroradiometer (MISR) Research Aerosol (RA) algorithm to the plumes of the 2010 Eyjafjallajökull eruption, multiple Etna plumes between the years 2000 and 2008, and the plumes of three Iceland volcanoes (Eyjafjallajökull 2010, Grímsvötn 2011, and Holuhraun 2014 – 2015), respectively. Scollo et al. (2012) found that particle type parameters from MISR RA such as the fraction of non-spherical and fine-mode particles well reflect the style of explosive activity, i.e., distinguish between ash-dominated and sulfate- or water vapor-dominated plumes. Kahn and Limbacher (2012) further demonstrated that MISR RA is suitable to investigate plume structures and plume particle evolution. Flower and Kahn (2020) used downwind changes in retrieved effective particle size, shape, and light-absorption to infer processes such as size-selective and size-independent gravitational settling, new particle formation, and particle oxidation or hydration.

Several modeling studies have investigated the impact of aerosol dynamics on the formation, properties, and lifetime of volcanic sulfate particles (e.g., Timmreck, 2012). Nevertheless, only a few studies have considered volcanic ash in their model. Niemeier et al. (2009, 2021) studied the effect of aerosol–

²This section is adapted from: Bruckert, J., L. Hirsch, Á. Horváth, R. A. Kahn, T. Kölling, L. O. Muser, C. Timmreck, H. Vogel, S. Wallis, G. A. Hoshyaripour, 2023: Dispersion and Aging of Volcanic Aerosols after the La Soufrière Eruption in April 2021, *Journal of Geophysical Research: Atmospheres*, **128**(8), e2022JD037694, <https://doi.org/10.1029/2022JD037694>.

radiation interaction on the ash and SO₂ dispersion assuming externally mixed aerosols, i.e., both pure ash and pure sulfate aerosols exist in the plume. The results of Niemeier et al. (2009) showed that additional heating and cooling caused by the radiative effect of very fine ash particles modify the evolution of the volcanic cloud. Niemeier et al. (2021) demonstrated that the volcanic emissions of very fine ash in the Northern Hemisphere change the wind patterns in the stratosphere by radiation interaction, influence the burden and lifetime of sulfate, and alter the radiative forcing. Muser et al. (2020) used the ICON-ART (ICOsahedral Nonhydrostatic model with Aerosol and Reactive Trace gases) model in which the volcanic aerosols (ash and sulfate) were internally mixed for the first time. Internally mixed means that particles can consist of different components, e.g., ash coated with sulfate. The results of Muser et al. (2020) revealed that aerosol dynamics led to faster removal of volcanic ash from the atmosphere following the Raikoke eruption in June 2019. Similarly, Abdelkader et al. (2017) found increased wet and dry deposition of aged dust particles due to increased hygroscopicity and particle size.

Muser et al. (2020) showed that aerosol–radiation interaction can lift the volcanic plume top even above the maximum height of emissions by absorbing SW and LW radiation, which is in agreement with observations (Chouza et al., 2020). This effect extends especially the lifetime of ash particles in the accumulation mode. Stenchikov et al. (2021) studied a Pinatubo-size eruption in the equatorial belt by including the radiative effects of SO₂, ash, sulfate, water vapor, and hydrometeors. Their simulations showed that the volcanic cloud rises by 1 km day⁻¹ during the first week, primarily due to the ash-induced heating and lofting. Zhu et al. (2020) showed that the ash particles controlled the chemistry and optical properties of volcanic clouds in the first days to weeks after the Mt. Kelud eruption in 2014. They concluded that persisting volcanic ash particles affected the stratospheric SO₂ lifetime and aerosol optical properties.

Despite the significant advancements made by these studies, the near-source evolution of volcanic aerosols and their impact on the early stage development of volcanic plumes are not well understood (Marshall et al., 2022).

1.3. Volcanic plume chemistry

Most dispersion models only consider the oxidation of SO₂ in the gas phase. However, comparisons of modeled and observed lifetimes of SO₂ indicate a too slow removal of SO₂ in early volcanic plumes (e.g., Feinberg et al., 2019; Zhu et al., 2020) and discrepancies between the simulated and observed sulfate aerosol removal (e.g., Dhomse et al., 2014; Mills et al., 2017; Dhomse et al., 2020). Recent studies highlighted the importance of scavenging by ash and liquids in removing SO₂ from the atmosphere (e.g., Tabazadeh and Turco, 1993; Textor et al., 2003) and aqueous-phase chemistry to oxidize SO₂ to sulfate (e.g., Liang and Jacobson, 1999; Hoshyaripour et al., 2015; Lachatre et al., 2022). Furthermore, ash and dust particles can take up SO₂ on the particle surfaces by adsorption and thereby reduce the SO₂

concentration in the gas phase (e.g., Usher et al., 2002; Maters et al., 2017; Urupina et al., 2019; Zhu et al., 2020).

Oxidation by hydroxyl radicals (OH) in the gas phase converts SO₂ to sulfuric acid (H₂SO₄), which rapidly forms sulfate aerosols. This can reduce OH levels in the stratosphere (e.g., Bekki, 1995) and troposphere (e.g., Jourdain et al., 2016; Pattantyus et al., 2018, and references therein) and lead to significant stratospheric dehydration as suggested by model calculations (Bekki, 1995). Jourdain et al. (2016) found that a reduction of OH by SO₂ and halogens from volcanic emissions in the troposphere can reduce the oxidizing capacity of the troposphere, which increases the lifetime of methane (CH₄).

Water vapor (H₂O) is the most abundant gas emitted during explosive volcanic eruptions and ambient water vapor can additionally be transported upwards due to air entrainment into the volcanic plume. Such direct injections are confirmed by modeling and observations (Sioris et al., 2016a,b). Although Sioris et al. (2016b) found in model and observational data that moderate-size volcanoes (volcanic explosivity index (VEI) 4 – 5) do not provide an effective mechanism for large-scale hydration of the stratosphere, water vapor can locally change atmospheric chemistry by forming OH (Bekki, 1995; LeGrande et al., 2016) or provide liquid solutions for scavenging (Tabazadeh and Turco, 1993; Textor et al., 2003) and aqueous-phase chemistry on water droplets in the troposphere (Lachatre et al., 2022). Abdelkader et al. (2023) performed simulations of Pinatubo-size volcanic eruptions. They found a quick deposition of injected water vapor in the lower stratosphere, which sediments as ice crystals and is irrelevant for chemistry. Nonetheless, at higher altitudes the injected water vapor accelerates the oxidation of SO₂ due to the production of OH.

Previous studies highlighted the importance of aqueous-phase chemistry in clouds on the oxidation pathway of SO₂. Liang and Jacobson (1999) found that the major sink of SO₂ in the aqueous phase is the oxidation by O₃ when the liquid water content (LWC) is large and pH > 4. Harris et al. (2013) performed Lagrange-type experiments with measurement sites upwind, downwind, and within an orographic cloud. They showed that the SO₂ oxidation catalyzed by natural transition metal ions (TMI) from mineral dust surfaces is the dominant oxidation pathway in clouds. In their experiments, hydrogen peroxide (H₂O₂) is consumed early in the lifetime of a cloud and the oxidation by O₃ in cloud droplets is very slow at low pH (<5.5).

Motivated by the finding of SO₂ oxidation in clouds, the aqueous-phase oxidation of SO₂ in volcanic plumes was investigated in model experiments. Figure 1.2 gives an overview on the chemical processes in volcanic plumes. Textor et al. (2003) examined the scavenging of hydrogen chloride (HCl, very high solubility in water), SO₂, and hydrogen sulfide (H₂S, lower solubility in water) by liquid and solid hydrometeors and by aggregates in a Plinian eruption plume with the Active Tracer High-Resolution Atmospheric Model (ATHAM) including microphysics and water vapor emissions. They found that despite scavenging, more than 25% of HCl and 80% of the sulfur gases reach the stratosphere because frozen hydrometeors dominate. Hoshyaripour et al. (2015) performed box model simulations considering also the temperature decrease with height in the plume. They found that liquid-phase reactions on coated

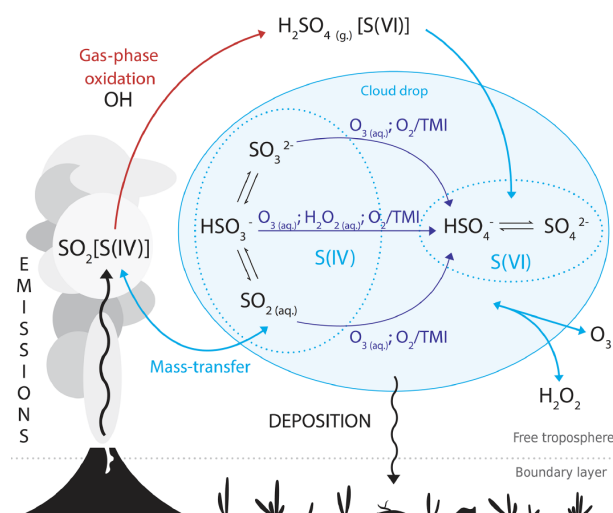


Figure 1.2.: Schematic illustration of the chemical processes in the gas- and liquid phase occurring in tropospheric volcanic plumes. Taken from Galeazzo et al. (2018).

ash particles scavenges more than 95% of HCl due to its high solubility in water, but only 3 – 20% of SO_2 is scavenged. Furthermore, they argued that SO_2 scavenging is enhanced in the presence of iron (Fe) ions (oxidation by TMI). Galeazzo et al. (2018) implemented an aqueous-phase sulfur oxidation module into a box model with an oxygen isotopic scheme to explore the absence of anomalous oxygen mass-independent fractionation (O-MIF) in volcanic sulfate in the troposphere. Their simulations revealed that oxidation by OH would cause a significant positive O-MIF in sulfate-rich volcanic plumes, which is in contradiction to measurements. However, cases where sulfur oxidation by dissolved oxygen (O_2) and TMI is dominant can explain the isotopic measurements of volcanic sulfate in the troposphere (Galeazzo et al., 2018). Lachatre et al. (2022) used a chemistry–transport model to investigate the 2012 Mt Etna eruption. They showed that the two main pathways contributing to sulfate production are the oxidation of SO_2 by OH in the gas phase (70%) and the aqueous oxidation by dissolved O_2 catalyzed by TMI (25%). Nevertheless, they also found that although the oxidation of SO_2 in the aqueous phase is faster than in the gas phase alone, less liquid water is available in mid-troposphere.

Bagnato et al. (2013) performed leaching experiments for 20 ash samples from the 2010 Eyjafjallajökull eruption and found major elements, such as sulfur, chlorine, and fluorine, on the surfaces of freshly fallen ash. The amount of these elements increased with increasing distance from the vent, indicating a gas adsorption on ash surfaces within the horizontal umbrella part of the plume. Further measurement experiments by Maters et al. (2017), Urupina et al. (2019), and Lasne et al. (2022) derived values for the uptake efficiency for ash particles sampled at different volcanoes globally (Maters et al., 2017) and for Icelandic dust sampled at different volcanoes (Urupina et al., 2019; Lasne et al., 2022). In all three studies the uptake efficiency depends on the composition of the particles. Zhu et al. (2020) studied the lifetime of SO_2 after the Mt Kelud eruption in 2014, and they found that the initial SO_2 lifetime is determined by SO_2 adsorption on ash rather than SO_2 oxidation by OH in the gas phase. Heterogeneous chemistry of

adsorbed sulfur with gaseous O_3 can lead to the formation of sulfate on various types of aerosol surfaces as it has been shown for dust (Usher et al., 2002) and calcium carbonate (Li et al., 2006), and evidence is also given for volcanic ash (Maters et al., 2017).

Although these studies significantly enhanced our understanding of gas–aerosol interaction by aqueous-phase chemistry and adsorption, the effect on the fate of SO_2 in the early plume development remains uncertain.

1.4. Research questions and outline

This thesis aims to close the gap between volcanic plume dynamics in the first days and further plume dispersion beyond this early period. This is relevant to reduce uncertainties when simulating the impact of volcanic eruptions on weather and climate. First, I coupled ICON-ART to the 1-D volcanic plume rise model FPlume to better represent the influence of the eruption dynamics on the ESPs. My developments enable simulating individual eruption phases of complex non-continuous eruptions and allow a comparison of modeled plumes to observations close to the volcano. This also permits to directly validate simulated and observed ash aging for the first time. Secondly, I extended a comprehensive gas-phase chemistry mechanism by aqueous-phase chemistry on aged ash and SO_2 adsorption on fresh ash surfaces to study the interaction of chemistry and aerosols beyond ash aging by condensation and nucleation with subsequent coagulation in the plume. Using these new developments, I address the following research questions:

1. How large is the influence of resolving the eruption phases on the predicted ash mass loading?
2. Can an online treatment of volcanic ESPs improve the predicted mass loading and dispersion of ash and SO_2 plumes?
3. What controls the near-source distribution of ash particles?
4. Which processes drive particle aging near the volcano and during the further transport?
5. What is the effect of aqueous-phase chemistry and gas adsorption by ash surfaces on the removal of gaseous SO_2 from the atmosphere in the first days?
6. How large is the effect of in-plume chemistry on background O_3 , OH , and CH_4 concentrations?

Along these research questions, this thesis is structured as follows. Chapter 2 gives information on the theoretical background relevant for this thesis. Afterwards, the ICON-ART modeling system including the new implementations regarding the ESPs and chemistry is introduced in Chapters 3. Chapter 4 describes the simulated cases and observational data to validate the model. The results on the importance of representing eruption phase-dependent ESPs, the analysis and validation of modeled aerosol aging, and the influence of different sulfur oxidation pathways are presented in Chapters 5, 6, and 7, respectively. Finally, Chapter 8 concludes the results and gives an outlook.

2. Volcanic ejection

Chemical reactions and aerosol dynamical processes in the early plumes of explosive volcanic eruptions are known to alter the formation and distribution of climate relevant secondary aerosol particles. Figure 2.1 gives an overview of the processes relevant for volcanic plume development in the first days. The components of this figure are explained in the next sections, starting with an overview on explosive eruptions (Section 2.1) and the plume dynamics (Section 2.2). Afterwards, Section 2.3 provides information on chemical reactions transforming volcanic SO_2 into other species. Finally, Section 2.4 contains details on the aerosol dynamical processes leading to secondary aerosol formation, aerosol aging, and their implications for aerosol–radiation interaction in the volcanic plume.

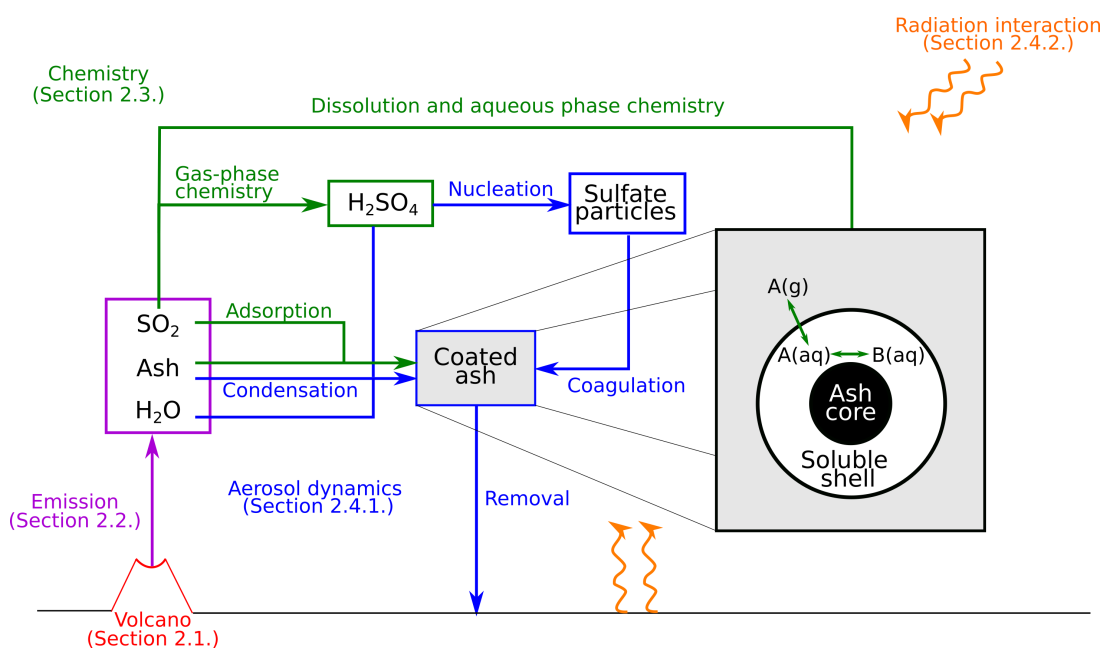


Figure 2.1.: Schematic illustration displaying the processes relevant for volcanic aerosols. The sections for background information are given in brackets. The box on the right side zooms into the processes happening on coated aerosol particles. The lengths are not to scale.

2.1. Volcanic eruptions from the volcanological perspective

Volcanic eruptions release lava, tephra, and gases from vents or fissures (Schmincke, 2004). Lava is defined as magma that reaches the Earth’s surface through a volcanic eruption. Tephra is a general term for all solid materials ejected into the atmosphere during a volcanic eruption. It ranges from very fine ash particles up to large fragments of rocks such as volcanic bombs. The composition of the gaseous mixture

that is released during an eruption strongly depends on the tectonic setting and the volcanic activity. Usually, the most abundant gases are water vapor (35 – 90 mol%), carbon dioxide (CO₂, 5 – 50 mol%), SO₂ (2 – 30 mol%), HCl, and hydrogen fluoride (HF) (Schmincke, 2004).

Magma is formed by partial melting of rocks in the Earth's mantle or in the lower crust, typically at depths from 10 to 200 km (Jain, 2014). It is a mixture of minerals and a small amount of dissolved gases. Any magma found on Earth consists to 99% of the ten elements silicon (Si), titanium (Ti), aluminium (Al), iron, magnesium (Mg), calcium (Ca), sodium (Na), potassium (K), hydrogen (H), and oxygen (O). However, the main difference of magma from different sites is the amount of silica (SiO₂) and dissolved gases. According to the SiO₂ content, magma can be divided into four main types: basaltic (48 – 52% SiO₂), andesitic (52 – 63% SiO₂), dacite (63 – 68% SiO₂), and rhyolite magma (68 – 77% SiO₂). With increasing SiO₂ content of the magma, the exit temperature decreases. The magma becomes less viscous, which influences also the plume dynamics (Section 2.2) by an exit velocity increase. Magmas with a high SiO₂ content are richer in sodium and potassium, but contain less iron, magnesium, and calcium compared to magmas with lower SiO₂ content (Jain, 2014). Beside the impacts on the plume dynamics, the composition of magma is directly linked to the composition of the dispersed ash particles with effects on the radiative properties (e.g., Pollack et al., 1973) and adsorption of gases (Maters et al., 2017).

There exist three volcanic eruption mechanisms (Schmincke, 2004): Magmatic, phreatomagmatic, and phreatic eruptions. In the magma reservoir, gases are usually dissolved under high pressures, and the magma is undersaturated in volatile compounds. During magmatic eruptions, magma ascends, which decreases the pressure of the rising magma. Moreover, the partial pressure of volatile compounds increases until supersaturation with respect to one or more gas species. Additionally, decreasing temperatures during the ascent lead to crystallization of the melt and, thus, the volatile compounds become more concentrated in the melt. In the following, gas bubbles start to grow. The growth of bubbles is complex and depends on the viscosity of the magma, the diffusivity, temperature, lithostatic pressure, concentration of volatiles, and the separation of bubbles from the melt. The presence of bubbles decreases the density of the melt, which increases the buoyancy and the ascent velocity of the magma. However, the viscosity increases with the loss of volatiles in the melt, which counteracts the increase of ascent velocity by buoyancy. Tephra and volcanic gases are finally released by an explosive decompression at the surface. During phreatic (or steam-blast) eruptions, magma heats ground or surface water, which evaporates water almost instantaneously and results in a steam explosion. Besides steam, the explosion ejects solid materials from fracturing the surrounding rocks, but no new magma. Phreatomagmatic eruptions are governed or triggered by contact of magma with water. Different from phreatic eruptions, phreatomagmatic eruptions can contain magmatic fragments (Schmincke, 2004). The mechanisms which trigger volcanic eruptions are diverse. An overview is given in Schmincke (2004).

In this thesis, the 2019 Raikoke and 2021 La Soufrière eruptions are investigated, which were both magmatic eruptions. The magma compositions of the Raikoke and the La Soufrière volcanoes are basaltic and basaltic-andesite, respectively (McKee et al., 2021; Joseph et al., 2022).

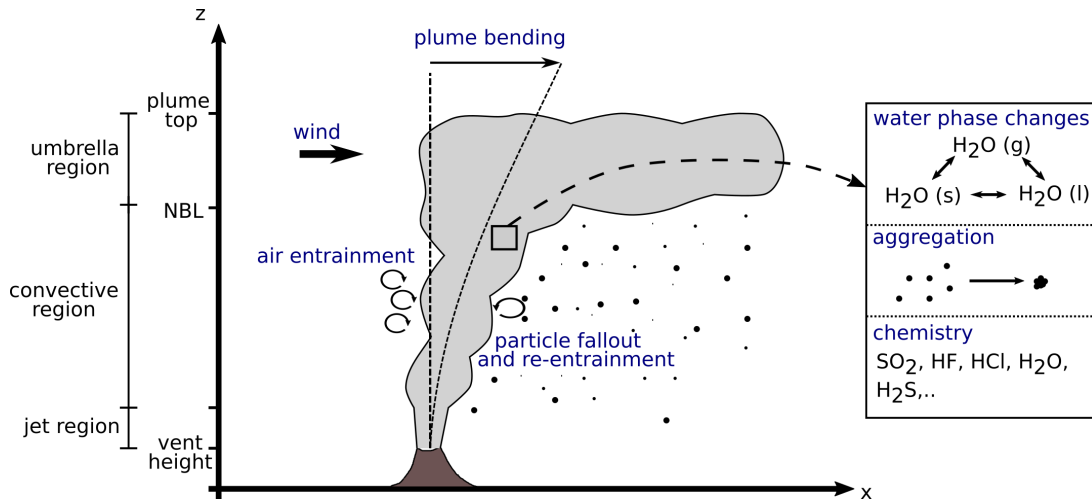


Figure 2.2.: Plume regions for large volcanic eruptions and dynamic processes relevant for plumes to reach the top height. The lengths are not to scale.

2.2. Plume dynamics of explosive volcanic eruptions

The development of an explosive volcanic eruption plume is driven by both volcanic and atmospheric conditions. During explosive eruptions, volcanoes release hot tephra and gases at high velocities into the atmosphere. The exit velocity, exit temperature, exit volatile fraction, and the vent radius determine the MER. The higher the exit velocity and the larger the vent radius, the higher is the MER. A larger exit temperature or a higher exit volatile fraction reduce the MER due to a lower density of the mixture. The total MER E_{tot} at the vent can be expressed by

$$E_{tot} = \pi r_v^2 \hat{\rho} v_e^2 \quad (2.1)$$

with r_v the vent radius, $\hat{\rho}$ the mixture density at the vent, and v_e the exit velocity (e.g., Folch et al., 2016). The volcanic eruption plumes consist of three main regions (Sparks et al., 1997). The dynamics are explained by using Figure 2.2. In the lowest region, the jet or gas-thrust region, the remaining momentum is the main driver of the upward motion of the mixture. In the atmosphere, ambient air is entrained into the plume by turbulent mixing. The entrained air heats and expands and thereby reduces the density of the plume until it becomes buoyant, i.e., the plume density is lower than the atmospheric density, and convection drives the plume upward. This part of the plume is called the convective region. The mixture rises and further cools until the height of the Neutral Buoyancy Level (NBL) is reached. This is where the plume density equals the ambient air density. The umbrella region forms above the NBL up to the plume top due to overshooting of the plume (Sparks et al., 1997). Here, the plume spreads horizontally by gravity currents and winds (e.g., Costa et al., 2013).

The atmosphere influences the plume by entrainment of air (e.g., Tate and Middleton, 2000; Carazzo et al., 2006, 2008) and wind effects (Bursik, 2001). The entrainment of less dense air, i.e., moist and / or

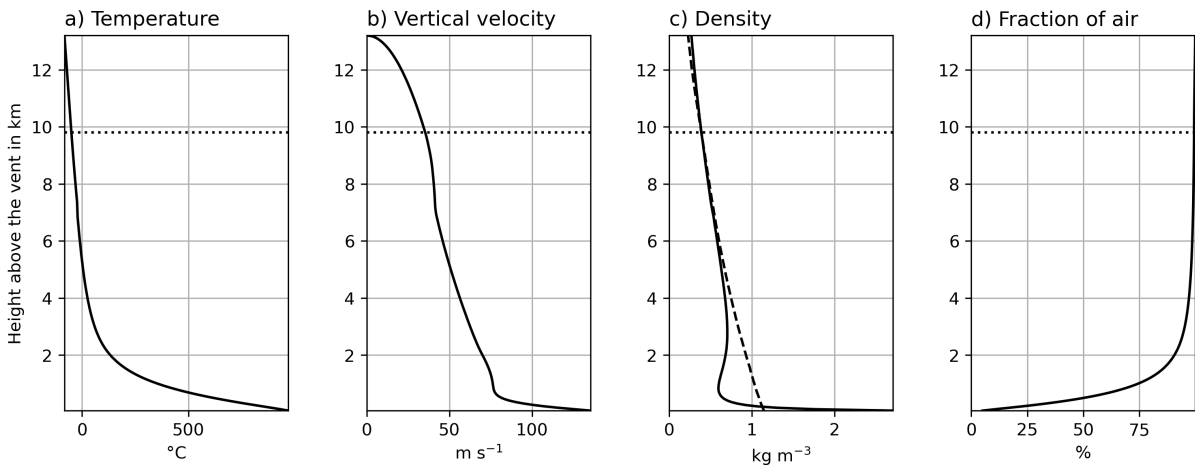


Figure 2.3.: Vertical profiles of temperature in $^{\circ}\text{C}$, velocity in m s^{-1} , plume (solid line) and air (dashed line) density in kg m^{-3} , and fraction of air in % obtained from the FPlume model for the 2019 Raikoke eruption. The dotted line indicates the NBL.

warmer air, reduces the mixture density of the plume faster and increases the buoyancy. Hence, the plume can reach higher altitudes or in other words, a smaller MER is needed to drive the plume up to a certain altitude. The wind has two opposite effects on the plume dynamics. On the one hand, stronger winds and especially a large radial and vertical wind shear increase the entrainment of ambient air into the plume, which increases the buoyancy. On the other hand, plume bending is larger in case of a higher wind velocity, which results in a lower plume top. Further important processes within volcanic plumes are the aggregation of particles (Brown et al., 2012), particle fallout, and the re-entrainment of particles (Ernst et al., 1996). Latent heat release by water-phase changes is an important source of energy that can drive the plume higher up in the atmosphere (Woods, 1993).

Figure 2.3 shows examples of vertical profiles of the temperature, the vertical velocity, the density of the plume and the atmospheric air and the fraction of entrained air for the 2019 Raikoke eruption derived from the 1-D volcanic plume rise model FPlume. The NBL is indicated by the dotted line. The temperature decreases quickly with height as the fraction of entrained colder air increases. This also reduces the plume density. The transition from the jet to the convective phase occurs at about 150 – 200 m altitude, where the curves of the air density and plume density intersect. In the lower convective region, the upward motion is still partly driven by momentum, however, the influence reduces with increasing altitude until approximately 800 m. The gradient in the vertical velocity becomes smaller, because the buoyancy is the major force rising the plume further upward. The gradient of the plume density changes the sign between 1 and 2 km because the entrainment of air gets lower whereas the reduction in temperature is still strong. Both the reduced air entrainment and the latent heat release in the plume lead to a smaller reduction of the plume density in the convective region than in the jet and lower convective region.

A number of models types exist that cover different processes related to volcanic plumes in the atmosphere (Textor et al., 2005). Plume models include a detailed description of the eruption plume dynamics

and allow the investigation of the plume development at the emission source. It is differentiated between three-dimensional (3-D) models considering the whole volume of the plume (e.g., ATHAM by Oberhuber et al. (1998)) and 1-D models, which calculate the plume development along the vertical plume axis (e.g., FPlume by Folch et al. (2016)).

2.3. Atmospheric chemistry

Chemical compounds enter the atmosphere by emissions from natural and anthropogenic sources. Chemical reactions transform these compounds into others and can present both sinks and sources for species. These compounds can also be removed by wet and dry deposition. Dry deposition describes the transfer of species to the Earth's surface without the aid of precipitation and occurs by turbulent diffusion. Wet deposition comprises all processes by which gases and particles are transferred to the Earth's surface in aqueous form. Gases can dissolve in airborne droplets such as cloud droplets, rain or fog. These droplets are removed from the atmosphere by precipitation (Seinfeld and Pandis, 2006).

Sections 2.3.1 to 2.3.3 introduce gas-phase chemistry, the dissolution of gases in water, and aqueous-phase chemistry. In each of these sections, examples which are relevant for the oxidation of (volcanic) SO₂ are given in order to demonstrate the implications of chemistry in case of volcanic eruptions.

2.3.1. Gas-phase chemistry

Chemical reactions can be unimolecular (first-order reaction), bimolecular (second-order reaction), and termolecular (third-order reaction).

1. Unimolecular reactions describe a decomposition of a molecule A into molecules B and C without intervention of a second molecule:



A typical example for a unimolecular reaction is the photolysis of species in the atmosphere or radioactive decay. The efficiency of a unimolecular reaction is expressed by the rate constant k_1 (in s⁻¹), which is related to the change of the number concentration $[A]$ of a compound A over time t as

$$\frac{d[A]}{dt} = -k_1[A]. \quad (2.2)$$

When assuming a constant k_1 over time, the integration of Equation (2.2) leads to an exponential decrease of $[A]$ over time. In chemical reactions, photolysis is indicated by $h\nu$ ($A + h\nu \rightarrow B + C$) with the Planck's constant h and the radiation frequency ν .

2. Bimolecular reactions are the most common kinetic reactions. They take place between two colliding reactants:



The temporal evolution of $[A]$ depends on the number concentrations of both compounds A and B and is given by

$$\frac{d[A]}{dt} = -k_2[A][B] \quad (2.3)$$

with k_2 the rate constant in $\text{cm}^3 \text{s}^{-1}$. Following Arrhenius (1889), k_2 is temperature-dependent and reads as

$$k_2(T) = A \exp\left(-\frac{\hat{E}}{R^*T}\right) \quad (2.4)$$

with T the temperature, $R^* = 8.314 \text{ J mol}^{-1} \text{ K}^{-1}$ the universal gas constant, and A and \hat{E} reaction-dependent parameters derived from experiments.

3. In termolecular reactions two molecules collide and produce an energetic intermediate:



By collision with a third body M (in the atmosphere either nitrogen (N_2) or O_2), the excess energy is removed and allows the formation of the product:



The rate of formation of the product AB was proposed by Lindemann in 1921 and further developed by Hinshelwood and is given by

$$\frac{d[AB]}{dt} = \frac{k_f k_s [A][B][M]}{k_s [M] + k_b} \quad (2.5)$$

with k_a and k_b the rate constants for the forward and backward reactions in (R3), respectively, and k_s the rate constant of Reaction (R4). $[M]$ is the concentration of the third body and is usually directly related to the atmospheric pressure. If $k_b \gg k_s[M]$, the reaction is third-order:

$$\frac{d[AB]}{dt} = \frac{k_f k_s}{k_b} [A][B][M] \quad (2.6)$$

If $k_b \ll k_s[M]$, the reaction is second-order:

$$\frac{d[AB]}{dt} = k_f [A][B] \quad (2.7)$$

When writing the rate equation in Equation 2.5 as a pseudo-second-order

$$\frac{d[AB]}{dt} = k_3[A][B], \quad (2.8)$$

k_3 can be expressed in terms of the high- and low-pressure limiting values $k_\infty = k_f$ and $k_0 = \frac{k_f k_s}{k_b}$ as

$$k_3 = \frac{k_0[M]k_\infty}{k_0[M] + k_\infty}. \quad (2.9)$$

The region between the low- and high-pressure limits is called the falloff region. However, this Lindemann–Hinshelwood theory assumes that a single collision with a molecule M is sufficient to deactivate AB' to AB. In reality, only a fraction of energy is removed by each collision. Therefore, Troe (1983) modified the rate constant as

$$k_3(T) = \frac{k_0(T)[M]}{1 + \frac{k_0(T)[M]}{k_\infty}} F \left(1 + \left[\log \left(\frac{k_0(T)[M]}{k_\infty} \right) \right]^2 \right)^{-1} \quad (2.10)$$

with

$$k_0(T) = k_0^{300} (T/300)^{-n} \quad (2.11)$$

and

$$k_\infty(T) = k_\infty^{300} (T/300)^{-m}. \quad (2.12)$$

F is the broadening factor and often has the value 0.6. The unit of the rate constant k_3 is $\text{cm}^6 \text{s}^{-1}$.

For more details on the order of reactions and derivations of rate constants, the reader is referred to the textbook by Seinfeld and Pandis (2006).

Stockwell and Calvert (1983) proposed a reaction chain in three steps for the oxidation of SO_2 by OH in the gas phase:



The oxidation of SO_2 is limited by the amount of available OH. In the stratosphere, OH production is mainly driven by the photolysis of O_3 . This reaction produces an oxygen atom in the excited state (O^1D), which can lead to the production of two OH radicals when reacting with H_2O (Seinfeld and

Pandis, 2006). Thus, the formation of H_2SO_4 depends on the diurnal cycle. H_2SO_4 rapidly condensates on existing particles or nucleates to form new sulfate (SO_4^{2-}) aerosols. More details on the processes of nucleation and condensation are given in Section 2.4.1.

2.3.2. Dissolution of gases in water

The dissolution of gas molecules in water is described by equilibrium equations:



This implies that there exists a flux from the gas phase into the aqueous phase and from the aqueous phase to the gas phase depending on the concentration of dissolved gas in water or strictly speaking in the interface between water and gas phase.

The temperature-dependent Henry's law coefficient H_A expresses the equilibrium between a gaseous species and a dissolved species:

$$[\text{A(aq)}] = H_A(T)p_A \quad (2.13)$$

with p_A the partial pressure of A in the atmosphere in atm and $[\text{A(aq)}]$ the concentration of A in the aqueous-phase in mol L^{-1} . The temperature dependence of the Henry's law coefficient is given by the Van't Hoff equation as

$$H_A(T) = H_A^0 \exp\left(-\frac{\Delta_{sol}H}{R^*} \left(\frac{1}{T} - \frac{1}{T^0}\right)\right) \quad (2.14)$$

with H_A^0 the Henry's law coefficient at 298.15 K for species A, $\Delta_{sol}H$ the enthalpy change of the dissolution, T the temperature, and $T^0 = 298.15$ K the reference temperature (Seinfeld and Pandis, 2006).

Henry's law (Equation (2.13)) describes the equilibrium partitioning between gas phase and aqueous phase without any consideration of the time scales of the uptake process. However, the uptake rate of gases to the droplet is a time-dependent process, which is also controlled by several factors such as gas-phase diffusion, interfacial mass transfer, aqueous-phase diffusion, and chemical reactions within the aqueous phase (Schwartz, 1986). For the use in cloud droplets and shells of coated aerosols, it has to be considered that Reaction (R8) also depends on the molecular diffusion of the dissolved gas into the droplet's interior. The flux of gas-phase species A into a droplet is described by the following rate (Jacob, 1986):

$$\Phi_{in} = \frac{3\eta L D_{g,A}}{r^2} [\text{A(g)}] \quad (2.15)$$

with L the LWC in vol vol^{-1} , $D_{g,A}$ the diffusion coefficient of species A in air, r the radius in cm, and $[\text{A(g)}]$ the gas-phase concentration of species A far from the droplet in molecules cm^{-3} . The coefficient correcting for the free molecular effects η was inter alia proposed by Fuchs and Sutugin (1971) as

$$\eta = \left\{ 1 + \left[\frac{1.33 + 0.71Kn^{-1}}{1 + Kn^{-1}} + \frac{4(1 - \alpha)}{3\alpha} \right] Kn \right\}^{-1} \quad (2.16)$$

with α the sticking coefficient. This coefficient represents the probability that a gas molecule impinging on the droplet surface will stick to that surface. The Knudsen number Kn is the ratio of the mean free path of air (λ_{air}) to the characteristic length scale (Seinfeld and Pandis, 2006) (i.e., the droplet radius r here):

$$\text{Kn} = \frac{\lambda_{air}}{r} = \frac{32 \cdot D_{g,A}}{3\pi \cdot (1 + M_A/M_{air}) \cdot \bar{c}_A} \cdot \frac{1}{r} \quad (2.17)$$

with M_A and M_{air} the molar masses of $A(g)$ and air, respectively. \bar{c}_A is the mean speed of $A(g)$ and is given by

$$\bar{c}_A = \left(\frac{8R^*T}{\pi M_A} \right)^{0.5} \quad (2.18)$$

As Reaction (R8) occurs in both directions until an equilibrium is reached, the rate for the flux out of the liquid phase is given by the flux into the aqueous phase (Equation (2.15)) divided by Henry's law (Equation (2.13)) and the LWC:

$$\Phi_{out} = \frac{3\eta D_{g,A}}{r^2} \frac{6.023 \cdot 10^{20} [A(aq)]}{H_A(T)R^*T} \quad (2.19)$$

The factor $6.023 \cdot 10^{20}$ converts the units of the aqueous-phase concentration into units of the gas-phase concentration (Jacob, 1986).

2.3.3. Aqueous-phase chemistry

In an aqueous solution, water ionizes to form a hydrogen ion (H^+) and a hydroxide ion (OH^-). This process is also called autoionization of water. An equilibrium is given by



with an equilibrium constant of $K'_w = \frac{[\text{H}^+][\text{OH}^-]}{[\text{H}_2\text{O}]} = 1.82 \times 10^{-18}$ at 298 K. As the concentration of H_2O molecules is much larger and only few ions are formed, the H_2O concentration can be assumed to be constant. Thus, the equilibrium constant can be approximated by

$$K_w = [\text{H}^+] [\text{OH}^-] = 1.0 \times 10^{-14} \text{ mol}^2 \text{ L}^{-2} \text{ at } 298 \text{ K}. \quad (2.20)$$

As each dissociated water molecule produces one hydrogen and one hydroxide ion, $[\text{H}^+] = [\text{OH}^-] = 1.0 \times 10^{-7} \text{ mol L}^{-1}$ holds. Based on the dissociation of H_2O , the dimensionless pH value is defined as

$$\text{pH} = -\log_{10} [\text{H}^+]. \quad (2.21)$$

At 298 K and for pure water, the pH value is 7.0. Acidic solutions have a pH value below 7.0 and basic solutions have a pH value above 7.0 (Seinfeld and Pandis, 2006).

When dissolving in water, many species also dissociate into ions ($AB(aq) \rightarrow A^- + B^+$). This process is reversible and it reaches an equilibrium quickly. The following example describes the two acidic dissociations of SO_2 in an aqueous solution (Seinfeld and Pandis, 2006):



The aqueous SO_2 solution of the first dissociation (R10) behaves like a weak acid and is also known as sulfurous acid. The second dissociation (R11) has almost no impact at pH values usually occurring in the atmosphere and is only shown for the sake of completeness (Seinfeld and Pandis, 2006). The equilibrium constants of these reactions are given by

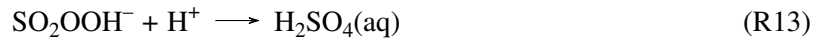
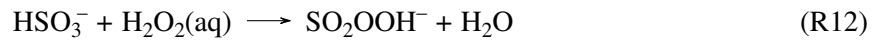
$$K_{s1} = \frac{[H^+][HSO_3^-]}{[SO_2 \cdot H_2O]} \quad (2.22)$$

and

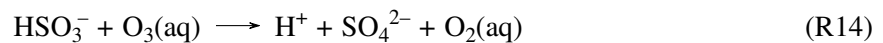
$$K_{s2} = \frac{[H^+][SO_3^{2-}]}{[HSO_3^-]} \quad (2.23)$$

Solving for $[HSO_3^-]$ and $[SO_3^{2-}]$ shows that the higher the concentration of H^+ in the solution (the lower the pH) the more the equilibria are shifted to the left side of the reactions (R10) and (R11). Thus, lower pH values also reduce the solubility of SO_2 in water, since the higher the concentration of $SO_2(aq)$ the lower the flux of SO_2 into the solution (see Section 2.3.2).

In the aqueous phase, HSO_3^- can be oxidized by $H_2O_2(aq)$:

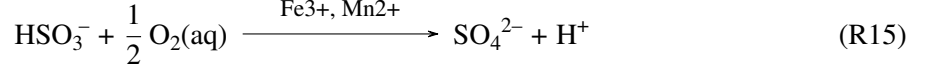


Previous studies found that $H_2O_2(aq)$ is a limiting factor for reaction (R12) (Liang and Jacobson, 1999; Harris et al., 2013; Lachatre et al., 2022). In such cases, HSO_3^- oxidation by $O_3(aq)$ can become an important pathway:



However, Liang and Jacobson (1999) and Harris et al. (2013) showed that the oxidation of HSO_3^- by $O_3(aq)$ is known to be less effective at pH lower 4 or 5.5, respectively.

Finally, when iron and manganese ions (Fe^{3+} , Mn^{2+}) originating from ash or dust particle surfaces are dissolved into the liquid, these can serve as catalysts for the oxidation of HSO_3^- by $\text{O}_2(\text{aq})$ (Harris et al., 2013; Hoshyaripour et al., 2015):



This reaction is responsible for 25% of the oxidation of volcanic SO_2 in the experiments of Lachatre et al. (2022) and, therefore, after the SO_2 oxidation in the gas phase, the second most important SO_2 oxidation pathway for volcanic eruptions in the troposphere.

In aqueous solution, sulfur is often described as S(IV) and S(VI) without further specification. S(IV) is the total dissolved sulfur in oxidation state 4 and comprises the species $\text{SO}_2(\text{aq})$, hydrogen sulfite (HSO_3^-), and sulfite (SO_3^{2-}). S(VI), i.e., sulfur in oxidation state 6, are the oxidized sulfur compounds hydrogen sulfate (HSO_4^-) and SO_4^{2-} .

2.3.4. Adsorption and heterogeneous chemistry

Gas adsorption by aerosols can influence the fate of reactive gases and changes the physiochemical properties of atmospheric aerosols. The probability of gas adsorption by particles is given by the dimensionless uptake coefficient γ . This coefficient is usually determined experimentally as the ratio of the number of adsorbed molecules to the theoretical number of gas–surface collisions. It depends on the particle type (related to the compositions), temperature, and radiation. The rate of adsorption of a gas A can be expressed as a pseudo-first order reaction rate and is given by

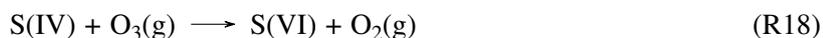
$$R_{ad} = \frac{1}{4} \gamma \bar{c}_A S_p [A] \quad (2.24)$$

with S_p the total surface area per unit volume of air (Seinfeld and Pandis, 2006).

It was shown that a higher SiO_2 content leads to a lower SO_2 adsorption and, thus, a lower uptake coefficient (Maters et al., 2017). Furthermore, the SO_2 uptake increases with decreasing temperature (Schmauss and Keppler, 2014) and UV-radiation flux (Lasne et al., 2022). The surface reactions relevant for the uptake are (Usher et al., 2002)



By heterogeneously reacting with gaseous O_3 the adsorbed S(IV) species can form S(VI)(Usher et al., 2002):



2.4. Atmospheric aerosols

Aerosols can be directly emitted into the atmosphere (e.g., sea salt, soot, pollen, mineral dust). These particles are also called primary aerosols. Secondary aerosols are produced from precursor gases and are not directly emitted. Volcanic eruptions emit ash as primary aerosols. Additionally, SO_2 is oxidized to H_2SO_4 in the gas phase, which is a precursor gas for the formation of sulfate aerosols (secondary aerosols). In this work, only particles are important which remain in the atmosphere for at least several hours to days, i.e., very fine ash and sulfate.

Aerosols have a wide spectrum of size distributions, which range from several nanometers to tens of microns (Whitby, 1978; Boucher, 2015). An aerosol size distribution can be divided into different modes according to their diameter. The diameters range from $0.01 \mu m$ to $0.1 \mu m$ in the Aitken mode, from $0.1 \mu m$ to $1 \mu m$ in the accumulation mode, and from $1 \mu m$ to $10 \mu m$ in the coarse mode. Larger particles are sometimes called supercoarse (Boucher, 2015) or giant mode particles (Muser et al., 2020). The Aitken mode mainly contains particles newly formed from gaseous precursors such as H_2SO_4 . Volcanic ash is typically larger and directly emitted into the accumulation, coarse, and giant mode. However, aerosol dynamical processes can modify a fresh size distribution.

2.4.1. Aerosol dynamical processes

Aerosol dynamical processes modify the size and composition of particles and comprise the processes of nucleation, condensation, coagulation, and sedimentation.

The process of nucleation in general describes the transformation of matter from one phase to another new thermodynamically stable phase, which has not been there before. Depending on whether nucleation occurs on existing foreign material or not, it is differentiated between heterogeneous and homogeneous nucleation, respectively. Furthermore, only a single species (homomolecular) or multiple species (heteromolecular) can be involved. In this work, the aerosol nucleation of sulfate droplets from gaseous H_2SO_4 and H_2O without an existing surface (homogeneous heteromolecular nucleation) is of relevance and the term 'nucleation' is exclusively used for this process throughout this thesis. Nucleation forms particles in the Aitken mode, which can grow by condensation and coagulation and reach larger modes (Seinfeld and Pandis, 2006).

During condensation, gaseous compounds (e.g., H_2SO_4 , H_2O) condense onto the surfaces of pre-existing aerosol particles such as volcanic ash or sulfate particles. It represents a dominant process that transfers mass from the gas to the particulate phase (Boucher, 2015) and leads to a growth of the particles. Conden-

Process	Number concentration	Mass concentration	Median diameter
Nucleation	increase	increase	decrease
Coagulation	decrease	no change	increase
Condensation	no change	increase	increase
Sedimentation	decrease	decrease	decrease

Table 2.1.: Changes in the number concentration, mass concentration, and median diameter due to aerosol dynamical processes.

sation occurs only when supersaturation is reached. H_2SO_4 is a gas with a very low saturation pressure, and, therefore, it condenses fast (Seinfeld and Pandis, 2006).

Coagulation is a process by which aerosol particles collide and stick to each other to form larger particles. It is mainly caused by Brownian motion, but can also result from the particles' motion produced by hydrodynamic, electrical, gravitational or other forces. Coagulation is particularly important when concentrations are large such as within volcanic plumes (Boucher, 2015).

Table 2.1 summarizes the effects aerosol dynamical processes have on the number and mass concentration and the median diameter of a size distribution.

Sedimentation depends on the particle size, shape, and density, and it is larger for bigger particles (Seinfeld and Pandis, 2006). Thus, aerosol aging can increase the sedimentation of aerosols as it was shown for volcanic aerosols by Muser et al. (2020) and dust by Abdelkader et al. (2017). Particles in the size range around half a micron (accumulation mode) have the smallest sedimentation velocity and remain in the atmosphere the longest (Boucher, 2015). In general, particles tend to accumulate in this mode ('accumulation mode') because of both the sedimentation of larger particles and the growth of smaller particles.

Besides leading to the growth of aerosols, condensation and coagulation can form internally mixed particles, which consist of more than one substance. In volcanic plumes, condensation of sulfate and water onto ash particles or coagulation of ash with sulfate particles forms coated ash, also called aged ash. This results in a plume composition with coated and uncoated particles (external mixture of internally mixed particles).

Activation is the process when aerosol particles serve as CCN or INPs for liquid and ice clouds, respectively. This process is reversible by evaporation or sublimation, which leave the remaining aerosol particle behind (Lohmann et al., 2016). Wet deposition either happens when aerosols served as CCN and are removed by precipitation or when aerosols are scavenged by falling hydrometeors (Seinfeld and Pandis, 2006).

2.4.2. Radiative properties of aerosols

Radiation transports energy by propagating electromagnetic waves. These waves consist of oscillating electric and magnetic fields, which propagate at the speed of light ($c = 2.9979 \cdot 10^8 \text{ m s}^{-1}$). The oscilla-

tions can be characterized by their frequency ν or their wavelength λ . They are related to the speed of light by

$$\lambda \nu = c. \quad (2.25)$$

Electromagnetic energy is carried by so called photons with energy $h\nu$, where $h = 6.63 \cdot 10^{-34}$ J s is the Planck's constant. The radiation spectrum emitted by a black body depends on its temperature (Planck's law). It is a distribution of energy contributed by photons of different wavelengths. The higher the temperature of a body the shorter the wavelength spectrum and the more energetic the emitted radiation (Liou, 2002). The solar spectrum is also called SW radiation and its wavelengths lie to 99% between approximately $0.22 \mu\text{m}$ (ultraviolet) and $5 \mu\text{m}$ (near-infrared (near-IR)). 99% of the terrestrial spectrum or LW radiation ranges from $4 \mu\text{m}$ (near-IR) to $100 \mu\text{m}$ (terrestrial IR) (Kraus, 2004).

Aerosols, gases, and clouds can interact with radiation by scattering (change of direction of the incident light) and absorption (conversion of radiation to other forms of energy, e.g, heat). Comprehensive explanations about the interactions of atmospheric constituents and particles with radiation can be found in literature, e.g., Liou (2002), Kraus (2004) or Seinfeld and Pandis (2006). Here, only the necessary basics are replicated.

Scattering and absorption reduce the intensity of radiation passing on the direct path through the atmosphere. The aerosol composition and the wavelength of the radiation determine whether photons are absorbed, scattered, or transmitted. The complex refractive index describes the optical properties of a particle as

$$B_\lambda = \text{Re}(B_\lambda) + i\text{Im}(B_\lambda). \quad (2.26)$$

B_λ is a wavelength-dependent property, which depends on the material of the particle. The real part $\text{Re}(B_\lambda)$ is the ratio of the speed of light in vacuum to the phase speed in the scattering medium (here in the atmosphere). The imaginary part $\text{Im}(B_\lambda)$ is a measure of the absorption efficiency of a medium. Based on the absorption efficiency, we can define a wavelength-dependent volume absorption coefficient β_a in m^{-1} as

$$\beta_a = \frac{4\pi\text{Im}(B_\lambda)}{\lambda}. \quad (2.27)$$

The sum of scattering and absorption is also called extinction. The Beer–Lambert law describes the wavelength-dependent attenuation of incident radiance I_λ when passing through a medium between two points in space z_1 and z_2 by

$$I_\lambda(\lambda, z_2) = I_\lambda(\lambda, z_1) \exp\left(-\int_{z_1}^{z_2} \beta_e(\lambda, z) dz\right) = I_\lambda(\lambda, z_1) \exp(-\tau(\lambda, z_1, z_2)) \quad (2.28)$$

with $\beta_e(\lambda, z)$ the volume extinction coefficient and τ the optical depth or optical thickness. In case of extinction by particles in an atmospheric layer, the optical depth is also called aerosol optical depth (AOD). β_e is the sum of the volume absorption coefficient β_a and the volume scattering coefficient β_s .

It can be derived from the extinction cross-section σ_e of a single particle (molecular extinction cross-section) and the number concentration N of the particles by

$$\beta_e(\lambda, z) = \sigma_e(\lambda, z)N(z) = Q_e \cdot A_p = Q_e \cdot \frac{\pi}{4}d_p^2 \quad (2.29)$$

with Q_e the extinction efficiency, A_p the area of the particle cross-section, and d_p the particle diameter. The volume scattering and absorption coefficients are defined comparably.

The ratio between the extinction by scattering and the total extinction is defined as the single scattering albedo (SSA):

$$\omega = \frac{\beta_s(\lambda)}{\beta_s(\lambda) + \beta_a(\lambda)} \quad (2.30)$$

ω is a dimensionless quantity and it ranges from 0 (extinction by absorption) to 1 (extinction by scattering).

Scattering is a physical process that occurs at molecules, aerosols, and cloud droplets. Scattering can redirect radiation in any direction. However, in atmospheric models the complexity is reduced to the relation of forward and backward scattering by the dimensionless asymmetry parameter g defined as

$$g = \int_{-1}^{+1} p(\theta) \cos(\theta) d\theta \quad (2.31)$$

with p the scattering phase function and θ the scattering angle. The asymmetry parameter ranges from -1 (pure backward scattering) to 1 (pure forward scattering). When the amount of backward and forward scattered photons is the same, g becomes equal to zero.

The distribution of angles of scattered radiation relative to the incident radiation depends on the dimensionless effective particle size:

$$x = \frac{\pi d_p}{\lambda} \quad (2.32)$$

Different scattering regimes were defined for typical particle sizes and wavelengths (Figure 2.4). Scattering at air molecules is negligible for most wavelengths of the solar and terrestrial spectrum. However, volcanic aerosols scatter radiation in the Rayleigh and Mie scattering regime (indicated by the grey box in Figure 2.4).

The theory of Mie (1908) describes the interaction of a plane electromagnetic wave and a spherical, isotropic, homogeneous, and non-magnetic particle. According to the theory, the optical properties of these particles only depend on the refractive index B_λ and the size parameter x . Extensions exist for stratified spheres, which allow to compute the scattering properties of internally mixed particles such as coated ash aerosols (Toon and Ackerman, 1981; Tarcea, 2004). Volcanic ash particles are highly non-spherical (Johnson et al., 2012). Hoshyaripour et al. (2019) found in a model that assuming non-sphericity of dust particles can reduce differences between modeled and observed total attenuated backscatter signals or other derived scattering properties (Hoshyaripour et al., 2019). Moreover, assuming Mie theory to analyze reflectance measurements from remote sensing instruments can cause significant errors in the AOD

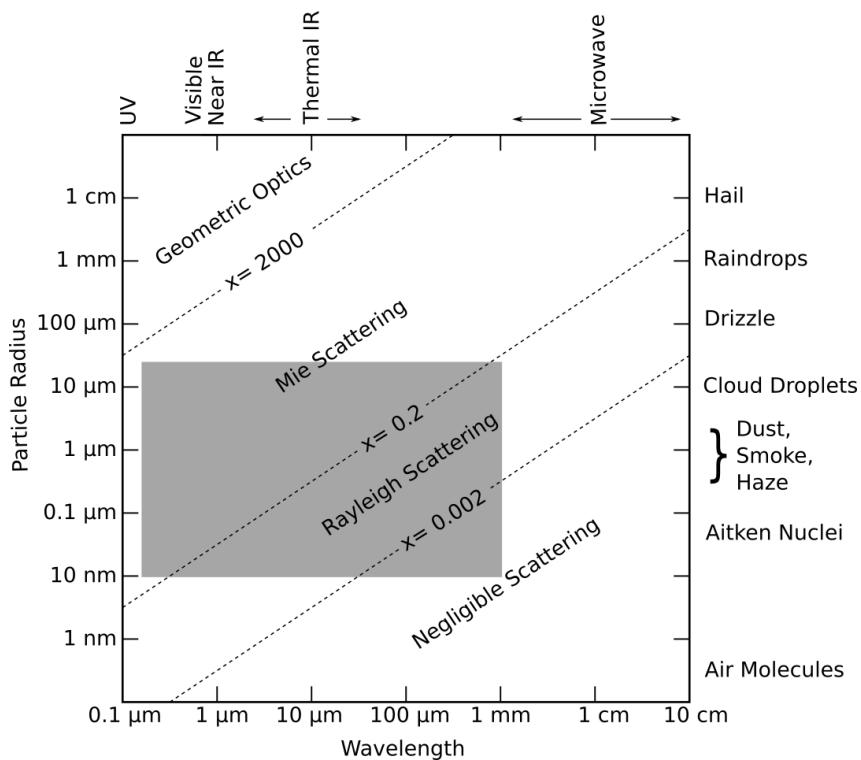


Figure 2.4.: Scattering regimes as a function of particle size and wavelength for typical atmospheric particles and wavelengths. The grey box highlights the wavelengths and particle sizes of volcanic aerosols that are relevant in this work. Adapted from Petty (2004).

(Mishchenko et al., 1995, 1997). Volcanic ash aging increases the sphericity of ash particles because liquid components condense on them and can build up a liquid shell.

The effects of aerosol–radiation interaction can be direct, semi-direct, and indirect. Absorption and scattering of solar and terrestrial radiation by aerosols can directly affect the Earth’s radiation budget. Volcanic aerosols can scatter incoming SW radiation and reduce the energy reaching the ground. This can lead to a cooling of the surface. Moreover, volcanic aerosols can absorb SW and LW radiation and heat the surrounding atmospheric layer. Heating of atmospheric layers can introduce a semi-direct effect. For example, local temperature changes due to absorption of radiation by volcanic aerosols can lead to changing wind patterns in the stratosphere (Niemeier et al., 2021). Finally, volcanic aerosols can act as CCN (mainly sulfate, Lohmann et al. (2016)) or INP (mainly ash, e.g., Isono et al. (1959a,b); Hoyle et al. (2011); Steinke et al. (2011)), which indirectly change the appearance of clouds (e.g., Twomey, 1974), and, thereby, affect the radiation budget (e.g., Malavelle et al., 2017; Haghighatnasab et al., 2022).

3. ICON-ART modeling system

This work uses ICON-ART to study volcanic eruptions. The ICON model for weather forecasts and climate simulations including the submodule ART for aerosols and trace gases is jointly developed at the German Weather Service (DWD), the Max-Planck-Institute for Meteorology (MPI-M), the German Climate Computing Center (DKRZ), and the Karlsruhe Institute of Technology (KIT). It allows seamless predictions from local to global scale (Zängl et al., 2015; Heinze et al., 2017; Giorgetta et al., 2018). ICON provides physics packages for climate projections, for numerical weather predictions, and for large eddy mode simulations. These configurations mainly differ in the physical parametrizations of subgrid processes, and the package choice depends on the application and the scale.

In the following, I first introduce ICON (Section 3.1) and ART (Section 3.2) in general. In my work, I included extensions for online volcanic emissions to improve the ESPs in ART, which is described in Section 3.3. Section 3.4 describes the representation of aerosol dynamical processes in ICON-ART, of which Muser (2022) studied the implications in detail. Section 3.5 describes the approaches to include chemical depletion in ICON-ART and the aqueous-phase chemistry mechanism I implemented to study the contribution of different processes in the conversion of gaseous SO_2 .

3.1. ICON model

ICON is a general circulation model that solves the full three-dimensional nonhydrostatic and compressible Navier-Stokes equations on a horizontally unstructured triangular grid. Therefore, a regular icosahedron is projected onto a sphere. Further refinements of the triangular grid achieve a higher horizontal resolution, which is denoted by $RnBk$. n is the number of equal sections the icosahedron is initially divided into, followed by k subsequent edge bisections. The average horizontal grid spacing $\overline{\Delta x}$ of the grid is then given by

$$\overline{\Delta x} = \sqrt{\frac{S_{earth}}{n_{cells}}} = \sqrt{\frac{4R_{earth}^2\pi}{n_{cells}}} \approx \frac{5050}{n2^k} \quad (3.1)$$

with S_{earth} the Earth's surface in km^2 , n_{cells} the number of grid cells given by $20n^24^k$, and R_{earth} the Earth's radius in km.

Nests are local refinements of the grid. In this work, the grid spacing of a nest is halved compared to the grid spacing of the coarser domain. ICON can further be used in the Limited Area Mode (LAM), which avoids the use of multiple nests to reach a desired grid spacing locally. The model then only simulates a chosen area, but the variables at the boundaries are regularly updated.

The dynamical core of ICON is based on the prognostic variables suggested by Gassmann and Herzog (2008). It numerically solves the momentum equations (Equations (3.2) and (3.3)), the continuity equation (Equation (3.4), conservation of mass), and the first law of thermodynamics (Equation (3.5), conservation of energy) and reads as follows:

$$\frac{\partial v_n}{\partial t} + \frac{\partial K_h}{\partial n} + (\zeta + f)v_t + w \frac{\partial v_n}{\partial z} = -c_{pd}\theta_v \frac{\partial \Pi}{\partial n} + f_F(v_n) \quad (3.2)$$

$$\frac{\partial w}{\partial t} + \mathbf{v}_h \cdot \nabla w + w \frac{\partial w}{\partial z} = -c_{pd}\theta_v \frac{\partial \Pi}{\partial z} - g_z \quad (3.3)$$

$$\frac{\partial \rho_a}{\partial t} + \nabla \cdot (\mathbf{v}\rho_a) = 0 \quad (3.4)$$

$$\frac{\partial \rho_a \theta_v}{\partial t} + \nabla \cdot (\mathbf{v}\rho_a \theta_v) = \tilde{Q} \quad (3.5)$$

with

$$\Pi = \left(\frac{R_d}{p_{00}} \rho_a \theta_v \right)^{R_d/c_{vd}} \quad (3.6)$$

the Exner function.

The prognostic variables are the horizontal wind component normal to the triangle edges v_n , the horizontal wind velocity tangential to the triangle edges v_t , the vertical wind component w , the density ρ_a , and the virtual potential temperature θ_v . Additional variables are the three-dimensional wind vector $\mathbf{v} = (v_t, v_n, w)$, the horizontal wind vector \mathbf{v}_h , the time t , the height z , the vertical component of the relative vorticity ζ , the Coriolis parameter f , the horizontal component of the kinetic energy $K_h = \frac{1}{2}(v_n^2 + v_t^2)$, the specific heat capacity of dry air at constant pressure c_{pd} and at constant volume c_v , the gas constant of dry air R_d , the acceleration due to gravity g_z , and the reference pressure $p_{00} = 1000$ hPa. Furthermore, $\frac{\partial}{\partial n}$ denotes a horizontal derivative normal to the triangle edges. $f_F(v_n)$ are the source and sink terms for horizontal momentum (e.g., due to friction and turbulence), and \tilde{Q} are the diabatic heat source terms. For more details on the dynamical core of ICON, the reader is referred to Zängl et al. (2015).

3.2. ART submodule

The ART submodule supplements the ICON model by including emissions, transport, aerosol dynamics, and gas-phase chemistry in the troposphere and stratosphere (Rieger et al., 2015; Weimer et al., 2017; Schröter et al., 2018; Muser et al., 2020). For each aerosol or chemical species a transport equation needs to be solved in ICON-ART. These equations are Hesselberg-averaged, which means that a variable Ψ can be decomposed into a barycentric mean with respect to the air density ρ_a and its fluctuations:

$$\hat{\Psi} = \Psi - \Psi'' = \frac{\rho_a \Psi}{\bar{\rho}_a} \quad (3.7)$$

Here, variables with a bar on top are Reynolds-averaged. The total time derivative and the continuity equation read as

$$\frac{\hat{d}}{dt} = \frac{\partial}{\partial t} + \hat{\mathbf{v}} \cdot \nabla \quad (3.8)$$

and

$$\frac{\hat{d}\bar{\rho}_a}{dt} = -\bar{\rho}_a \nabla \cdot \hat{\mathbf{v}} \quad (3.9)$$

with $\hat{\mathbf{v}}$ the barycentric mean of the velocity (Rieger et al., 2015).

3.2.1. Aerosol tracers

The size distribution of the aerosols is represented by several log-normal distributions. When assuming externally mixed aerosols, each aerosol mode l has one prognostic variables for both the number concentration and the mass mixing ratio, which are transported ('two-moment scheme'). Internally mixed aerosol modes are described by one prognostic variable for the number concentration and additional prognostic variables for the mass mixing ratios of all compounds in the mode. More details on the treatment of internally mixed aerosols are given in Section 3.4. This section focuses on the general description of the log-normal distributions and transport equations exemplary on the basis of externally mixed particle.

The Hesselberg-averaged specific number concentration $\hat{\Psi}_{0,l}$ and mass mixing ratio $\hat{\Psi}_{3,l}$ of a mode l are given by

$$\hat{\Psi}_{0,l} = \frac{\overline{\rho_a \frac{N_l}{\rho_a}}}{\rho_a} = \frac{\overline{N_l}}{\rho_a} \quad (3.10)$$

and

$$\hat{\Psi}_{3,l} = \frac{\overline{\rho_a \frac{M_l}{\rho_a}}}{\rho_a} = \frac{\overline{M_l}}{\rho_a} \quad (3.11)$$

with N_l the number concentration, M_l the mass concentration, and ρ_a the density of air. These two expressions represent the zeroth and third moment of the size distribution of mode l . The log-normal distributions for the mass specific number concentration and mass mixing ratio as functions of the aerosol diameter d_p are given by

$$\hat{\psi}_{0,l}(\ln d_p) = \frac{\hat{\Psi}_{0,l}}{\sqrt{2 \cdot \pi \cdot \ln \sigma_l}} \cdot \exp\left(-\frac{(\ln d_p - \ln d_{0,l})^2}{2 \cdot \ln^2 \sigma_l}\right) \quad (3.12)$$

and

$$\hat{\psi}_{3,l}(\ln d_p) = \frac{\hat{\Psi}_{3,l}}{\sqrt{2 \cdot \pi \cdot \ln \sigma_l}} \cdot \exp\left(-\frac{(\ln d_p - \ln d_{3,l})^2}{2 \cdot \ln^2 \sigma_l}\right). \quad (3.13)$$

Besides $\hat{\Psi}_{0,l}$ ($\hat{\Psi}_{3,l}$), the shape parameters of the log-normal distribution are the standard deviation σ_l and the median diameter $d_{0,l}$ ($d_{3,l}$). In ART, the standard deviation σ_l is kept constant during the whole simulation, which allows to calculate the diameter of the number distribution as

$$d_{0,l} = \sqrt[3]{\frac{\hat{\Psi}_{3,l}}{\frac{\pi}{6} \cdot \rho_p \cdot \exp\left(\frac{9}{2} \cdot \ln^2 \sigma_l\right) \cdot \hat{\Psi}_{0,l}}} \quad (3.14)$$

with ρ_p the particle density. The median diameter of the number concentration can be converted to the median diameter of the mass distribution with

$$\ln(d_{3,l}) = \ln d_{0,l} + 3 \cdot \ln^2 \sigma_l. \quad (3.15)$$

The transport equations for the specific number concentration and mass mixing ratio for aerosol tracers in flux-form read as

$$\begin{aligned} \frac{\partial \overline{\rho_a \hat{\Psi}_{0,l}}}{\partial t} = & -\nabla \cdot (\hat{\mathbf{v}} \overline{\rho_a \hat{\Psi}_{0,l}}) - \nabla \cdot (\overline{\mathbf{v}'' \rho_a \Psi_{0,l}''}) - \frac{\partial}{\partial z} (v_{sed,0,l} \overline{\rho_a \hat{\Psi}_{0,l}}) \\ & - W_{0,l} - Ca_{0,l} + Nu_{0,l} + E_{0,l} \end{aligned} \quad (3.16)$$

and

$$\begin{aligned} \frac{\partial \overline{\rho_a \hat{\Psi}_{3,l}}}{\partial t} = & -\nabla \cdot (\hat{\mathbf{v}} \overline{\rho_a \hat{\Psi}_{3,l}}) - \nabla \cdot (\overline{\mathbf{v}'' \rho_a \Psi_{3,l}''}) - \frac{\partial}{\partial z} (v_{sed,3,l} \overline{\rho_a \hat{\Psi}_{3,l}}) \\ & - W_{3,l} - Ca_{3,l} + Nu_{3,l} + Co_{3,l} + E_{3,l}. \end{aligned} \quad (3.17)$$

Here, the terms $\nabla \cdot (\hat{\mathbf{v}} \overline{\rho_a \hat{\Psi}_{k,l}})$ and $\nabla \cdot (\overline{\mathbf{v}'' \rho_a \Psi_{k,l}''})$ denote the changes of the k -th moment of mode l due to advection and turbulent fluxes, respectively. $\frac{\partial}{\partial z} (v_{sed,k,l} \overline{\rho_a \hat{\Psi}_{k,l}})$ describes the sedimentation flux with $v_{sed,k,l}$ the sedimentation velocity. $W_{k,l}$ and $Ca_{k,l}$ represent the removal of particles due to wet deposition and coagulation, respectively. Wet deposition in ICON-ART considers the scavenging by raindrops below clouds. The particle formation due to nucleation $Nu_{k,l}$ is only considered for the Aitken mode ($l = Ait$). $Co_{3,l}$ describes the increase in mass due to condensation of gaseous compounds onto mode l and is only a source term for the third moment. Finally, $E_{k,l}$ denotes the emission.

For a comprehensive description of the advection scheme and more information on the parametrization of the turbulent fluxes, the sedimentation flux, and the wet deposition, the reader is referred to Rieger et al. (2015), Rieger (2016), and references therein. Recent developments in ICON-ART include the representation of nucleation, condensation, and coagulation (Section 3.4). These processes lead to the formation of new particles and aging of aerosols.

3.2.2. Gas-phase tracers

The barycentric-averaged mass mixing ratio of a chemical tracer in ICON-ART is expressed by the ratio of the partial density of a gas g and the density of air ρ_a :

$$\hat{\Psi}_g = \frac{\overline{\rho_a \frac{\rho_g}{\rho_a}}}{\overline{\rho_a}} = \frac{\overline{\rho_g}}{\overline{\rho_a}} \quad (3.18)$$

The evolution of a chemical tracer g in time and space is given by the diffusion equation for gases (here in flux-form) as

$$\frac{\partial(\overline{\rho_a \hat{\Psi}_g})}{\partial t} = -\nabla \cdot (\hat{\mathbf{v}} \overline{\rho_a \hat{\Psi}_g}) - \nabla \cdot (\overline{\rho_a \mathbf{v}'' \Psi_g''}) + P_g - L_g + E_g. \quad (3.19)$$

The terms on the right hand side of the equation are the flux divergence that contain the horizontal and vertical advection of the tracer, the changes by turbulent fluxes, the chemical production rate, chemical loss rate, and the emission.

3.3. Emissions from volcanic eruptions with FPlume¹

In previous versions of ICON-ART, volcanic eruptions were parameterized by a very simplistic approach. The total MER E_{tot} was calculated using the empirical relationship by Mastin et al. (2009):

$$E_{tot} = \left(\frac{1}{0.3535} H \right)^{\frac{1}{0.241}} \quad (3.20)$$

with H the height of the plume in km. Then, the MER was multiplied by a fixed factor to only consider the very fine ash, which is relevant for the long-range transport of ash in the atmosphere. Afterwards, the mass was distributed over three ash modes (accumulation, coarse, and giant) and emitted along a Gaussian profile of the following shape:

$$f_e(z^*) = 0.0076 + 0.9724 \cdot \exp \left(- \left(\frac{z^* - 0.4481}{0.3078} \right)^2 \right) \quad (3.21)$$

with $z^* = z/H$ the normalized plume height. Equation (3.21) was afterwards normalized by its integral to ensure the correct total ash mass emissions and units at discrete point sources in each model layer between bottom and top height of the plume:

$$E(z^*) = E_{tot} \frac{f_e(z^*)}{\int_0^1 f_e(z^*) dz^*} \quad (3.22)$$

¹Parts of this section are adapted from: Bruckert, J., G. A. Hoshyaripour, Á. Horváth, L. O. Muser, F. J. Prata, C. Hoose, and B. Vogel, 2022: Online treatment of eruption dynamics improves the volcanic ash and SO₂ dispersion forecast: case of the 2019 Raikoke eruption. *Atmospheric Chemistry and Physics*, **22** (5), 3535–3552, doi:10.5194/acp-22-3535-2022.

This approach was developed for the specific case of the 2010 Eyjafjallajökull eruption (Rieger et al., 2015). However, it is not suitable for all explosive volcanic eruptions as it neglects the setting of the volcano. Furthermore, the feedback between the atmosphere and plume cannot be considered.

This work uses a more generic approach to model the plume dispersion after explosive volcanic eruptions. I coupled the 1-D volcanic plume rise model FPlume by Folch et al. (2016) to ICON-ART. FPlume solves the equations of the buoyant plume theory (Morton et al., 1956) along a vertical plume axis and further considers ambient air entrainment, plume bending due to wind, particle wet aggregation, energy supply due to water phase changes, and particle fallout and reentrainment of particles. FPlume provides two solving strategies. The first one calculates the plume height from a given MER directly. The second strategy derives the MER from a given plume height iteratively by approaching the actual MER with the bisection method (Folch et al., 2016). Figure 3.1 schematically explains the coupling between ICON-ART and FPlume. It shows the case for a FPlume-derived MER based on a prescribed plume height, as usually the MER is unknown, and plume height is available from measurements. Nevertheless, the same procedure also works for prescribed MERs and derived plume heights.

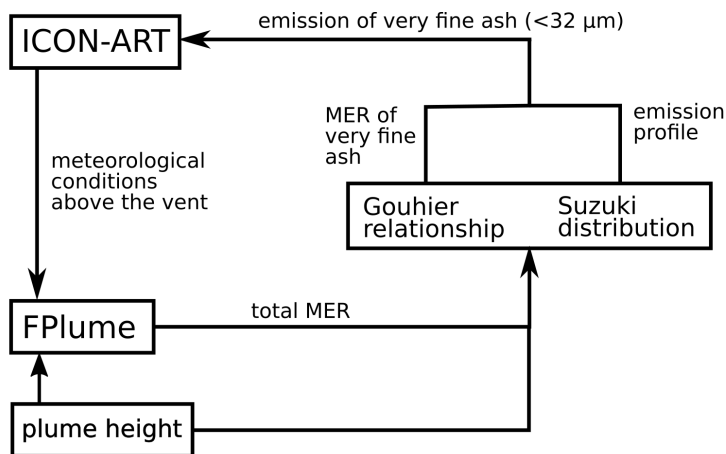


Figure 3.1.: Schematic illustration explaining the coupling between the ICON-ART model and the 1-D plume rise model FPlume for the case of a given plume height. The Gouhier relationship refers to Gouhier et al. (2019). The equation for the Suzuki distribution was derived by Suzuki (1983) and is described in Marti et al. (2017).

The vertical profiles for wind, temperature, pressure, and humidity simulated with ICON serve as meteorological inputs for FPlume. In addition to meteorological data, FPlume needs estimates of the exit temperature, exit velocity, and exit volatile fraction, which depend on the type and setting of the volcano. These values are prescribed (details are given in Section 4.1.3). During every time step in which the volcano should be active, FPlume first calculates the plume properties, i.e., the total MER in the case of a given plume height (as here) or plume height in the case of a given MER. Secondly, the fraction of very fine ash is determined based on the plume height and the total MER by using the relationship of Gouhier et al. (2019). Gouhier et al. (2019) derived fit equations for the very fine ash fraction based on observations of 22 past volcanic eruptions between 1.5 and 40 km plume height. Depending on the SiO_2

content and whether the conduit is opened or closed, different fractions of very fine ash were derived (Table 3.1).

SiO ₂ content	Conduit	Fraction of very fine ash
Low	closed	$25.95E_{tot}^{1.72}H^{1.95}$
	open	$25.95E_{tot}^{1.72}H^{1.40}$
High	closed	$25.95E_{tot}^{1.62}H^{1.95}$
	open	$25.95E_{tot}^{1.62}H^{1.40}$

Table 3.1.: Empirical relationships for the fraction of very fine ash derived by Gouhier et al. (2019).

Using the fraction of very fine ash, ash is emitted into ICON-ART by multiplying the MER of very fine ash with the vertical profile derived from the normalized Suzuki distribution (Suzuki, 1983) in the last step :

$$S^*(z) = \frac{E_{tot} \left(\left(1 - \frac{z}{H} \right) \exp \left(4.0 \left(\frac{z}{H} - 1 \right) \right) \right)^{5.0}}{\text{MAX} \left(S \left(\frac{z}{H} \right) \right)} \quad (3.23)$$

with $S(z)$ the Suzuki distribution as the numerator of the equation. Here, $S(z)$ assumes the same factors as in Marti et al. (2017) and describes the vertical emission profile. E_{tot} is the emission rate of very fine ash and z refers to the vertical coordinate. To ensure the correct total ash mass emission and units when the particles are released into ICON-ART at discrete point sources in each model layer between the bottom and top height of the plume, Equation (3.23) is further normalized by the vertical integral of $S^*(z)$ as it was also done in Equation (3.22).

For the coupling, the mass of particles larger than $32 \mu\text{m}$ is completely disregarded, as this fraction has been shown to be irrelevant for long-range transport (Rose and Durant, 2009). Only the MER is used from FPlume, and the very fine ash fraction and emission profile are calculated independently instead of using the vertical distribution of mass from FPlume due to two main reasons. (1) Offline analysis revealed that the mass profiles for the predefined bin sizes strongly depends on the assumption of the initial total grain size distribution (TGSD) at the vent. As information on the TGSD is often lacking, using FPlume mass profiles leads to a less generic approach and large uncertainties. (2) ICON-ART includes only the ash modes which are relevant for long-range transport, and the size distribution of these modes differs from the TGSD at the vent. Thus, I would have to convert the FPlume size bins into ICON-ART modes, which requires several assumptions and increases the uncertainty of the emissions. More details on the initialization of the ash particles is given in Section 4.1.3.

Besides ash, SO₂ can also be emitted. Different from the ash emission, the current implementation prescribes the MER of SO₂ based on satellite estimates, but it releases the gas into ICON-ART with the

same profile and phases as the ash. This simplification was necessary as usually no further information on temporal SO₂ emission is available. Yet, during volcanic eruptions in general it is possible that the ash and SO₂ are emitted at different phases of the eruption (Thomas and Prata, 2011) or are separated by gravitation in the early stage of the volcanic plume (Schneider et al., 1999; Prata et al., 2017).

3.4. Aerosol dynamic processes

Condensation and coagulation can generate internally mixed particles. Therefore, the three modes previously defined by Rieger et al. (2015) and used in e.g., Gasch (2016) and Hoshyaripour et al. (2019) have been replaced by a set of seven log-normal modes in Muser et al. (2020) for a volcanic particle distribution. Muser et al. (2020) assumed four size ranges with different mixing states, namely the Aitken (as soluble), accumulation (as soluble, insoluble, and mixed), coarse (as insoluble and mixed), and giant mode (as insoluble). Table 3.2 summarizes the components used in the different modes in this work. In case of volcanic eruptions, soluble particles consist of mainly SO₄²⁻ and H₂O, and they occur in the Aitken and accumulation mode. Insoluble particles consist of volcanic ash and exist in the accumulation, coarse, and giant mode. Mixed particles are characterized by an insoluble core coated by soluble substances. In case of volcanic plumes, mixed particles mainly consist of ash coated by SO₄²⁻ and H₂O.

	Insoluble components: Ash	Soluble components: SO ₄ ²⁻ , H ₂ O, ammonium (NH ₄ ⁺), nitrate (NO ₃ ⁻)
Aitken	–	soluble
Accumulation	insoluble, mixed	soluble, mixed, (insoluble)
Coarse	insoluble, mixed	mixed, (insoluble)
Giant	insoluble	–

Table 3.2.: Soluble and insoluble components available in the different mixing states of the Aitken, accumulation, coarse, and giant mode as considered in this work. Brackets indicate when components are needed for technical reasons to enable particle shifting from an insoluble to a mixed mode.

The model solves the prognostic equations for number density (zeroth moment) and mass concentration (third moment) for each mode while keeping the standard deviations of the modes constant, as explained in Section 3.2.1. This induces that the diameter can change due to aerosol dynamics. For the Aitken mode, nucleation, condensation, and coagulation are considered. The accumulation and coarse modes are affected by condensation and coagulation only. Shifting of particles into another modes occurs either when the 5% mass threshold of soluble coating on insoluble particles is exceeded (shift from insoluble to mixed mode) or a threshold diameter of the soluble mode is exceeded (shift into larger mode). The threshold value of 5% is based on Weingartner et al. (1997).

3.4.1. Gas–particle partitioning with ISORROPIA II

The ISORROPIA II model (Fountoukis and Nenes, 2007) was coupled to ICON-ART by Muser et al. (2020) to compute gas–particle partitioning. It is an extension of the ISORROPIA model by Nenes et al.

(1998). ISORROPIA II treats the thermodynamics of the potassium–sodium–magnesium– calcium– ammonium–sodium–sulfate–nitrate–chloride–water (K^+ – Ca^{2+} – Mg^{2+} – NH_4^+ – Na^+ – SO_4^{2-} – NO_3^- – Cl^- – H_2O) aerosol systems and derives an equilibrium state for these species in the gas, liquid, and solid phase. Fountoukis and Nenes (2007) made several assumptions to reduce the computational costs and increase numerical stability. Two assumptions are relevant for this thesis (Muser, 2022). First, as H_2SO_4 has a very low vapor pressure, it is assumed to remain in the aerosol phase after nucleation and condensation. In ICON-ART, the parametrizations used for the nucleation and condensation of H_2SO_4 are independent of ISORROPIA II (Sections 3.4.2 and 3.4.3). Second, in SO_4^{2-} rich solutions, it is assumed that the gaseous species ammonia (NH_3) and the aqueous species NO_3^- and Cl^- do not perturb the thermodynamic equilibrium significantly.

3.4.2. Nucleation

The nucleation of sulfate particles in ICON-ART follows the parametrization of Kerminen and Wexler (1995). New sulfate particles nucleate when a critical concentration c_{crit} of H_2SO_4 is reached, which is given by

$$c_{crit} = 0.16 \exp \left(0.1T - 3.5 \frac{RH}{100} - 27.7 \right) \quad (3.24)$$

with T the temperature in K and RH the relative humidity in %. The unit of the critical concentration is $\mu g m^{-3}$. In ICON-ART, if the H_2SO_4 concentration $c_{H_2SO_4}$ exceeds the critical concentration c_{crit} , the concentration above this threshold nucleates into the soluble Aitken mode with a rate of

$$Nu_{3,sol_Ait} = \frac{c_{H_2SO_4} - \frac{c_{crit}}{\rho_p}}{\Delta t}. \quad (3.25)$$

This parametrization only refers to the mass rate of nucleated particles. The number concentration (in kg^{-1}) is calculated from the assumed size distribution as

$$Nu_{0,sol_Ait} = \frac{6}{\pi \rho_p} \cdot \frac{\exp(4.5 \cdot \ln^2(\sigma_{sol_Ait}))}{d_{0,Ait}^3} \cdot Nu_{3,sol_Ait}. \quad (3.26)$$

A detailed description of the nucleation parametrization is given in Riemer (2002).

3.4.3. Condensation

The gas–particle partitioning for gaseous species in ICON-ART is calculated with the ISORROPIA II model, as described in Section 3.4.1. However, the condensation of H_2SO_4 onto existing particles is parameterized based on Whitby et al. (1991) and was adapted from Riemer (2002). As condensation leads to a growth of existing particles and no new particles are generated, condensation only affects the third moment of the size distribution. The zeroth moment remains unchanged.

The condensation rate of the third moment of mode l is calculated as

$$\tilde{C}_{O_3,l} = \frac{6}{\pi} \chi_T \int_0^\infty \chi(d_{3,l}) \psi_{3,l}(d) dd_{3,l} = \frac{6}{\pi} \chi_T I_l. \quad (3.27)$$

χ_T is size-independent and depends on thermodynamic variables. I_l abbreviates the integral. $\chi(d_{3,l})$ is size-dependent and differs for different size regimes, which are defined by the dimensionless Knudsen number:

$$\text{Kn}_l = \frac{2\lambda_{air}}{d_{0,l}} \quad (3.28)$$

with λ_{air} the mean free path of air. A Knudsen number $\text{Kn} > 10$ defines the free-molecular regime (fm) in which particles behave as free moving particles comparable to air molecules. For $\text{Kn} < 0.1$, the particles are considered to be suspended in air (continuum regime). Kn values between 1 and 10 define the transition regime, and values from 0.1 to 1 indicate the near-continuum regime (nc). The expressions for $\chi(d_l)$ in the near-continuum and free-molecular regimes are given by

$$\chi_{nc}(d_l) = 2\pi D_{g,H_2SO_4} d_l \quad (3.29)$$

and

$$\chi_{fm}(d_l) = \frac{\pi \alpha \bar{c}_{H_2SO_4}}{4} d_l^2 \quad (3.30)$$

with D_{g,H_2SO_4} the diffusion coefficient of H_2SO_4 , α the accommodation coefficient, and $\bar{c}_{H_2SO_4}$ the mean molecular velocity of H_2SO_4 . These two formulations (Equations (3.29) and (3.30)) allow to evaluate the integral I_l for the two regimes separately by

$$I_l^{nc} = 2\pi D_{g,H_2SO_4} M_{1,l} \quad (3.31)$$

and

$$I_l^{fm} = \frac{\pi \alpha \bar{c}_{H_2SO_4}}{4} M_{2,l} \quad (3.32)$$

with $M_{k,l}$ the k -th moment of the particle size distribution. The harmonic mean of both expressions (Equations (3.31) and (3.32)) gives an expression for the condensation rate of the third moment over the entire size range:

$$\tilde{C}_{O_3,l} = \frac{6}{\pi} \chi_T I_l = \frac{6}{\pi} \chi_T \frac{I_{l,fm} \cdot I_{l,nc}}{I_{l,fm} + I_{l,nc}} \quad (3.33)$$

The elimination of χ_T is based on the assumption that the production rate of H_2SO_4 is much slower than its condensation. Hence, an equilibrium state in which the total condensation rate equals the production rate of H_2SO_4 , is reached:

$$\tilde{C}_{O_3} = \sum_l \tilde{C}_{O_3,l} = \dot{M}_3 \quad (3.34)$$

\dot{M}_3 is the third moment production rate of gaseous H_2SO_4 . From the formulation of a dimensionless coefficient

$$\Omega_l = \frac{\tilde{C}o_{3,l}}{\tilde{C}o_3} = \frac{\tilde{C}o_{3,l}}{\dot{M}} = \frac{I_l}{\sum_l I_l} \quad (3.35)$$

the mode-dependent condensation rate follows:

$$\tilde{C}o_{3,l} = \dot{M}_3 \Omega_l \quad (3.36)$$

Thus, the condensation rate not depends on χ_T anymore but on the integral I_l and the production rate of H_2SO_4 . This corresponds to a condensation rate for the mass mixing ratio of

$$Co_{3,l} = \frac{\pi}{6} \frac{\rho_{\text{H}_2\text{SO}_4}}{\rho_a} \dot{M}_3 \Omega_l. \quad (3.37)$$

As \dot{M}_3 is not available in ICON-ART, the condensation rate of the mass mixing ratio is approximated by the H_2SO_4 mass mixing ratio $c_{\text{H}_2\text{SO}_4}$ and the model time step Δt as

$$Co_{3,l} = \frac{c_{\text{H}_2\text{SO}_4}}{\Delta t} \Omega_l. \quad (3.38)$$

3.4.4. Coagulation

Coagulation leads to an increase of the particle median diameter and a reduction of the number concentration. The parametrizations of the coagulation terms $Ca_{0,l}$ and $Ca_{3,l}$ of Equations (3.16) and (3.17) are based on the work of Riemer (2002) and references therein (mainly Whitby et al. (1991)), and are applied in ICON-ART as described in Muser (2022). These works differentiates between intra- and inter-modal coagulation, i.e., coagulation of particles in the same mode and coagulation of particles in different modes, respectively. According to Muser (2022), resulting particles remain in the same mode for intra-modal coagulation and are assigned to the mode with larger diameter for inter-modal coagulation. When a mixed mode is involved, the resulting particle is assigned to the mixed mode. In case of coagulation of an insoluble mode with a soluble mode, the resulting particle first stays in the insoluble mode within the coagulation routine. However, in case the mass of soluble species in the insoluble mode reaches a threshold of 5%, the particle is shifted into the mixed mode in a subsequent routine.

The coagulation rates for the zeroth and third moment are

$$Ca_{0,i} = Ca_{0,ii} + Ca_{0,ij} \quad (3.39)$$

and

$$Ca_{3,i} = Ca_{3,ij} \quad (3.40)$$

with the terms $Ca_{k,ii}$ and $Ca_{k,ij}$ for the intra- and inter-modal coagulation rates of the k -th moment, respectively. i and j denote two different modes. Intra-modal coagulation always reduces the zeroth

moment and does not change the third moment of a particle size distribution. For inter-modal coagulation, the zeroth and third moment can either increase, decrease, or stay the same, depending on the mixing state and the sizes of modes i and j . The zeroth moment of the larger mode stays constant when coagulating with a smaller mode, whereas the third moment is increasing. The zeroth and third moment of the smaller mode, however, are both decreasing during coagulation with a larger mode.

ICON-ART only considers coagulation due to Brownian motion and neglects electrostatic forces. The formulation of the coagulation rate follows Whitby et al. (1991), and it reads for a system of two modes i and j as

$$\tilde{C}a_{0,ii} = \frac{1}{2} \int_0^\infty \int_0^\infty \beta(d_1, d_2) \psi_{0,i}(d_1) \psi_{0,i}(d_2) dd_1 dd_2, \quad (3.41)$$

$$\tilde{C}a_{0,ij} = \int_0^\infty \int_0^\infty \beta(d_1, d_2) \psi_{0,i}(d_1) \psi_{0,j}(d_2) dd_1 dd_2, \quad (3.42)$$

and

$$\tilde{C}a_{3,ij} = \int_0^\infty \int_0^\infty d_1^3 \beta(d_1, d_2) \psi_{0,i}(d_1) \psi_{0,j}(d_2) dd_1 dd_2. \quad (3.43)$$

The coagulation coefficient β depends on the sizes of coagulating particles. General expressions for β are complex and usually only numerical solutions exist for all sizes. However, analytical solutions are available for certain size regimes. The method by Whitby et al. (1991) uses analytic solutions of the coagulation integrals in Equations (3.41) to (3.43) for the near-continuum and free-molecular regime and applies a harmonic mean to receive an expression for the full size range. A detailed derivation of these solutions can be found in the original publication by Whitby et al. (1991), or in Riemer (2002) and Muser (2022). The harmonic means for inter-modal coagulation are given by

$$\tilde{C}a_{0,ij} = \frac{\tilde{C}a_{0,ij}^{nc} \tilde{C}a_{0,ij}^{fm}}{\tilde{C}a_{0,ij}^{nc} + \tilde{C}a_{0,ij}^{fm}} \quad (3.44)$$

and

$$\tilde{C}a_{3,ij} = \frac{\tilde{C}a_{3,ij}^{nc} \tilde{C}a_{3,ij}^{fm}}{\tilde{C}a_{3,ij}^{nc} + \tilde{C}a_{3,ij}^{fm}} \quad (3.45)$$

with $\tilde{C}a_{k,ij}^{nc}$ and $\tilde{C}a_{k,ij}^{fm}$ the coagulation rates of the k -th moment for the near continuum and free molecular regime, respectively. The solution for $\tilde{C}a_{ii}$ is derived analogously. These means are then used in Equations (3.41) to (3.43) to determine the coagulation rate for the zeroth moment $\tilde{C}a_{0,i}$ and third moment $\tilde{C}a_{3,i}$ of mode i .

In ICON-ART, the coagulation rate $\tilde{C}a_{k,l}$ of the k -th moment is converted to the coagulation rate of the mass mixing ratio and number mixing ratio by

$$Ca_{0,l} = \frac{1}{\rho_a} \tilde{C}a_{0,l} \quad (3.46)$$

and

$$Ca_{3,l} = \frac{\rho_{p,l}}{\rho_a} \tilde{C}a_{3,l}, \quad (3.47)$$

respectively.

3.4.5. Aerosol–radiation interaction

In ICON-ART, two options are available to calculate the radiative fluxes in the model atmosphere: the Rapid Radiative Transfer Model (RRTM) by Mlawer et al. (1997) and ecRad by Hogan and Bozzo (2018). RRTM computes the SW and LW fluxes for 30 spectral bands, which cover wavelengths of 0.2 – 1000 μm . 14 of these 30 bands represent the SW radiation up to 3.846 μm and 16 bands refer to the LW radiation. RRTM was the first radiative model in ICON and is now replaced by ecRad. The advantages of ecRad in ICON are the regular maintenance and documentation of the code, more consistent parametrizations, and a flexible and modular coding of the model (Rieger et al., 2019). The number of bands in the LW and SW is the same as in RRTM.

RRTM and ecRad require the mass extinction coefficient k_e , the single scattering albedo ω , and the asymmetry parameter g in all wavelength bands to account for the radiative effects of aerosols (Gasch et al., 2017). The calculation of the optical properties needs the mass mixing ratio (for k_e and ω) and the refractive indices of the particles. As ICON-ART considers different particle sizes and mixing states, the optical properties are determined for each mode individually. The optical properties of volcanic ash aerosols were derived by Mie calculations. These calculations were performed offline, and the results for each mode and each of the 30 wavelength bands are stored in look-up tables. This was necessary because the Mie calculations are computationally expensive. For each mode, only one set of optical properties was derived, which should be representative for the mode in the whole volcanic plume.

The ICON-ART setup used in this work considers insoluble particles as spherical ash particles without coating, soluble particles as water-sulfate mixtures, and mixed mode particles as ash particles coated with a water-sulfate shell. The Mie calculations for these particles were performed with wavelength-dependent refractive indices of insoluble particles by Walter (2019) and mixed particles by Muth (2019) and Muser (2022). Furthermore, ICON-ART uses refractive indices for the soluble mode based on the Mie calculations for water-sulfate mixtures from Gordon et al. (2017). Based on Gordon et al. (2017) and measurements conducted by Rosen (1971), ICON-ART assumes a volume mixture of 50% water and 50% sulfate for the soluble particles and the shell of mixed particles. Although this assumption neglects the dependence on the atmospheric humidity, it is necessary to reduce the amount of Mie calculations.

The coating ratio, defined as the fraction of the shell diameter to the particle diameter, is assumed to be 0.2 for the Mie calculations (Muth, 2019).

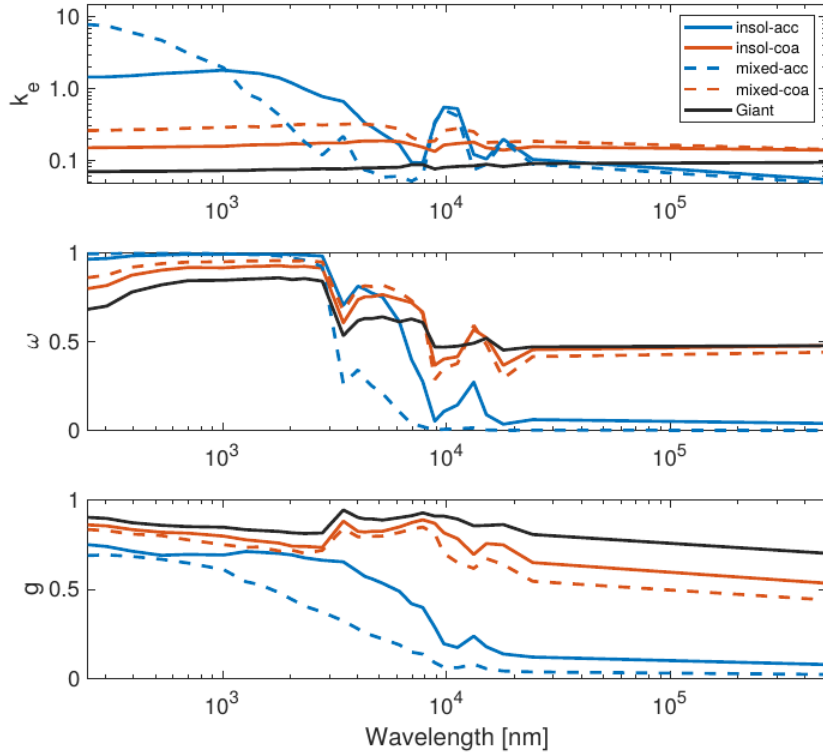


Figure 3.2.: Optical properties of volcanic ash modes at different wavelengths. The upper, central, and lower panels show the extinction coefficient k_e , the SSA ω , and the asymmetry parameter g , respectively. Solid lines indicate insoluble modes and dashed lines indicate mixed modes. Taken from Muser et al. (2020).

Figure 3.2 shows the results of the Mie calculations and is taken from Muser (2022). It presents the wavelength-dependent extinction coefficient k_e , the SSA ω , and the asymmetry parameter g for the different modes. The extinction coefficient is higher for smaller particles than for larger ones in the short wavelengths (visible and near-IR range, Figure 3.2 top). In the LW range, the differences between the modes are smaller. Furthermore, the extinction coefficient is slightly higher for coated than for uncoated ash particles in the coarse mode at all displayed wavelengths. For the accumulation mode, the extinction coefficient is higher for the coated ash particles in the SW and lower in the near-IR compared to uncoated particles in the same size mode. The differences in the LW for coated and uncoated particles are only small (Figure 3.2 top).

The SSA indicates whether extinction is dominated by scattering or absorption. An ω -value close to one (zero) means extinction mainly occurs by scattering (absorption). For all modes, scattering dominates in the SW (Figure 3.2 middle). However, the scattering is higher for smaller particles than for larger ones. In the LW, the absorption increases and even dominates for the accumulation mode particles. The mixing state only slightly influences ω at most wavelengths, except for accumulation mode ash particles in the near- and mid-IR range. Here, coated ash particles are more absorbing than uncoated

ones (Figure 3.2 middle). Absorption heats particles, which warm the surrounding atmosphere. This can have implications for the plume development (Muser et al., 2020) and atmospheric dynamics (Niemeier et al., 2021).

The asymmetry parameter g determines whether the particles scatter radiation preferentially to the front (g close to 1) or back (g close to -1). Figure 3.2 (bottom) shows that forward scattering is larger than backward scattering for all modes. A slight decrease in g for the giant and coarse modes with increasing wavelength is visible, whereas the decrease for the accumulation mode particles is larger. Furthermore, coating causes a slightly smaller g . Although this does not affect the radiation budget in ICON-ART, it needs to be considered when comparing modeled backscatter signals with measurements from remote sensing (Hoshyaripour et al., 2019).

The assumptions made to derive the optical properties of the modes were necessary to reduce the computational costs and due to missing observational or experimental data. The most important assumptions made for the optical properties in ICON-ART are:

- The refractive indices from Walter (2019) were derived for the 2010 Eyjafjallajökull eruption. The Raikoke and La Soufrière volcanoes, of which the eruptions were studied in this work, might differ in the mineralogy and therefore the emitted particles might produce other refractive indices.
- The Mie theory only considers spherical particles. Liquid particles fulfill this assumption, but it is not justified in case of freshly emitted volcanic ash (Bagheri and Bonadonna, 2016). Nevertheless, particle aging leads to coating of liquids on the ash surface, which results in a more spherical shape of mixed particles (Lohmann et al., 2016).
- The particle diameter and the mixing state were used for the Mie calculations. However, particle aging, relative humidity, and vertical separation of smaller and larger particles due to sedimentation can modify the diameters, and the mixing states of the modes are not constant within the plume.

On the one hand, these assumptions can introduce errors in ICON-ART. On the other hand, it is necessary to keep in mind that both modeled backscatter signals and measurements from remote sensing rely on assumptions on the particle size distribution (PSD) of the volcanic plume. Hence, especially absolute values can differ between signals from remote sensing measurements and modeled signals.

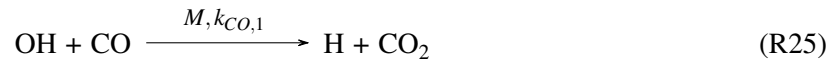
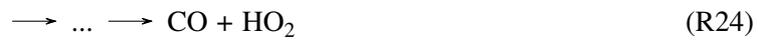
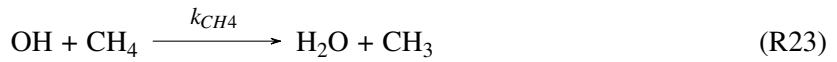
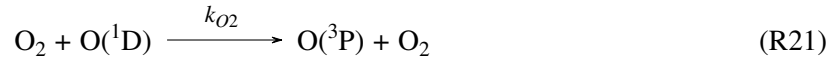
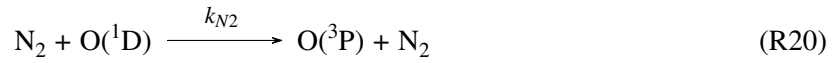
3.5. Gas-phase chemistry

ICON-ART offers three options to run simulations with gas-phase chemistry: The lifetime approach (Rieger et al., 2015), a simplified OH-chemistry (Weimer et al., 2017), and complex chemistry mechanisms (Schröter et al., 2018). In the lifetime approach, chemical tracers are depleted or react into other substances based on a given value for their lifetime in the atmosphere. As this method is largely simplified and neglects the dependence of chemical reactions on the diurnal cycle, it was not used in this thesis. Instead, the simplified OH-mechanism (Section 3.5.1) was used for global simulations in Chapters 6 and

7 and a complex gas-phase mechanism supplemented by a mechanism for aqueous-phase chemistry on aerosols (Section 3.5.2) for LAM simulations in Chapter 7.

3.5.1. Simplified OH-chemistry

The simplified OH-mechanism for gas-phase chemistry provided in ART is described in Weimer et al. (2017). It is a set of parametrizations that calculates the loss rate of tracers by OH depletion and photolysis depending on space and time. The tropospheric OH concentration is modeled by a simplified model that contains the most important chemistry and photolysis reactions relevant for OH formation and depletion (Jacob, 1999):



Reaction and photolysis rates are denoted as k and J , respectively. Derived from this reaction system, the OH concentration is given by

$$[\text{OH}] = \frac{2[\text{O}(^1\text{D})]k_{H_2O}[\text{H}_2\text{O}]}{k_{CH_4}[\text{CH}_4] + (k_{CO,1} + k_{CO,2})[\text{CO}]} \quad (\text{3.48})$$

with a $\text{O}(^1\text{D})$ -concentration of

$$[\text{O}(^1\text{D})] = \frac{J_{O_3}[\text{O}_3]}{k_{O_2} + k_{N_2}[\text{N}_2] + k_{H_2O}[\text{H}_2\text{O}]} \quad (\text{3.49})$$

The O_3 concentration is a climatological value. An online-photolysis module derives the O_3 photolysis rate J_{O_3} in ICON-ART (Weimer et al., 2017, and references therein). The concentration of H_2O comes from the ICON microphysics, and the concentrations of O_2 and N_2 are converted to number concentrations from volume mixing ratios of 20.946% and 78.084%, respectively.

Besides the gases needed for the simple OH-model, further additional gases can be picked (e.g., SO₂). The depletion of these additional gases then occurs by reaction with OH or by photolysis, e.g.,



3.5.2. Chemistry mechanism with MECCA

ART can furthermore model chemical reactions using the Module Efficiently Calculating the Chemistry of the Atmosphere (MECCA, Sander et al. (2011)), which has been integrated into ICON-ART by Schröter et al. (2018). The MECCA tool calculates the non-linear system of ordinary differential equations (ODEs) of a chemical mechanism with the Kinetic PreProcessor (KPP) by Sandu and Sander (2006). Depending on the experiment, the user can choose an appropriate chemistry mechanism from a set of chemical reactions. MECCA provides different solvers for the ODEs such as several Rosenbrock methods, Runge–Kutta methods, and backward differentiation formulas. The temporal integration for the simulations in this thesis were performed with the third-order Rosenbrock ODE solver RODAS3 (Sandu et al., 1997). Third-order solvers generally compute the stiff system of ODEs with sufficient precision for atmospheric conditions (Sander et al., 2011).

3.6. Aqueous-phase chemistry and adsorption

In this thesis, I used the MOZART-4 (Model for OZone And Related chemical Tracers – version 4) gas-phase chemistry mechanism (Emmons et al., 2010) and modified the mechanism for the case of volcanic emissions. The ODEs for this mechanism were calculated by using MECCA. The complete MOZART-4 mechanism was reduced to inorganic chemistry, but it includes reactions containing C1-organic compounds such as CH₄. CH₄ influences the removal of OH radicals, which in turns affects the chemistry of volcanic gases (Jacob, 1999). The reduction of the MOZART-4 chemistry mechanism is a compromise between providing the most relevant reactions, which directly or indirectly affect the chemistry in explosive volcanic eruption plumes, and limiting the amount of computational costs. A complete list of gas-phase reactions and their reaction rate coefficients considered for Chapter 7 is summarized in Table B.1 (first and second block). The total number of reactions in the reduced MOZART-4 mechanism is 108 gas-phase and 27 photolysis reactions.

To account for the dissolution of volcanic gases in water, I extended the mechanism by 47 equilibrium and aqueous-phase reactions (Table B.1, third block). Most of the rate coefficients for these reactions depend on the LWC in the atmosphere. As I only considered large explosive volcanic eruptions with major emissions occurring into the upper troposphere and stratosphere, I assumed the amount of liquid water droplets (cloud droplets) to be low and that aqueous-phase chemistry only occurs on coated ash. Therefore, the term aerosol liquid water content (ALWC) is used in the following to distinguish from LWC, which is typically used for liquid cloud droplets.

Technically, aqueous-phase chemistry on coated aerosols was solved by assigning two additional tracers to the mixed accumulation and coarse modes (e.g., A_aq_mixed_acc and A_aq_mixed_coa) for every aqueous-phase tracer in the mechanism (e.g., A_aq). In order to limit the computational costs, only the tracers assigned to the aerosol modes are transported but not the actual aqueous-phase chemical tracer. In ICON-ART, the order of the routines is emission, aerosol dynamics, chemistry, and removal. This means for the procedure that after the aerosol routines the mass mixing ratios of an aqueous-phase compound in the mixed aerosol modes are added and written onto the chemical tracer. This chemical tracer is then considered in the mechanism, and the resulting mass mixing ratios are distributed onto the aerosol mixed modes again according to their ALWCs.

To consider the oxidation of SO₂ by O₂ and TMI, I initialized the aqueous-phase concentration of Fe³⁺ in the mixed modes with 0.5 μM (0.5·10⁻³ mol m⁻³). This value is in agreement with Galeazzo et al. (2018).

In case an experiment includes the emission of water vapor from the volcanic eruption, the MER of water vapor is written onto the chemical H₂O tracer in ART instead of the ICON qv-tracer (mixing ratio of water vapor) because of two reasons; (1) to avoid a lofting of the plume by latent heat release due to phase changes of the emitted water vapor and (2) to not consider the emitted water vapor when reading the atmospheric profiles by FPlume. In order to receive the effects of water vapor emissions and atmospheric humidity on aerosol dynamical processes and chemistry, the qv-tracer is added to the gaseous H₂O tracer before the relevant processes in ART and subtracted afterwards again. In ART, a deposition parametrization reduces the emitted gaseous H₂O amount from the atmosphere without latent heat release when the equilibrium vapor pressure of H₂O over ice is exceeded. With this approach, the simulations could not account for the effects of (supercooled) liquid droplets formed from volcanic water vapor emissions on in-plume aqueous-phase chemistry.

The adsorption rate of SO₂ on ash is parameterized using Equation (2.24). This rate depends on the total ash surface area of the insoluble accumulation and coarse modes and an uptake coefficient. Urupina et al. (2019) and Lasne et al. (2022) measured uptake coefficients for the BET (Brunauer–Emmett–Teller method) surface area of different Icelandic ash samples on the order of 10⁻⁸ and a coverage saturation of 10¹⁶ molecules cm⁻². Riley et al. (2003) reported that the BET surface areas for different ash samples are one to two orders higher than that of geometric surfaces. Therefore, an uptake coefficient for the geometric surface of 1·10⁻⁶ was chosen in the model. For an uptake coefficient range of 10⁻⁵ to 10⁻⁷, the impact on the results is on the order of less than 5%. Adsorbed sulfur compounds can react with gaseous O₃ to form SO₄²⁻ on insoluble ash modes (Usher et al., 2002; Maters et al., 2017).

4. Simulated cases, observational data, and validation techniques

This chapter introduces the simulated cases and gives an overview about all observational products used in this thesis either as input for ICON-ART or to validate the simulations. Furthermore, validation techniques for comparison of ICON-ART with the different observational products are given in the respective sections.

4.1. Simulated cases

Two recent volcanic eruptions are studied in this thesis: the 2019 Raikoke eruption and the 2021 La Soufrière eruption. Both eruptions are introduced in more detail in the next two sections.

4.1.1. 2019 Raikoke eruption

The Raikoke is an island near the center of the Kuril Islands in the Sea of Okhotsk in the northwest Pacific (48.29°N, 153.24°E). The Raikoke volcano is a stratovolcano, i.e., a conical volcano made of many hardened lava and tephra layers. Its lava is primary basaltic (McKee et al., 2021). The height of the vent is 550 m above sea level.

The last Raikoke eruption took place on 21 June 2019. It was characterized by ten eruption phases of 5 to 14 km plume height lasting between 5 min and 3 h (Horváth et al., 2021b). Such complexity leads to further difficulties in deriving reasonable ESPs for plume dispersion forecasts. The constant emission rate and profile used by Muser et al. (2020) caused an approximately 6 h time lag between the time series of modeled and observed ash mass loadings. Kloss et al. (2021) investigated the SO₂ transport following the 2019 Raikoke eruption with observations and models. They found enhanced stratospheric AODs in the whole Northern Hemisphere for more than one year following the Raikoke eruption when using an SO₂ setup which realistically represents the transport of volcanic compounds during the first hours after the Raikoke eruption. De Leeuw et al. (2021) found that simulating the correct burden of SO₂ is sensitive to the fraction emitted into the lower stratosphere and, therefore, depends strongly on the chosen emission profile.

4.1.2. 2021 La Soufrière eruption

The La Soufrière volcano is located on the Caribbean island of Saint Vincent (13.33°N, 61.18°E) in Saint Vincent and the Grenadines. As the Raikoke, the La Soufrière volcano is a stratovolcano. Its lava

is primary basaltic-andesite (Joseph et al., 2022). The elevation of the crater is 1234 m above sea level. The latest major eruption started on 09 April 2021 and lasted 13 days. It was characterized by 43 eruption phases in the first four days with plume heights between 5 and 19 km and further five eruption phases until 22 April 2021 (Horváth et al., 2022). Babu et al. (2022) investigated the long-range transport of the La Soufrière plume using Ozone Monitoring Instrument (OMI) observations. They found that the volcanic plume reached the western North Pacific region about ten days after the eruption.

4.1.3. Model configurations

I coupled ICON-ART with FPlume as described in Section 3.3 in order to simulate volcanic eruptions with ICON-ART. Several input conditions have to be assumed for the simulations such as input for the FPlume model, the assumed PSD for the ash emission in ICON-ART, and the emission of SO₂.

The Raikoke emits primary basaltic lava (McKee et al., 2021), and I assumed the following exit conditions for FPlume. The exit temperature of 1273 K and exit water mass fraction of 3% were the same for all eruption phases; the exit velocity $v_{e,ph}$ of the individual phases ph was a linear function of the plume height above the vent H_{ph} between 4000 and 14000 m, where the exit velocity was set to 90 and 150 m s⁻¹, respectively. Hence, the following equation calculated $v_{e,ph}$ based on H_{ph} :

$$v_{e,ph} = 6\text{s}^{-1} \frac{H_{ph}}{1000} + 66\text{ms}^{-1} \quad (4.1)$$

The assumptions for the exit conditions were taken from the ranges considered in Koyaguchi and Woods (1996) and Mastin (2007) (exit temperature of 1173 – 1373 K, exit velocity of 80 – 150 m s⁻¹, and exit volatile fraction of 2 – 4%), which reasonably represent basaltic eruptions (Hoshyaripour et al., 2015). However, the range of reasonable exit temperatures, velocities, and volatile fractions as well as the fact that these values might vary significantly during an eruption, can affect the MER calculations. Observations on these parameters are usually not available, and, therefore, I used values in the middle of the range. Based on offline analysis with FPlume, I expect the resulting MERs to be insensitive to the input vent conditions (temperature, velocity, and volatile fraction) in the range of 20% (not shown). The equation for the very fine ash fraction by Gouhier et al. (2019) depends on whether the SiO₂ content is high or low and whether the conduit was opened or closed. As no information on the conduit has been available so far, I averaged the very fine ash fraction for the cases of low-SiO₂ – closed conduit and low-SiO₂ – opened conduit.

For the La Soufrière eruption, the same estimates of the exit temperature, exit velocity, and exit volatile fraction as well as the calculation strategy of the fine ash fraction were chosen as in the case of the Raikoke eruption due to a similar composition of the magma. Basaltic and basaltic-andesite magma compositions on average lead to similar exit conditions.

The emission of ash into the ICON-ART modes followed Muser et al. (2020). The total mass of very fine ash was evenly distributed as insoluble tracers over the accumulation, coarse, and giant modes. The

three insoluble modes were emitted as log-normal distributions with median diameters of 0.8, 2.98, and 11.35 μm , respectively. The standard deviations were 1.4 for each mode.

The SO_2 emission from the volcanoes was based on measurements of total SO_2 mass emitted into the atmosphere (Section 4.2). For the simulations, the SO_2 release was distributed over the eruption phases by linearly adjusting to the eruption height and length of each phase. The phase-dependent MER of SO_2 was given by

$$E_{ph} = \bar{E}_{\text{SO}_2} \cdot \frac{H_{ph}}{H_T}, \quad (4.2)$$

where \bar{E}_{SO_2} is the mean emission derived from the observed total amount of released SO_2 and H_{ph} is the phase plume height (above the vent). H_T is the phase duration-weighted mean plume height derived as

$$H_T = \frac{\sum_{ph=1}^{n_{ph}} H_{ph} \cdot t_{ph}}{\sum_{ph=1}^{n_{ph}} t_{ph}} \quad (4.3)$$

with n_{ph} the number of eruption phases and t_{ph} the phase duration. Finally, the SO_2 release was vertically distributed according to the Suzuki profiles (Suzuki (1983), Section 3.3).

4.2. Observational volcanic input

FPlume needs input data for the plume height to solve for the MER. The input plume heights used in this thesis were derived from satellite observations by Horváth et al. (2021b) and Horváth et al. (2022). At daytime, the geometric side-view technique by Horváth et al. (2021a) was applied for the 2019 Raikoke eruption (Horváth et al., 2021b) and the 2021 La Soufrière eruption (Horváth et al., 2022). This technique exploits the near-limb view, i.e., at a vertical zenith angle (VZA) larger than 80° , provided by geostationary satellites. Such views see the vertical columns protruding from the Earth's ellipsoid from a close-to-orthogonal direction and can be used to derive point estimates of the eruption column heights in the vicinity of the vent by a simple height-by-angle method. The uncertainty of these estimated plume heights lays within a range of ± 500 m. For this work, the geometric plume heights were derived from the Geostationary Operational Environmental Satellite 17 (GOES-17) for both eruptions at daytime. For the Raikoke eruption this technique could be used for the entire time span because the eruption only took place at day. However, the La Soufrière volcano also actively emitted during the night. Plume heights at night were temperature-derived from GOES-16 (smaller VZA as GOES-17 to avoid limb cooling effects), where the plume heights were given by the altitude at which the minimum measured $11 \mu\text{m}$ -brightness temperature matches to an atmospheric profile (Horváth et al., 2022). The time between two consecutive images from GOES-16 and GOES-17 is 10 min, which gives the uncertainty of the derived beginning and end of an eruption phase.

As FPlume only considers the emissions of ash and H_2O as the only volatile compound, I additionally emitted a phase-dependent SO_2 amount according to Equation (4.2) based on observations. The total mass of SO_2 emitted during the 2019 Raikoke eruption was about 1.5 Tg. It was estimated by

Muser et al. (2020) using data from the TROPOspheric Monitoring Instrument (TROPOMI) onboard the ESA/EU Copernicus Sentinel-5 Precursor (S5P) satellite and the infrared Advanced Himawari Imager (AHI) onboard the geostationary satellite platform Himawari-8. The total SO₂ mass emitted during the first four days (09 April 2021, 12 UTC to 13 April 2021, 12 UTC) of the La Soufrière eruption was on the order of 0.4 Tg as estimated from TROPOMI by Sandra Wallis (personal communication).

4.3. Separation of the volcanic plume from the background

In order to study the evolution of the ash and SO₂ plumes in the atmosphere following an eruption, I had to separate the plumes from the background mixing ratios due to technical reasons. In ICON-ART, the aerosol modes are initialized with 100 particles per kg air to avoid a division by zero in the diameter calculation routines. I used the following mixing ratio thresholds above which a grid cell is considered as inside the plume: 0.001, 0.01, 1.0, and 100.0 μg kg⁻¹ for the Aitken, accumulation, coarse, and giant modes, respectively. The corresponding threshold of SO₂ was 10 ppm. The threshold values are based on Muser et al. (2020).

4.4. Himawari ash and SO₂ loading¹

To validate the model results in Chapter 5, I use column SO₂ and ash mass loadings estimated from the 16-band visible and infrared AHI onboard the Himawari-8 geostationary satellite at every full hour. Himawari-8 is operated by the Japan Aerospace Exploration Agency (JAXA) and the Japan Meteorological Agency (JMA). A detailed description of the data product and methods used here is given in Muser et al. (2020) and references therein. In short, SO₂ was retrieved by the AHI band centered near 7.3 μm, where the absorption of SO₂ is high. A further retrieval scheme, as described in Prata et al. (2004), was applied to minimize the interference with vapor and clouds. For volcanic ash retrievals, the AHI bands near 11.2 and 12.4 μm were considered. The lower detection threshold was < 0.2 g m⁻² for volcanic ash. The ash retrievals were corrected by a mask that accounts for pixels that contain meteorological clouds but which were classified as completely cloud covered. Hereby, only pixels inside a 0.1 g m⁻² contour line were considered, and a 9 × 9 median filter smoothed out “spikes”.

I compare the Himawari-8 and ICON-ART ash and SO₂ column loadings by means of the SAL (Structure, Amplitude, Location) method developed by Wernli et al. (2008) and extensively tested by Wernli et al. (2009). The advantage of this method is that it compares the agreement of objects in two dimensional data fields (e.g., model results and satellite observations) according to their structure, amplitude, and location. The method was originally developed to verify precipitation forecasts (Wernli et al., 2008, 2009), however, it has also been successfully applied for transport forecasts of volcanic compounds (e.g., Muser et al., 2020; de Leeuw et al., 2021) and is used in this study for volcanic ash and SO₂ as well.

¹This section is adapted from: Bruckert, J., G. A. Hoshyaripour, Á. Horváth, L. O. Muser, F. J. Prata, C. Hoose, and B. Vogel, 2022: Online treatment of eruption dynamics improves the volcanic ash and SO₂ dispersion forecast: case of the 2019 Raikoke eruption. *Atmospheric Chemistry and Physics*, **22** (5), 3535–3552, doi:10.5194/acp-22-3535-2022.

The structure component *S* compares model and observations with respect to the volume of the defined objects. The value ranges between -2 and 2 . Positive values indicate objects that are too large and / or too flat, whereas negative values indicate objects that are too small and / or too peaked. A value of zero refers to a perfect forecast with respect to the structure. The amplitude component *A* evaluates the domain-averaged relative deviation of the forecasts from observations. It is positive when the model overestimates the predicted quantity and vice versa (it also ranges between -2 and 2). For a perfect forecast of the amplitude, *A* is zero. The location component *L* consists of two parts: *L1* describes the agreement between the forecast and observation in terms of the normalized difference between the centers of mass, whereas *L2* refers to the average distance between the center of mass of all objects and the individual objects. Both *L1* and *L2* can reach values between 0 and 1 so that *L* in total can have values between 0 and 2 with a perfect forecast with respect to the location at $L = 0$ (Wernli et al., 2008, 2009).

For the SAL comparison of Himawari-8 and ICON-ART data, I derived 6 h-averages from both datasets at every full hour. Furthermore, I interpolated ash and SO_2 values onto a regular grid at $120^\circ\text{W} - 80^\circ\text{E}$ and $20 - 85^\circ\text{N}$ with a resolution of 0.1° . However, before interpolation, I applied a 5×5 pixel mean averaging to fill gaps in the mapped satellite data, considering only values different from zero. Otherwise, the linear interpolation would have led to a loss of information when mapping on a coarser grid because the regular grid is about 4 to 5 times coarser than the retrieval grid. These gaps in the satellite data originated from mapping the native format onto a regular latitude–longitude grid as needed for the SAL analysis and are due to the increasing pixel sizes towards the edges of the retrieval domain.

To define objects in the SAL analysis, I used a threshold of 0.2 g m^{-2} for modeled and observed ash because this is the detection threshold for the Himawari-8 ash retrievals. For SO_2 , a threshold of 2.5 g m^{-2} for the model and observations was used to remove background SO_2 concentrations in Himawari-8 data. This was necessary because I did not initialize the model with realistic background conditions in Chapter 5 and, therefore, I can only compare the observed and modeled SO_2 plumes from the eruption.

4.5. BCO²

The simulation results of the La Soufrière case are compared to vertical radar data from the Barbados Cloud Observatory (BCO, MPI-M (2021), downloaded from <https://observations.mpimet.mpg.de/repository/entry/show?entryid=656dc652-e02f-43c9-9378-7307a5143377>) in Chapter 6. The BCO is located on the east coast of the island of Barbados (13.16°N and 59.43°W) at Deebles Point. The BCO has been operating since 01 April 2010 by MPI-M to advance the understanding of clouds, circulation, and climate sensitivity at the edge of the inter-tropical convergence zone (Stevens et al., 2016). The La Soufrière volcano is approximately 150 km west of Barbados. Usually north-eastern trade

²This section is adapted from: Bruckert, J., L. Hirsch, Á. Horváth, R. A. Kahn, T. Kölling, L. O. Muser, C. Timmreck, H. Vogel, S. Wallis, G. A. Hoshyaripour, 2023: Dispersion and Aging of Volcanic Aerosols after the La Soufrière Eruption in April 2021, *Journal of Geophysical Research: Atmospheres*, **128**(8), e2022JD037694, <https://doi.org/10.1029/2022JD037694>.

winds are prevailing in this region (Stevens et al., 2016). However, at the time of the eruption, Barbados was located at the downwind site of the volcano, which enables the model validation near the volcano. The BCO is equipped with standard meteorological instruments for temperature, humidity, pressure, wind, rain rate, and solar irradiance measurements, but several remote sensing instruments to study the vertical distribution of overpassing clouds are also installed. In this study, I compared modeled volcanic compounds to equivalent radar reflectivity data from the Ka-Band (35.5 GHz) cloud radar at BCO to validate the emissions. The temporal resolution of the radar data is 10 s and the vertical resolution is 32 m. The radar measures at a range from 150 m up to 18.9 km altitude (Ka-Band Cloud Radar, 2022). Klingebiel et al. (2019) used the BCO Ka-Band radar together with other remote sensing instruments to investigate the sea salt aerosol distribution. As they were able to detect sea salt particles larger than 500 nm, I argue that the Ka-Band radar is able to detect fine mode ash. Thus, I do not need to exclude ICON-ART modes, when I compare the simulation with the BCO radar reflectivities.

4.6. MISR³

In Chapter 6, plume height and aerosol property data derived from MISR onboard the Terra satellite are compared to ICON-ART La Soufrière simulations on 10 April 2021 at 14:36 UTC, at the Terra overpass time. MISR is a passive sensor measuring upwelling shortwave radiation in four spectral bands in the visible and near-IR (446, 558, 672, and 866 nm). MISR provides near-simultaneous coverage at multiple viewing angles, which makes it possible to derive the elevation of lofted features such as volcanic plumes from the parallax between the views. For this purpose, the MISR INteractive eXplorer (MINX) software was developed. It is a stand-alone software package used to map volcanic, dust, and wildfire smoke plume elevations from MISR hyper-stereo data (Nelson et al., 2008, 2013). The resulting MINX elevations give a distribution of heights or vertical extent of the plume, keying on the layer of maximum spatial contrast, rather than a value for the absolute plume top height. MISR plume heights are retrieved at the nominal horizontal resolution of 1.1 km. The vertical uncertainty is in the range of 250 to 500 m (Nelson et al., 2013). In this study, I compare the spatial coverage of the individual eruption phases and their top heights relative to each other in MISR data and simulated ICON-ART data.

The MISR RA algorithm derives constraints on aerosol amount, particle size, shape, and light-absorption properties from the angular-spectral distribution of the scattered light (Kahn and Limbacher, 2012). Thereby, modeled radiances are compared with actual radiances measured by the MISR instrument. From this retrieval algorithm, I used the derived total AOD, non-spherical fraction, and SSA to investigate gradients in the horizontal distribution of the particle amount, particle aging, and scattering properties within the emitted volcanic plume. The high optical depth of the near-source plume offers favorable conditions for the MISR particle-property retrievals. The values and gradients of the particle-property

³This section is adapted from: Bruckert, J., L. Hirsch, Á. Horváth, R. A. Kahn, T. Kölling, L. O. Muser, C. Timmreck, H. Vogel, S. Wallis, G. A. Hoshyaripour, 2023: Dispersion and Aging of Volcanic Aerosols after the La Soufrière Eruption in April 2021, *Journal of Geophysical Research: Atmospheres*, **128**(8), e2022JD037694, <https://doi.org/10.1029/2022JD037694>.

retrievals are then compared to the same ICON-ART modeled properties at the same plume height as the MINX height.

4.7. CALIPSO⁴

The CALIPSO satellite (Cloud–Aerosol Lidar and Infrared Pathfinder Satellite Observation) is a joint mission between NASA (National Aeronautics and Space Administration) and the French space agency CNES (Centre National d’Etudes Spatiales) and was launched on 28 April 2016. The CALIOP (Cloud–Aerosol Lidar with Orthogonal Polarization) instrument onboard CALIPSO provides high-resolution vertical profiles of aerosols and clouds. The measurements are based on the backscattered signal at two wavelengths (532 and 1064 nm). Two channels receive orthogonally polarized components of the 532 nm backscattered signal, whereas the 1064 nm backscatter intensity is only received at one channel (Winker et al., 2009).

I use total attenuated backscatter signals at 532 nm from CALIOP L1 data version 4.11 (downloaded from https://asdc.larc.nasa.gov/data/CALIPSO/LID_L1-Standard-V4-11/2021/04/) and compare this to simulated signals of the La Soufrière plume in Chapter 6. Furthermore, I use the CALIOP depolarization ratio at 532 nm from the ratio of the perpendicular and parallel attenuated backscatter at 532 nm. This allows an estimation whether the plume is dominated by spherical (i.e., coated particles or droplets) or non-spherical compounds (i.e., uncoated aerosol particles) (Winker et al., 2009). In total, 13 CALIPSO overpasses traversed the La Soufrière plume within the first four days of the eruption.

In order to compare the CALIPSO total attenuated backscatter signal with ICON-ART modeled data, the forward operator described by Hoshyaripour et al. (2019) was applied. The attenuated backscatter signal at 532 nm wavelength was calculated as

$$\varepsilon(z) = \beta_b(z) \exp\left(-2 \sum_{i=1}^z \beta_e(z_i) \Delta z_i\right) \quad (4.4)$$

with z the model level, β_b the volume backscattering coefficient at 532 nm in m^{-1} , and β_e the volume extinction coefficient at 532 nm in m^{-1} . β_b and β_e were determined by summing over all modes l :

$$\beta_e = \sum_l k_{e,l} \rho_a m_l \quad (4.5)$$

$$\beta_b = \sum_l k_{b,l} \rho_a m_l \quad (4.6)$$

with ρ_a the density of air in kg m^{-3} and m_l the mass mixing ratio of mode l in kg kg^{-1} . $k_{e,l}$ and $k_{b,l}$ are the mass specific extinction and mass specific backscattering coefficients for the individual modes

⁴This section is adapted from: Bruckert, J., L. Hirsch, Á. Horváth, R. A. Kahn, T. Kölling, L. O. Muser, C. Timmreck, H. Vogel, S. Wallis, G. A. Hoshyaripour, 2023: Dispersion and Aging of Volcanic Aerosols after the La Soufrière Eruption in April 2021, *Journal of Geophysical Research: Atmospheres*, **128**(8), e2022JD037694, <https://doi.org/10.1029/2022JD037694>.

4. Simulated cases, observational data, and validation techniques

at 532 nm in $\text{m}^2 \text{kg}^{-1}$. For simplification, the values for $k_{e,l}$ and $k_{b,l}$ were fixed within each mode and depend only on average values for the radius and composition of mode l .

5. Plume dynamics and lofting after the 2019 Raikoke eruption¹

In this chapter, I aim to link complex ESPs during the first hours of volcanic eruptions to the fate of volcanogenic gases and aerosols. As a case study, I investigate the ash and SO₂ dispersion of the Raikoke eruption on 21 and 22 June 2019 and examine the effects of online treatment of the ESPs on the development of the plume. The 2019 Raikoke eruption was characterized by nine shorter eruption phases between 18 UTC on 21 June and 7 UTC on 22 June and one continuous eruption phase between 22.40 UTC and 01.55 UTC. I performed global simulations with ICON-ART using a horizontal grid spacing of 13.2 km (R3B07 grid) and 90 vertical levels up to 75 km. I simulated 72 h starting from 21 June, 12.00 UTC initialized with analysis data provided by DWD.

I performed three experiments: 1) a reference experiment in which FPlume calculated the ESPs with a varying very fine ash fraction and aerosol–radiation interaction activated in ICON-ART (FPlume-rad); 2) the second experiment also calculated the ESPs with FPlume, but neglected the interaction of aerosols and radiation (FPlume-norad). The comparison of FPlume-rad and FPlume-norad allows to quantify the lofting of the volcanic plume due to radiation; 3) the third experiment derived ESPs with the empirical relationship by Mastin et al. (2009), and it emitted volcanic compounds with a prescribed very fine ash fraction from the reference case (mean value for each phase) along a Suzuki profile (Equation (3.23)). It further assumed aerosol–radiation interaction (Mastin-rad). Thus, the experiments FPlume-rad and FPlume-norad calculated the ESPs online within the simulation, whereas in Mastin-rad the ESPs were derived offline independent of the atmosphere and vent conditions. All experiments resolved the different eruption phases. Table A.1 summarizes the prescribed input parameters for the FPlume-rad experiment associated with the eruption phases. These values were fixed within each phase. The time limits for the phases and plume heights above the vent are based on satellite images from GOES-17 as described in Section 4.2. Due to the 10-minute temporal resolution of the GOES-17 data, the uncertainty in the start and end time of each individual eruption phase is smaller than ± 10 min.

Figure 5.1 shows the plume height in the top panel and the MER of very fine ash that is released into ICON-ART by FPlume (red dots) and the Mastin relationship (blue dots) in the bottom panel. The fraction of very fine ash relative to the total MER predicted by FPlume is on the order of 1.5 – 3 % (not shown). In most phases, the MER calculated with FPlume is lower than the MER calculated with the Mastin equation, and the difference tends to be higher for larger plume heights. Since the exit parameters are fixed during each phase in the reference case, variation of the MER derived by FPlume must be due to

¹This section is adapted from: Bruckert, J., G. A. Hoshyaripour, Á. Horváth, L. O. Muser, F. J. Prata, C. Hoose, and B. Vogel, 2022: Online treatment of eruption dynamics improves the volcanic ash and SO₂ dispersion forecast: case of the 2019 Raikoke eruption. *Atmospheric Chemistry and Physics*, **22** (5), 3535–3552, doi:10.5194/acp-22-3535-2022.

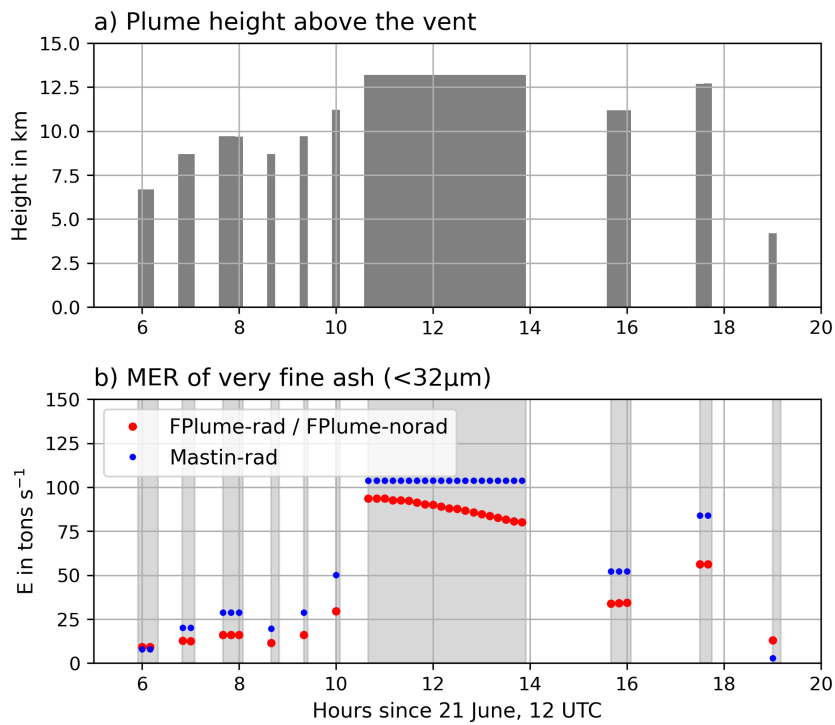


Figure 5.1.: a) Assumed plume heights in km above the vent from GOES-17 derived with the geometric side-view technique, and b) MER for very fine ash in tons s^{-1} calculated with FPlume-derived total MER times the very ash fraction from Gouhier et al. (2019) (red) and calculated with Mastin-derived total MER times the very fine ash fraction derived in the FPlume experiment (blue). The very fine ash fraction is the same in both experiments to allow a direct comparison of the impacts of FPlume- and Mastin-derived MER on the dispersion in the atmosphere. Active eruption phases are indicated by the gray shading.

changes in the atmospheric conditions. As the relationship by Mastin et al. (2009) neglects atmospheric conditions and the very fine ash fraction is fixed within one phase, the MER of the very fine ash is constant within each phase. The vertical profiles of the meteorological variables in Figure C.1a indicate increasing temperatures in most levels below 10 km during the long eruption phase between 9 and 14 h after simulation start. Additionally, the specific humidity increases by up to 1 g kg^{-1} in the lower 2 km (Figure C.1c). When warmer and moist air is entrained into the plume, the plume density reduces faster due to the lower ambient air density and the release of latent heat. This effect results in a higher positive buoyancy and a lower MER to reach a fixed height. In addition, the wind speed decreases in the lower 4 km between 9 and 14 h after simulation start (Figure C.1d), which reduces the plume bending, and, subsequently, the MER needed to reach a fixed height sinks.

According to the MER values in Figure 5.1, the total mass of very fine ash emitted in the model for all eruption phases together is about $1.21 \cdot 10^9 \text{ kg}$ using FPlume and $1.48 \cdot 10^9 \text{ kg}$ using Mastin-derived MERs.

The emission profiles used for the emission of ash and SO_2 are given in Figure 5.2 for the ten eruption phases in comparison with emission profiles used in previous studies on the same eruption (Muser et al., 2020; de Leeuw et al., 2021; Kloss et al., 2021). The profiles are normalized with respect to the

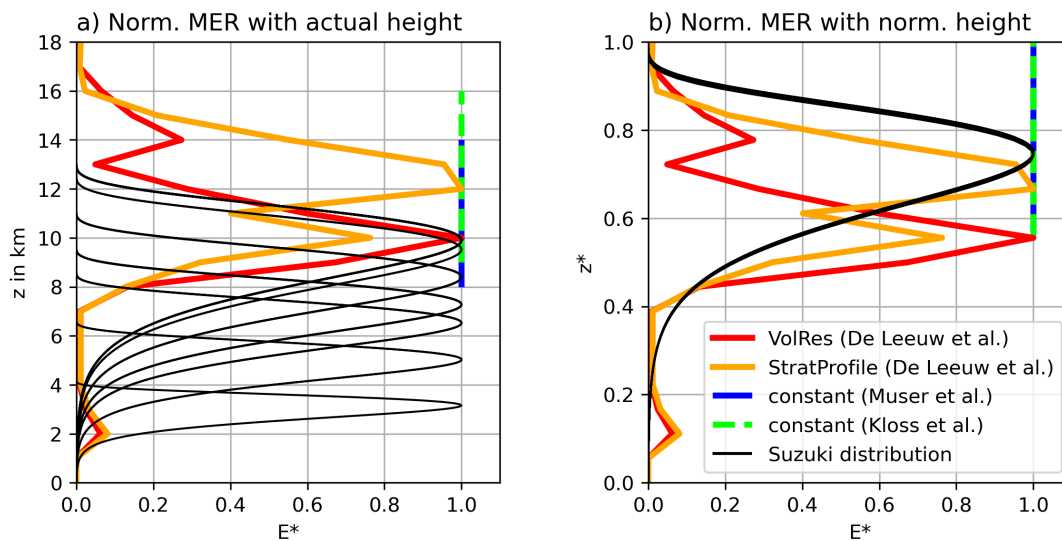


Figure 5.2.: Comparison of the Suzuki profiles for the ten eruption phases used in this work with profiles from previous studies. a) Normalized with respect to MER, but with actual emission heights; b) Normalized with respect to MER and emission height.

emission rate in both panels. The profiles in the right panel are additionally normalized with respect to the maximum plume height. For simplification, Kloss et al. (2021) and Muser et al. (2020) emitted volcanic compounds only in the upper third of the plume (green and blue lines). Both works assume a constant plume height during the entire eruption without considering the individual eruption phases. The ten emission profiles used in this work are given in black. By normalizing the height, it becomes obvious that the relative distribution of the mass is almost independent of the plume height (Figure 5.2b).

De Leeuw et al. (2021) emitted only SO_2 during the entire eruption along the red profile in Figure 5.2. The profile was obtained from satellite measurements (Infrared Atmospheric Sounding Interferometer (IASI) retrieval) by the Volcano Response (VolRes) team (<https://wiki.earthdata.nasa.gov/display/volres>) during the first two days of the eruption. It is likely that this profile developed due to an overlay of profiles from different eruption phases and subsequent plume dynamics and transport processes. However, de Leeuw et al. (2021) found that using this profile leads to a too short SO_2 e-folding time in the NAME model (Numerical Atmospheric–dispersion Modelling Environment). The authors argued that the amount of SO_2 emitted into the stratosphere is too low, and they re-distributed the mass according to the yellow curve in Figure 5.2. It is possible that the need for an adjusted profile occurs because ash emissions and aerosol–radiation interaction, which leads to a lofting of the plume top, were missing in their simulations (personal communication on 17 November 2020).

5.1. Validation of mass loading

The 2019 Raikoke eruption injected ash and SO_2 up to 14 km into the atmosphere. Figure 5.3 shows mean ash (left) and SO_2 (right) column loadings on 22 June, 0 – 23 UTC (top row) and 23 June, 0 –

23 UTC (bottom row) in the reference simulation FPlume-rad. The volcanic plume first spreads with westerly winds and is then dragged into a low pressure system over the Northern Pacific Ocean. In the mass loadings of both compounds, no clear horizontal separation of the ash and SO₂ plume is visible (compare Figure 5.3 left and right side). However, I further investigate the separation of ash and SO₂ in the vertical column in Section 5.3 after I validated the setup.

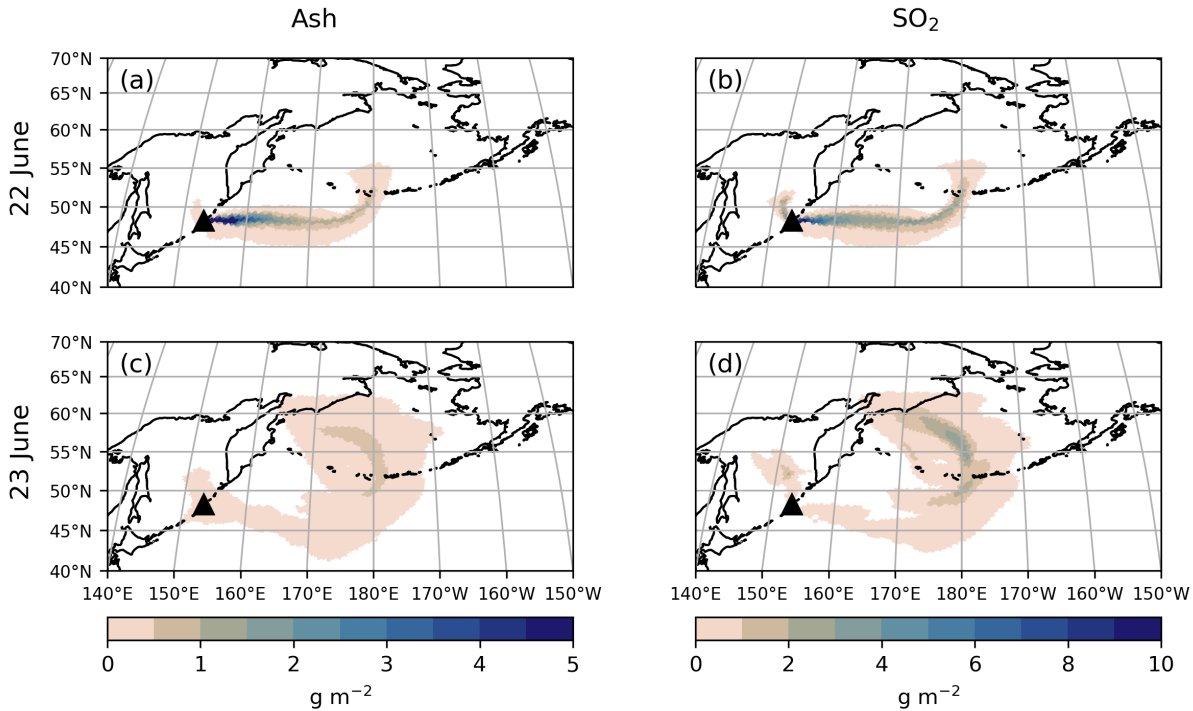


Figure 5.3.: Simulated daily mean column mass loadings for ash (left) and SO₂ (right) on 22 June 2019, 0 – 23 UTC (top row) and 23 June 2019, 0 – 23 UTC (bottom row) in g m^{-2} . The results are based on the FPlume-rad experiment.

Figure 5.4a shows the temporal evolution of the ash loading in the atmosphere following the Raikoke eruption for different experiments and observations. The temporal resolution of the data is 1 h. The Himawari-8 data reveal a steep increase of ash mass at 22 UTC on 21 June until a peak of 1.0 Tg is reached at 5 UTC on 22 June and the curve remains above 1.0 Tg for 5 h. The maximum at 7 UTC (22 June) of 1.1 Tg is followed by a descent to 0.3 – 0.5 Tg.

Muser et al. (2020) (green curve) emphasized that aerosol processes account for the ash removal. Nucleation, condensation, and coagulation increase the size of aerosol particles and, thus, lead to a faster sedimentation. However, Muser et al. (2020) were not able to quantitatively explain the time lag between model and observations during the first hours of the eruption (18 UTC on 21 June until 3 UTC on 22 June). Besides, the continuous emission with a constant MER led to a slight overestimation of the ash mass loading (Muser et al., 2020). I have closed these gaps as follows.

The maximum of total ash derived with ICON-ART coupled with FPlume (online treatment) in both experiments with and without radiation–aerosol interaction coincides very well with the Himawari-8

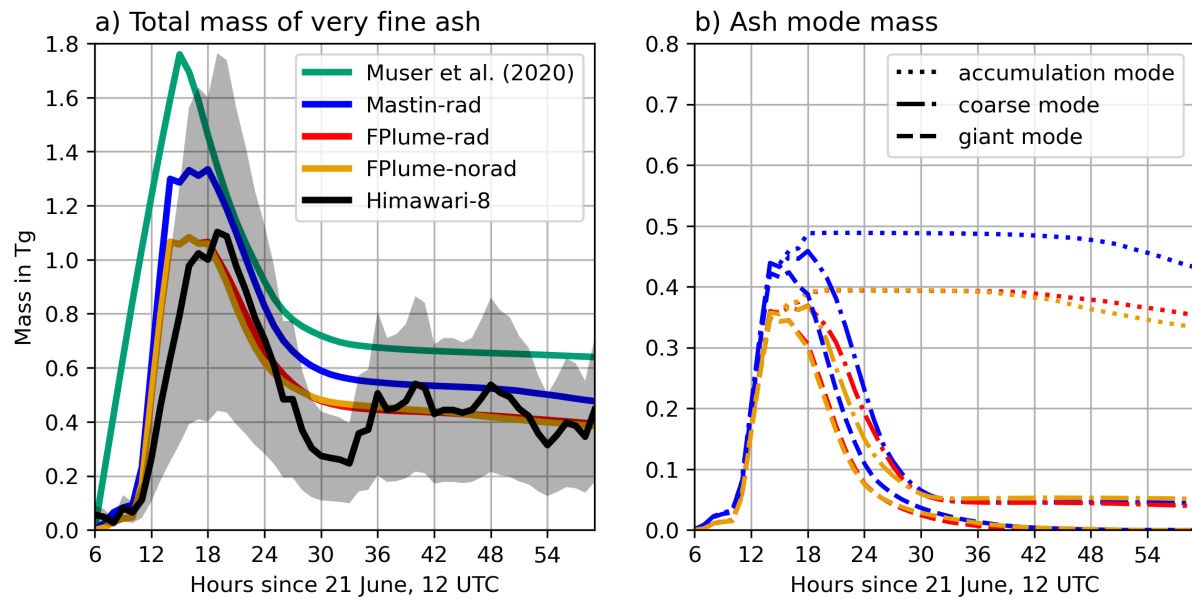


Figure 5.4.: (a): Temporal evolution of the total amount of very fine ash in the atmosphere in Tg for Himawari-8 observations (black) with an estimated uncertainty range (gray shading), simulated by Muser et al. (2020) with one constant emission phase (green), simulated with ICON-ART with and without aerosol–radiation interaction, each with phase-dependent FPlume MERs and a very fine ash fraction derived with the relationship by Gouhier et al. (2019) (red and yellow), and simulated with ICON-ART, eruption-phase dependent Mastin MERs, and the same very fine ash fraction as for the red curve (blue). (b): Temporal evolution of the simulated mass for the different ash modes (dotted: accumulation mode; dash-dotted: coarse mode; dashed: giant mode). The colors refer to the model experiment shown in the left panel.

data (in Figure 5.4 compare red and yellow curve with black curve). The total ash derived with Mastin (different MERs but the same fine ash fractions and emission profiles as in the FPlume experiments) overestimates the amount of ash during the first 12 h after the onset of the eruption (blue curve). Thus, neglecting meteorological effects and other plume-related processes in the case of the Raikoke eruption (offline treatment), as it is often done in volcanic dispersion forecasts, results in a higher MER especially in the long continuous phase of the eruption. This subsequently increases ash emissions into ICON-ART (Figure 5.1).

All simulation experiments in Figure 5.4a include aerosol dynamics and have correctly reproduced the fallout of particles as indicated by the decrease of ash after two days. From Figure 5.4b, where the temporal development of the different modes is shown, I can conclude that the decrease of ash after two days is mainly due to the removal of coarse and giant mode particles. The total ash from the simulations with FPlume displays the best agreement with the Himawari-8 data in this analysis (Figure 5.4a). However, the other curves remain mostly within the error range of Himawari-8 data as well (gray shading). Thus, I conclude that the online treatment of the plume development improves the ash loading prediction during the first hours and days after the eruption. After about 30 h, the aerosol dynamical processes become more important, and the differences between the experiments decrease.

5.2. Validation of dispersion using SAL

For the quantitative validation of the forecast quality, I performed a SAL analysis using 6 h-averaged SO_2 and ash mass loadings. I compare the results of the FPlume-rad experiment and the Himawari-8 satellite data. Figure 5.5 shows the values for the structure on the abscissa, the amplitude on the ordinate, and the location in colors. I do not discuss the SAL values for the FPlume-norad and Mastin-rad cases here because FPlume-norad only shows very small differences to the FPlume-rad case in all SAL values, and Mastin-rad only changes the amplitude value due to the larger MER compared to FPlume-rad. Based on the analysis of hourly to daily mean values, I conclude that 6 h-averages provide a reasonable compromise between both reproducing the details and reducing the amount of missing values and noise (not shown).

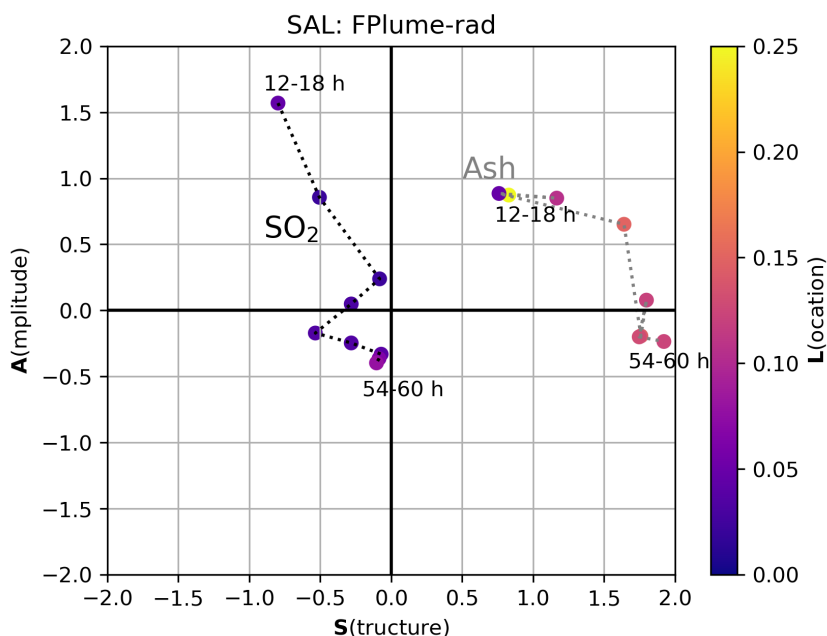


Figure 5.5.: SAL values for ash and SO_2 in the reference experiment (FPlume-rad) with $S(\text{structure})$ on the abscissa, $A(\text{mplitude})$ on the ordinate, and $L(\text{ocation})$ in colors. The dotted lines connect consecutive hours to visualize the temporal development (black for SO_2 and gray for ash). The labels of the hours are given relative to the start of the simulation on 21 June, 2019 at 12 UTC.

The location of the SO_2 plume agrees very well between model and observations throughout the whole simulation period. This is shown by the location values, which are close to zero. The SO_2 structure and amplitude values are close to zero between 24 to 72 h after the beginning of the simulation on 21 June at 12 UTC. Thus, there is a high agreement between model and observations during this period. However, during the first 24 h, the model prediction shows higher amplitude values and a low structure value, indicating a larger mass loading and a less diffuse SO_2 plume in the model compared to the satellite estimates. I argue that the discrepancy in the amplitude between model and observations during the first hours of the Raikoke eruption stems from the possible underestimation of SO_2 amount by the satellite

retrievals due to the dense ash plume covering the region around the volcano. In addition, the simulation is also affected by the uncertainties of input parameters (e.g., start and end time of individual eruption phases, plume heights, exit conditions).

The model also predicts the location of the ash plume very well (Figure 5.5). The positive structure values indicate that the modeled ash loading is more diffusive over the domain. Figure C.2 (first and second column) compares all 6 h-mean ash loadings. The large spread of the modeled ash plume across large parts of the northern Pacific Ocean is not seen in the observations, which is the main reason for the high structure value in Figure 5.5. I argue that Himawari-8 measurements of ash at this time might be hampered by water and ice clouds overlapping and obscuring the ash plume. This argument further explains why the temporal evolution of the Himawari-8 measurements in Figure 5.4a shows variations between 30 and 60 h although the emission from Raikoke ceased.

The high amplitude value for ash between 12 and 36 h, despite the almost perfect agreement in the total mass in Figure 5.4, also stems from the larger spread of the modeled ash plume in the beginning. The reason is that the background values are considered zero and the amplitude in the SAL analysis, unlike the object-based structure and location values, is a domain-averaged quantity.

I have shown that the model setup realistically represents the amount of ash following the 2019 Raikoke eruption, and the dispersion of the ash and SO₂ agrees well with the observations. In the next step, I analyze the vertical distribution of the ash and SO₂ plumes.

5.3. Vertical separation of SO₂ and ash plumes

In this section, I discuss the evolution of the ash and SO₂ plume top heights and focus on the radiative effects on the plume dynamics.

Figure 5.6 shows the top height of the ash, sulfate, and SO₂ plumes for the FPlume-rad and FPlume-norad experiments (a), the resulting vertical temperature difference on 23 June, 12 UTC (b), and the vertical distribution of SO₂, sulfate, and ash mixing ratios on the same date (c). The plume top height in a) is defined as the maximum height of all grid cells in the plume that were separated from background mixing ratios as explained in Section 4.3. The average plume height in a) is the mean height weighted by the mass of all grid cells that are considered inside the plume. The values in b) and c) were horizontally averaged over the whole detected plume, again excluding grid cells outside the plume. In b) and c), I picked 23 June at 12 UTC because it allows a direct comparison to Figure 8 in Muser et al. (2020), which only shows the ash plume top height. The lines for the plume top height and mass averaged height are smoothed by a Savitzky–Golay filter to remove 'steps' due to the low vertical resolution at upper atmospheric model levels. The difference in height between FPlume-rad and FPlume-norad remains similar, regardless of the use of this filter. However, the increasing plume height already starting before the beginning of the eruption is a result of the filtering.

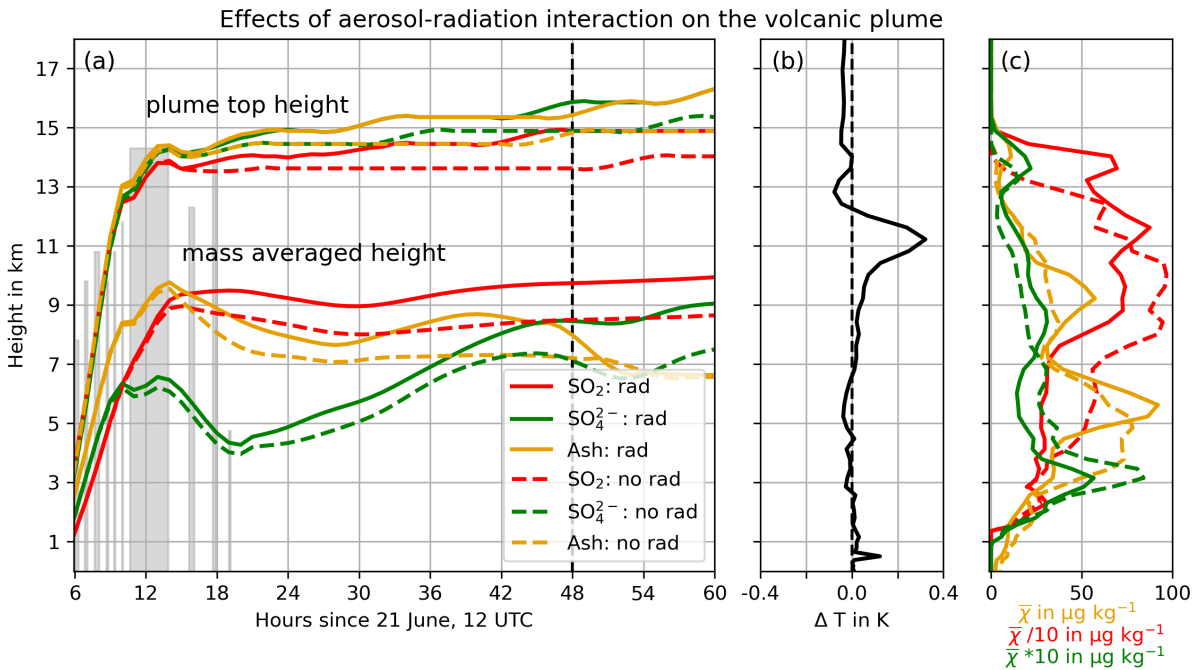


Figure 5.6.: (a): Temporal evolution of the SO₂ (red), sulfate (green), and ash (yellow) plume top heights and mass-averaged height for the FPlume-rad (solid) and FPlume-norad (dashed) experiments smoothed by a Savitzky–Golay filter. The gray bars indicate the duration and height of the ten individual eruption phases. These durations and heights are based on the analysis of the GOES-17 data, which serve as inputs for FPlume; (b): vertical profile of the temperature difference between FPlume-rad and FPlume-norad in the ash plume 48 h after the start of the simulation; (c): vertical SO₂ (red), sulfate (green), and ash (yellow) profiles after 48 h for the FPlume-rad (solid) and FPlume-norad (dashed) experiment.

During the first hours after the beginning of the eruption, the plume top heights for ash and SO₂ mainly rise due to the higher eruption heights of later eruption phases. The gray bars, which indicate the eruption height, coincide well with the top height (Figure 5.6a).

Shortly after the end of the long eruption phase, there is a clear separation of the ash, sulfate, and SO₂ plume top heights between the FPlume-rad and the FPlume-norad experiments. The effect of the ash lofting due to radiation was already investigated in detail by Muser et al. (2020) with the same model system. They found that the absorption of SW and LW radiation by ash particles leads to a warming and rising of the ash plume. I compare the vertical profile of the temperature difference between the FPlume-rad and FPlume-norad experiments here with the vertical temperature difference in Muser et al. (2020) on 23 June, 12 UTC. A single large positive anomaly of approximately 0.3 K near 11 km occurs in my simulation (Figure 5.6b). Subsequently, the whole ash plume rises to higher altitudes. In contrast, Muser et al. (2020) found two distinct temperature anomaly peaks around 10 km and 14 km on the order of 0.25 K each, which result in the formation of two maxima in the ash mixing ratios near 10 km and 15 km. The resulting uplift during the first 12 h in the ash plume in my simulation is about 33% of the resulted lofting in Muser et al. (2020), which is likely related to the lower erupted ash mass.

In the first hours during and after the eruption, the absorption-induced warming of the ash plume also causes the SO₂ plume to rise in FPlume-rad (Figure 5.6a and c) although SO₂ itself absorbs neither solar nor terrestrial radiation in the model setup used here. Sulfate interacts with radiation in the model, but it mainly scatters radiation rather than absorbing it. It seems that the ash plume top height separates from the SO₂ plume top height with increasing time (Figure 5.6a). However, it is more difficult to separate the SO₂ plume from the background concentrations than to separate the ash plume. This can be seen in Figure 5.6c at the top at one specific time step. The mixing ratios which are clearly different from zero indicate similar top heights for the ash, sulfate, and SO₂ plumes. In the model, aerosol–radiation interaction induces a warming of the entire volcanic plume top level, which results in a lofting of all compounds available in that level. A separation of the ash and SO₂ plume tops in the model is therefore only possible after a vertical separation due to sedimentation.

The evolution of the mass-averaged height of the ash and SO₂ plumes indicate an opposite behavior than the plume top height. The mass average of the SO₂ plume is generally higher than for the ash plume. In Figure 5.7a and c, the vertical distributions of the ash and SO₂ mass concentrations in kg m⁻³ confirm that the SO₂ plume is about 5 km higher on average than the ash plume after three days. This is in agreement with several existing studies (e.g., Timmreck, 2012; Robock, 2000), which emphasized a fast removal of ash after volcanic eruptions related to the sedimentation of these particles. The step-wise reduction of the ash in the mass averaged height is related to the loss of the giant mode during the first 24 h and a large fallout of the coarse mode until about 50 h relative to simulation start (Figure 5.4b and C.3).

The mass-averaged height of the sulfate plume increases in multiple steps. It is higher in the case with aerosol–radiation interaction. The step-wise increase is related to the conversion of SO₂ via H₂SO₄ to sulfate. This conversion mainly occurs at daytime, and it is faster the more OH and H₂O are available.

The vertical profiles of the SO₂ mixing ratios in FPlume-rad and FPlume-norad indicate that aerosol–radiation interaction smooths and reduces the vertical gradient of the SO₂ mixing ratios up to 7 km in the troposphere. In the stratosphere, a second peak occurs above the maximum emission height (Figure 5.6c). The vertical profiles of the sulfate mixing ratio show a distinct peak at about 3 km in both experiments which decreases with increasing altitude. As this peak is lower in altitude than the peak in the ash vertical profiles around 5.5 km, it is rather related to decreasing nucleation rates with height than to sedimentation because ash particles have a larger density than sulfate particles.

In the next step, I compare the vertical distribution of a characteristic ash particle radius \bar{R} , which is calculated as follows:

$$\bar{R} = \frac{\sum_{i=1}^5 r_{m,i} \cdot N_i}{\sum_{i=1}^5 N_i} \quad (5.1)$$

For the overall characteristic radius \bar{R} , I considered the five ash modes $i = [1, 5]$ (insoluble and mixed accumulation, insoluble and mixed coarse, and giant modes) and calculated \bar{R} at every grid cell. r_m is

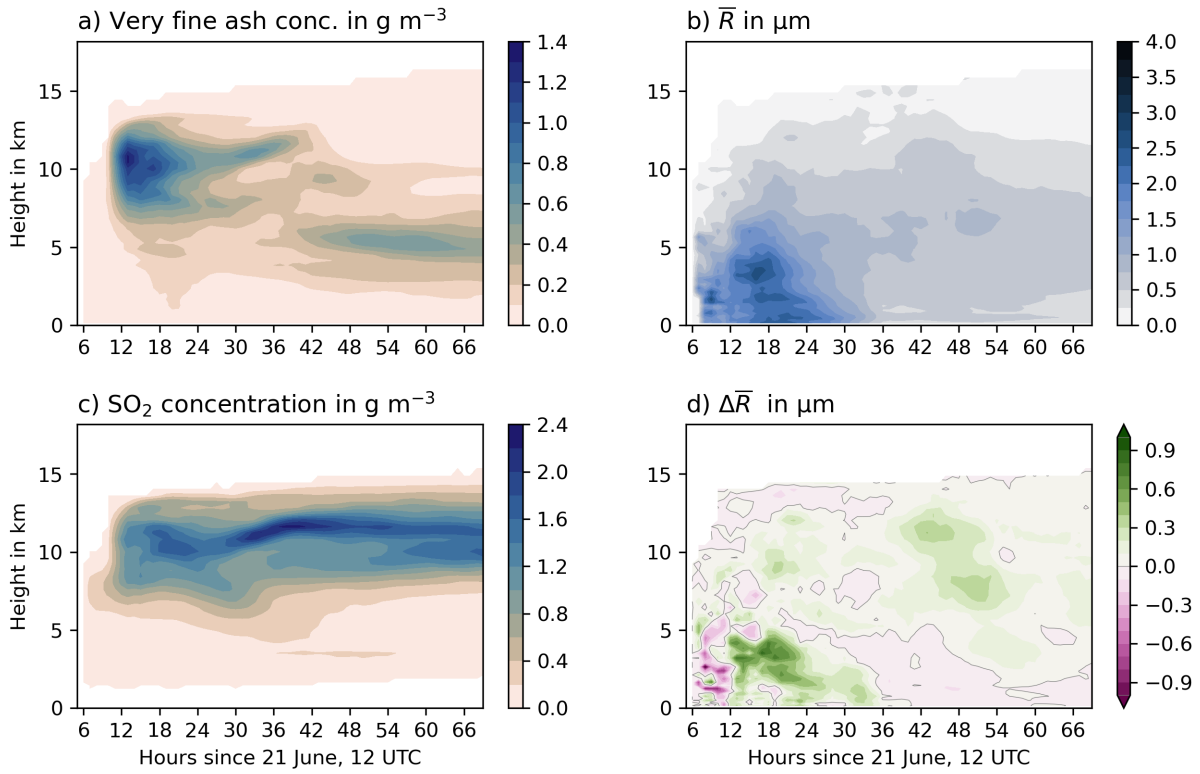


Figure 5.7.: Temporal evolution of the horizontally-integrated vertical distribution of a) ash mass concentration and c) SO_2 mass concentration in the FPlume-rad experiment. b) Horizontally-averaged number-weighted characteristic ash radius (Equation 5.1) for FPlume-rad and d) the difference between FPlume-rad and FPlume-norad.

the median radius of the log-normal distribution and N is the number of particles per grid box. The vertical distribution of the horizontally-averaged characteristic radius in Figure 5.7b also shows the loss of the larger particles (coarse and giant mode) during the first 24 h. Afterwards, the values of the mean characteristic radius are below $1.5 \mu\text{m}$ with a maximum around 5 to 6 km. In comparison to the FPlume-norad experiment, the characteristic radius is higher on average compared to the FPlume-rad experiment because aerosol–radiation interaction slows down the removal of larger particles from the atmosphere (Figure 5.7d). This effect is visible in the removal of the accumulation mode, which is reduced in FPlume-rad (Figure 5.4b). Compared to the FPlume-norad, the removal of the coarse modes in FPlume-rad is delayed by about 1 h between 18 and 25 h after the simulation start (Figure 5.4b). After about 30 h, the amount of the coarse mode is slightly lower in FPlume-rad than in FPlume-norad, because the particle radius is larger at most altitudes (Figure 5.4b and 5.7d). The temporal removal of the giant mode only shows small differences between FPlume-rad and FPlume-norad (Figure 5.4b). The larger mean characteristic radius after approximately 48 h is due to an increasing removal of accumulation mode particles in FPlume-norad compared to FPlume-rad (Figure 5.7d and 5.4b).

Both the main SO_2 mass and the main ash mass are restricted to a narrower vertical range after three simulation days than at the end of the eruption (around 13 h after simulation start). The location of the main SO_2 mass is between 8 and 14 km and between 4 and 7 km for the main ash mass (Figure 5.7).

Thus, for initializing long-range and climate simulations, a release of SO_2 and ash at these altitudes is justified if the sedimentation during the first hours is considered in the total emission rate.

Despite the clear vertical separation of the ash and SO_2 plume, the horizontal separation in both model and observations remains small in the first three days after the eruption. Nevertheless, a strong vertical wind shear can result in the horizontal separation of the ash and SO_2 plumes on longer time scales as it was found for this eruption in Kloss et al. (2021).

6. Aerosol aging in model and observations after the 2021 La Soufrière eruption¹

Previous studies showed implications of aerosol aging on the sulfate particle removal from the atmosphere (Muser et al., 2020). However, a direct comparison of aerosol aging in models to observations is still missing. In this chapter, I investigate the evolution of the volcanic plume during the first four days after the beginning of the 2021 La Soufrière eruption and study the distribution of aged ash particles. Different from the study on the Raikoke eruption in the previous chapter, this eruption offers a good opportunity to validate modeled aerosol aging because of the availability of observational datasets.

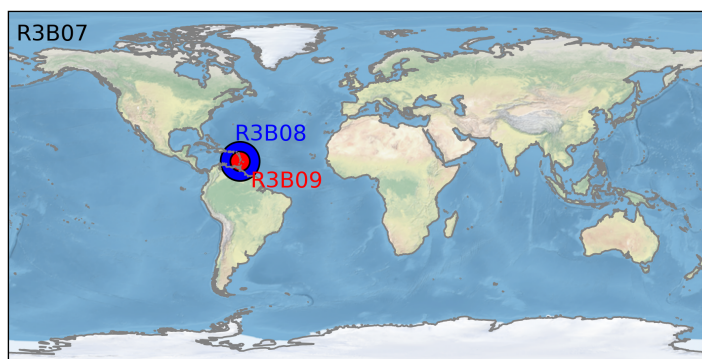


Figure 6.1.: Setup for the simulation of the 2021 La Soufrière eruption with a global R3B07 domain and two nests of 10° and 5° radius with a R3B08 and R3B09 grid around the volcano, respectively.

In order to investigate and validate the modeled ash aging, I performed a global ICON-ART simulation with a 13.2 km horizontal grid spacing and further horizontal grid refinements to 6.6 km and 3.3 km grid spacing around the volcano by using two nests with a radius of 10° and 5°, respectively (Figure 6.1). The innermost nest resolved convection processes, whereas the global domain and the coarser nest used the Tiedtke–Bechtold scheme for parameterized convection (Tiedtke, 1989; Bechtold et al., 2008). Two-way nesting was enabled, which allowed an update of the fields in the parent domain by the child domain at every time step. The model used 90 vertical levels to resolve the atmosphere up to 75 km. The model time steps were 60, 30, and 15 s in the global domain, and first and second nests, respectively. The simulation started at 12 UTC on 9 April 2021, and the meteorology was initialized by analysis data provided by the DWD. The experiment further included aerosol–radiation interactions, but it neglected the interaction of aerosols and clouds.

¹This section is adapted from: Bruckert, J., L. Hirsch, Á. Horváth, R. A. Kahn, T. Kölling, L. O. Muser, C. Timmreck, H. Vogel, S. Wallis, G. A. Hoshyaripour, 2023: Dispersion and Aging of Volcanic Aerosols after the La Soufrière Eruption in April 2021, *Journal of Geophysical Research: Atmospheres*, **128**(8), e2022JD037694, <https://doi.org/10.1029/2022JD037694>.

The La Soufrière eruption started on 09 April at 12.41 UTC (Joseph et al., 2022) and was characterized by 43 individual phases in the first four days and 49 phases during the entire eruption period from 09 to 22 April (Horváth et al., 2022). The detected eruption phases lasted between 10 min and 1 h, and they reached plume heights between 5.7 and 18.3 km above the vent. Figure 6.2 summarizes the assumed plume heights and the resulting MER of very fine ash for the 43 individual eruption phases.

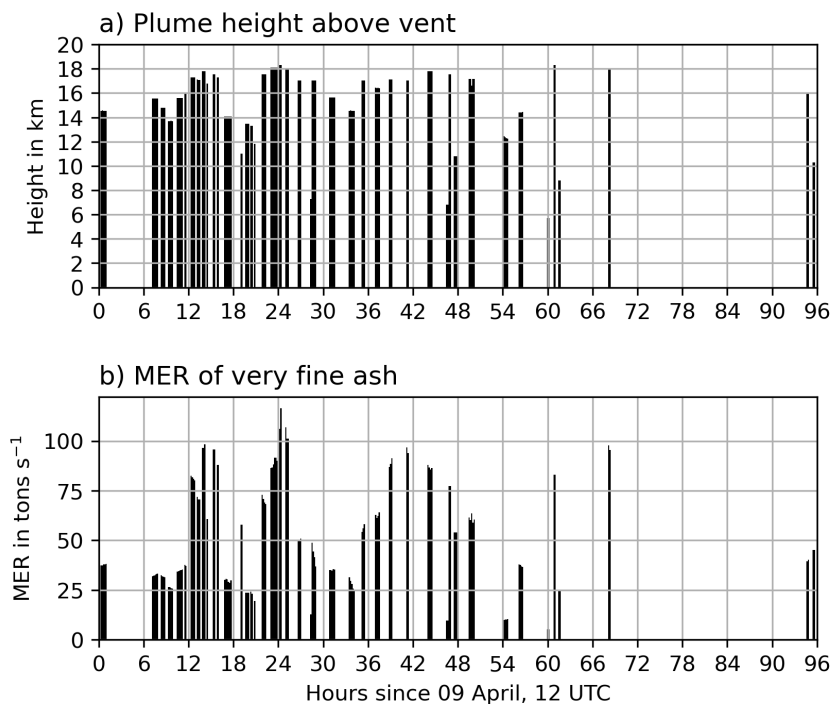


Figure 6.2.: a) Prescribed plume heights from satellite estimates and b) online-calculated emissions of very fine ash in the first 96 h of the 2021 La Soufrière eruption. The emission of very fine ash is obtained from the MER derived from FPlume and a very fine ash parametrization from Gouhier et al. (2019). The bars indicate the timing of the individual eruption phases as well as their length.

6.1. Vertical distribution of ash near the volcanic source

In this section, I first validate the modeled volcanic emission with observed radar reflectivity data from BCO approximately 150 km east of the La Soufrière volcano. Figure 6.3 shows in the top row the temporal development of equivalent radar reflectivity from BCO for all targets in dBZ (decibel relative to the equivalent reflectivity factor Z), and the bottom row depicts the temporal development of total ash concentrations in $\mu\text{g m}^{-3}$ for the ICON-ART experiment at the same location. The left column (a and c) shows raw data. The right column (b and d) depicts the radar data gridded onto the ICON-ART vertical grid (Figure 6.3b) and the simulated data masked according to the points of no detected reflectivity in the BCO radar measurements (Figure 6.3d).

A noticeable difference between model and observations occurs between 3 and 8 km altitude from 48 to 72 h after the start of the eruption. The radar shows no reflection, whereas ICON-ART indicates enhanced

ash concentrations. The BCO data shows increased rain intensity before this period (not shown). This causes an ash removal by wet deposition, which is underestimated in the model due to the lack of precipitation. As the rain does not only occur above the BCO site but also upwind of Barbados, this leads to a stronger removal from the atmosphere and less ash transport towards Barbados from surface to 8 km altitude.

The radar observations indicate several maxima in the reflectivity data up to 18 km most likely originating from reflection by volcanic ash particles from the La Soufrière eruption. Good agreement with the model is especially visible when using the radar reflectivity mask onto the simulated ash concentrations (right column). Although this is only a qualitative analysis, it confirms that considering the individual phases of the La Soufrière eruption is important to correctly represent the development of the volcanic plume in the near-field of the volcano. The maximum height of detection for the BCO radar is around 19 km, which explains the discrepancy between model and observations at altitude ranges above. Discrepancies at 16 to 18 km arise from both a lower sensitivity of the radar and strong radar attenuation at lower altitudes. Further reasons for the differences between model and observations are related to both model and measurement uncertainties. The most important model errors are associated with the initialization of the volcanic emissions and problems in the representation of the dispersion and fallout of aerosol particles. On the observational side, dense ash or other particles in the atmosphere weaken the penetration of the radar signal, which underestimates the reflectivity in higher altitudes (above 5 km).

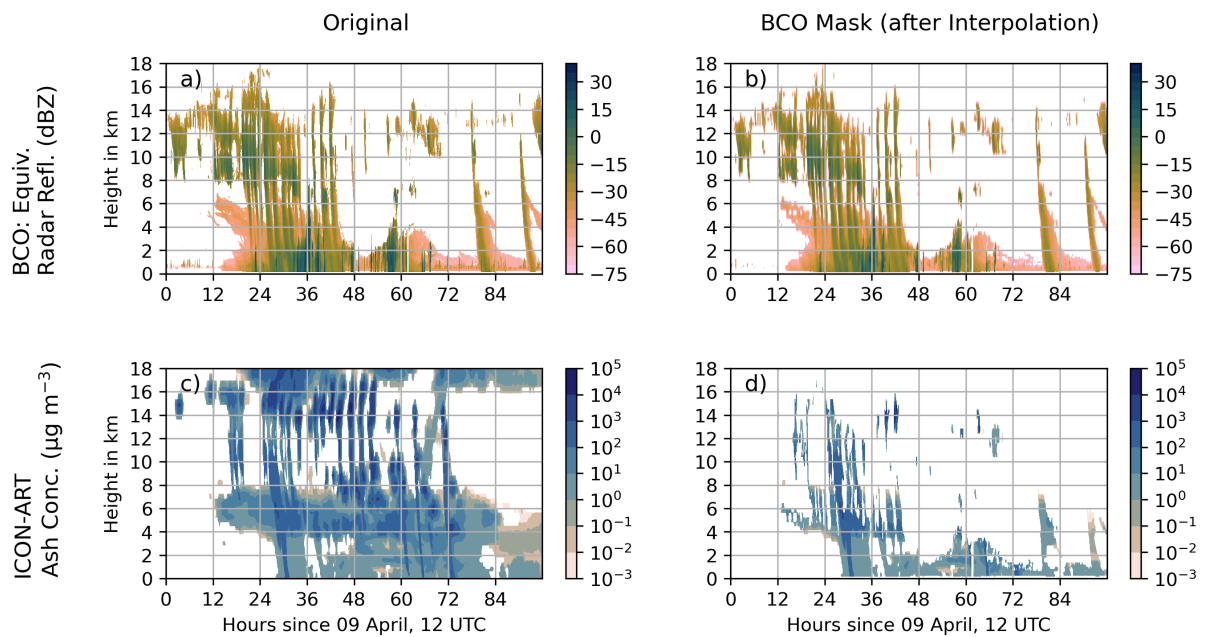


Figure 6.3.: Top row: BCO equivalent radar reflectivity for all targets in dBZ; bottom row: ICON-ART ash concentration above Barbados in $\mu\text{g m}^{-3}$. The left column shows the original data and the right column shows the data after interpolation onto the ICON-ART vertical grid for the BCO data (top right) and the ICON-ART ash concentration with the interpolated BCO mask (bottom right).

Both the radar observations and the modeled ash concentrations indicate vertically orientated streaks below the peaks of the eruption phases. These vertical streaks are not related to fall streaks, but rather originate from a vertical wind shear affecting the dispersion of the plume column. The gravitational settling velocity of the emitted particles is on the order of up to $5 \times 10^{-4} \text{ m s}^{-1}$ for the accumulation mode (around $0.8 \mu\text{m}$ in diameter) to 0.04 m s^{-1} for the giant mode (around $12 \mu\text{m}$ in diameter) assuming spherical particles. The distance from the volcano is roughly 150 km and the temporally varying horizontal wind profile above Barbados ranges from 0 to 25 m s^{-1} (Figure C.4). Based on these factors, I can calculate a typical settling height change of the particles between the La Soufrière volcano and Barbados. The gravitational settling is on the order of a few meters for the accumulation mode and a few hundred meters for the giant mode during the transport from the volcano to Barbados. Therefore, the vertical streaks in Figure 6.3 cannot be related to particle fallout. The vertical distribution split into the different modes further supports the transport of particles at different wind speeds instead of fall streaks, because the vertical streaks are visible for all particle sizes in the model (Figure C.5).

I conclude that the timing of the volcanic emissions in the model is well represented and allows a distinction of the individual eruption phases. This confirms that the near-source distribution of very fine ash is mainly affected by eruption dynamics and the wind shear rather than aerosol dynamical processes.

6.2. Plume dispersion

In this section, I focus on the volcanic plume dispersion across the Atlantic Ocean. Figure 6.4 shows 24 h-averages from 10 April at 12 UTC till 11 April at 11 UTC (a, b, c, d) and from 12 April at 12 UTC till 13 April at 11 UTC (e, f, g, h) for total very fine ash (a, e), coated ash (mixed ash, b, f), SO_2 (c, g), and sulfate (d, h) column loadings. The simulated fields show a dispersion of the volcanic plume towards the east across the Atlantic Ocean. The plume reaches the African coast after approximately 2.5 days. The main direction of the volcanic ash and SO_2 dispersion in the model is similar to the findings by Babu et al. (2022). The structures of the ash, SO_2 , and sulfate plumes look similar, indicating transport of all compounds at the same altitude with low vertical separation or a small vertical wind shear in the altitude of the main mass transport.

On both days, the total ash and SO_2 plumes show maximum column loadings east of the volcano spreading zonally and decreasing column loadings towards the edges of the plume. In contrast, multiple local maxima occur in the coated ash and sulfate plumes. Figure 6.5 shows the temporal development of the very fine ash mass, the SO_2 mass, and the sulfate mass in the soluble and mixed modes to explain the differences between the 24 h-averages in Figure 6.4. The peaks in the column loadings of ash and SO_2 are mainly driven by processes which are independent of the diurnal cycle such as emission, transport, and sedimentation (Figure 6.5a and b). In the case of the sulfate plume (Figure 6.4c and g), multiple local maxima occur because the sulfate production depends on the availability of OH, which is predominantly produced during daytime (Figure 6.5c, blue curve). Coated ash forms by condensation of water

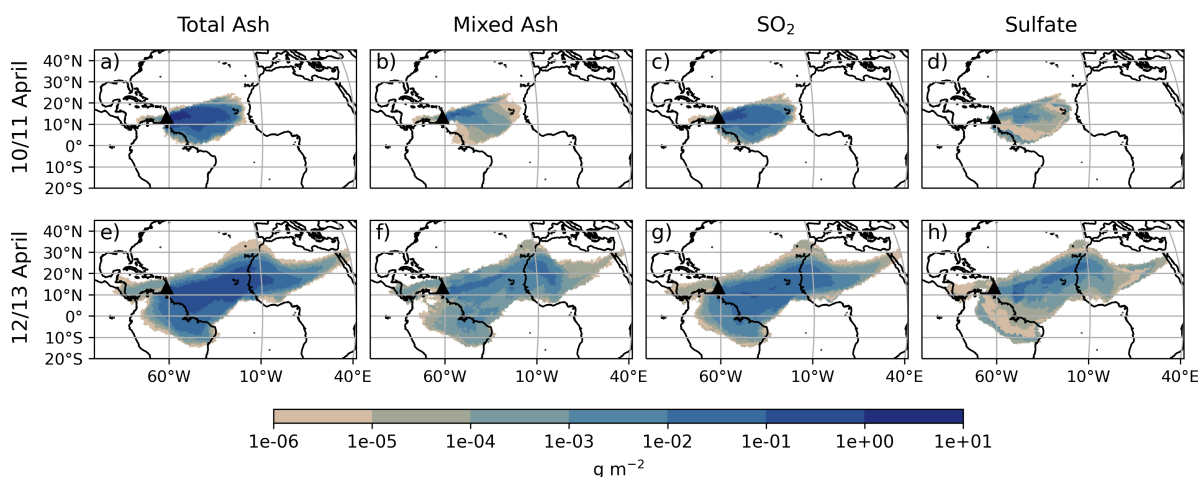


Figure 6.4.: 24 h-averages for a) total very fine ash, b) coated ash, c) SO₂, and d) sulfate column loadings in g m⁻² for 10 April 2021 at 12 UTC till 11 April 2021 at 11 UTC. e, f, g, h) same as a, b, c, and d but for 12 April 2021 at 12 UTC till 13 April 2021 at 11 UTC. The black triangle indicates the location of the La Soufrière volcano.

and / or H₂SO₄ onto pre-existing particles or by coagulation with sulfate particles. Thus, the coated ash formation also depends on the diurnal cycle, however, the curve of the sulfate mass on ash aerosols is smoother due to coagulation during night (Figure 6.5c, blue curve).

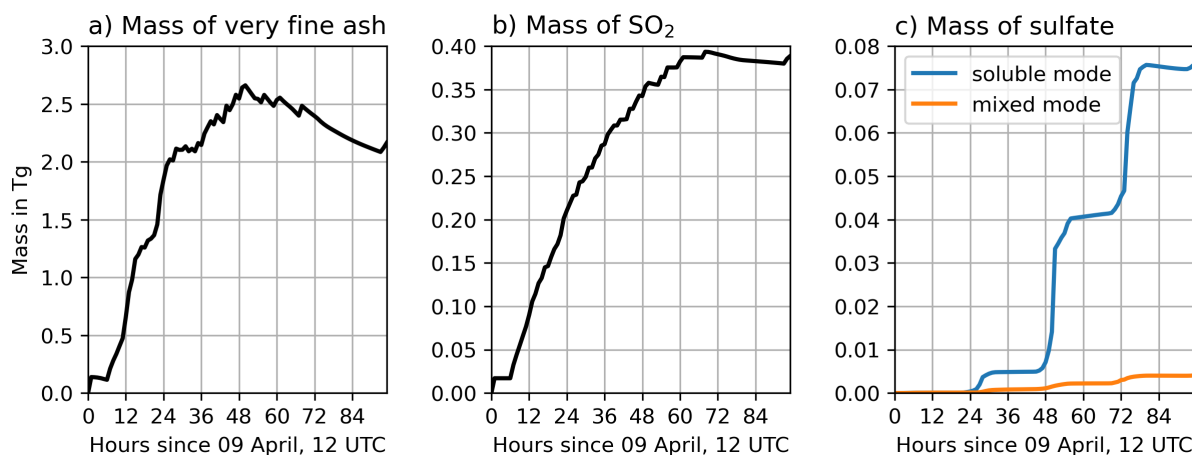


Figure 6.5.: Temporal evolution of the a) very fine ash mass, b) SO₂ mass, and c) sulfate mass in the soluble mode (blue) and coated on ash particles in the mixed mode (orange) in Tg.

In order to understand the driving processes, I focus on the formation of coated ash and sulfate in comparison with observations close to the volcano and during the further plume dispersion in the next sections.

6.3. Proximal aging of the aerosols

In this section, aerosol aging in the ICON-ART model is compared to observations from MISR. MISR derives spatial aerosol properties at the top of plumes. Before validating and investigating the aerosol

aging in the model, I compare the plume top heights in model and MISR observations to ensure a comparison of the aerosol properties on the same altitudes.

6.3.1. Plume height validation

Due to the narrow coverage of the MISR instrument (approximately 380 km wide swath, Kahn and Limbacher (2012)), which is especially significant at low latitudes due to its polar orbit, the volcanic plume is only observed on 10 April 2021 at 14:36 UTC. Fortunately, MISR happened to capture the approximate peak of the eruption event. I used a threshold of $AOD > 0.2$, to separate the modeled ash plume from background concentrations. This value is similar to the particle-property retrieval threshold of MISR (Kahn et al., 2001; Kahn and Gaitley, 2015).

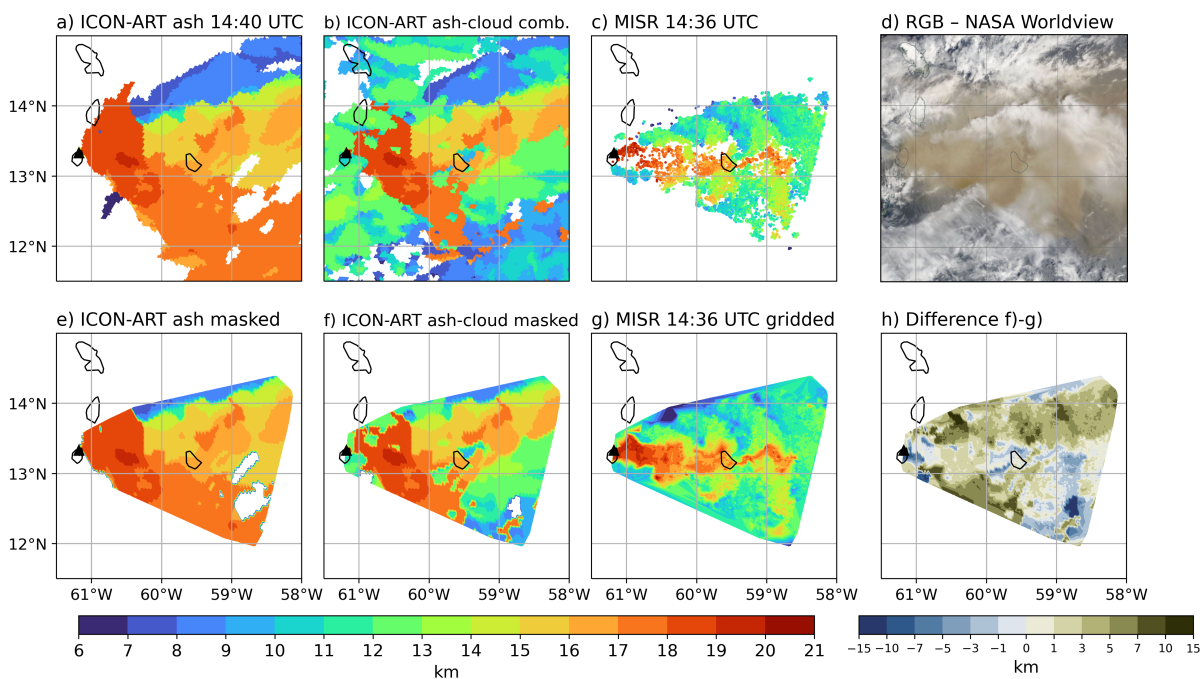


Figure 6.6.: a) ICON-ART ash plume top heights with a detection threshold of $AOD > 0.2$ at 14:40 UTC on 10 April 2021; b) ICON-ART combined ash plume top heights and cloud top heights; c) MISR plume top heights at 14:36 UTC on 10 April 2021; d) MODIS true color image on 10 April 2021 at 14:36 UTC from the NASA Worldview webpage (<https://worldview.earthdata.nasa.gov/?t=2021-04-10-T09%3A12%3A58Z>); e and f) same as a and b, but interpolated on a regular latitude–longitude grid and only showing values where MISR data are available; g) same as c, but interpolated on a regular latitude–longitude grid; h) difference between ICON-ART ash–cloud combined heights and MISR heights (f minus g).

Figure 6.6 shows the simulated and observed plume top heights (a – c, e – g), a true color image from the NASA Worldview webpage (d, <https://worldview.earthdata.nasa.gov/?t=2021-04-10-T09%3A12%3A58Z>) observed by the Moderate Resolution Imaging Spectroradiometer (MODIS), and the difference between the simulated and observed heights (f minus g in panel h). The first three plots in the top row display the original data (a, b, c), whereas the data in the bottom row is interpolated onto a regular latitude–longitude grid and only shows values where MISR heights are available (d, e, f). The

ICON-ART ash plume top heights are higher than the MISR heights in large parts of the displayed region (Figure 6.6a and c). The MINX stereo algorithm used to derive the MISR heights is sensitive to contrast features in atmospheric aerosol plumes or clouds and the Earth's surface over land and water, which might complicate a separation of meteorological clouds and ash plumes (Nelson et al., 2008). The NASA Worldview image in Figure 6.6d reveals a thick meteorological cloud north of Barbados. Furthermore, most of the area beneath the brownish ash plume is covered by meteorological clouds. Stereo matchers generally track the lower layer in a two-layered scene when the optical depth of the top layer is relatively small (e.g., Mitra et al., 2021). I therefore combined the simulated ash top heights with the cloud top heights from the model. The cloud top heights are obtained from the vertical profiles of liquid water and cloud-ice mixing ratios at every point in the region of interest (maximum height where profiles are non-zero). Next, I combined the ash plume top heights and the maximum cloud heights such that if the ash column AOD above the cloud is lower than a prescribed threshold, the cloud height is used and otherwise or in the absence of clouds the ash height is used. I achieved the best agreement with the observations when using a modeled AOD threshold of 10.0, where clouds are present (elsewhere the detection threshold of $\text{AOD} > 0.2$ was applied). The result is given in Figure 6.6b and f.

The ash–cloud combined heights from the model agree better with the MISR heights than the raw ash plume top heights. Although the threshold and assumptions used to derive the ash–cloud combined height are iterative, this procedure highlights the role of clouds in obtaining the correct ash plume top height from satellite observations, especially when comparing with model simulations. I further want to note here that volcanic eruptions often emit large amounts of water vapor. This water vapor can condense and / or freeze, and coat on ash particles. So, the distinction between the ash plume and water or ice clouds in the immediate vicinity of the volcano might be ambiguous.

The MISR dataset covers a smaller region than I modeled with ICON-ART, which gives the impression that ICON-ART ash and even ash–cloud combined heights differ significantly from the MISR observed heights. However, when only viewing the region where MISR data is available, there is a good agreement between ICON-ART ash–cloud combined and MISR heights with respect to the maximum and minimum plume heights (Figure 6.6f and g). Between the volcano and Barbados along 13.1°N , the differences are on the order of $\pm 5\%$ indicating a good agreement when the ash plume is thick and less cloud is visible (Figure 6.6d). Further, it is possible to distinguish different eruption phases in the plume height data. However, the eruption phases seem more apparent and more confined along the latitude of the eruption in the MISR observations than in the model. In the northern part of the plume, there is a positive bias in the ICON-ART heights relative to the MISR heights because the model could not reproduce the thick cloud north of Barbados (Figure 6.6e – g).

The south-eastern direction of the dominant ash dispersion in ICON-ART at the plume top (Figure 6.6a, b, e, and f) originates from a clockwise rotation of the horizontal winds with height in the model (Figure C.6). The observations, in contrast, show a largely zonal dispersion. This is a limitation of the model rather than a MISR retrieval artifact. The most likely problem here is the vertical resolution in upper

cells of the plume (around 20 km altitude), which is on the order of 800 m. In case the prescribed plume height for the emission is between two levels, it is assigned to the upper level. The uncertainty in the determination of the emission height is on the order of ± 500 m and might additionally lead to an imprecise emission profile and, thus, a wrong direction of transport in the upper layers of the plume. Considering these large uncertainties in the ESPs, the error in the modeled winds is of minor importance here.

6.3.2. Aerosol properties

The previous section revealed similarities but also differences between the top height from MISR MINX and ICON-ART, which are mainly related to the presence of meteorological clouds in the plume region. Therefore, I compare the aerosol properties such as AOD, fraction of spherical particles, and SSA at the level of the MISR cloud top height. The layer thickness (needed for the AOD) was calculated as the difference between the maximum and minimum height (from MISR MINX) in a $0.6^\circ \times 0.6^\circ$ box around the individual data point. The box size is in the range of the spatial resolution of the MISR MINX (Nelson et al., 2013) and MISR RA (Limbacher and Kahn, 2014). The simulated fraction of spherical particles was calculated as the AOD of spherical particles (sulfate and coated ash) divided by the total AOD for comparison with MISR RA in this section.

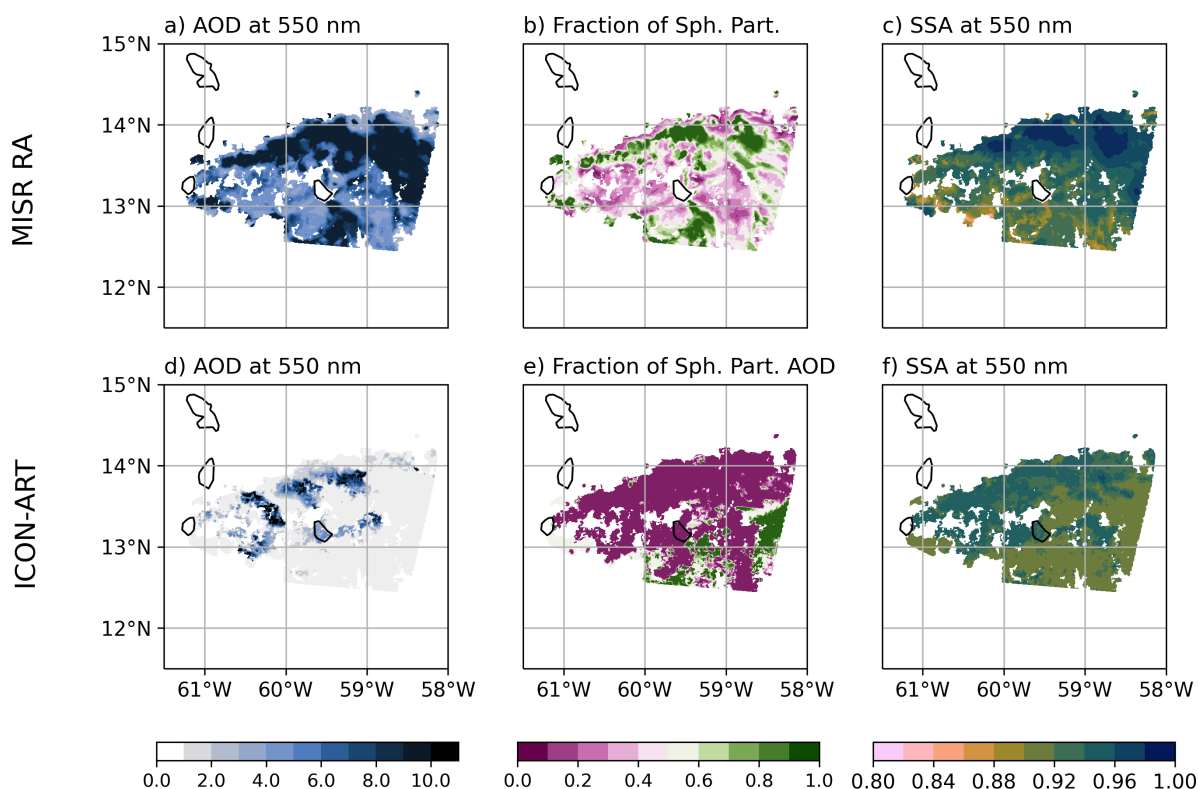


Figure 6.7.: a, b, and c) MISR plume AOD at 550 nm, MISR fraction of spherical particles, and MISR SSA at 550 nm, respectively; d, e, f) same as a, b, and e but for ICON-ART at the altitude range of the MISR volcanic plume as detected by MINX. ICON-ART fraction of spherical particles was calculated as the AOD of spherical particles divided by the total AOD.

Figure 6.7 shows the spatial maps of particle property values from the MISR RA and ICON-ART for the plume AOD at 550 nm, the fraction of spherical particles, and the SSA at 550 nm. The AOD refers to the amount of particles in the plume column, assessed at mid-visible wavelengths. The fraction of spherical particles gives information about the aging of the plume. The SSA indicates the composition of the plume. I only qualitatively compare the two datasets and concentrate on the spatial gradients in the plume. The absolute values of the retrieved parameters are highly uncertain due to the large amount of meteorological clouds in the region around La Soufrière and the retrieval assumptions.

The AOD values in both MISR RA and ICON-ART indicate a thick plume branch between La Soufrière and a half degree north of Barbados (Figure 6.7a and d). The values in the other parts of the plume are strongly reduced. However, the spatial reduction of the AOD values in ICON-ART is stronger than in the MISR RA. I note that the total AOD has to be treated with caution due to uncertainties in the thickness of the volcanic plume in the model simulation and the meteorological clouds that can affect the MISR retrieval, either with cloud contamination or by hygroscopic particle growth. In particular, the thick cloud band north of Barbados along the main direction of the plume dispersion, which is visible in the NASA Worldview image (Figure 6.6d), is missing in the simulation.

The MISR RA and ICON-ART agree very well in terms of fraction of spherical particles and SSA south of Barbados. Especially the observed pattern and inferred evolution of particle aging along the longitudes below 15.3°N are well represented by ICON-ART. With increasing distance from the source, the fraction of spherical particles increases due to the formation of sulfate and / or condensation of H₂SO₄ and / or water on ash. The SSA decreases from west to east because the scattering is larger for aged volcanic particles than for fresh ash (Muser et al., 2020).

North of Barbados, the MISR fraction of spherical particles and SSA show that the plume is dominated by strongly scattering spherical particles, such as sulfate, and / or hydrometeors (Figure 6.7b and c). As the NASA Worldview image in Figure 6.6d shows a thick band of meteorological clouds north of Barbados, the large fraction of spherical particles in the north might be a result of a large abundance of hydrometeors. In ICON-ART, the northern part of the plume mainly consists of non-spherical particles which are only slightly more light-scattering than south of Barbados. However, ICON-ART is not able to capture the meteorological cloud band north of Barbados. Instead, increased SSA values in the model occur because the ash particles in the northern plume are slightly smaller on average. A reason might be that the modeled plume heights are closer to the observed heights in the northern part than to the observed heights in the southern part (Figure 6.6e and g). The ICON-ART aerosol properties in Figure 6.7d and f then refer to a higher plume height relative to the actual maximum modeled plume height, and the plume contains on average smaller particles due to sedimentation of the larger ones.

The MISR RA fraction of spherical particles appears more noisy, especially in the northern part of the plume (Figure 6.7b). This part is also largely covered by clouds (Figure 6.6d), which increase the measurement uncertainties. Kahn et al. (2001) report increased confidence in MISR aerosol type retrieval when the component contributes at least about 20% to the total AOD.

The individual eruption phases of the La Soufrière eruption are especially visible in the ICON-ART AOD and manifest as individual arcs of plumes (Figure 6.7d). In the AOD of the MISR RA, the eruption phases are smoothed out, although they can be distinguished in the MISR MINX plume top heights (Figure 6.6c). The southern part of the plume in ICON-ART reveals low AOD values (Figure 6.7d). I therefore argue that the large plume top heights in the southern plume in Figure 6.6e originate from a thin plume layer rather than indicating a large mass transport in the wrong direction.

With the comparison to the MISR aerosol product, I looked at the horizontal distribution of the plume aging close to the eruption. In the next section, I investigate differences of the aging in model and observations at larger distances from the volcano.

6.4. Distal aging of the aerosols

In this section, I first validate the far-distance aging of the La Soufrière aerosol particles by comparing ICON-ART with CALIOP attenuated backscatter and depolarization ratio signals. Afterwards, I focus on the aging and sulfate production at different altitudes and with increasing distance from the source region in the model.

6.4.1. Validation along satellite track

The CALIPSO satellite passed over the volcanic plume on 13 April 2021 around 5 UTC. Figure 6.8a shows the modeled ash and sulfate column loading at this time from the ICON-ART experiment in colors together with the CALIPSO ground track (red line). The corresponding total attenuated backscatter signals from the CALIOP instrument and ICON-ART are given in Figure 6.8b and d, respectively. Figure 6.8c refers to the CALIOP depolarization ratio and Figure 6.8e is the modeled fraction of spherical particles defined as the mass of spherical particles divided by the total mass. The fraction of spherical particles only shows areas where the ICON-ART total attenuated backscatter signal is larger than $2 \times 10^{-4} \text{ km}^{-1} \text{ sr}^{-1}$, in order to clearly separate the modeled plume from background concentrations. 89 h after the eruption start, the ash plume covers most parts of the tropical and subtropical Atlantic Ocean, and North-West Africa (Figure 6.8a).

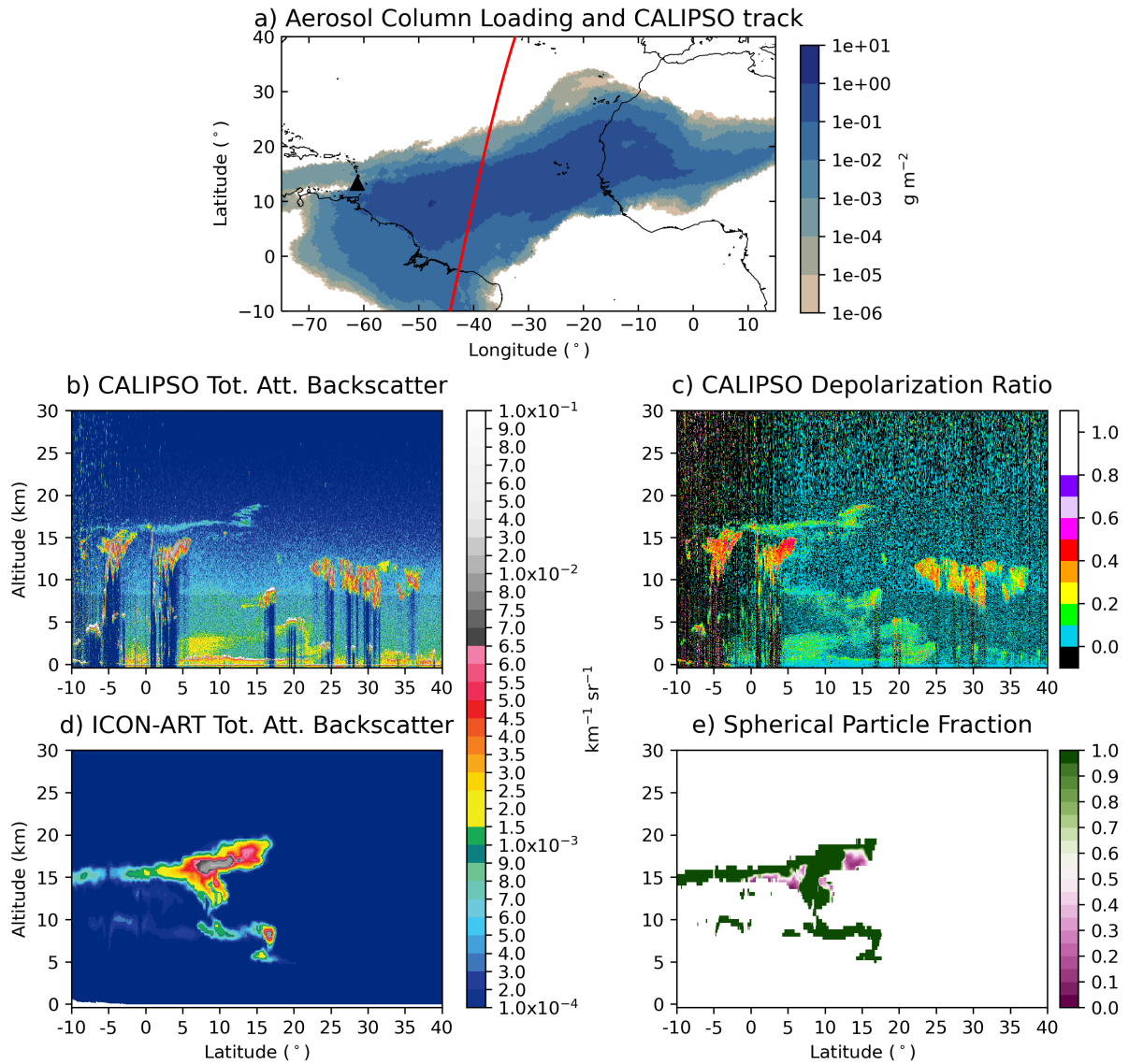


Figure 6.8.: a) Ash and sulfate column loading in g m^{-2} from the ICON-ART experiment together with the CALIPSO ground track in red on 13 April 2021 around 5 UTC and the La Soufrière volcano as a black triangle. According b) CALIPSO total attenuated backscatter at 532 nm, c) CALIPSO depolarization ratio at 532 nm, d) ICON-ART total attenuated backscatter at 532 nm for ash and sulfate, and e) ICON-ART spherical particle fraction. The ICON-ART spherical particle fraction is calculated as the ratio of spherical particle mass and total aerosol mass and only areas where the ICON-ART total attenuated backscatter is larger than $2 \times 10^{-4} \text{ km}^{-1} \text{ sr}^{-1}$ are shown. All plots correspond to 5 UTC on 13 April 2021, which is the approximate time of the CALIPSO overpass.

Based on the modeled attenuated backscatter signals, the volcanic plume in ICON-ART reaches a top height of 20 km between 15°N and 20°N along the satellite path, which agrees well with the uppermost signal in the CALIOP data at the same location (Figure 6.8b and d). A stratospheric volcanic plume layer exist between 10°S and 15°N in an altitude range from 15 to 20 km in both CALIOP measurements and ICON-ART modeled data. However, the strength of the signal is larger in ICON-ART. Besides larger particle concentration itself, a large source of uncertainty is also the calculation of the ICON-ART attenuated backscatter signals (see Section 4.7).

The stratospheric volcanic plume layer consists of mainly spherical particles because the CALIOP depolarization ratio is between 0.1 and 0.2 (Figure 6.8c). The ICON-ART spherical particle fraction mainly agrees with this finding, at least for the uppermost part of this stratospheric volcanic plume layer (Figure 6.8e). The upper tropospheric regions of the plume in ICON-ART (between 10 and 15 km), where non-spherical particles are dominant, are lacking in both the CALIOP total attenuated backscatter and CALIOP depolarization ratio.

In the troposphere, ICON-ART total attenuated backscatter signals are enhanced between 10°S and 18°N and 5 to 10 km, which is only partly visible in the total attenuated backscatter signals of CALIOP (Figure 6.8b and d). However, the CALIOP depolarization ratio reveals spherical particles (depolarization ratio of about 0.1 to 0.3) close to the locations of increased total attenuated backscatter signals in the troposphere in ICON-ART (Figure 6.8c and d). The ICON-ART spherical particle fraction in Figure 6.8e shows that the plume is dominated by spherical particles at this location, which agrees well with the features in the CALIOP depolarization ratio (Figure 6.8c).

The CALIOP attenuated backscatter data show two distinct signals around 5°S and 5°N between 12 and 16 km altitude with a depolarization ratio of about 0.4 (Figure 6.8b and c). The attenuated backscatter in ICON-ART is very low in this area (Figure 6.8c and e). The CALIPSO vertical feature mask reveals that these features arise from ice clouds (not shown) as well as the attenuated backscatter signals north of 25° between 8 and 12 km in Figure 6.8b. The weakly depolarizing features below 5 km altitude north of 5°N (Figure 6.8b and c), which are not simulated by ICON-ART, are dust and sea salt aerosols according to the CALIPSO aerosol subtypes (not shown).

Besides this time step, the CALIPSO satellite crossed the volcanic plume from the La Soufrière eruption on twelve additional occasions. The agreement between CALIOP measurements and ICON-ART is similar for these dates (Figures C.7-C.17).

6.4.2. Temporal average

Having validated the aging with different types of datasets at fixed locations, I now examine whether aerosol aging is height-dependent. Figure 6.9a and b shows height-longitude cross sections averaged over all model output time steps (hourly global output) along the latitudes 11.08°N to 15.58°N ($\pm 2.5^\circ$ of the latitude of the volcano) for the spherical modes (mixed + soluble) and mixed mode proportions of the total ash and sulfate mass. These quantities are related to the particle composition and aging.

Figure 6.9c and d depicts the same but for the accumulation and coarse mode proportions of the total ash mass, i.e., this provides information on particle size. The total ash mass always refers to the sum of accumulation insoluble and mixed, coarse insoluble and mixed, and the insoluble giant mode masses.

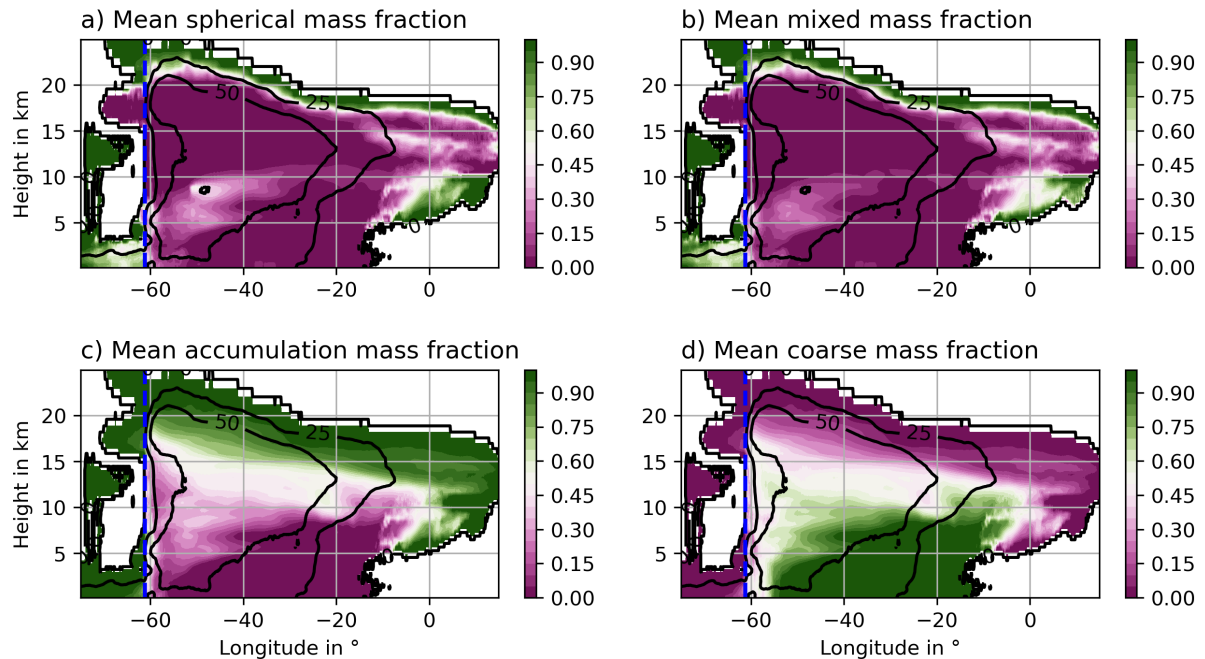


Figure 6.9.: Height-longitude cross-section of temporal averages over all 96 h for the latitudes $\pm 2.5^\circ$ around the latitude of the volcano (13.33°N) for the a) spherical particle mass (mixed mode + soluble mode) fraction of the total ash and sulfate mass, b) mixed mode fraction of the total ash and sulfate mass, c) accumulation mode fraction of the total ash mass, and d) coarse mode fraction of the total ash mass. The contour lines indicate the number of hours where ash is detected at the location and the blue dashed line refers to the longitude of the La Soufrière eruption.

In large part, the volcanic plume is dominated by uncoated ash particles, as Figure 6.9a is dominated by values close to zero. The fraction of the spherical particle mass is on the same order or larger than the mass of uncoated particles at the plume top, the eastern edge of the plume, and directly west of the volcano close to the surface and between 10 and 15 km.

The maximum plume height assumed for emissions was 18.3 km and the vent height was about 1.2 km. However, the upper plume reached altitudes larger than 20 km. Muser et al. (2020) showed that aerosol–radiation interaction can lead to a warming of the plume and a lofting of the plume top. Lofting brings particles to regions of higher O_3 and, thus, larger OH concentration, which increases aging and sulfate production. Furthermore, ash aging slightly increases the scattering properties in the SW range compared to pure ash particles. However, the increase in SW radiation extinction for aged particles is larger than for pure ash particles (compare Figure 3.2). Hence, aerosol aging increases aerosol–radiation interaction, which might even lead to stronger lofting and the formation of a spherical particle-dominated plume top. Although, Muser et al. (2020) found a faster removal of aged particles from the atmosphere within the

first four days due to a stronger increase in the particle diameter, the particle growth in the upper plume is too small to significantly affect the sedimentation velocities of coated particles here.

The fraction of spherical particles increases towards the eastern edge of the plume because there is more time for sulfate production and particle aging. As the main transport pathway of the plume is eastward, more time was available for sulfate production and particle aging west of the volcano as well.

Coated ash particles make the largest contribution to the spherical particle mass, whereas the contribution of sulfate is much lower in most parts of the plume (compare Figure 6.9a and b). This is partly related to the fact that the mass of mixed particles is larger than the mass of soluble particles due to the ash core. Nevertheless, an exception occurs between 60°W and 40°W up to about 9 km. In this region the formation of sulfate is enhanced due to the large availability of OH and water in the troposphere. With increasing distance from the source, the fraction of sulfate diminishes. This is likely due to coagulation with ash particles. The coated particles increase in diameter, which leads to a faster removal from the atmosphere. This can be seen in Figure 6.9b below 10 km between 60°W and 15°W because the mixed mode fraction also decreases with increasing distance from the source, but more slowly than the fraction of the spherical modes in Figure 6.9a.

The ash plume consists mainly of particles in the accumulation mode at the plume top and particles in the coarse mode closer to the surface (Figure 6.9c and d). As coarse mode particles are larger and heavier than particles in the accumulation mode, they sediment faster and increase the fraction of larger particles from plume top towards the surface. When comparing Figure 6.9c and d, the fraction values between 55°W and 60°W and from surface to 15 km are closer to 0.5 for the coarse mode fraction than for the accumulation mode fraction. At this distance from the volcano, the plume still contains a considerable amount of particles in the giant mode. Everywhere else, the colors seem to be switched, meaning the ash plume only consists of particles in the accumulation and coarse modes.

The highest fraction of coated particles in the troposphere below 13 km (Figure 6.9b) is collocated with the highest fraction of accumulation mode particles in the troposphere (Figure 6.9c). This results from the larger available surface area of accumulation mode particles compared to coarse mode particles, which increases the condensation of H₂SO₄ onto ash particles. Furthermore, the shift from the insoluble mode into the mixed mode occurs faster because the threshold of 5% soluble mass on insoluble ash is reached earlier.

7. Sulfur chemistry in explosive volcanic eruptions

The previous chapter showed that ash emissions and aerosol dynamics lead to a coating of ash particles, which is reasonably modeled by ICON-ART. However, ash not only removes sulfur from the atmosphere by condensation or nucleation and coagulation (Muser et al., 2020), it also allows dissolution of gases in the liquid shell of coated ash particles (Hoshyaripour et al., 2015). These dissolved gases might undergo chemical reactions in the aqueous phase (e.g., Tabazadeh and Turco, 1993; Liang and Jacobson, 1999; Hoshyaripour et al., 2015; Lachatre et al., 2022). This chapter investigates the chemical fate of volcanic sulfur in the eruption plume in more detail, which has implications for climate. Besides gas-phase chemistry, this chapter also considers aqueous-phase chemistry on coated ash and SO₂ adsorption on ash surfaces.

The computational costs for experiments including complex chemistry mechanisms are very high because of the large number of tracers. Therefore, the modeled period after the volcanic emissions can only be short, and I study again the 2019 Raikoke eruption because the emissions occurred during a shorter period compared to the 2021 La Soufrière eruption. I simulated 30 h starting from 21 June 2019, 12 UTC.

The experiments were performed in a LAM domain, which is shown in Figure 7.1. The horizontal grid spacing in the LAM domain was approximately 2.5 km (R2B10). The temporal resolution was 16 s and the atmosphere was vertically resolved by 90 vertical levels up to 50 km altitude. The simulation was initialized by analysis fields provided by DWD, which were remapped onto the region of interest. The lateral boundaries of the LAM area were updated by the meteorology and chemistry every two hours.

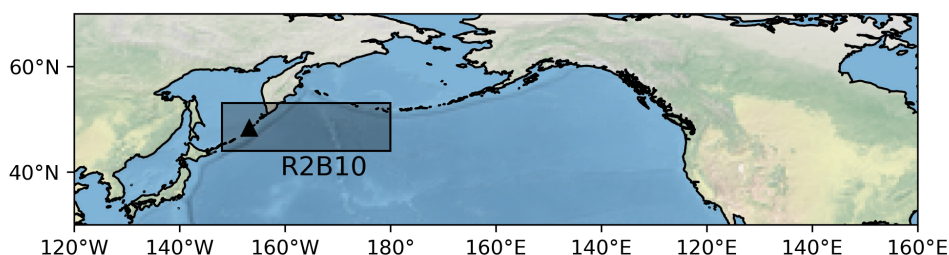


Figure 7.1.: LAM area for the chemistry experiments in case of the 2019 Raikoke eruption. The simulations were performed on a LAM area of 2.5 km horizontal grid spacing (R2B10).

The background concentrations of the most abundant chemical species (listed in Section B) were initialized with data from the Community Atmosphere Model with chemistry (CAM-chem (2019), Lamarque et al. (2012)) provided by the National Center for Atmospheric Research (NCAR, downloaded from

<https://www.aocom.ucar.edu/cam-chem/cam-chem.shtml>). CAM-chem predicts tropospheric and stratospheric concentrations of various species with the MOZART-4 chemistry mechanism, which was also used here in ICON-ART. In all experiments including emissions, ash and SO₂ were emitted as explained in Section 4.1.3 and as it was done in Chapter 5. The reference experiment only considered gas-phase chemistry. Additional experiments were performed to investigate the role of aqueous-phase chemistry in the shells of coated ash and SO₂-adsorption on fresh ash in the oxidation of volcanic SO₂ and the impact of water vapor emissions on aqueous-phase chemistry. Table 7.1 gives an overview about the experiments. Water vapor emissions were calculated with FPlume.

The fate of SO₂ in the first hours of the horizontal plume dispersion is determined in the next section and discussed in context of already existing literature. Afterwards, the effect of in-plume chemistry on the concentrations of OH, O₃, and CH₄ is investigated.

Name	Chemistry mechanism	Ash and SO ₂ emission	H ₂ O emission	Aerosol–radiation interaction
REFERENCE	only gas-phase	✓		
AQUEOUS	gas- and aqueous-phase	✓		
AQwithH2O	gas- and aqueous-phase	✓	✓	
ADSORPTION	gas-phase, SO ₂ -adsorption on ash	✓		
ARI	only gas-phase	✓		✓
NoEmiss	only gas-phase			

Table 7.1.: Raikoke chemistry experiments.

7.1. Chemical fate of volcanic SO₂

Different experiments were performed to investigate the oxidation of SO₂ in the early stage of the plume. Figure 7.2 shows the temporal development of the SO₂(g), S(IV), sulfate, ash, and aerosol liquid water burdens for the REFERENCE, AQUEOUS, AQwithH2O, ADSORPTION, and ARI experiments. The two main points here are: (1) the aqueous-phase chemistry does not play a role in removing SO₂ during the horizontal plume spreading in the first days, although it has been shown that this pathway plays a large role during the plume rise (Tabazadeh and Turco, 1993; Hoshyaripour et al., 2015) and in tropospheric eruptions (Lachatre et al., 2022); (2) SO₂ adsorption on ash particles removes SO₂ most effectively in the first hours and increases the amount of liquid water on aerosols. The next two sections investigate these findings in more detail and compare them with previous studies.

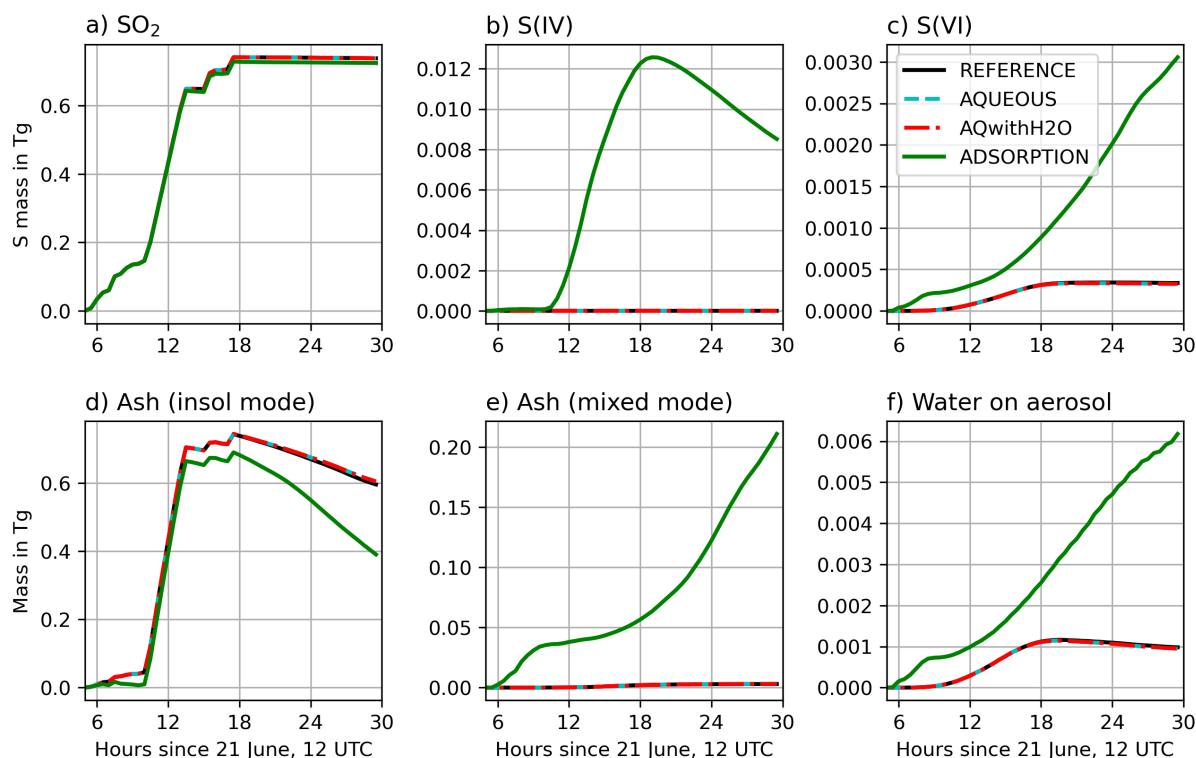


Figure 7.2.: Temporal development of the mass burden of SO₂(g), S(IV), S(VI), ash in the insoluble mode, ash in the mixed mode, and liquid water in the aerosol phase after 21 June 2019, 12 UTC in different experiments.

7.1.1. Aqueous-phase chemistry on aged aerosols

Previous studies found that dissolution and aqueous-phase chemistry effectively remove sulfur compounds and other species from the gas phase (e.g., Tabazadeh and Turco, 1993; Liang and Jacobson, 1999; Harris et al., 2013; Hoshyaripour et al., 2015). Nevertheless, the temporal development of the SO₂ burden in Figure 7.2a reveals almost no effect on the removal of SO₂ after the Raikoke eruption. Figure 7.3 shows maps of averaged column loadings of gaseous SO₂ and aqueous S(VI), S(IV), and H₂O from top to bottom for 18 – 30 h after simulation start for the AQUEOUS experiment, the anomalies between AQwithH₂O and AQUEOUS, and the anomalies between REFERENCE and AQUEOUS from left to right. The column loading of H₂O on the ash particles is on the order of up to a few mg m⁻², 4 – 5 orders of magnitude lower than the column loading of SO₂. This low ALWC makes dissolution of gases and aqueous-phase chemistry on coated aerosols negligible (right column).

The sulfate and water content is slightly larger when only considering gas-phase chemistry because the formation of H₂SO₄ increases when gaseous SO₂ is larger. Additionally, OH can dissolve in water and lower the gaseous OH concentrations. Sulfate coating increases the hygroscopic behavior of aerosol particles and, therefore, increases the liquid water on the aerosol particles in the experiment with gas-phase chemistry (Figure 7.3h and k). However, the differences are too small to play a role here.

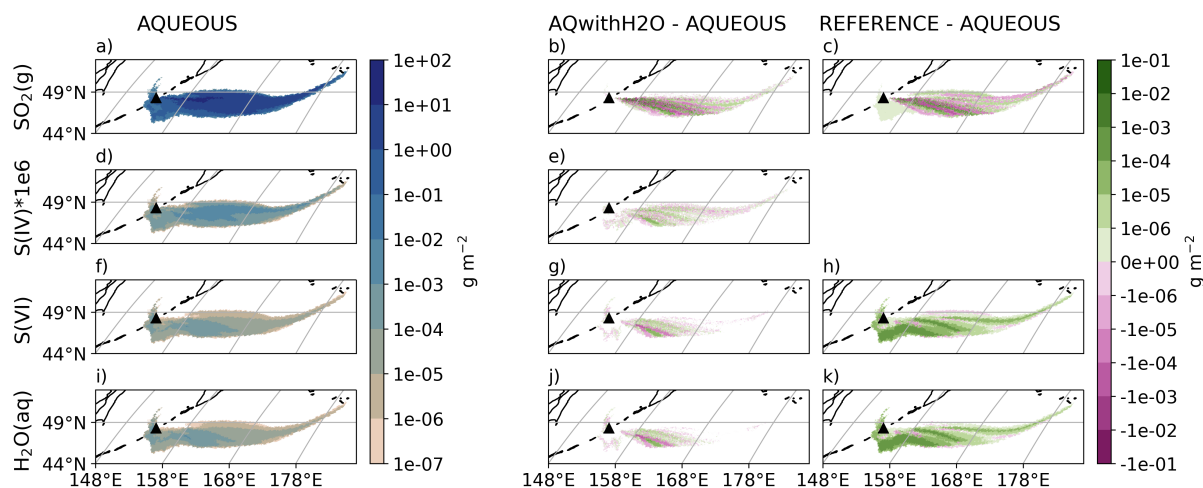


Figure 7.3.: 12 h-averaged (18 to 30 hours after simulation start) column loadings of gaseous SO_2 , $\text{S}(\text{VI})$, $\text{S}(\text{IV})$, and liquid water on coated aerosols (top to bottom) in g m^{-2} for AQUEOUS, difference between AQUEOUS and AQwithH2O, and difference between AQUEOUS and REFERENCE (first, second, and third column).

As volcanic eruptions also emit large amounts of water vapor, it can increase the amount of liquid water on aerosols. I performed a simulation with water vapor emissions. The emission of additional water vapor from the eruption has almost no effects on the results because it deposits quickly and is not available for condensation or gas-phase chemistry anymore (Figure 7.3 middle column). The water vapor was emitted onto the ART H_2O chemical tracer. The emission into the ICON tracer for the water vapor mixing ratio and water phase changes calculated in the ICON microphysics would have been favorable, but technical reasons prevent this with the current implementation of FPlume (see Section 3.6). It is possible that the simple deposition routine for the chemical H_2O tracer (Section 3.6) removed too much water vapor although small amounts of supercooled liquid droplets could exist in the plume.

It is likely that the ALWC increases in a warmer and more humid environment. Therefore, time–height cross-sections of the volcanic plume of the same compounds and experiments as in Figure 7.3 are given in Figure 7.4. The amount of aerosol liquid water is largest below 7 km due to the larger atmospheric humidity (Figure 7.4i). It increases with increasing amount of sulfate (Figure 7.4f), which itself depends on the diurnal cycle of the H_2SO_4 production. The mass of sulfur in oxidation state 4 reaches a maximum between 12 and 18 h at 6 to 7 km (Figure 7.4d). The location of this maximum is driven by both the liquid water on the particles and the amount of gaseous SO_2 (Figure 7.4a and i).

The difference between REFERENCE and AQUEOUS in the amount of water on aerosols reaches a maximum at around 4 km after 24 h (Figure 7.4k), which is related to both the higher sulfate mass on ash in REFERENCE (Figure 7.4h) and the atmospheric humidity. These differences occur at the lower boundary of the gaseous SO_2 plume (Figure 7.4a), i.e., where the humidity within the SO_2 plume is expected to be highest.

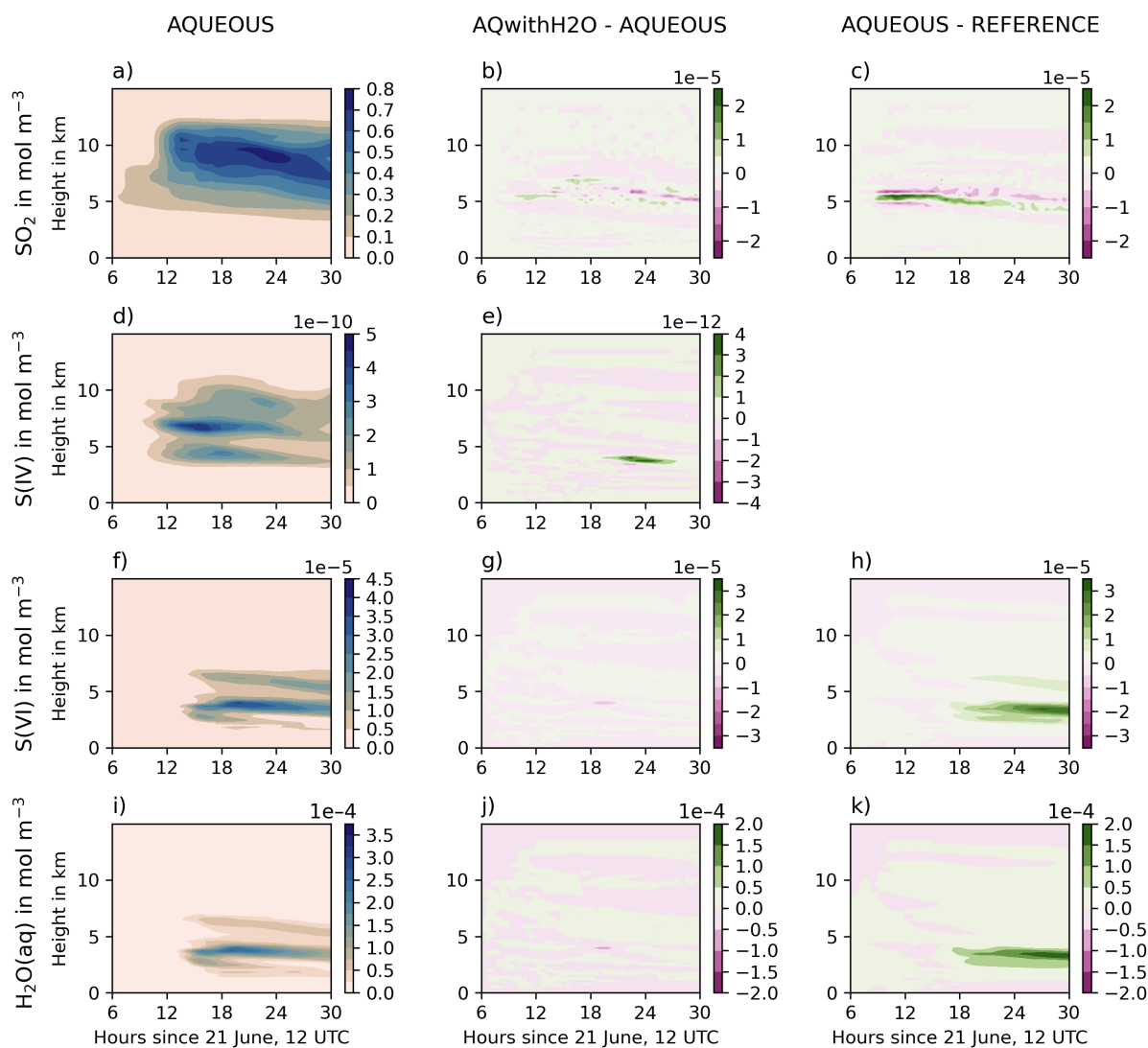


Figure 7.4.: Time–height cross-sections of horizontally-integrated concentrations of gaseous SO₂, S(VI), S(IV), and liquid water on coated aerosols (top to bottom) in mol m⁻³ for AQUEOUS (first column), the difference between AQwithH₂O and AQUEOUS (second column), and the difference between REFERENCE and AQUEOUS (third column).

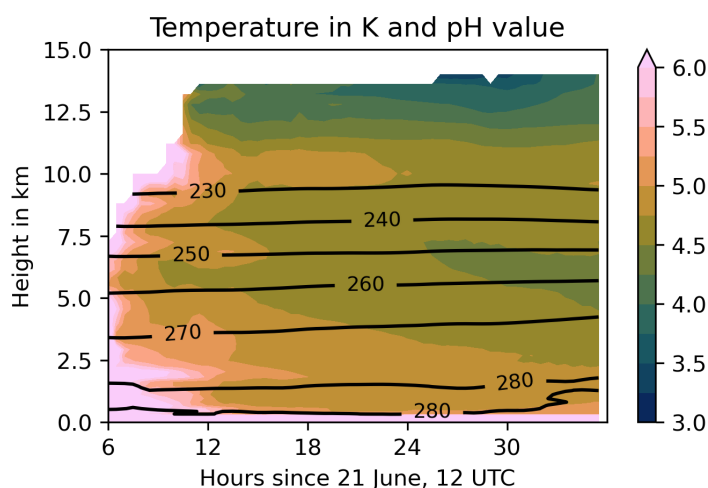


Figure 7.5.: Time–height cross-section of the horizontally-averaged aerosol shell pH value indicated in colors and the ambient temperature in K indicated in contours.

The emissions during the Raikoke eruption occurred mainly in the upper troposphere lower stratosphere (UTLS) region, where ambient temperatures reach a minimum. This could also lead to a freezing of coated particles, when the liquid water on the aerosols is high compared to the amount of oxidized species in the solution. In Figure 7.5, the height-dependent temporal development of the pH value is plotted in colors and the temperature is plotted in contours. The pH value is in most parts below 4.5 – 5, which makes freezing of the soluble shell unlikely despite the low temperatures (on the order of -40°C above 10 km) (e.g., Tabazadeh and Turco, 1993).

7.1.2. SO_2 adsorption on ash

Different from aqueous-phase chemistry, the experiment with adsorption of SO_2 on ash surfaces reduces the amount of SO_2 in the gas phase slightly (Figure 7.2a, experiment ADSORPTION). The oxidation by O_3 via adsorbed sulfur increases the sulfate amount on ash aerosols and causes a faster aerosol aging (Figure 7.2c and e).

Figure 7.6 shows time–height cross-sections of different compounds in the REFERENCE experiment (first two rows) and the effect of SO_2 adsorption on the evolution of these species (ADSORPTION – REFERENCE, last two rows). The largest sulfate anomaly between the two experiments arise after about 15 h at altitudes where both SO_2 and ash concentrations are high or in other words where the amount of adsorbable gas and adsorption surfaces are enhanced (around 6 to 11 km, Figure 7.6a, e, h, and i). The enhanced coating of sulfate on ash particles leads to a shifting of particles from the insoluble to the mixed modes especially between 5 and 10 km (Figure 7.6k and l). Thus, SO_2 adsorption provides an effective mechanism for aerosol aging in altitudes where water vapor, OH, and H_2SO_4 concentrations are low (compare Section 7.1.1).

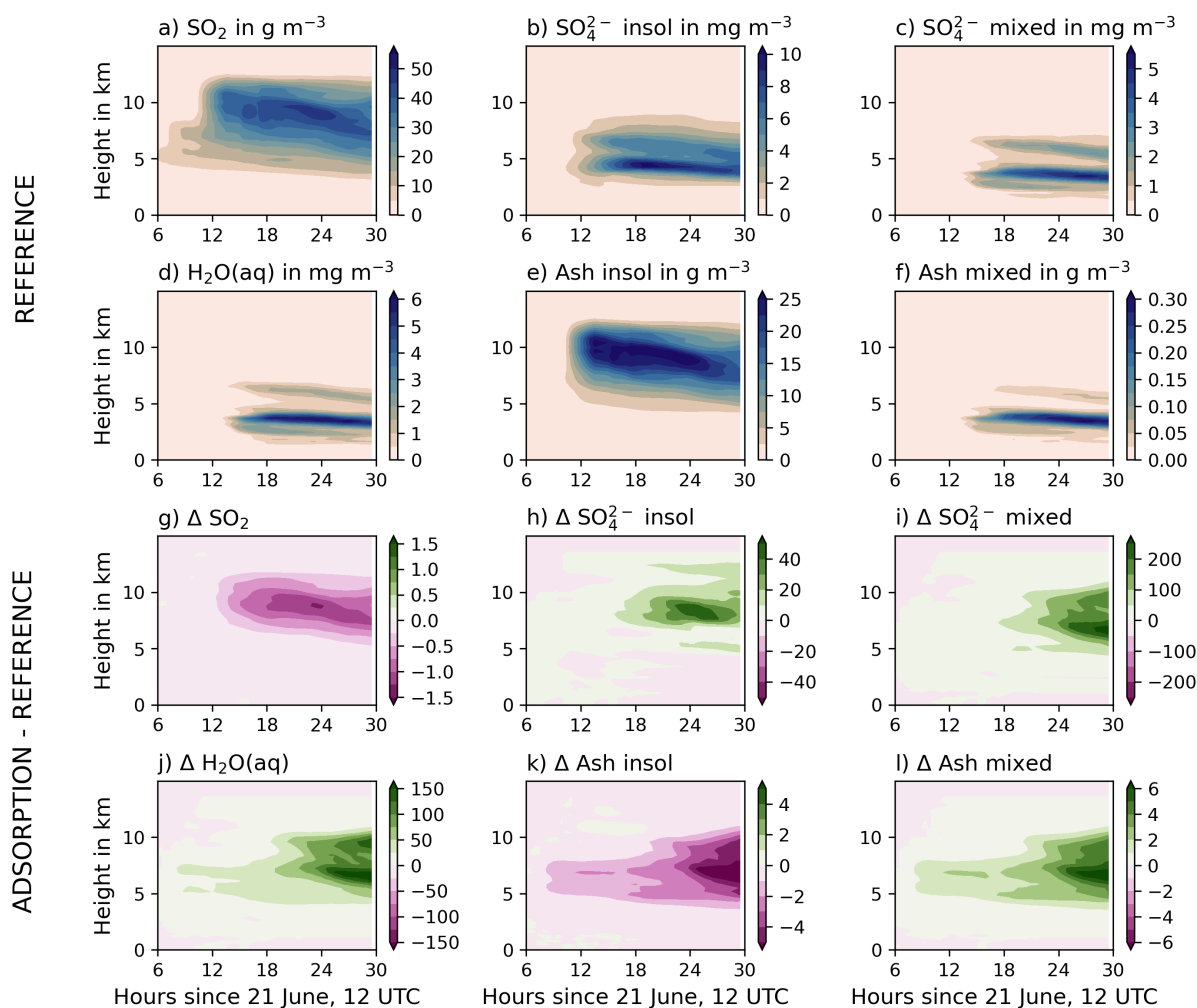


Figure 7.6.: a – f: Time–height cross-section for horizontally-integrated concentrations of SO₂(g), sulfate in the insoluble mode, sulfate in the mixed mode, liquid water on aerosols, ash in the insoluble mode, and ash in the mixed mode in the REFERENCE experiment; g – l: Difference between ADSORPTION and REFERENCE of the same compounds as in a – f) (same units).

The increased coated sulfate mass changes the hygroscopic behavior of ash and results in an accumulation of water on the particles (Figure 7.2j). The differences in liquid water on aerosols between the REFERENCE and ADSORPTION experiment are the largest around 6 to 10 km, agreeing with the altitude of the highest sulfate anomalies (Figure 7.6h, i). Whether increased sulfate production followed by water accretion together with volcanic water vapor emissions and comprehensive microphysics increases the importance of aqueous-phase chemistry, needs evaluation in further studies with longer simulations.

7.1.3. Discussion

My simulations show a negligible effect of aqueous-phase chemistry in the early stage of the Raikoke plume due to a low ALWC and a quick removal of volcanic water from the vapor phase. These findings are in agreement with the simulations conducted by Textor et al. (2003). With the 3-D plume model

ATHAM and parametrizations for scavenging (no complex chemistry mechanism), they found that 99% of hydrometeors in the plume of Plinian eruptions during the plume rise are frozen leading to a very low scavenging of HCl and SO₂ by liquid droplets. Instead, additional scavenging by ice particles reduces the amount of gas reaching the stratosphere to about 25% for HCl and to about 90% for SO₂. SO₂ scavenging by ice particles was neglected in this thesis. However, these processes together with volcanic water emissions and a comprehensive microphysical scheme might give further insights into the removal mechanisms of SO₂ during the horizontal plume spreading after large volcanic eruptions.

At first glance, the results presented here seem to be in contrast to the findings by Hoshyaripour et al. (2015), who found a 3 – 20% scavenging of SO₂ on coated ash by using a comprehensive chemistry mechanism and a box model for volcanic plumes. Nevertheless, important differences in their setup and the one used here are the temperatures and time scales. The box model by Hoshyaripour et al. (2015) was designed to also consider the hot temperatures during the rise of the plume. This allows the formation of large amounts of liquid droplets and larger liquid shells, which enhances the aqueous-phase chemistry. An additional water vapor release from the eruption can further strengthen the formation of liquid water. In this thesis, most of the volcanic compounds are released into the UTLs by keeping the temperature profiles of ICON. Thus, the processes occur in an environment with (1) low background H₂O levels in vapor and liquid phase, and (2) additional emitted water vapor deposits quickly and is not available anymore for chemistry or condensation on aerosols. This suggests that aqueous-phase chemistry is important during the emission, but plays a negligible role in removing SO₂ from the atmosphere during the further plume development. Additionally, the results might look different for smaller volcanic eruptions (Lachatre et al., 2022) or at higher altitudes (Abdelkader et al., 2023).

Zhu et al. (2020) found that adsorption alone removed 43% of the SO₂ mass within the first two months after the 2014 Mt Kelud eruption. However, the authors used a significantly higher uptake coefficient ($3 \cdot 10^{-3}$ instead of 10^{-6}) to obtain agreement between their model results and observations. Using the same uptake coefficient here causes a drastic removal of SO₂ already during the emissions (Figure 7.7a), which would need to be compensated by larger emissions to fit the observations of SO₂ mass in the first hours after the eruption. The uptake occurs almost instantaneously causing a quick loss of ash due to the growth of particles (Figure 7.7b – f), which is significantly different from the findings in Chapter 5. Furthermore, Chapter 6 revealed a good agreement between modeled and observed aerosol aging (MISR RA) close to the volcano (Figure 6.7). Although the SO₂ emission during the La Soufrière eruption was much lower compared to the Raikoke eruption, the uptake coefficient used in Zhu et al. (2020) would certainly reduce the agreement between modeled and observed aerosol aging in the first minutes to hours due to a quick formation of aged particles. The reason why the drastic loss of ash was not observed in the simulations by Zhu et al. (2020) might be that the emissions were realized in a line along 2 to 12°S and assuming a vertical profile. This leads to lower concentration gradients at the beginning. The horizontal grid spacing used here (2.5 km) is on the order of a typical plume radius (up to a radius of 12 km in the Raikoke umbrella region based on FPlume offline simulations).

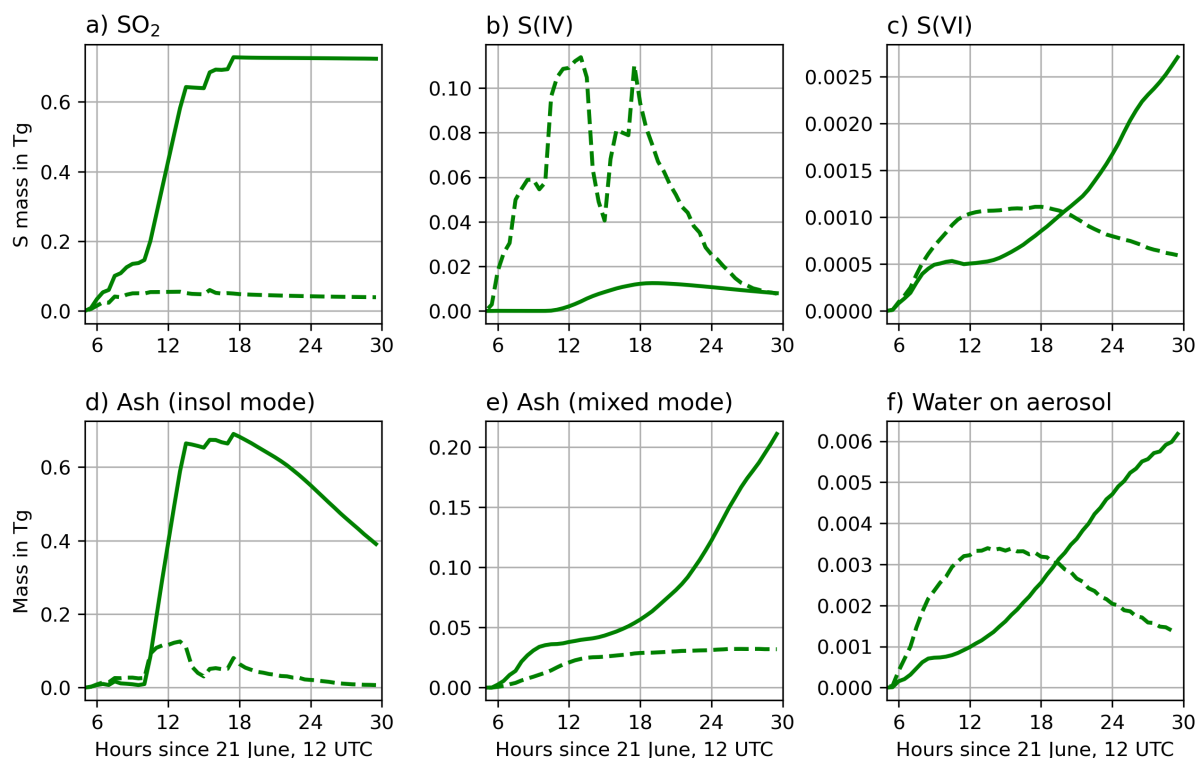


Figure 7.7.: As Figure 7.2, but only for the ADSORPTION experiment (solid) and an experiment with gas-phase chemistry and SO₂-adsorption on ash assuming the uptake coefficient from Zhu et al. (2020) (dashed).

Zhu et al. (2020) chose the uptake coefficients measured in experiments by Maters et al. (2017). The uptake coefficients used in this thesis were experimentally derived by Urupina et al. (2019). Both studies assumed ambient tropospheric temperature conditions (approximately 25°C). Maters et al. (2017) measured initial uptakes of SO₂ i.e., 'an uptake on the fresh surface at the first instance of its interaction with gas' (Urupina et al., 2019), whereas the steady-state uptake reported in Urupina et al. (2019) 'is an ongoing phenomenon reflecting the ability of the surface to adsorb gas continuously' (Urupina et al., 2019). Lasne et al. (2022) argued that the high uptake coefficient of Zhu et al. (2020) needed to match simulations with observations might be due to missing photolysis processes in the model.

According to Schmauss and Keppler (2014), lower temperatures enhance the adsorption of SO₂ on ash surfaces and reduce the concentrations in the gas phase stronger. However, no uptake coefficients were derived that can be used here. A temperature-, humidity-, and radiation-dependent parametrization for the uptake coefficient will be helpful to scale the uncertainties in the modeled SO₂ adsorption during the volcanic plume dispersion in the first hours and in the plume development beyond.

7.2. Impacts of sulfur emissions on atmospheric chemistry

This section determines the effect of volcanic emissions on the OH, O₃, and CH₄ concentrations in the volcanic plume. Figure 7.8 displays the temporal evolution of these concentrations depending on the

altitude in the experiment without volcanic emissions (NoEmiss) in the first row and the effects of volcanic emissions only considering gas-phase chemistry (second row), the effects of gas-phase chemistry and aerosol–radiation interaction (third row), and the effects of gas-phase chemistry and SO₂ adsorption (fourth row). The region of the plume is defined as the grid cells where the SO₂ concentration exceeds 10 ppm in the REFERENCE experiment. This procedure is different from the previous plots, because here no plume can be defined based on the NoEmiss experiment.

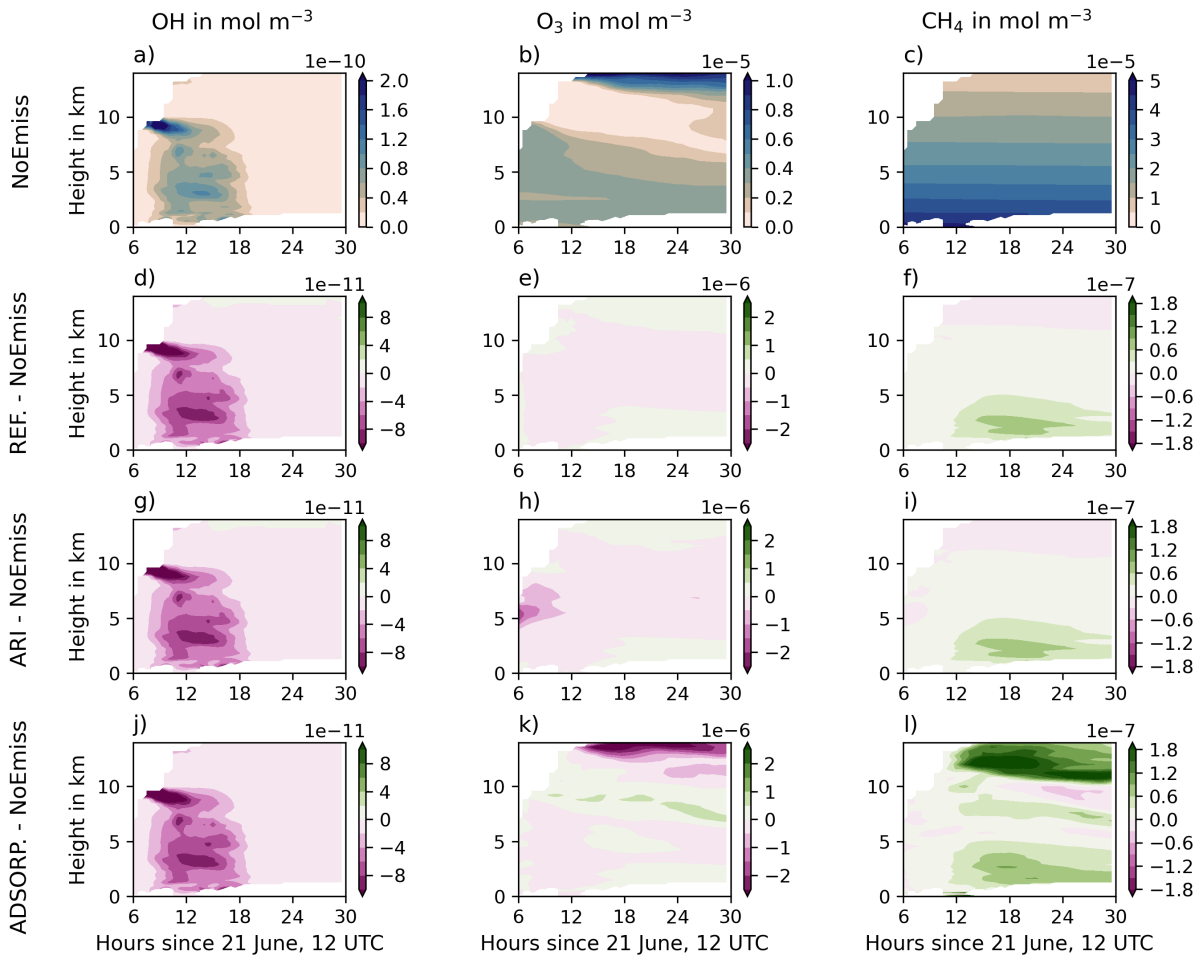


Figure 7.8.: Time–height cross-section of horizontally-averaged OH (first column), O₃ (second column), and CH₄ (third column) concentrations in mol m⁻³ in the volcanic plume in the NoEmiss experiment (first row), the difference between the REFERENCE and noEmiss (second row), the difference between ARI and noEmiss (third row), and the difference between ADSORPTION and NoEmiss (fourth row). For all experiments, the plume was defined where SO₂ concentration exceeds 10 ppm in the REFERENCE case.

OH concentrations are enhanced between 8 and 18 h after simulation start, which agrees well with the local daytime (Figure 7.8a). Including volcanic emissions drastically reduces OH concentrations especially at day when OH is produced (Figure 7.8d, g, j). Volcanic SO₂ reacts with OH (and water and oxygen) to form H₂SO₄, a reaction that is limited by the abundance of OH.

The reaction of OH is an important sink for CH₄ in the atmosphere (Table B.1, Jourdain et al. (2016)). All experiments including volcanic emissions show an increase of CH₄ up to 6 km altitude after 12 h, which is related to the lower amount of OH. In the experiment including SO₂ adsorption on ash (ADSORPTION), the CH₄ concentration up to 5 km is largest compared to the other experiments and further shows large positive anomalies at the plume top (above 11 km). O₃ photochemical reactions produce O(¹D), which is an important sink for CH₄ in the stratosphere, especially during daytime (Table B.1). In the ADSORPTION experiment, the reaction of gaseous O₃ with adsorbed SO₂ reduces the photochemical production of O(¹D) from O₃ (Figure 7.8k and l).

SO₂ adsorption on ash and subsequent oxidation by O₃ reduces the O₃ concentration to about 10% at the plume top (Figure 7.8b and k). For larger volcanic eruptions, the oxidation of adsorbed S(IV) might increase with increasing altitude due to higher concentrations of O₃ in the center of the ozone layer. Nevertheless, the oxidation of adsorbed S(IV) on ash in larger volcanic eruptions is subjected to further research.

The lower amount of O₃ at the beginning of the eruption around 4 to 8 km in the experiment ARI arises from temperature and radiation changes in the plume (Figure 7.8h).

These results show that volcanic emissions can disturb background chemistry fields. Here, the concentrations of OH, O₃, and CH₄ were initialized with CAM-chem chemistry for the most abundant components. OH is a major oxidizing species in the atmosphere. The reaction of CH₄ with OH represents an important source of stratospheric water and, thus, gas-phase chemistry and SO₂ adsorption in volcanic plumes indirectly also slow down water vapor production in the stratosphere. Additionally, O₃ and CH₄ both absorb radiation. To what extent changes in OH, O₃, and CH₄ background concentrations due to different SO₂ oxidation pathways influence stratospheric chemistry on climate scales, needs further investigations.

8. Conclusions

The aim of this thesis was to close the gap between early plume processes and the impact of volcanism on weather and climate. The main focus was on the representation of the ESPs, the impact of early aerosol aging, and chemistry at the early stage of a volcanic eruption. I developed a model setup in which the ESPs were improved by (1) coupling ICON-ART with FPlume to account for the effect of changing volcanic and meteorological conditions and (2) a delineation of eruption phases. With this setup, I simulated the 2019 Raikoke eruption, which emitted volcanic ash and gases in ten individual eruption phases. The dispersion of the 2019 Raikoke eruption plume was addressed in several studies (e.g., Muser et al., 2020; de Leeuw et al., 2021), in which the ESPs, however, were strongly simplified and led to large discrepancies between model and observations in the first hours during and after the eruption. Based on my simulations, I am able to answer the following research questions:

1. How large is the influence of resolving the eruption phases on the predicted ash mass loading?

A large improvement of the total ash burden forecast is demonstrated in the first 12 h by resolving the individual eruption phases of the Raikoke eruption. This delineation of eruption phases halves the error and reduces the ash mass overestimation from 37% to 18% compared to AHI observations from the Himawari-8 satellite. Furthermore, the maximum amount of ash is better represented between 8 and 12 h after the beginning of the eruption (plateau instead of sharp peak).

2. Can an online treatment of volcanic ESPs improve the predicted mass loading and dispersion of ash and SO₂ plumes?

Besides resolving the eruption phases, online calculations of ESPs by FPlume further improve the temporal evolution of the simulated ash mass, which shows an almost perfect agreement with the observed evolution of ash mass loading. In addition to the mass loading, the predicted spatial dispersion of the ash and SO₂ plume also agrees well with the AHI observations from Himawari-8 as the SAL analysis reveals. However, I hypothesized that the validation of the simulated ash and SO₂ dispersion is partially hampered by a dense ash plume in the beginning of the eruption and by overlapping water and ice clouds later on.

The results confirm that coupling ICON-ART and the plume rise model enables detailed treatment of the plume dynamics (phases and ESPs) and leads to significant improvements of the ash and SO₂ dispersion forecast. This approach can benefit the operational forecast of ash and SO₂ especially in the case of complex and non-continuous volcanic eruptions like that of Raikoke in 2019. Furthermore, it allows to study processes in multi-day non-continuous eruptions, such as the 2021 La Soufrière eruption.

The available observations during the 2021 La Soufrière eruption offered a unique opportunity to validate emissions and aging of volcanic ash in ICON-ART directly for the first time. This can have implications for the further plume development, weather (by modifying clouds), and climate. The La Soufrière eruption was characterized by 43 individual phases in the first four days and 49 phases during the entire eruption period from 09 to 22 April 2021. In order to simulate this eruption, I used the same setup as for the simulation of the 2019 Raikoke eruption. In addition to providing an accurate ash mass, this setup allowed a comparison between model and observations close to the volcano, where the individual eruption phases were still separated from each other.

I compared the results with different products from remote sensing instruments, i.e., total attenuated backscatter from CALIOP onboard CALIPSO, plume heights, AOD, fraction of spherical particles, and SSA from MISR onboard Terra, and equivalent radar reflectivity from BCO. This enables me to answer the following research questions:

3. What controls the near-source distribution of ash particles?

The near-source distribution of ash particles is strongly driven by the emissions, and the consideration of the individual eruption phases is important for modeling the 2021 La Soufrière eruption. My results show that volcanic aerosol aging begins already close to the volcano. It is especially visible in the plume part south of Barbados in both the model and observations. A comparison with the northern part is only possible to a limited extent due to the complicating presence of meteorological clouds in the MISR data. Muser et al. (2020) found that aerosol dynamics have a huge impact on the lifetime and the vertical distribution of volcanic ash in the atmosphere in the first four days after the 2019 Raikoke eruption. However, close to the volcano, ash aging has a minor effect on the distribution of the ash plume because the time for particle growth is short (a few hours) as revealed by my results.

4. Which processes drive particle aging near the volcano and during the further transport?

The rate of aging is faster in the troposphere than above the tropopause. I argued that the lower abundance of OH in the stratosphere reduces sulfate particle formation and the condensation of H₂SO₄ onto existing particles. Furthermore, lower relative humidity in the stratosphere reduces the condensation of water onto the aerosols. As a consequence, the coagulation of ash particles with sulfate is also reduced in the stratosphere. However, spherical particles dominate the plume top across all longitudes. Muser et al. (2020) found a lofting of the volcanic plume top due to aerosol–radiation interaction. I showed in Chapter 5 that the absorption of radiation by ash in volcanic plumes also leads to a rise of the SO₂ plume top. In addition to the previous findings from Muser et al. (2020) and Chapter 5, I argue that lofting by aerosol–radiation interaction might be stronger for coated ash than for pure ash (at least as long as particle growth is small). Together with faster SO₂ oxidation rates, this causes a formation of a plume top dominated by spherical particles.

In Chapters 5 and 6, I assumed a simplified OH chemistry mechanism for the formation of H₂SO₄ from volcanic SO₂. A complex chemistry mechanism including aqueous-phase chemistry and adsorption of SO₂ on ash helped to understand gas–aerosol partitioning of sulfur compounds in the early plume dispersion. This permits to answer the following research questions.

5. What is the effect of aqueous-phase chemistry and gas adsorption by ash surfaces on the removal of gaseous SO₂ from the atmosphere in the first days?

Different from simulations during the plume rise (e.g., Tabazadeh and Turco, 1993; Hoshyaripour et al., 2015), my simulations showed that the influence of aqueous-phase chemistry is negligible during the horizontal dispersion of the plume in the first days due to the low liquid water amount on coated aerosols. Additionally emitted volcanic water vapor deposits quickly and has no impact on the plume chemistry. However, adsorption of SO₂ on freshly emitted (non-coated) ash increases the amount of sulfate on aerosols and the fraction of coated particles on the first day after the 2019 Raikoke eruption. This increased amount of sulfate results in an accumulation of liquid water on aerosols due to a larger hygroscopicity of the particles.

6. How large is the effect of in-plume chemistry on background O₃, OH, and CH₄ concentrations?

The oxidation of SO₂ strongly depends on the availability of OH, which is a limiting factor for the aerosol aging. The reaction with gaseous SO₂ drastically reduces daytime OH concentration. As OH is a major oxidizing species in the atmosphere, the removal of CH₄ decreases as a result of the gas-phase SO₂ oxidation in the early volcanic plume. SO₂ adsorption and the heterogeneous reaction with O₃ reduce O₃ concentrations predominately at the plume top, where O₃ concentrations are largest. As a consequence, less O(¹D) is produced from O₃ photolysis that can serve as a sink for CH₄ in the upper part of the plume.

Despite the efforts to precisely represent the eruption dynamics, input parameters (e.g., start and end time of individual eruption phases, plume heights, and exit conditions) are still major sources of uncertainty in my simulations. FPlume needs input parameters for the plume height, exit temperature, exit velocity, and exit volatile fraction. In the lack of direct measurements for specific eruptions, I relied on the available data and estimations for eruptions with similar conditions (tectonic setting, explosivity index, and magma composition). Based on offline analysis, I estimated the uncertainties in the MER due to errors in the input parameters to be in a range of 20%, which will not significantly change my results.

8.1. Outlook

The results in Chapter 7 indicated a negligible SO₂ oxidation via aqueous-phase chemistry on the first day after the eruption, which was related to the low ALWC in the dispersing volcanic plume. The experiment including adsorption of SO₂ on ash surfaces, however, indicated a quicker aerosol aging, which increased

the amount of liquid water in coated aerosols. Whether this leads to an increasing relevance of aqueous-phase chemistry in the further plume development should be clarified in future works. To investigate this further, a reduction of the number of tracers is needed to be able to run simulations on a larger domain for several days. Additionally, current developments on seamless predictions with ICON-ART allow to consider plume and aerosol dynamics as well as gas–aerosol interactions during the early stage of the volcanic plume in simulations covering several weeks to months.

The effect of water vapor emissions on chemistry during the plume dispersion in my simulations in Chapter 7 was not relevant due to a quick removal of H₂O from the gas phase. Although the coupling to FPlume significantly improves the volcanic emissions, it neglects the temperature changes in the vertical column above the vent. Especially in the jet and lower convective region of the plume, emitted and entrained water stays in the gas phase due to the heat from the volcano (see Figure 2.3a) and changes the gas- and aqueous-phase chemistry (Tabazadeh and Turco, 1993; Hoshyaripour et al., 2015). The effects of aqueous-phase chemistry during the plume rise on the dispersing plume can be studied by simulating volcanic plumes as multiphase flows in ICON-ART in the future. This approach is currently developed. A coupling of multiphase flows to the achievements made in this thesis and previous work by Muser et al. (2020) with respect to aerosol dynamics and chemistry is planned for the future. Whether a larger abundance of supercooled droplets, possibly driven by a reduction of the freezing temperature due to sulfate in the liquid phase, reaches the stratosphere and increases the importance of aqueous-phase chemistry on the first day needs to be investigated in the future as well.

For my simulations, I assumed an equal ash mass emission into the accumulation, coarse, and giant modes as derived by Muser et al. (2020) for the 2019 Raikoke eruption from measurements of similar eruptions. The results in Chapter 5 revealed a good agreement of the modeled and observed ash mass in the following days, which suggests a reasonably assumed PSD. Observations for the total ash mass in case of the 2021 La Soufrière eruptions are not available and the mass could not be validated. Uncertainties in the PSD do not only affect the sedimentation of ash mass but also the condensation of H₂SO₄ on ash. The larger the surface (i.e., the smaller the particles), the stronger the condensation. The impact of an assumed PSD on aerosol dynamics will be the focus of future work. To study this, a development of forward operators in ICON-ART can help to directly compare physiochemical and optical properties (complex refractive index) modeled with different PSDs to satellite observations of the same properties. Volcanic ash from different volcanic eruptions cover a wide range of silica contents, which has to be included in the description of the complex refractive index.

Chapter 6 revealed large differences in the plume heights and aerosol properties between model results and MISR observations in some regions of the plume. These regions were also largely covered by clouds, which hampered a comparison of model and observations. It is possible that sulfate and ash aerosols acted as CCNs and INs, respectively. In my simulations, the interaction of aerosols and clouds was not considered and is the topic of ongoing work.

A. FPlume input parameters

2019 Raikoke eruption

Date	Time in UTC	Plume height in m (a.s.l.)	Exit temperature in K	Exit velocity in m s^{-1}	Exit volatile fraction in %	SO ₂ mass emission rate in kg s^{-1}
21 June	17.55 – 18.20	7250	1273	106	3	43865
21 June	18.50 – 19.05	9250	1273	118	3	56960
21 June	19.40 – 20.05	10250	1273	124	3	63507
21 June	20.40 – 20.50	9250	1273	118	3	56960
21 June	21.20 – 21.25	10250	1273	124	3	63507
21 June	22.00 – 22.05	11750	1273	133	3	73327
21/22 June	22.40 – 01.55	13750	1273	145	3	86421
22 June	03.40 – 04.05	11750	1273	133	3	73327
22 June	05.40 – 05.55	13250	1273	142	3	83148
22 June	07.00 – 07.10	4750	1273	91	3	27498

Table A.1.: Eruption phase and exit conditions as assumed in FPlume for the 2019 Raikoke eruption.

2021 La Soufrière eruption

Date	Time in UTC	Plume height in m (a.s.l.)	Exit temperature in K	Exit velocity in m s^{-1}	Exit volatile fraction in %	SO ₂ mass emission rate in kg s^{-1}
09 April	12.45 – 13.05	15800	1273	153	3	4838
09 April	19.05 – 19.55	16800	1273	159	3	5146
09 April	20.15 – 20.55	16050	1273	155	3	4915
09 April	21.15 – 21.55	14950	1273	148	3	4577
09 April	22.25 – 23.15	16850	1273	160	3	5161
09 April	23.25 – 23.45	17300	1273	162	3	5299
10 April	00.15 – 00.55	18550	1273	170	3	5683
10 April	01.05 – 01.35	18350	1273	169	3	5622
10 April	01.45 – 02.15	19050	1273	173	3	5837
10 April	02.25 – 02.35	18050	1273	167	3	5530
10 April	03.15 – 03.35	18800	1273	171	3	5760
10 April	03.45 – 04.05	18550	1273	170	3	5683
10 April	04.45 – 05.45	15300	1273	150	3	4685
10 April	06.55 – 07.15	12800	1273	135	3	3917
10 April	07.35 – 08.05	14720	1273	147	3	4507
10 April	08.15 – 08.35	14550	1273	146	3	4454
10 April	08.45 – 08.55	13050	1273	137	3	3994
10 April	09.45 – 10.25	18800	1273	171	3	5760
10 April	10.55 – 11.55	19350	1273	175	3	5929
10 April	12.05 – 12.25	19550	1273	176	3	5990
10 April	12.55 – 13.25	19300	1273	174	3	5914
10 April	14.35 – 15.05	18300	1273	168	3	5606
10 April	16.10 – 16.55	8550	1273	110	3	2611
10 April	16.25 – 17.05	18300	1273	168	3	5606
10 April	18.45 – 19.35	16900	1273	170	3	5176
10 April	21.25 – 22.15	15800	1273	153	3	4838
10 April	23.05 – 23.35	18300	1273	168	3	5606
11 April	00.55 – 01.35	17675	1273	165	3	5414
11 April	02.45 – 03.15	18380	1273	169	3	5631
11 April	05.05 – 05.25	18300	1273	168	3	5606
11 April	08.00 – 08.35	19050	1273	173	3	5837

11 April	10.25 – 10.45	8050	1273	170	3	2458
11 April	10.45 – 11.05	18800	1273	171	3	5760
11 April	11.25 – 11.55	12050	1273	131	3	3379
11 April	13.25 – 14.15	18400	1273	169	3	5637
11 April	18.00 – 18.45	12600	1273	134	3	3855
11 April	20.05 – 20.45	15675	1273	153	3	4800
12 April	00.00 – 00.10	6950	1273	100	3	2120
12 April	00.45 – 01.05	19550	1273	176	3	5990
12 April	01.25 – 01.45	10050	1273	119	3	3072
12 April	08.05 – 08.25	19300	1273	174	3	5914
13 April	10.25 – 10.55	17300	1273	162	3	5299
13 April	11.25 – 11.45	11550	1273	128	3	3379
13 April	11.55 – 12.05	8800	1273	111	3	2688

Table A.2.: Eruption phase and exit conditions as assumed in FPlume for the 2021 La Soufrière eruption.

B. Chemistry mechanism of Chapter 7

The fields of the most abundant gas-phase species for the chemistry experiments performed in Chapter 7 were initialized with data from CAM-chem. These species are

- ozone (O_3),
- hydrogen peroxide (H_2O_2),
- hydroperoxyl (HO_2),
- hydroxyl (OH),
- carbon monoxide (CO),
- methane (CH_4),
- acetic acid (CH_3OOH),
- nitrogen monoxide (NO),
- nitrous oxide (N_2O),
- dinitrogen pentoxide (N_2O_5),
- nitrogen dioxide (NO_2),
- nitrate (NO_3),
- ammonia (NH_3),
- ammonium (NH_4),
- nitric acid (HNO_3),
- peroxyntic acid (HNO_4),
- sulfur dioxide (SO_2), and
- dimethyl sulfide (DMS, $(CH_2)_2S$).

Type	Reaction	Rate equation	k_1	k_2	Ref.
gas	$O(^3P) + O_2 + M \rightarrow O_3 + M$	1)			E10
gas	$O(^3P) + O_3 \rightarrow 2 O_2$	a)	$8.0 \cdot 10^{-12}$	-2060.0	E10
gas	$O(^3P) + O(^3P) + M \rightarrow O_2 + M$	a)	$2.76 \cdot 10^{-34}$	720.0	E10
gas	$O_2(^1S) + O(^3P) \rightarrow O(^3P) + O_2(^1D)$	$8.0 \cdot 10^{-14}$			E10
gas	$O_2(^1S) + O_2 \rightarrow O_2 + O_2(^1D)$	$3.9 \cdot 10^{-17}$			E10
gas	$O_2(^1S) + N_2 \rightarrow N_2 + O_2(^1D)$	a)	$1.8 \cdot 10^{-15}$	45.0	E10
gas	$O_2(^1S) + O_3 \rightarrow O_2(^1D) + O_3$	a)	$3.5 \cdot 10^{-11}$	-135.0	E10
gas	$O_2(^1S) + CO_2 \rightarrow CO_2 + O_2(^1D)$	$4.2 \cdot 10^{-13}$			E10
gas	$O_2(^1S) \rightarrow O_2$	0.085			E10
gas	$O_2(^1D) + O(^3P) \rightarrow O(^3P) + O_2$	$1.3 \cdot 10^{-16}$			E10
gas	$O_2(^1D) + O_2 \rightarrow 2 O_2$	a)	$3.6 \cdot 10^{-18}$	-220.0	E10
gas	$O_2(^1D) + N_2 \rightarrow N_2 + O_2$	$1.0 \cdot 10^{-20}$			E10
gas	$O_2(^1D) \rightarrow O_2$	$2.58 \cdot 10^{-4}$			E10
gas	$O(^1D) + N_2 \rightarrow N_2 + O(^3P)$	a)	$2.15 \cdot 10^{-11}$	110.0	E10
gas	$O(^1D) + O_2 \rightarrow O(^3P) + O_2(^1S)$	a)	$3.135 \cdot 10^{-11}$	55.0	E10
gas	$O(^1D) + O_2 \rightarrow O(^3P) + O_2$	a)	$3.3 \cdot 10^{-11}$	55.0	E10
gas	$O(^1D) + H_2O \rightarrow 2 OH$	a)	$1.63 \cdot 10^{-10}$	60.0	E10
gas	$O(^1D) + N_2O \rightarrow 2 NO$	a)	$6.7 \cdot 10^{-11}$	20.0	E10
gas	$O(^1D) + N_2O \rightarrow N_2 + O_2$	a)	$4.7 \cdot 10^{-11}$	20.0	E10
gas	$O(^1D) + O_3 \rightarrow 2 O_2$	$1.2 \cdot 10^{-10}$			E10
gas	$O(^1D) + CH_4 \rightarrow CH_3O_2 + OH$	$1.125 \cdot 10^{-10}$			E10
gas	$O(^1D) + CH_4 \rightarrow HCHO + H + HO_2$	$3.0 \cdot 10^{-11}$			E10
gas	$O(^1D) + CH_4 \rightarrow HCHO + H_2$	$7.5 \cdot 10^{-12}$			E10
gas	$O(^1D) + H_2 \rightarrow H + OH$	$1.1 \cdot 10^{-10}$			E10
gas	$O(^1D) + HCl \rightarrow Cl + OH$	$1.5 \cdot 10^{-10}$			E10
gas	$H + O_2 + M \rightarrow HO_2 + M$	b)	$4.4 \cdot 10^{-32} (\frac{T}{300})^{1.3}$	$4.7 \cdot 10^{-11} (\frac{T}{300})^{0.2}$	E10
gas	$H + O_3 \rightarrow O_2 + OH$	a)	$1.4 \cdot 10^{-10}$	-470.0	E10
gas	$H + HO_2 \rightarrow 2 OH$	$7.2 \cdot 10^{-11}$			E10
gas	$H + HO_2 \rightarrow H_2 + O_2$	$6.9 \cdot 10^{-12}$			E10
gas	$H + HO_2 \rightarrow H_2O + O(^3P)$	$1.6 \cdot 10^{-12}$			E10
gas	$OH + O(^3P) \rightarrow H + O_2$	a)	$2.2 \cdot 10^{-11}$	120.0	E10
gas	$OH + O_3 \rightarrow HO_2 + O_2$	a)	$1.7 \cdot 10^{-12}$	-940.0	E10
gas	$OH + HO_2 \rightarrow H_2O + O_2$	a)	$4.8 \cdot 10^{-11}$	250.0	E10
gas	$OH + OH \rightarrow H_2O + O(^3P)$	$1.8 \cdot 10^{-12}$			E10
gas	$OH + OH + M \rightarrow H_2O_2 + M$	b)	$6.9 \cdot 10^{-31} (\frac{T}{300})^{1.0}$	$2.6 \cdot 10^{-11}$	E10
gas	$OH + H_2 \rightarrow H + H_2O$	a)	$2.8 \cdot 10^{-12}$	-1800.0	E10
gas	$OH + H_2O_2 \rightarrow H_2O + HO_2$	$1.8 \cdot 10^{-12}$			E10
gas	$HO_2 + O(^3P) \rightarrow O_2 + OH$	a)	$3.0 \cdot 10^{-11}$	200.0	E10
gas	$HO_2 + O_3 \rightarrow OH + 2 O_2$	a)	$1.0 \cdot 10^{-14}$	-490.0	E10

gas	$\text{HO}_2 + \text{HO}_2 \rightarrow \text{H}_2\text{O}_2 + \text{O}_2$	2)			E10
gas	$\text{H}_2\text{O}_2 + \text{O}({}^3\text{P}) \rightarrow \text{HO}_2 + \text{OH}$	a)	$1.4 \cdot 10^{-12}$	-2000.0	E10
gas	$\text{N}({}^2\text{D}) + \text{O}_2 \rightarrow \text{NO} + \text{O}({}^1\text{D})$		$5.0 \cdot 10^{-12}$		E10
gas	$\text{N}({}^2\text{D}) + \text{O}({}^3\text{P}) \rightarrow \text{N} + \text{O}({}^3\text{P})$		$7.0 \cdot 10^{-13}$		E10
gas	$\text{N} + \text{O}_2 \rightarrow \text{NO} + \text{O}({}^3\text{P})$	a)	$1.5 \cdot 10^{-11}$	-3600.0	E10
gas	$\text{N} + \text{NO} \rightarrow \text{N}_2 + \text{O}({}^3\text{P})$	a)	$2.1 \cdot 10^{-11}$	100.0	E10
gas	$\text{N} + \text{NO}_2 \rightarrow \text{N}_2\text{O} + \text{O}({}^3\text{P})$	a)	$5.8 \cdot 10^{-12}$	220.0	E10
gas	$\text{NO} + \text{O}({}^3\text{P}) + \text{M} \rightarrow \text{NO}_2 + \text{M}$	b)	$9.0 \cdot 10^{-32} \left(\frac{T}{300}\right)^{1.5}$	$3.0 \cdot 10^{-11}$	E10
gas	$\text{NO} + \text{HO}_2 \rightarrow \text{NO}_2 + \text{OH}$	a)	$3.5 \cdot 10^{-12}$	250.0	E10
gas	$\text{NO} + \text{O}_3 \rightarrow \text{NO}_2 + \text{O}_2$	a)	$3.0 \cdot 10^{-12}$	-1500.0	E10
gas	$\text{NO}_2 + \text{O}({}^3\text{P}) \rightarrow \text{NO} + \text{O}_2$	a)	$5.1 \cdot 10^{-12}$	210.0	E10
gas	$\text{NO}_2 + \text{O}({}^3\text{P}) + \text{M} \rightarrow \text{NO}_3 + \text{M}$	b)	$2.5 \cdot 10^{-31} \left(\frac{T}{300}\right)^{1.8}$	$2.2 \cdot 10^{-11} \left(\frac{T}{300}\right)^{0.7}$	E10
gas	$\text{NO}_2 + \text{O}_3 \rightarrow \text{NO}_3 + \text{O}_2$	a)	$1.2 \cdot 10^{-13}$	-2450.0	E10
gas	$\text{NO}_2 + \text{NO}_3 + \text{M} \rightarrow \text{N}_2\text{O}_5 + \text{M}$	b)	$2.0 \cdot 10^{-30} \left(\frac{T}{300}\right)^{4.4}$	$1.4 \cdot 10^{-12} \left(\frac{T}{300}\right)^{0.7}$	E10
gas	$\text{N}_2\text{O}_5 + \text{M} \rightarrow \text{NO}_2 + \text{NO}_3 + \text{M}$	3)			E10
gas	$\text{NO}_2 + \text{OH} + \text{M} \rightarrow \text{HNO}_3 + \text{M}$	b)	$1.8 \cdot 10^{-30} \left(\frac{T}{300}\right)^{3.0}$	$2.8 \cdot 10^{-11}$	E10
gas	$\text{HNO}_3 + \text{OH} \rightarrow \text{H}_2\text{O} + \text{NO}_3$	4)			E10
gas	$\text{NO}_3 + \text{NO} \rightarrow 2 \text{NO}_2$	a)	$1.5 \cdot 10^{-11}$	170.0	E10
gas	$\text{NO}_3 + \text{O}({}^3\text{P}) \rightarrow \text{NO}_2 + \text{O}_2$		$1.0 \cdot 10^{-11}$		E10
gas	$\text{NO}_3 + \text{OH} \rightarrow \text{HO}_2 + \text{NO}_2$		$2.2 \cdot 10^{-11}$		E10
gas	$\text{NO}_3 + \text{HO}_2 \rightarrow \text{NO}_2 + \text{OH} + \text{O}_2$		$3.5 \cdot 10^{-12}$		E10
gas	$\text{NO}_2 + \text{HO}_2 + \text{M} \rightarrow \text{HNO}_4 + \text{M}$	b)	$2.0 \cdot 10^{-31} \left(\frac{T}{300}\right)^{3.4}$	$2.9 \cdot 10^{-12} \left(\frac{T}{300}\right)^{1.1}$	E10
gas	$\text{HNO}_4 + \text{OH} \rightarrow \text{H}_2\text{O} + \text{NO}_2 + \text{O}_2$	a)	$1.3 \cdot 10^{-12}$	380.0	E10
gas	$\text{HNO}_4 + \text{M} \rightarrow \text{HO}_2 + \text{NO}_2 + \text{M}$	5)			E10
gas	$\text{Cl} + \text{O}_3 \rightarrow \text{ClO} + \text{O}_2$	a)	$2.3 \cdot 10^{-11}$	-200.0	E10
gas	$\text{Cl} + \text{H}_2 \rightarrow \text{H} + \text{HCl}$	a)	$3.05 \cdot 10^{-11}$	-2270.0	E10
gas	$\text{Cl} + \text{H}_2\text{O}_2 \rightarrow \text{HCl} + \text{HO}_2$	a)	$1.1 \cdot 10^{-11}$	-980.0	E10
gas	$\text{Cl} + \text{HO}_2 \rightarrow \text{HCl} + \text{O}_2$	a)	$1.8 \cdot 10^{-11}$	170.0	E10
gas	$\text{Cl} + \text{HO}_2 \rightarrow \text{ClO} + \text{OH}$	a)	$4.1 \cdot 10^{-11}$	-450.0	E10
gas	$\text{Cl} + \text{HCHO} \rightarrow \text{HCl} + \text{HO}_2 + \text{CO}$	a)	$8.1 \cdot 10^{-11}$	-30.0	E10
gas	$\text{Cl} + \text{CH}_4 \rightarrow \text{CH}_3\text{O}_2 + \text{HCl}$	a)	$7.3 \cdot 10^{-12}$	-1280.0	E10
gas	$\text{ClO} + \text{O}({}^3\text{P}) \rightarrow \text{Cl} + \text{O}_2$	a)	$2.8 \cdot 10^{-11}$	85.0	E10
gas	$\text{ClO} + \text{OH} \rightarrow \text{Cl} + \text{HO}_2$	a)	$7.4 \cdot 10^{-12}$	270.0	E10
gas	$\text{ClO} + \text{OH} \rightarrow \text{HCl} + \text{O}_2$	a)	$6.0 \cdot 10^{-13}$	230.0	E10
gas	$\text{ClO} + \text{HO}_2 \rightarrow \text{HOCl} + \text{O}_2$	a)	$2.7 \cdot 10^{-12}$	220.0	E10
gas	$\text{ClO} + \text{NO} \rightarrow \text{Cl} + \text{NO}_2$	a)	$6.4 \cdot 10^{-12}$	290.0	E10
gas	$\text{ClO} + \text{NO}_2 + \text{M} \rightarrow \text{ClONO}_2 + \text{M}$	b)	$1.8 \cdot 10^{-31} \left(\frac{T}{300}\right)^{3.4}$	$1.5 \cdot 10^{-11} \left(\frac{T}{300}\right)^{1.9}$	E10
gas	$\text{ClO} + \text{ClO} \rightarrow 2 \text{Cl} + \text{O}_2$	a)	$3.0 \cdot 10^{-11}$	-2450.0	E10
gas	$\text{ClO} + \text{ClO} \rightarrow \text{Cl}_2 + \text{O}_2$	a)	$1.0 \cdot 10^{-12}$	-1590.0	E10
gas	$\text{ClO} + \text{ClO} \rightarrow \text{Cl} + \text{OClO}$	a)	$3.5 \cdot 10^{-13}$	-1370	E10
gas	$\text{ClO} + \text{ClO} + \text{M} \rightarrow \text{Cl}_2\text{O}_2 + \text{M}$	b)	$1.6 \cdot 10^{-32} \left(\frac{T}{300}\right)^{4.5}$	$2.0 \cdot 10^{-12} \left(\frac{T}{300}\right)^{2.4}$	E10
gas	$\text{Cl}_2\text{O}_2 + \text{M} \rightarrow 2 \text{ClO} + \text{M}$	6)			E10

gas	$\text{HCl} + \text{OH} \rightarrow \text{Cl} + \text{H}_2\text{O}$	a)	$2.6 \cdot 10^{-12}$	-350.0	E10
gas	$\text{HCl} + \text{O}({}^3\text{P}) \rightarrow \text{Cl} + \text{OH}$	a)	$1.0 \cdot 10^{-11}$	-3300.0	E10
gas	$\text{HOCl} + \text{O}({}^3\text{P}) \rightarrow \text{ClO} + \text{OH}$	$1.7 \cdot 10^{-13}$			E10
gas	$\text{HOCl} + \text{Cl} \rightarrow \text{ClO} + \text{HCl}$	a)	$2.5 \cdot 10^{-12}$	-130.0	E10
gas	$\text{HOCl} + \text{OH} \rightarrow \text{ClO} + \text{H}_2\text{O}$	a)	$3.0 \cdot 10^{-12}$	-500.0	E10
gas	$\text{ClNO}_3 + \text{O}({}^3\text{P}) \rightarrow \text{ClO} + \text{NO}_3$	a)	$2.9 \cdot 10^{-12}$	-800.0	E10
gas	$\text{ClNO}_3 + \text{OH} \rightarrow \text{HOCl} + \text{NO}_3$	a)	$1.2 \cdot 10^{-12}$	-330.0	E10
gas	$\text{ClNO}_3 + \text{Cl} \rightarrow \text{Cl}_2 + \text{NO}_3$	a)	$6.5 \cdot 10^{-12}$	135.0	E10
gas	$\text{CH}_4 + \text{OH} \rightarrow \text{CH}_3\text{O}_2 + \text{H}_2\text{O}$	a)	$2.45 \cdot 10^{-12}$	-1775.0	E10
gas	$\text{CH}_3\text{O}_2 + \text{NO} \rightarrow \text{HCHO} + \text{NO}_2 + \text{HO}_2$	a)	$2.8 \cdot 10^{-12}$	300.0	E10
gas	$\text{CH}_3\text{O}_2 + \text{HO}_2 \rightarrow \text{CH}_3\text{OOH} + \text{O}_2$	a)	$4.1 \cdot 10^{-13}$	750.0	E10
gas	$\text{CH}_3\text{OOH} + \text{OH} \rightarrow \text{CH}_3\text{O}_2 + \text{H}_2\text{O}$	a)	$3.8 \cdot 10^{-12}$	200.0	E10
gas	$\text{HCHO} + \text{NO}_3 \rightarrow \text{CO} + \text{HO}_2 + \text{HNO}_3$	a)	$6.0 \cdot 10^{-13}$	-2058.0	E10
gas	$\text{HCHO} + \text{OH} \rightarrow \text{CO} + \text{H}_2\text{O} + \text{H}$	a)	$5.5 \cdot 10^{-12}$	125.0	E10
gas	$\text{HCHO} + \text{O}({}^3\text{P}) \rightarrow \text{HO}_2 + \text{OH} + \text{CO}$	a)	$3.4 \cdot 10^{-11}$	-1600.0	E10
gas	$\text{CO} + \text{OH} + \text{M} \rightarrow \text{CO}_2 + \text{HO}_2 + \text{M}$	b)	$5.9 \cdot 10^{-33} \left(\frac{T}{300}\right)^{1.4}$	$1.1 \cdot 10^{-12} \left(\frac{T}{300}\right)^{-1.3}$	E10
gas	$\text{CO} + \text{OH} \rightarrow \text{CO}_2 + \text{H}$	7)	$1.5 \cdot 10^{-13} \left(\frac{T}{300}\right)^{-0.6}$	$2.1 \cdot 10^9 \left(\frac{T}{300}\right)^{-6.1}$	E10
gas	$\text{CH}_3\text{O}_2 + \text{CH}_3\text{O}_2 \rightarrow 2 \text{HCHO} + 2 \text{HO}_2$	a)	$5.0 \cdot 10^{-13}$	-424.0	E10
gas	$\text{CH}_3\text{O}_2 + \text{CH}_3\text{O}_2 \rightarrow \text{HCHO} + \text{CH}_3\text{OH}$	a)	$1.9 \cdot 10^{-14}$	706.0	E10
gas	$\text{CH}_3\text{OH} + \text{OH} \rightarrow \text{HCHO} + \text{HO}_2$	a)	$2.9 \cdot 10^{-12}$	-345.0	E10
gas	$\text{CH}_3\text{OOH} + \text{OH} \rightarrow 0.7 \text{CH}_3\text{O}_2 + 0.3 \text{OH} + 0.3 \text{HCHO} + \text{H}_2\text{O}$	a)	$3.8 \cdot 10^{-12}$	200.0	E10
gas	$\text{SO}_2 + \text{OH} [+ \text{O}_2 + \text{H}_2\text{O}] \rightarrow \text{H}_2\text{SO}_4$	b)	$3.3 \cdot 10^{-31} \left(\frac{T}{300}\right)^{3.3}$	$1.5 \cdot 10^{-12}$	E10
gas	$\text{DMS} + \text{OH} \rightarrow \text{SO}_2$	a)	$1.1 \cdot 10^{-11}$	-240.0	E10
gas	$\text{DMS} + \text{OH} \rightarrow 0.5 \text{SO}_2 + 0.5 \text{HO}_2$	8)			E10
gas	$\text{DMS} + \text{NO}_3 \rightarrow \text{HNO}_3 + \text{SO}_2$	a)	$1.0 \cdot 10^{-12}$	500.0	E10
gas	$\text{NH}_3 \rightarrow \text{NH}_4$	0.0			E10
gas	$\text{NH}_3 + \text{OH} \rightarrow \text{H}_2\text{O}$	a)	$1.7 \cdot 10^{-12}$	-710.0	E10
photo	$\text{O}_2 + h\nu \rightarrow \text{O}({}^3\text{P}) + \text{O}({}^1\text{D})$	f(rad)			E10
photo	$\text{O}_2 + h\nu \rightarrow 2 \text{O}({}^3\text{P})$	f(rad)			E10
photo	$\text{O}_3 + h\nu \rightarrow \text{O}({}^1\text{D}) + \text{O}_2({}^1\text{D})$	f(rad)			E10
photo	$\text{O}_3 + h\nu \rightarrow \text{O}({}^3\text{P}) + \text{O}_2$	f(rad)			E10
photo	$\text{N}_2\text{O} + h\nu \rightarrow \text{N}_2 + \text{O}({}^1\text{D})$	f(rad)			E10
photo	$\text{NO} + h\nu \rightarrow \text{N} + \text{O}({}^3\text{P})$	f(rad)			E10
photo	$\text{NO}_2 + h\nu \rightarrow \text{NO} + \text{O}({}^3\text{P})$	f(rad)			E10
photo	$\text{N}_2\text{O}_5 + h\nu \rightarrow \text{NO}_2 + \text{NO}_3$	f(rad)			E10
photo	$\text{N}_2\text{O}_5 + h\nu \rightarrow \text{NO} + \text{O}({}^3\text{P}) + \text{NO}_3$	f(rad)			E10
photo	$\text{HNO}_3 + h\nu \rightarrow \text{NO}_2 + \text{OH}$	f(rad)			E10

photo	$\text{NO}_3 + h\nu \rightarrow \text{NO}_2 + \text{O}({}^3\text{P})$	f(rad)			E10
photo	$\text{NO}_3 + h\nu \rightarrow \text{NO} + \text{O}_2$	f(rad)			E10
photo	$\text{HNO}_4 + h\nu \rightarrow 0.667 \text{NO}_2 + 0.667 \text{HO}_2 + 0.333 \text{NO}_3 + 0.333 \text{OH}$	f(rad)			E10
photo	$\text{CH}_3\text{OOH} + h\nu \rightarrow \text{HCHO} + \text{H} + \text{OH}$	f(rad)			E10
photo	$\text{HCHO} + h\nu \rightarrow \text{CO} + \text{H}_2$	f(rad)			E10
photo	$\text{H}_2\text{O} + h\nu \rightarrow \text{H} + \text{OH}$	f(rad)			E10
photo	$\text{H}_2\text{O} + h\nu \rightarrow \text{H}_2 + \text{O}({}^1\text{D})$	f(rad)			E10
photo	$\text{H}_2\text{O}_2 + h\nu \rightarrow 2 \text{OH}$	f(rad)			E10
photo	$\text{Cl}_2 + h\nu \rightarrow 2 \text{Cl}$	f(rad)			E10
photo	$\text{ClO} + h\nu \rightarrow \text{ClO} + \text{O}({}^3\text{P})$	f(rad)			E10
photo	$\text{Cl}_2\text{O}_2 + h\nu \rightarrow 2 \text{Cl} + \text{O}_2$	f(rad)			E10
photo	$\text{HOCl} + h\nu \rightarrow \text{Cl} + \text{OH}$	f(rad)			E10
photo	$\text{HCl} + h\nu \rightarrow \text{Cl} + \text{H}$	f(rad)			E10
photo	$\text{ClNO}_3 + h\nu \rightarrow \text{Cl} + \text{NO}_3$	f(rad)			E10
photo	$\text{ClNO}_3 + h\nu \rightarrow \text{ClO} + \text{NO}_2$	f(rad)			E10
photo	$\text{CO}_2 + h\nu \rightarrow \text{CO} + \text{O}({}^3\text{P})$	f(rad)			E10
photo	$\text{CH}_4 + h\nu \rightarrow 0.47 \text{CH}_3 + 0.47 \text{H} + 0.763 \text{H}_2 + 0.0954 \text{HCHO} + 0.0954 \text{O}({}^3\text{P}) + 0.175 \text{OH} + 0.175 \text{HO}_2 + 0.233 \text{CO}_2 + 0.201 \text{CO} + 0.0265 \text{H}_2\text{O}$	f(rad)			E10
aq.	$\text{HO}_2 \rightarrow \text{HO}_2(\text{aq})$	c)	0.1	$21.0 \cdot 10^{-2}$	LJ99
aq.	$\text{HO}_2(\text{aq}) \rightarrow \text{HO}_2$	d)	$2.0 \cdot 10^3$	-13.2	LJ99
aq.	$\text{H}_2\text{O}_2 \rightarrow \text{H}_2\text{O}_2(\text{aq})$	c)	0.1	$15.1 \cdot 10^{-2}$	LJ99
aq.	$\text{H}_2\text{O}_2(\text{aq}) \rightarrow \text{H}_2\text{O}_2$	d)	$1.1 \cdot 10^5$	-13.2	LJ99
aq.	$\text{O}_3 \rightarrow \text{O}_3(\text{aq})$	c)	0.1	$21.0 \cdot 10^{-2}$	J86, LJ99
aq.	$\text{O}_3(\text{aq}) \rightarrow \text{O}_3$	d)	$1.1 \cdot 10^{-2}$	-4.76	J86, LJ99
aq.	$\text{HCl} \rightarrow \text{Cl}^- + \text{H}^+$	c)	0.1	$20.0 \cdot 10^{-2}$	J86, LJ99
aq.	$\text{Cl}^- + \text{H}^+ \rightarrow \text{HCl}$	d)	$2.05 \cdot 10^6$	-18.0	J86, LJ99
aq.	$\text{SO}_2 \rightarrow \text{SO}_2(\text{aq})$	c)	0.1	$12.2 \cdot 10^{-2}$	J86, LJ99
aq.	$\text{SO}_2(\text{aq}) \rightarrow \text{SO}_2$	d)	1.2	-6.27	J86, LJ99
aq.	$\text{OH} \rightarrow \text{OH}(\text{aq})$	c)	0.1	$23.1 \cdot 10^{-2}$	J86, LJ99

aq.	$\text{OH(aq)} \rightarrow \text{OH}$	d)	25	-10.5	J86, LJ99
aq.	$\text{H}_2\text{O(aq)} \rightarrow \text{H}^+ + \text{OH}^-$	0.0			
aq.	$\text{H}^+ + \text{OH}^- \rightarrow \text{H}_2\text{O(aq)}$	0.0			
aq.	$\text{HO}_2\text{(aq)} \rightarrow \text{H}^+ + \text{O}_2^-$	e)	$1.6 \cdot 10^{-5}$	0.0	LJ99
aq.	$\text{H}^+ + \text{O}_2^- \rightarrow \text{HO}_2\text{(aq)}$	e)	$1.6 \cdot 10^{-5}$	0.0	LJ99
aq.	$\text{SO}_2\text{(aq)} \rightarrow \text{HSO}_3^- + \text{H}^+$	e)	$6.0 \cdot 10^{-2}$	-4.0	LJ99
aq.	$\text{HSO}_3^- + \text{H}^+ \rightarrow \text{SO}_2\text{(aq)}$	e)	$6.0 \cdot 10^{-2}$	-4.0	LJ99
aq.	$\text{HSO}_3^- \rightarrow \text{SO}_3^{2-} + \text{H}^+$	e)	$6.3 \cdot 10^{-8}$	-3.0	LJ99
aq.	$\text{SO}_3^{2-} + \text{H}^+ \rightarrow \text{HSO}_3^-$	e)	$6.3 \cdot 10^{-8}$	-3.0	LJ99
aq.	$\text{H}_2\text{O}_2\text{(aq)} \rightarrow \text{OH(aq)} + \text{OH(aq)}$	$7.219 \cdot 10^{-4}$			SP06
aq.	$\text{H}_2\text{O}_2\text{(aq)} + \text{OH(aq)} \rightarrow \text{H}_2\text{O(aq)} + \text{HO}_2\text{(aq)}$	$1.495 \cdot 10^{-5}$			SP06
aq.	$\text{HO}_2\text{(aq)} + \text{O}_2^- \rightarrow \text{H}_2\text{O}_2\text{(aq)} + \text{OH}^-$	$5.535 \cdot 10^{-5}$			SP06
aq.	$\text{HO}_2\text{(aq)} + \text{HO}_2\text{(aq)} \rightarrow \text{H}_2\text{O}_2\text{(aq)}$	$4.594 \cdot 10^{-7}$			SP06
aq.	$\text{O}_2^- + \text{O}_3\text{(aq)} \rightarrow \text{OH(aq)} + \text{OH}^-$	$8.303 \cdot 10^{-4}$			SP06
aq.	$\text{O}_3\text{(aq)} + \text{OH(aq)} \rightarrow \text{HO}_2\text{(aq)}$	$1.661 \cdot 10^{-3}$			SP06
aq.	$\text{HSO}_3^- + \text{OH(aq)} \rightarrow \text{SO}_4^{2-} + \text{H}^+$	a)	$1.15 \cdot 10^{-9}$	-1500.0	SP06
aq.	$\text{HSO}_3^- + \text{O}_3\text{(aq)} \rightarrow \text{SO}_4^{2-} + \text{H}^+$	a)	$7.04 \cdot 10^{-8}$	-5530.0	SP06
aq.	$\text{HSO}_3^- + \text{H}_2\text{O}_2\text{(aq)} \rightarrow \text{SO}_4^{2-} + \text{H}^+ + \text{H}_2\text{O(aq)}$	a)	$3.55 \cdot 10^{-7}$	-4430.0	SP06
aq.	$\text{SO}_3^{2-} + \text{OH(aq)} \rightarrow \text{SO}_4^{2-} + \text{H}^+$	a)	$1.23 \cdot 10^{-4}$	5280.0	SP06
aq.	$\text{SO}_3^{2-} + \text{O}_3\text{(aq)} \rightarrow \text{SO}_4^{2-} + \text{H}^+$	a)	$2.49 \cdot 10^{-12}$	5300.0	SP06
aq.	$\text{HSO}_3^- + \text{Fe}^{3+} \rightarrow \text{Fe}^{2+} + \text{SO}_4^{2-} + \text{H}^+$	$2.0 \cdot 10^{-16}$			SP06
aq.	$\text{Fe}^{2+} + \text{OH(aq)} \rightarrow \text{FeOH}^{2+}$	a)	$7.64 \cdot 10^{-13}$	-1100.0	SP06
aq.	$\text{Fe}^{2+} + \text{O}_2^- \rightarrow \text{Fe}^{3+} + \text{H}_2\text{O}_2\text{(aq)} + 2 \text{OH}^-$	$1.66 \cdot 10^{-14}$			SP06
aq.	$\text{Fe}^{2+} + \text{HO}_2^- \rightarrow \text{Fe}^{3+} + \text{H}_2\text{O}_2\text{(aq)} + \text{OH}^-$	$2.0 \cdot 10^{-15}$			SP06
aq.	$\text{Fe}^{2+} + \text{H}_2\text{O}_2\text{(aq)} \rightarrow \text{Fe}^{3+} + \text{OH(aq)} + \text{OH}^-$	$8.7 \cdot 10^{-20}$			SP06
aq.	$\text{Fe}^{2+} + \text{O}_3\text{(aq)} \rightarrow \text{Fe}^{3+} + \text{OH(aq)} + \text{OH}^-$	$9.47 \cdot 10^{-16}$			SP06
aq.	$\text{Fe}^{3+} + \text{O}_2^- \rightarrow \text{Fe}^{2+}$	$2.49 \cdot 10^{-13}$			SP06
aq.	$\text{Fe}^{3+} + \text{SO}_4^{2-} \rightarrow \text{FeSO}_4^+$	$5.32 \cdot 10^{-18}$			SP06
aq.	$\text{FeSO}_4^+ \rightarrow \text{SO}_4^{2-} + \text{Fe}^{3+}$	$4.49 \cdot 10^{-20}$			SP06
aq.	$\text{Fe}^{2+} + \text{O}_3\text{(aq)} \rightarrow \text{FeO}^{2+} + \text{O}_3^-$	$1.36 \cdot 10^{-15}$			SP06
aq.	$\text{Fe}^{3+} + \text{Cl}^- \rightarrow \text{FeCl}_2\text{(aq)}$	$7.97 \cdot 10^{-21}$			SP06
aq.	$\text{FeCl}_2\text{(aq)} \rightarrow \text{Fe}^{3+} + \text{Cl}^-$	$1.53 \cdot 10^{-21}$			SP06
aq.	$\text{FeOH}^{2+} + \text{HSO}_3^- \rightarrow \text{Fe}^{2+} + \text{SO}_3^- + \text{H}_2\text{O(aq)}$	$4.98 \cdot 10^{-20}$			SP06

aq.	$\text{FeO}^{2+} + \text{HSO}_3^- \rightarrow \text{Fe}^{3+} + \text{SO}_3^- + \text{OH}^-$	$4.15 \cdot 10^{-16}$			SP06
aq.	$\text{FeOH}^{2+} + \text{HO}_2(\text{aq}) \rightarrow \text{Fe}^{2+} + \text{H}_2\text{O}(\text{aq})$	$2.16 \cdot 10^{-16}$			SP06
aq.	$\text{FeOH}^{2+} + \text{O}_2^- \rightarrow \text{Fe}^{2+} + \text{OH}^-$	$2.49 \cdot 10^{-13}$			SP06
ad.	$\text{SO}_2 + [\text{OH}(\text{s}) + \text{O}^{2-}(\text{s})] = \text{S(IV)}$	f)	10^{-6}	$1.5 \cdot 10^{16}$	U19
ad.	$\text{S(IV)} + \text{O}_3 = \text{SO}_4^{2-}$	f)	10^{-6}	$1.5 \cdot 10^{16}$	U02, M17

Table B.1.: Chemical reactions considered in chapter 6. The rate equations follow:

a) Arrhenius (1889): $k = k_1 \cdot \exp(k_2/T)$ with T the temperature, and the reaction dependent parameters k_1 in $\text{cm}^3 \text{ molecules}^{-1} \text{ s}^{-1}$ and $k_2 = E/R$ in K,

b) Troe (1983): $k = (k_1 \cdot [M]) / (1 + (k_1 \cdot [M]) / k_2) \cdot 0.6^{1 + (\log(k_1 \cdot [M]) / k_2)^2)^{-1}}$ with $[M]$ the air concentration in molecules cm^{-3} ,

c) Jacob (1986): $k_{in} = 3\eta LD_g / r^2$ with $\eta = (1 + ((1.33 + 0.71 \cdot Kn^{-1}) / (1 + Kn^{-1}) + (4 \cdot (1 - k_1)) / (3k_1)) \cdot Kn)^{-1}$ the coefficient correcting for the free molecular effect with Kn the Knudsen number, $D_g = k_2$ the diffusion coefficient, L the liquid water content, and r the droplet radius,

d) Jacob (1986): $k_{out} = k_{in} / (0.082 T L k_1 \cdot \exp(-500 \cdot k_2 (1/T - 1/298)))$,

e) Liang and Jacobson (1999): $k = k_1 \cdot \exp(-500 \cdot k_2 (1/T - 1/298)) \cdot 6.023 \cdot 10^{20} L$,

f) Urupina et al. (2019): if the number of adsorbed molecules is smaller than k_2 (saturation coverage) then $k_{ad} = 0.25 \bar{c}_A A_p \gamma$, where $k_1 = \gamma$ the uptake coefficient, \bar{c}_A the mean speed of gas, A_p the total surface area per volume of air,

1) $6.0 \cdot 10^{-34} \cdot [M] \cdot (300/T)^{2.4}$,

2) $(3.5 \cdot 10^{-13} \cdot \exp(430/T) + 1.7 \cdot 10^{-33} \cdot [M] \cdot \exp(1000/T)) \cdot (1 + 1.4 \cdot 10^{-21} \cdot [H_2O] \cdot \exp(2200/T))$,

3) $k_{NO_2+NO_3} \cdot 3.703704 \cdot 10^{24} \cdot \exp(-11000/T)$,

4) $2.4 \cdot 10^{-14} \cdot \exp(460/T) + 6.5 \cdot 10^{-34} \cdot \exp(1335/T) \cdot [M] / (1 + 6.5 \cdot 10^{-34} \cdot \exp(1335/T) [M] / (2.7 \cdot 10^{-34} \cdot \exp(2199/T)))$,

5) $k_{NO_2+HO_2} \cdot \exp(-10900/T) / 2.1 \cdot 10^{-27}$,

6) $k_{ClO+ClO} / (9.3 \cdot 10^{-28} \cdot \exp(8835/T))$,

7) $k_b / [M]$ with k_b from b), and

8) $1.7 \cdot 10^{-42} \cdot \exp(7810/T) \cdot 0.21 \cdot [M] / (1 + 5.5 \cdot 10^{-31} \cdot \exp(7460/T) \cdot 0.21 \cdot [M])$.

f(rad) indicates radiation dependent reaction rates. The references for the equations can be found in Emmons et al. (2010) (E10), Jacob (1986) (J86), Liang and Jacobson (1999) (LJ99), Seinfeld and Pandis (2006) (SP06), Usher et al. (2002) (U02), Urupina et al. (2019) (U19), and Maters et al. (2017) (M17).

C. Additional figures

Figures for Chapter 5

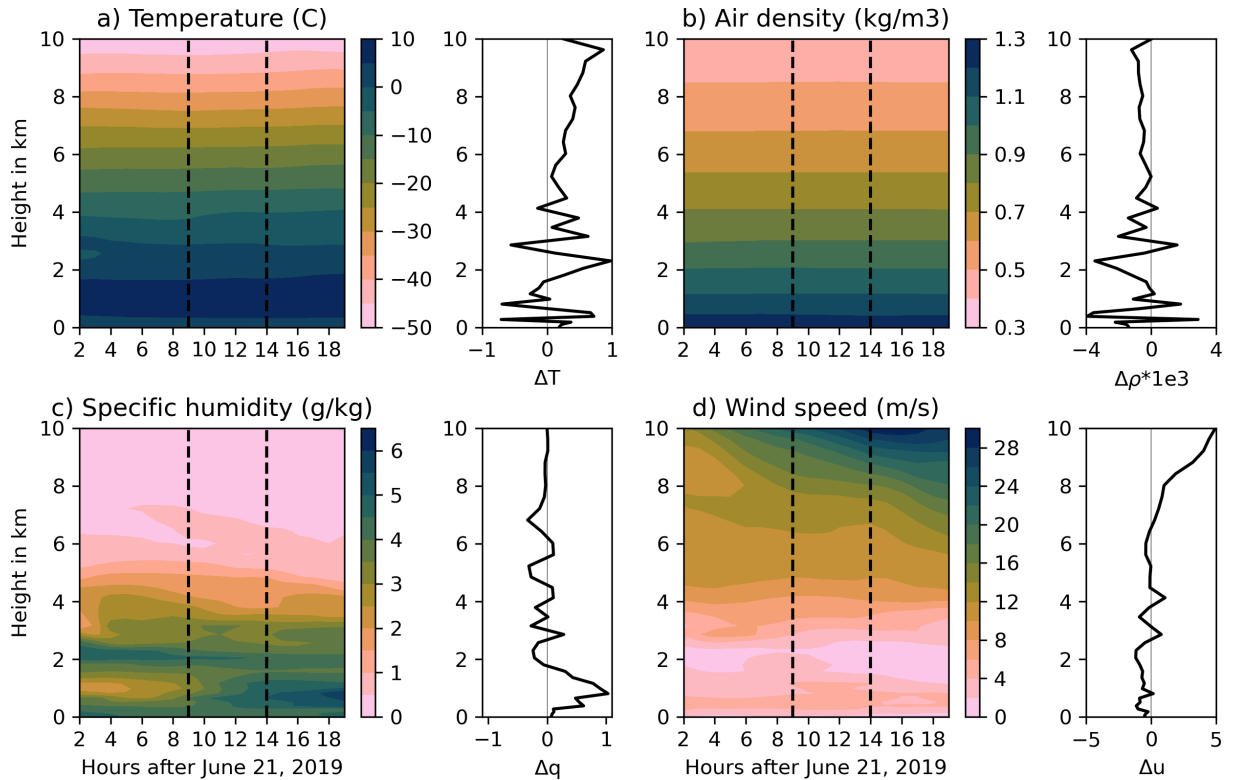


Figure C.1.: Meteorological conditions above the vent in the first 20 h after simulation start to explain variations in the FPlume-derived MER. Four different atmospheric variables are shown: a) temperature in $^{\circ}\text{C}$, b) air density in kg m^{-3} , c) specific humidity in g kg^{-1} , and d) the wind speed in m s^{-1} . For each variable the temporal development in the vertical axis above the vent is given over time in contours and the difference between the two time steps indicated by the vertical dashed lines in the contour plot (later step minus earlier time step).

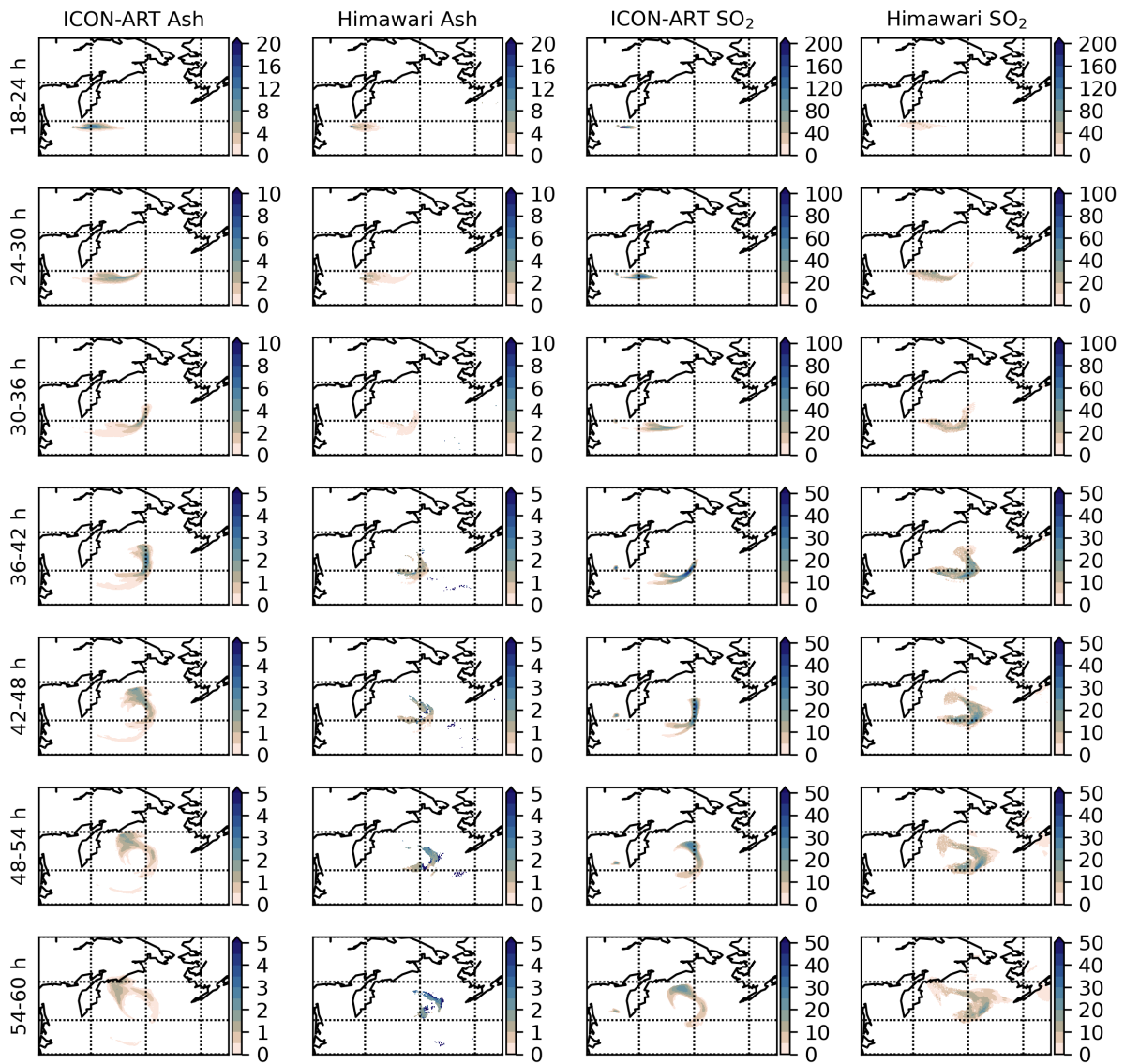


Figure C.2.: Comparison plots for seven ash and SO_2 6 h-averaged column loadings (row 1 to 7) in order to explain the discrepancy between simulated ICON-ART data and Himawari-8 observed data in the SAL analysis. First and second column: ash column loadings (in g m^{-2}) from the ICON-ART FPlume-rad experiment and Himawari-8. Third and fourth column: SO_2 column loadings (in g m^{-2}) from the ICON-ART FPlume-rad experiment and Himawari-8.

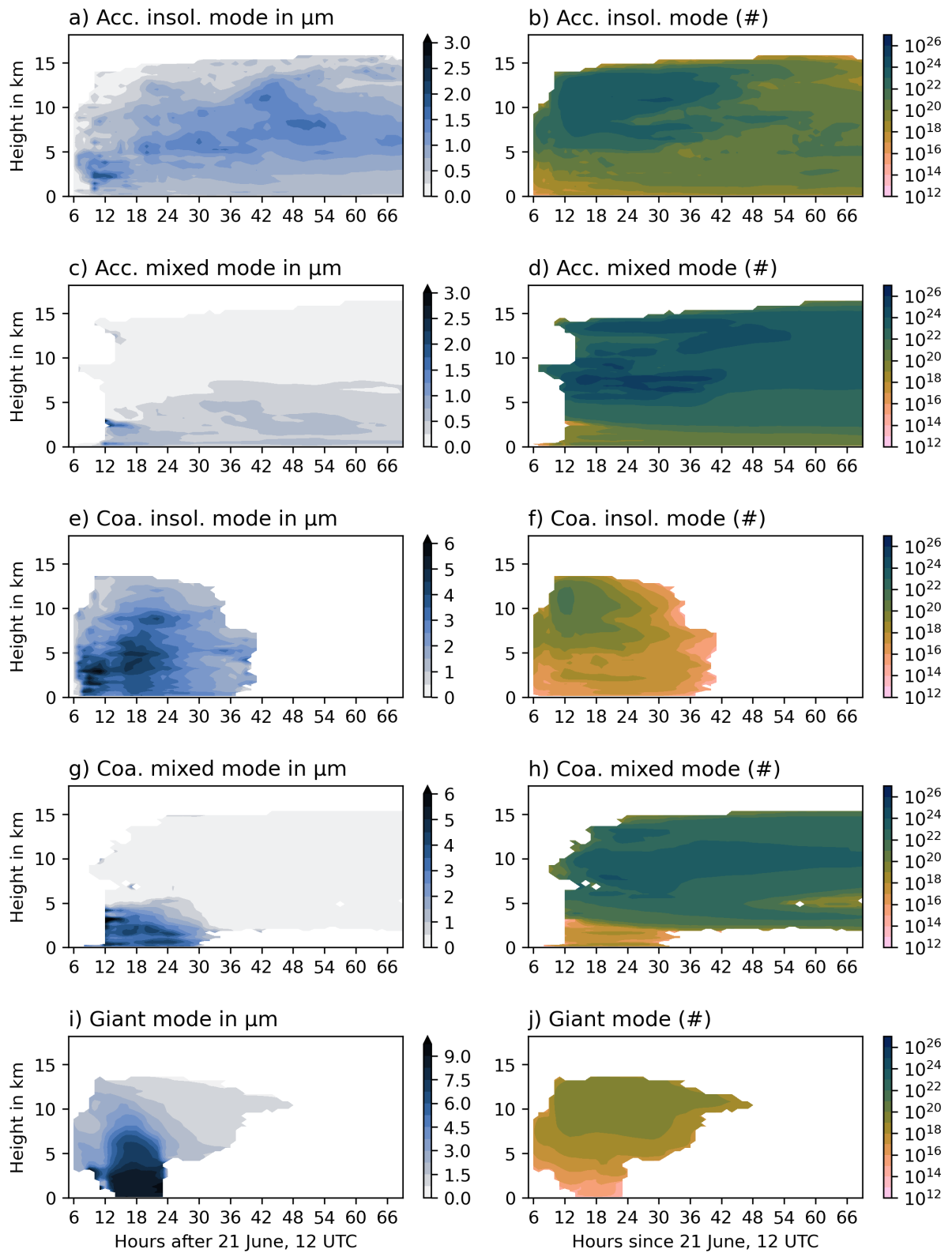


Figure C.3.: Horizontally averaged ash particle characteristic radius of the log normal distribution in μm (left, Eq. 5) and horizontal sum of the particle number (right) of the different ash modes: insoluble accumulation (a, b), mixed accumulation (c, d), insoluble coarse (e, f), mixed coarse (g, h), and giant mode (i, j).

Figures for Chapter 6

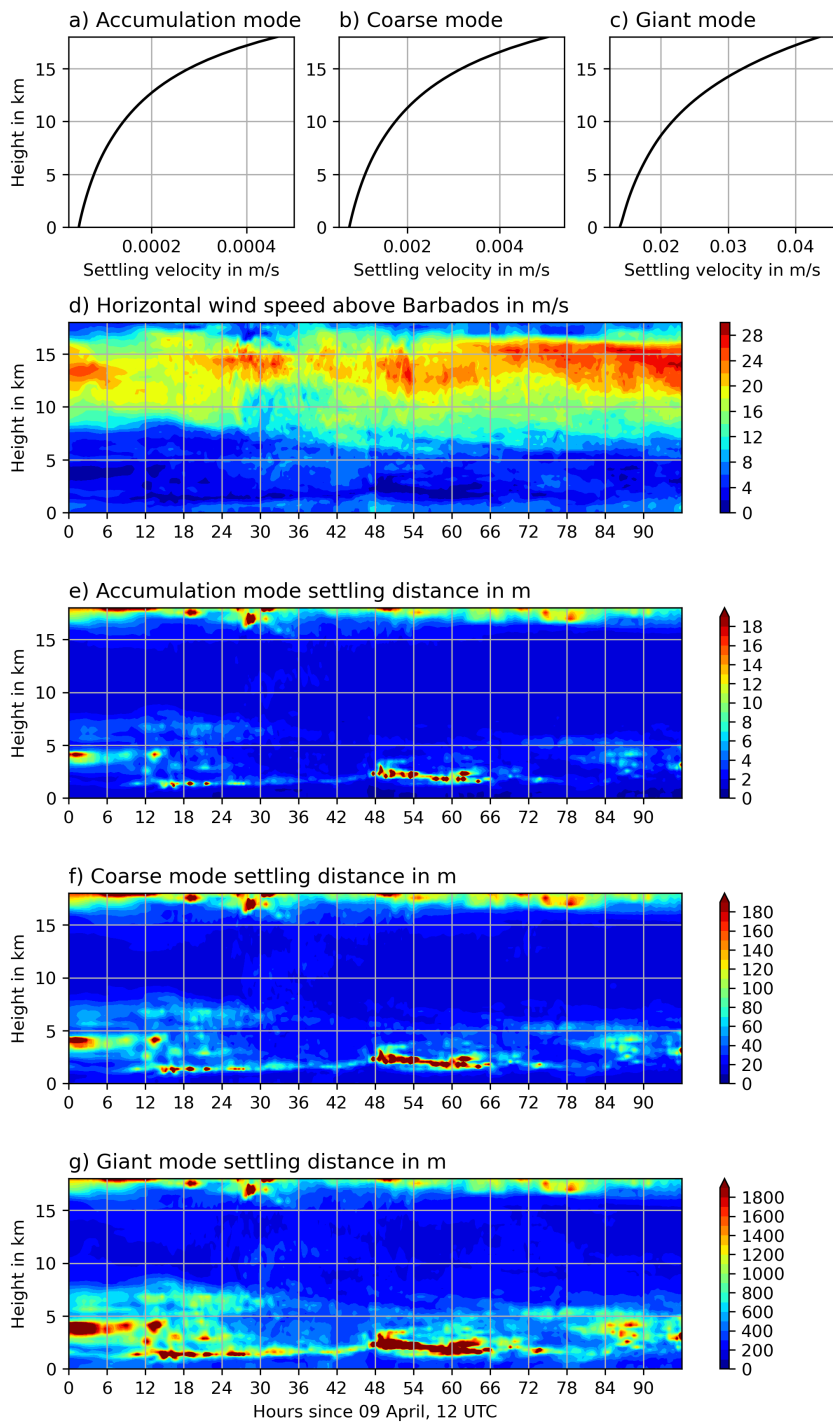


Figure C.4.: Height-dependent settling velocity for the a) accumulation, b) coarse, and c) giant mode. d) shows the height-dependent wind speed above Barbados over time, and e, f, g) the vertical settling distance for the accumulation, coarse, and giant mode during the direct transport with the winds from the location of the La Soufrière volcano towards Barbados, respectively.

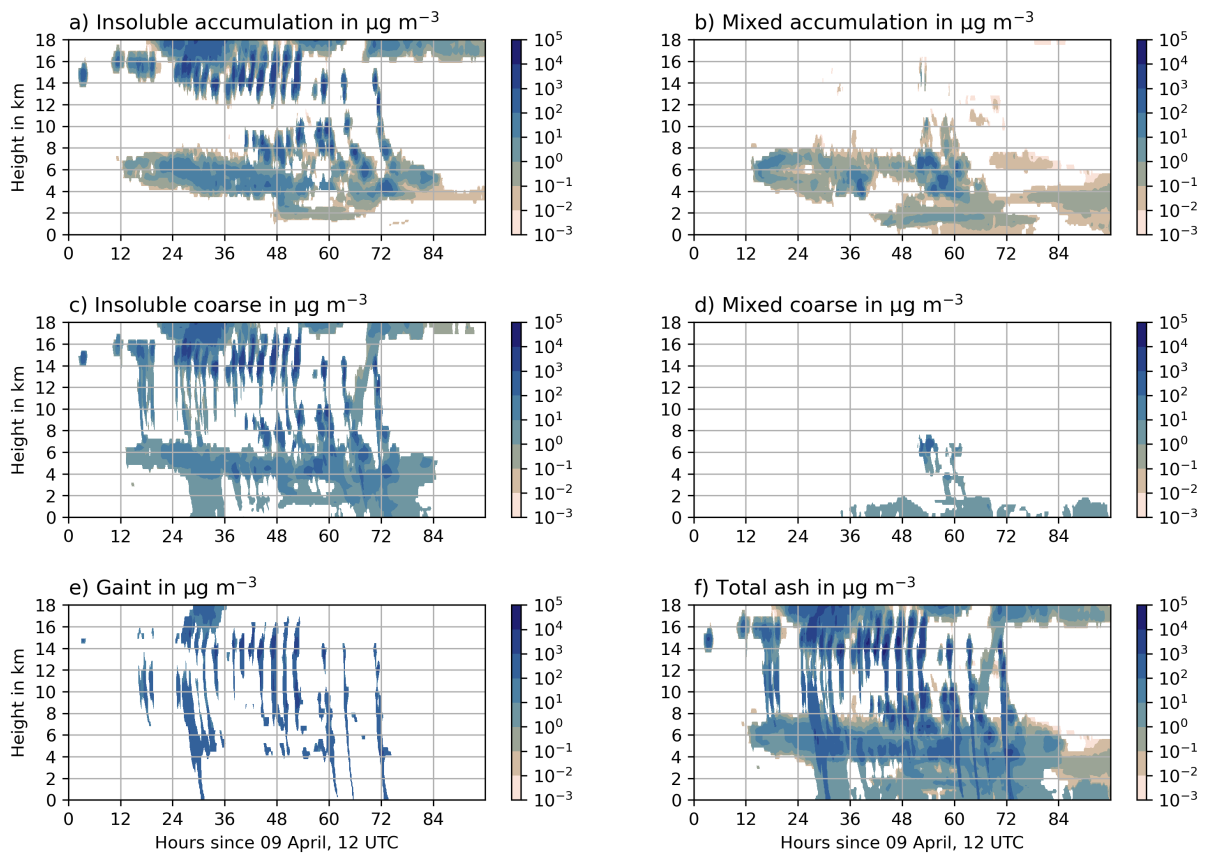


Figure C.5.: Ash concentration in $\mu\text{g m}^{-3}$ above Barbados split into the different modes: a) insoluble accumulation mode, b) mixed accumulation mode, c) insoluble coarse mode, d) mixed coarse mode, and e) giant mode. f) shows the total ash concentration and is the same as in Figure 6.3c.

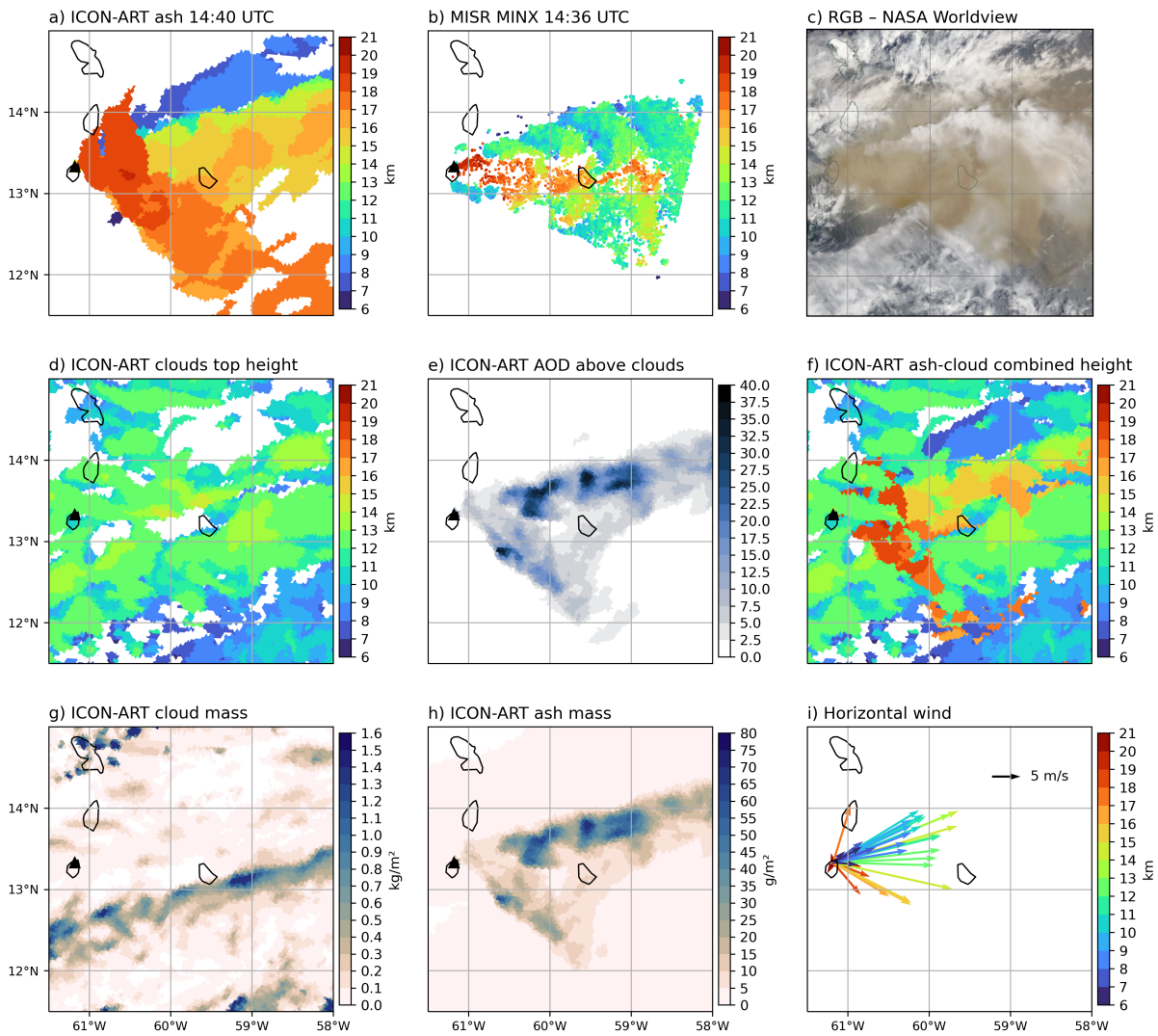


Figure C.6.: a) ICON-ART ash plume top heights with a detection threshold of $\text{AOD} > 0.2$ at 14:40 UTC on 10 April 2021, b) MISR plume top height at 14:36 UTC on 10 April 2021, c) MODIS RGB image at 14:36 UTC on 10 April 2021 from NASA Worldview webpage, d) ICON-ART cloud top heights, e) ICON-ART column AOD above cloud top from d, f) ICON-ART combined ash plume top heights and cloud top heights (if AOD from e larger than 10.0 or in the absence of clouds, the ash plume top height is used, else the maximum cloud height is used), g) ICON-ART cloud particle (liquid, solid, snow, rain drops) mass in kg m^{-3} , e) ICON-ART ash mass in kg m^{-3} , and f) horizontal winds at the La Soufrière volcano in different altitudes.

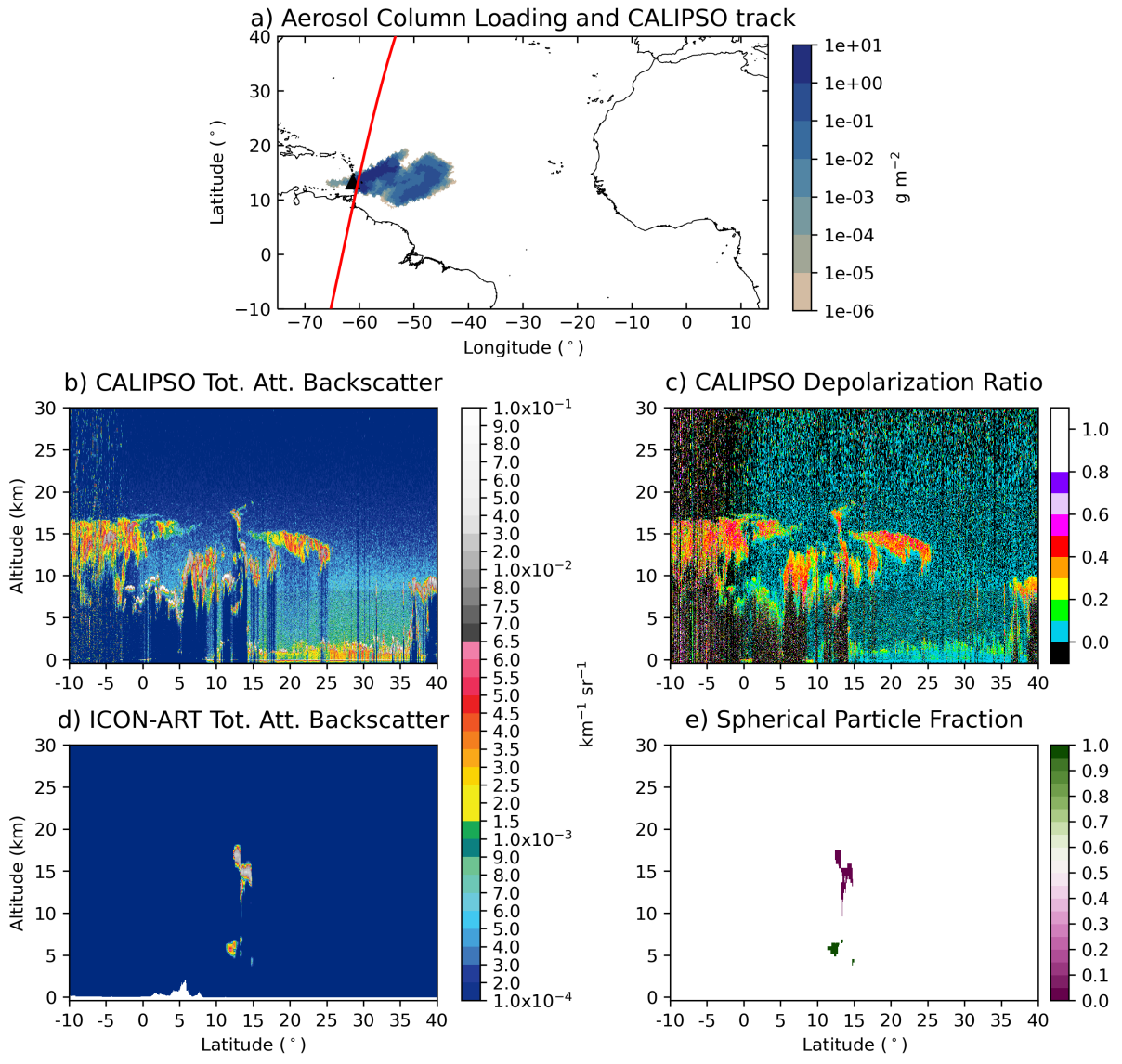


Figure C.7.: As Figure 6.8, but for 6 UTC on 10 April 2021.

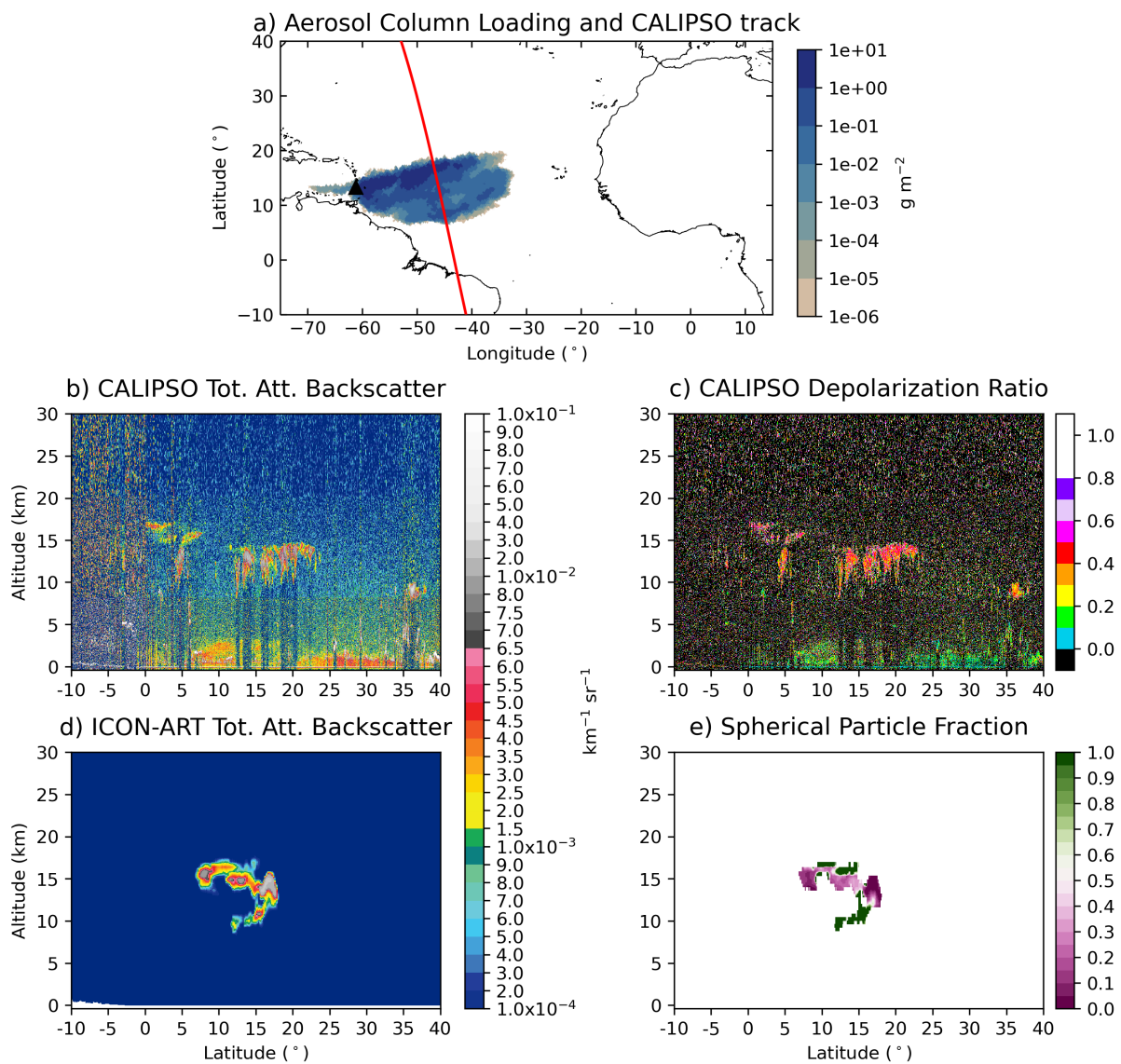


Figure C.8.: As Figure 6.8, but for 17 UTC on 10 April 2021.

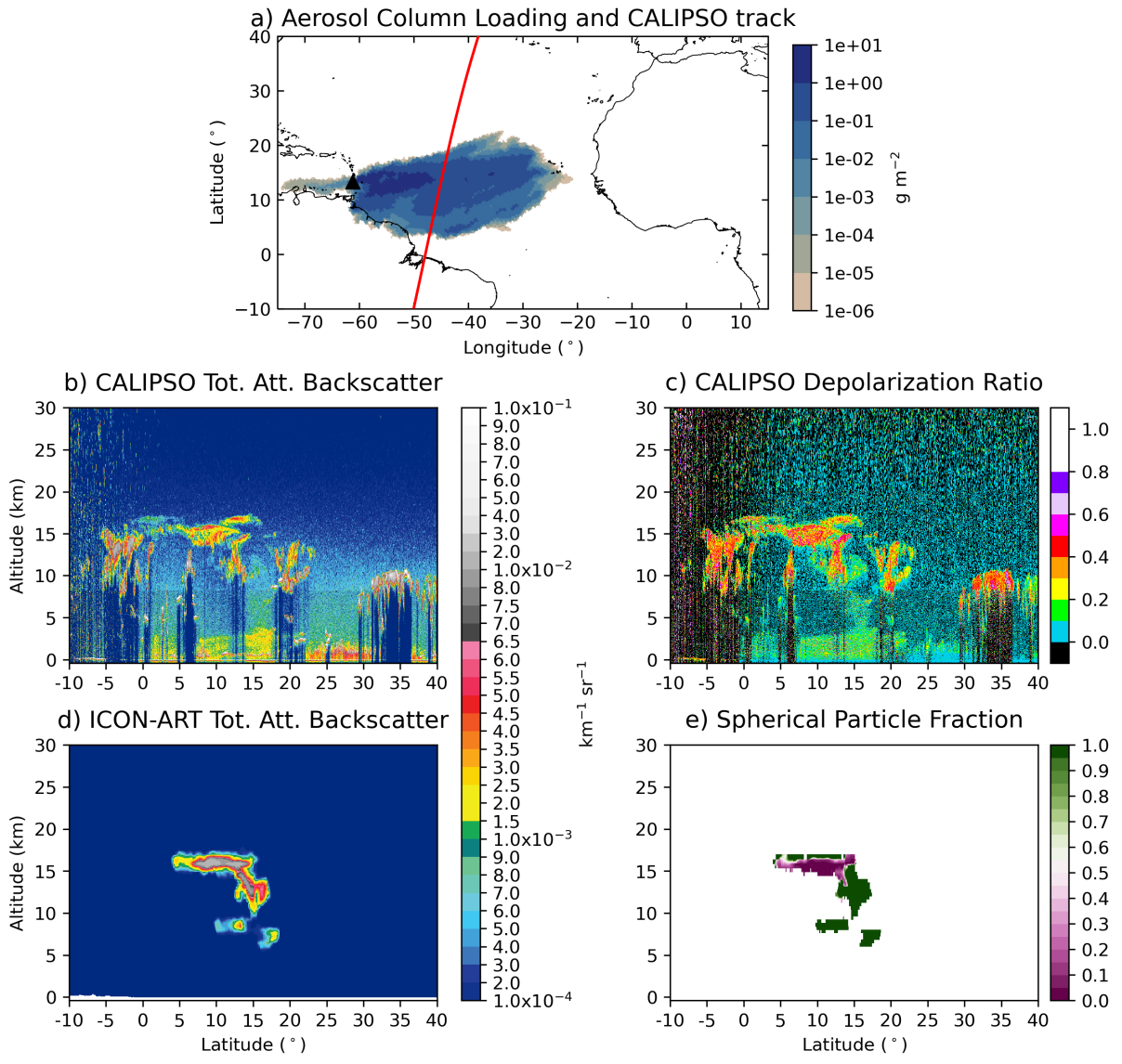


Figure C.9.: As Figure 6.8, but for 5 UTC on 11 April 2021.

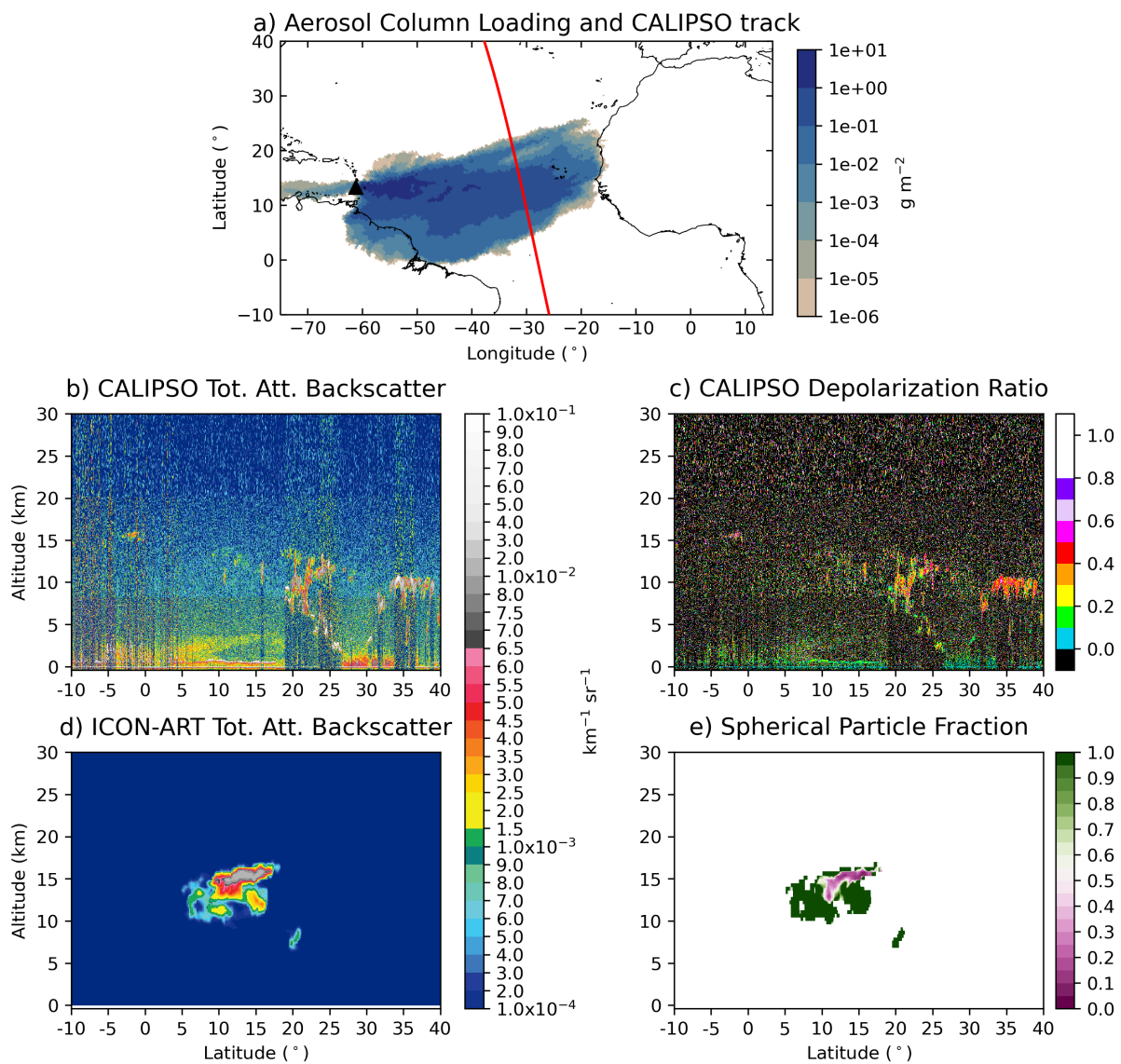


Figure C.10.: As Figure 6.8, but for 16 UTC on 11 April 2021.

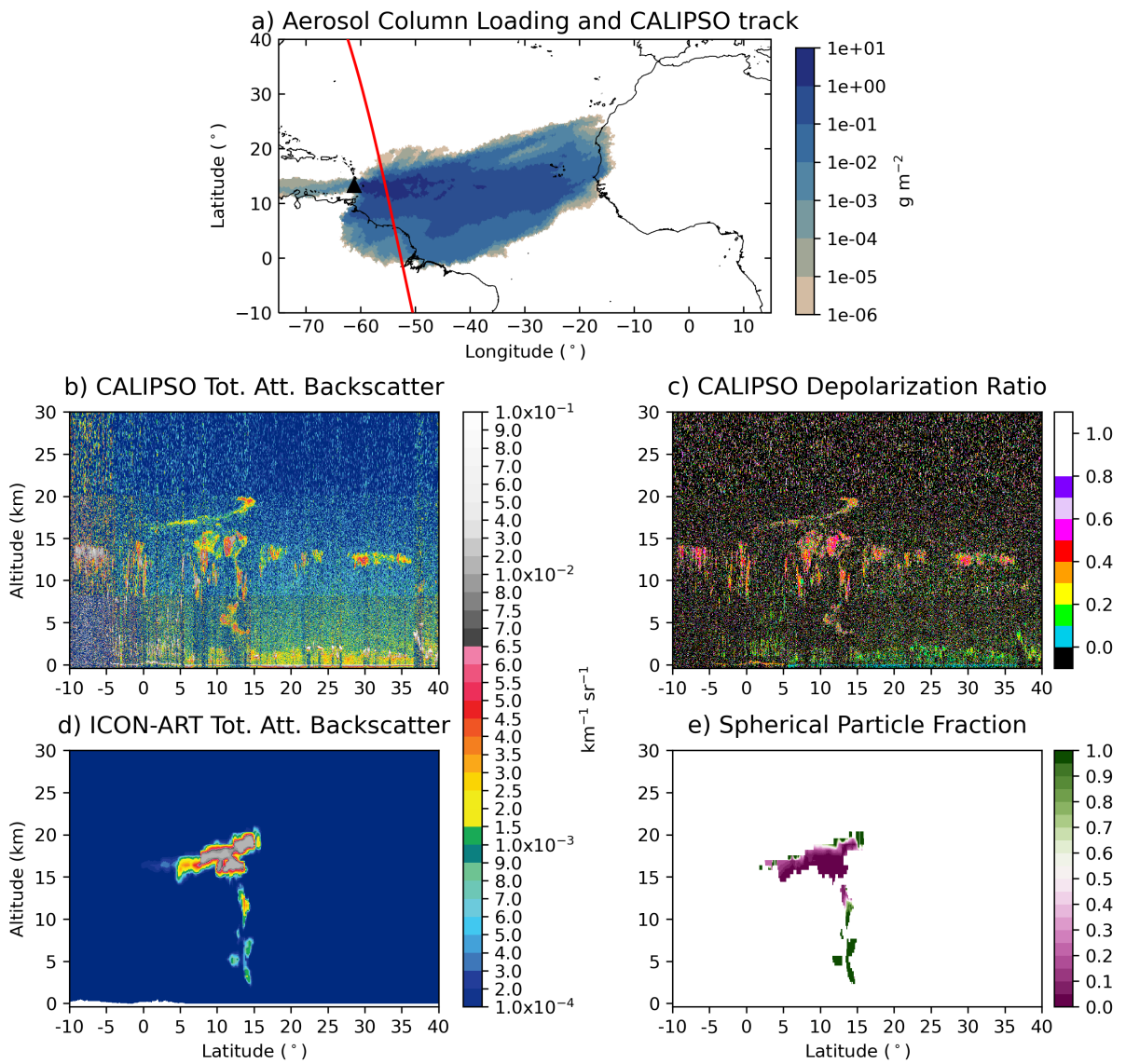


Figure C.11.: As Figure 6.8, but for 18 UTC on 11 April 2021.

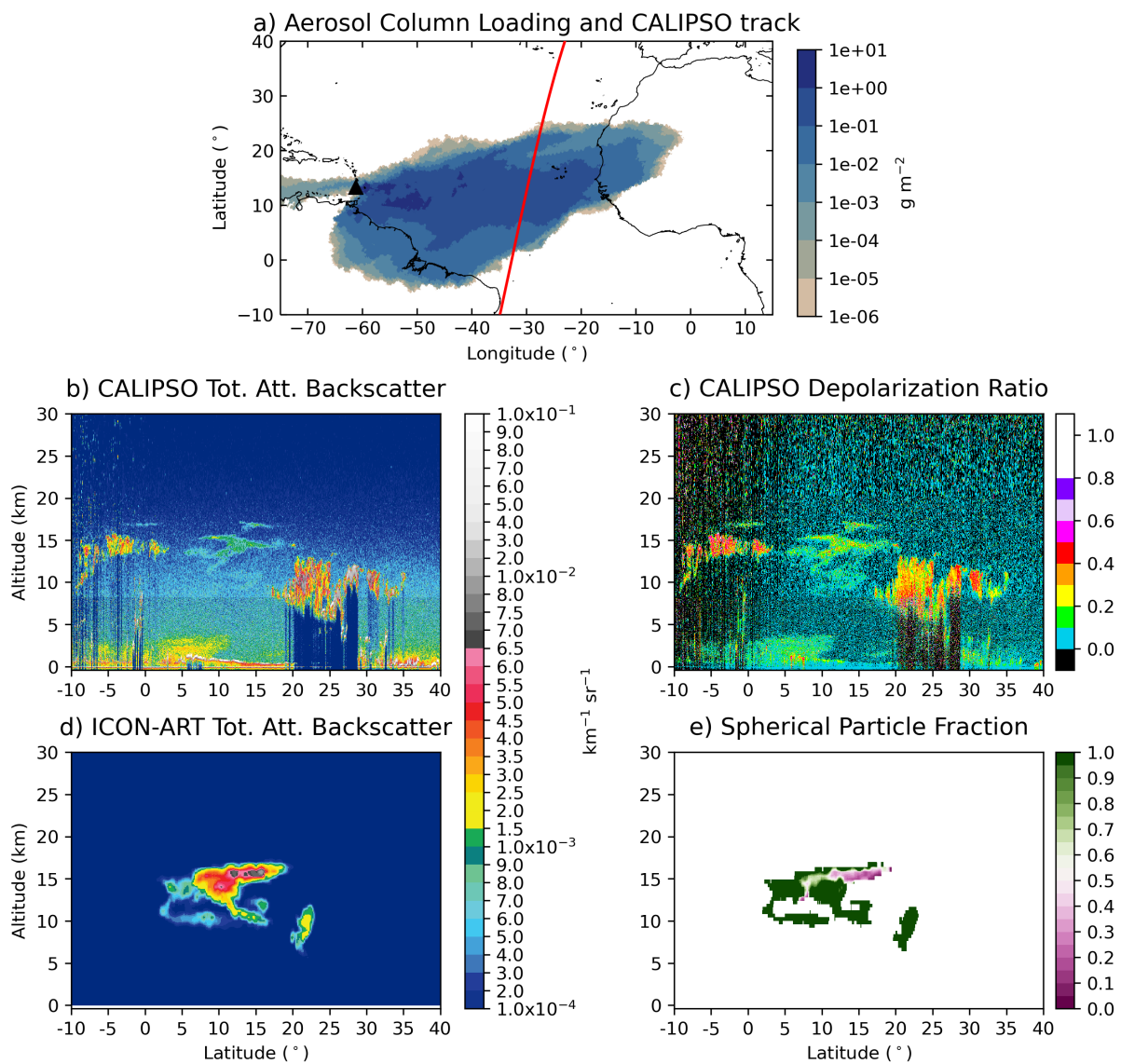


Figure C.12.: As Figure 6.8, but for 4 UTC on 12 April 2021.

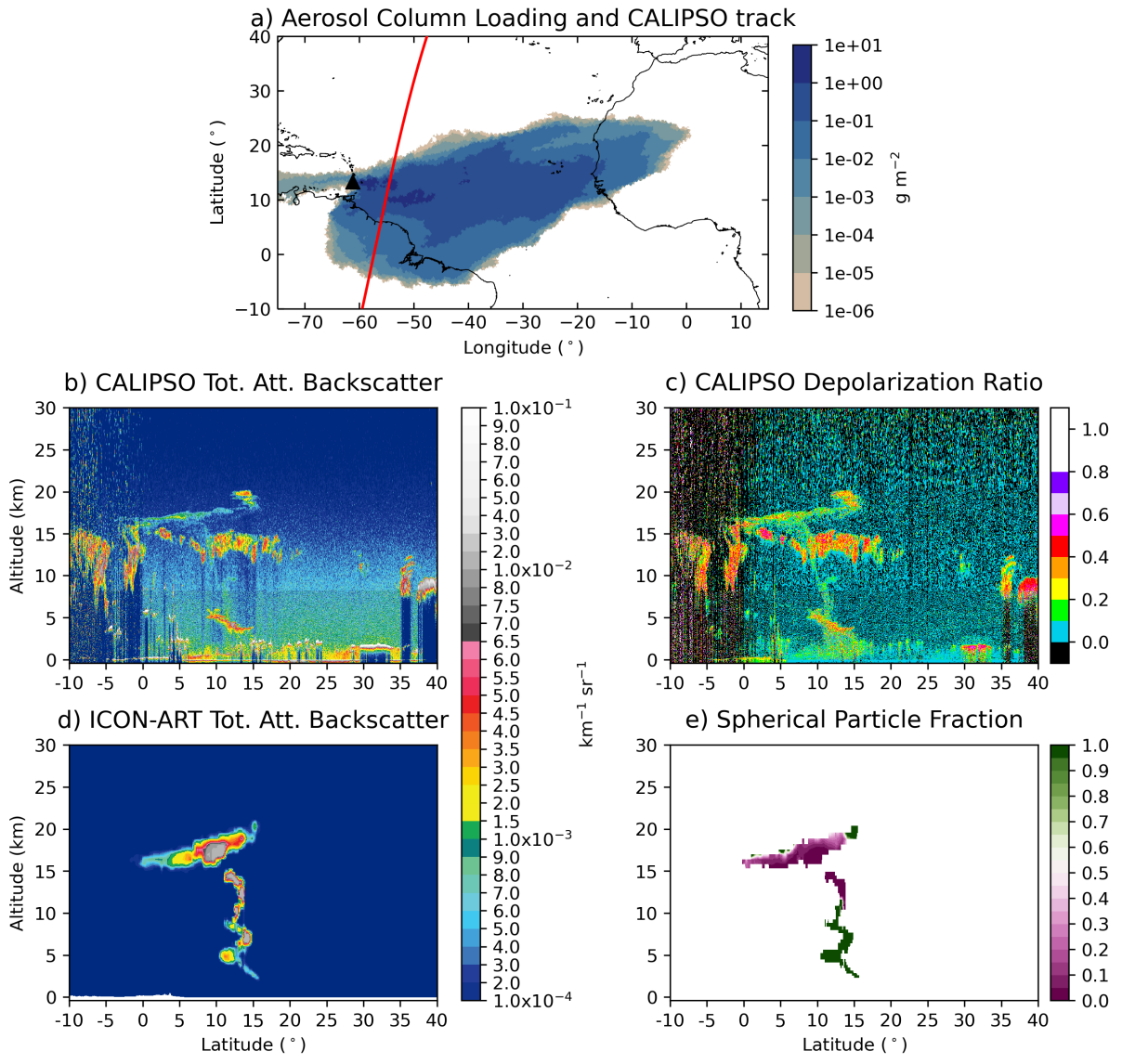


Figure C.13.: As Figure 6.8, but for 6 UTC on 12 April 2021.

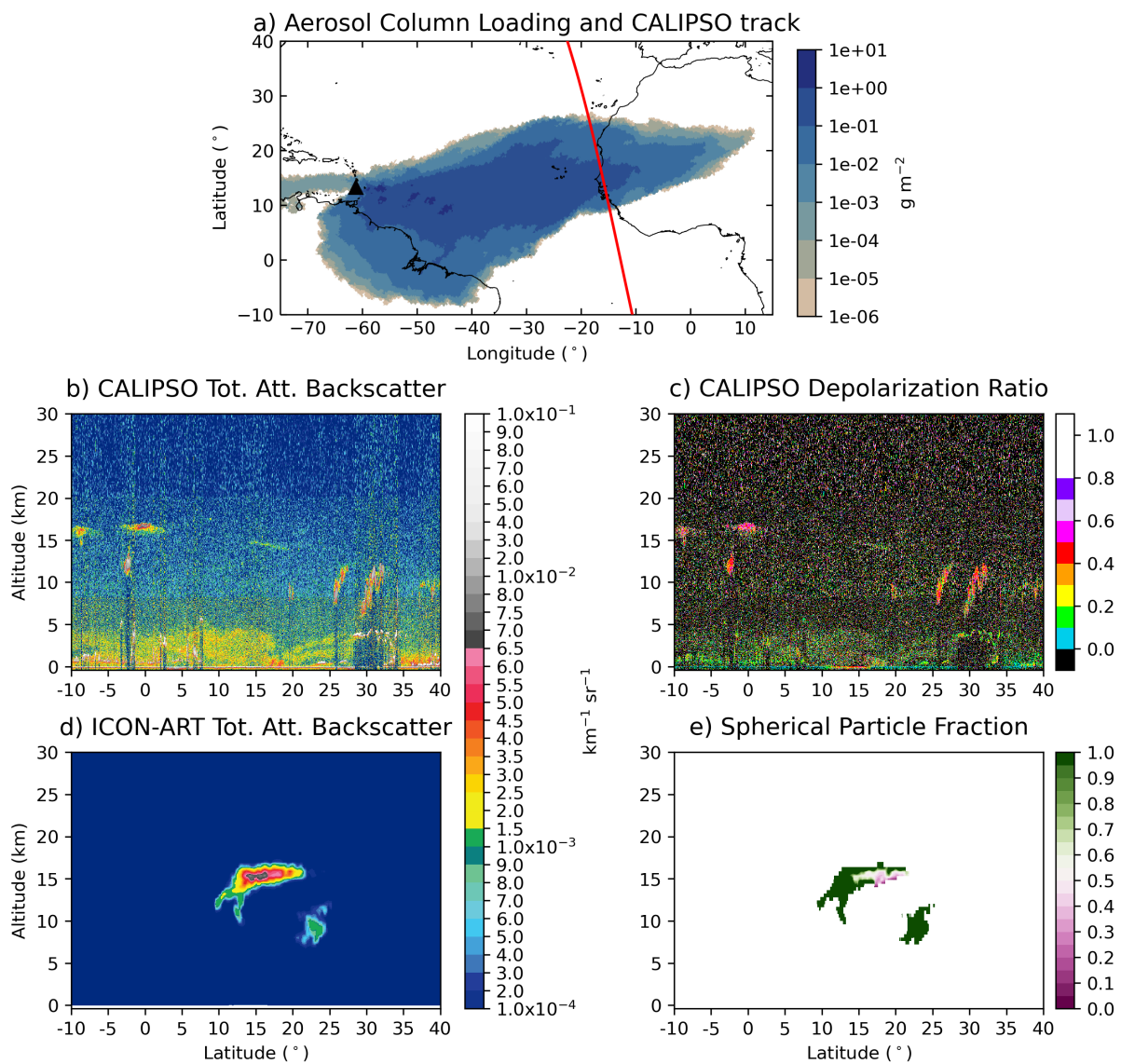


Figure C.14.: As Figure 6.8, but for 15 UTC on 12 April 2021.

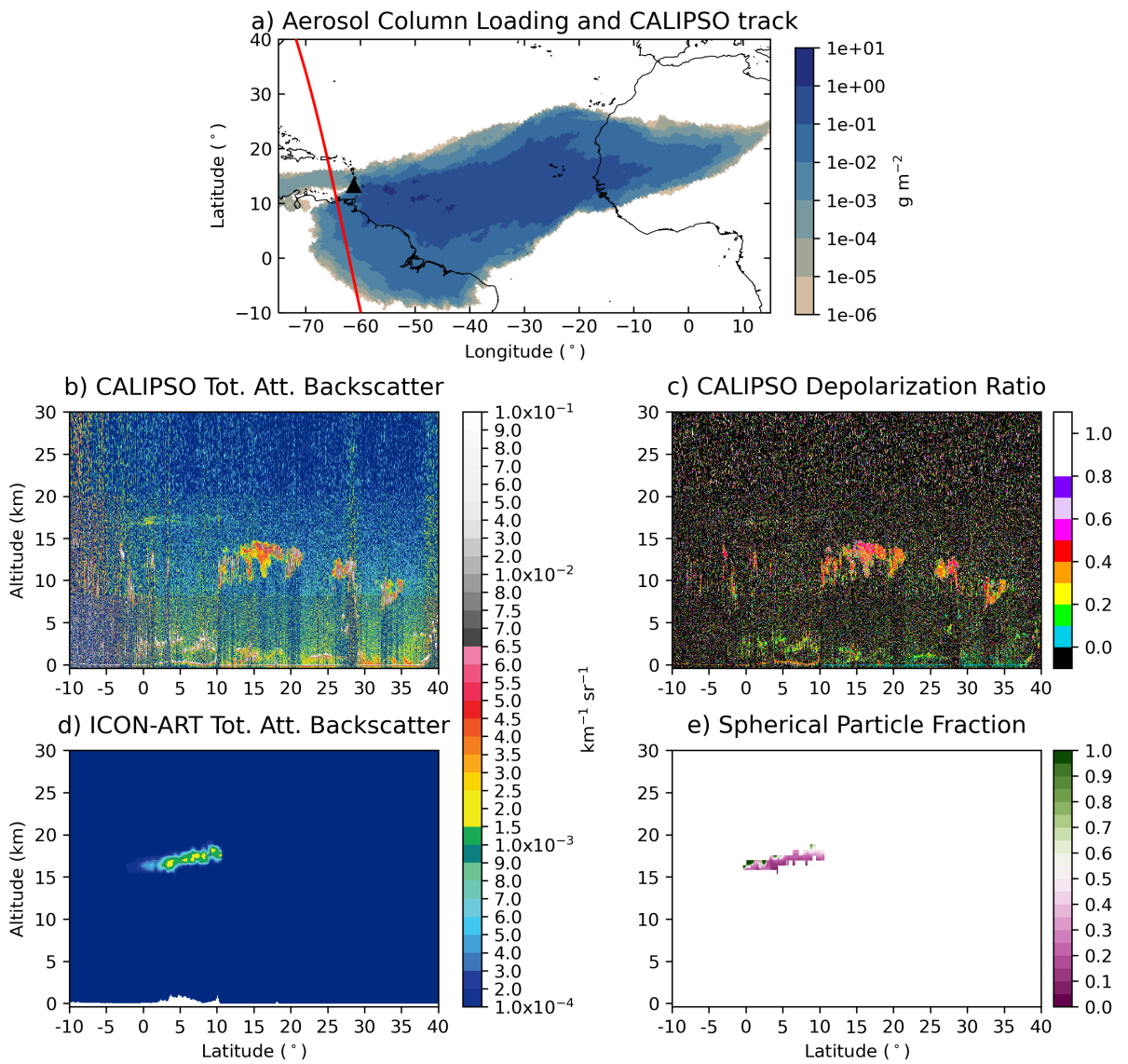


Figure C.15.: As Figure 6.8, but for 18 UTC on 12 April 2021.

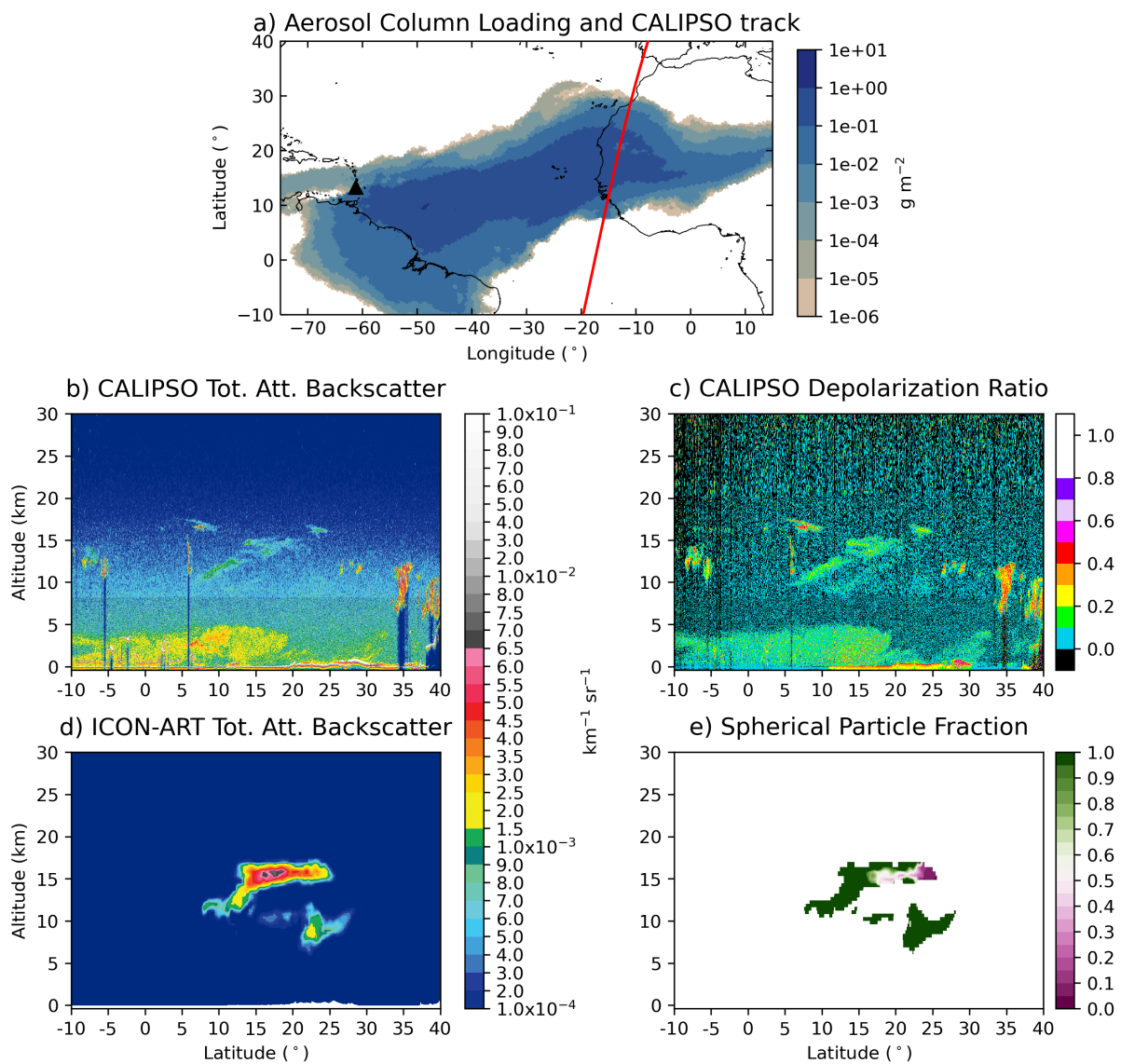


Figure C.16.: As Figure 6.8, but for 3 UTC on 13 April 2021.

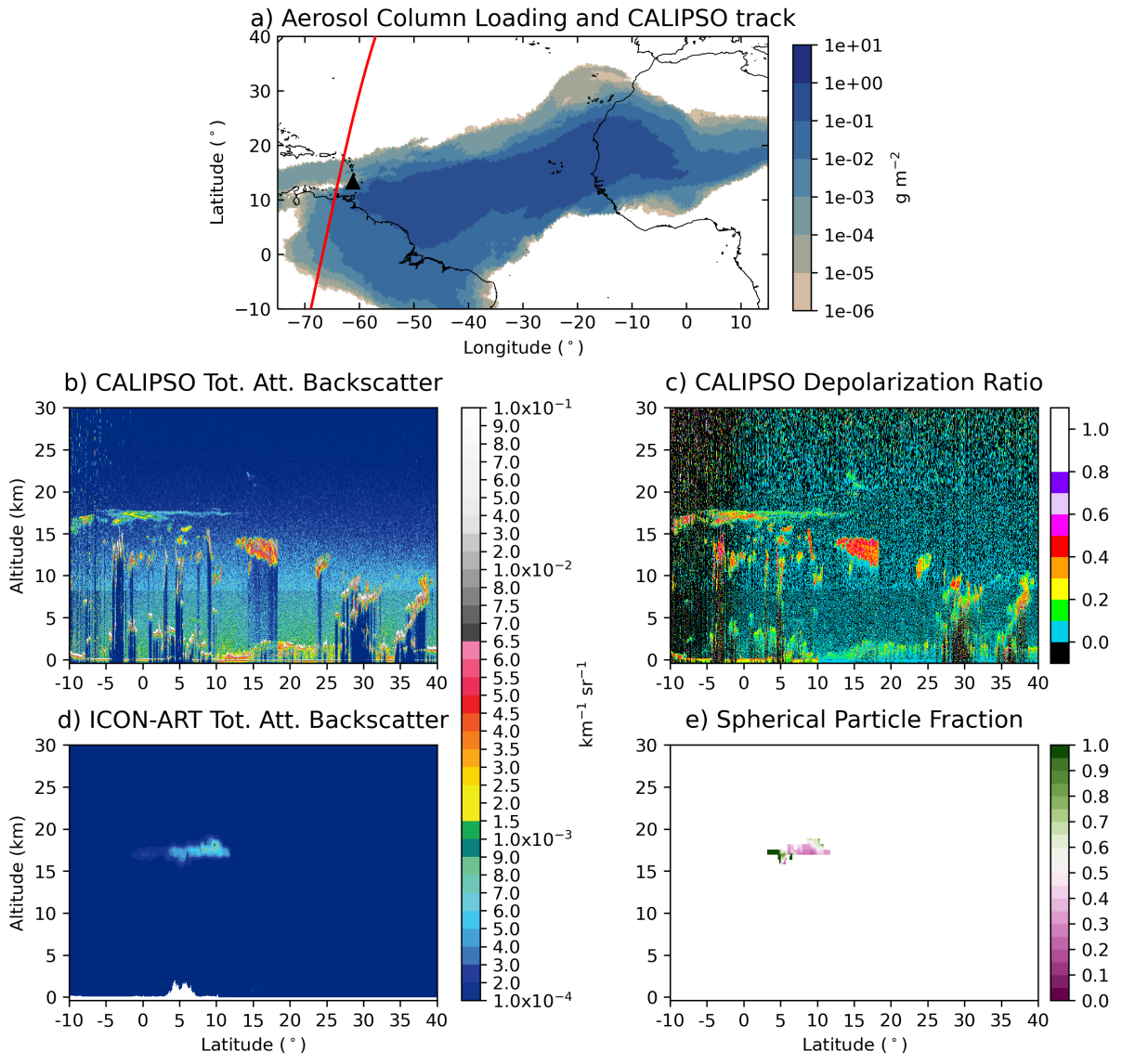


Figure C.17.: As Figure 6.8, but for 7 UTC on 13 April 2021.

D. Symbols and acronyms

Acronyms

1-D	one-dimensional
3-D	three-dimensional
AHI	infrared Advanced Himawari Imager
ALWC	aerosol liquid water content
AOD	aerosol optical depth
ATHAM	Active Tracer High-Resolution Atmospheric Model
BCO	Barbados Cloud Observatory
BET	Brunauer-Emmett-Teller method
CALIOP	Cloud-Aerosol Lidar with Orthogonal Polarization
CALIPSO	Cloud-Aerosol Lidar and Infrared Pathfinder Satellite Observation
CAM-chem	Community Atmosphere Model with chemistry
CCN	cloud condensation nuclei
CNES	Centre National d'Etudes Spatiales
DFG	Deutschen Forschungsgemeinschaft
DKRZ	German Climate Computing Center
DWD	German Weather Service
ESP	eruption source parameter
GOES-16	Geostationary Operational Environmental Satellite 16
GOES-17	Geostationary Operational Environmental Satellite 17
IASI	Infrared Atmospheric Sounding Interferometer
ICON-ART	ICOsahedral Nonhydrostatic model with Aerosol and Reactive Trace gases
IN	ice nucleating particle
IR	infrared
JAXA	Japan Aerospace Exploration Agency
JMA	Japan Meteorological Agency
KIT	Karlsruhe Institute of Technology
KPP	Kinetic PreProcessor
LAM	limited area mode
LW	long-wave
LWC	liquid water content
MECCA	Module Efficiently Calculating the Chemistry of the Atmosphere
MER	mass eruption rate
MINX	MISR INteractive eXplorer

MISR	Multiangle Imaging SpectroRadiometer
MISR RA	MISR Research Aerosol algorithm
MODIS	MOderate Resolution Imaging Spectroradiometer
MOZART-4	Model for OZone And Related chemical Tracers (Version 4)
MPI-M	Max-Planck-Institute for Meteorology
MOCAGE	Modèle de Chimie Atmosphérique de Grande Echelle
NAME	Numerical Atmospheric-dispersion Modelling Environment
NASA	National Aeronautics and Space Administration
NBL	neutral buoyancy level
NCAR	National Center for Atmospheric Research
NMMB-MONARCH-ASH	Nonhydrostatic Multiscale Model on the B-grid – Multiscale Online Nonhydrostatic AtmospheRe CHEmistry model – ASH
ODE	ordinary differential equation
O-MIF	anomalous oxygen mass-independent fractionation
PSD	particle size distribution
RRTM	Rapid Radiative Transfer Model
S5P	ESA/EU Copernicus Sentinel-5 Precursor
SAL (method)	structure, amplitude, location (method)
SSA	single scattering albedo
SW	shortwave
TGSD	total grain size distribution
TROPOMI	TROPOspheric Monitoring Instrument
UTLS	upper troposphere lower stratosphere
UV	ultraviolet
VEI	volcanic explosivity index
VolRes	Volcanic Response team
VZA	vertical zenith angle
WRF/ARW	Weather Research and Forecasting Model / Advanced Research WRF

Chemical species

Al	aluminium
Ca / Ca ²⁺	calcium
CH ₄	methane
Cl ⁻	chlorine
CO ₂	carbon dioxide
Fe	iron
H	hydrogen
H ⁺	hydrogen ion
H ₂ O	water
H ₂ O ₂	hydrogen peroxide
H ₂ S	hydrogen sulfide
HCl	hydrogen chloride
HF	hydrogen fluoride
HSO ₃ ⁻	hydrogen sulfite
HSO ₄ ⁻	hydrogen sulfate
H ₂ SO ₄	sulfuric acid
K / K ⁺	potassium
Mg / Mg ²⁺	magnesium
N ₂	nitrogen
Na / Na ⁺	sodium
NH ₃	ammonia
NH ₄ ⁺	ammonium
NO ₃ ⁻	nitrate
O	oxygen
O(¹ D)	atomic oxygen (excited state)
O ₂	oxygen
O ₃	ozone
OH	hydroxyl radical
OH ⁻	hydroxide ion
S(IV)	dissolved sulfur in oxidation state 4 (SO ₂ , HSO ₃ ⁻ , SO ₃ ²⁻)
S(VI)	dissolved sulfur in oxidation state 6 (HSO ₄ ⁻ , SO ₄ ²⁻)
Si	silicon
SiO ₂	silica
SO ₂	sulfur dioxide
SO ₃ ²⁻	sulfite
SO ₄ ²⁻	sulfate
Ti	titanium

Physical variables and constants

Symbol	Description	Unit
[A]	number concentration of species A	molecules cm ⁻³ (gas phase) or mol L ⁻¹ (aqueous phase)
A_p	area of the particle cross-section	m ²
α	sticking or accommodation coefficient	–
B_λ	spectral complex refractive index	–
β	coagulation coefficient	m ³ s ⁻¹
β_a	volume absorption coefficient	m ⁻¹
β_b	volume backscattering coefficient	m ⁻¹
β_e	volume extinction coefficient	m ⁻¹
β_s	volume scattering coefficient	m ⁻¹
c	speed of light	m s ⁻¹
\bar{c}_A	mean speed of species A	m s ⁻¹
c_{crit}	critical concentration for nucleation	kg m ⁻³
$c_{H_2SO_4}$	mass mixing ratio of H ₂ SO ₄	kg kg ⁻¹
c_{pd}	specific heat capacity of dry air at constant pressure	J kg ⁻¹ K ⁻¹
c_v	specific heat capacity of dry air at constant volume	J kg ⁻¹ K ⁻¹
$Ca_{0,l}$	coagulation rate of mass specific number concentration	kg ⁻¹ s ⁻¹
$\tilde{C}a_{0,l}$	coagulation rate of zeroth moment	m ⁻³ s ⁻¹
$Ca_{3,l}$	coagulation rate of mass mixing ratio	kg kg ⁻¹ s ⁻¹
$\tilde{C}a_{3,l}$	coagulation rate of third moment	m ³ m ⁻³ s ⁻¹
$Co_{3,l}$	condensation rate of mass mixing ratio	kg kg ⁻¹ s ⁻¹
$\tilde{C}o_{3,l}$	condensation rate of third moment	m m ⁻³ s ⁻¹
$\chi(d)$	particle size dependent term for condensation rate	m ³ s ⁻¹
χ_T	particle size independent term for condensation rate	–
$D_{g,A}$	diffusion coefficient of species A in air	m ² s ⁻¹
$d_{k,l}$	median diameter for k -th moment of mode l	m
d_p	particle diameter	m
E^*	normalized MER	–
\hat{E}	activation energy in Arrhenius equation	J mol ⁻¹

$E_{0,l}$	emission rate of mass specific number concentration	$\text{kg}^{-1} \text{s}^{-1}$
$E_{3,l}$	emission rate of mass mixing ratio	$\text{kg kg}^{-1} \text{s}^{-1}$
E_g	emission rate of gas g	kg s^{-1}
E_{ph}	SO ₂ emission rate of phase ph	kg s^{-1}
\bar{E}_{SO_2}	mean SO ₂ emission	kg s^{-1}
E_{tot}	total mass eruption rate	kg s^{-1}
ϵ	total attenuated backscatter	$\text{km}^{-1} \text{sr}^{-1}$
η	coefficient correcting for free molecular effects	–
F	broadening factor in Troe equation	–
f	Coriolis parameter	s^{-1}
f_e	function of emission profile	–
\mathbf{f}_F	source and sink terms for horizontal momentum	N kg^{-1}
g	asymmetry parameter	–
g_z	acceleration due to gravity	m s^{-2}
γ	uptake coefficient	–
H	plume height	m
h	Planck's constant	J s
H_A	Henry's law coefficient of species A	$\text{mol L}^{-1} \text{atm}^{-1}$
H_A^0	Henry's law coefficient of species A at 273 K	$\text{mol L}^{-1} \text{atm}^{-1}$
H_{ph}	plume height of phase ph	m
H_T	phase duration-weighted mean plume height	m
$\Delta_{sol}H$	enthalpy change of dissolution	kcal mol^{-1}
I_l	integral for condensation rate of mode l	s^{-1}
I_λ	spectral radiance	$\text{W m}^2\text{sr}^{-1}$
J_g	photolysis rate coefficient of gas g	s^{-1}
K_h	horizontal component of the kinetic energy	m^2s^{-2}
k_i	rate coefficient ($i = 0, 1, 2, \dots, \infty, a, b, \dots$)	differs
Kn	Knudsen number	–
K_w	equilibrium constant of water autoionization	M^2
L_g	chemical loss rate of gas g	kg s^{-1}
λ	wavelength	m
λ_{air}	mean free path of air	m

\dot{M}_3	production rate of third moment of condensable material	s^{-1}
M_A	molar mass of species A	$kg\ mol^{-1}$
M_{air}	molar mass of air	$kg\ mol^{-1}$
$M_{k,l}$	k -th moment of particle size distribution of mode l	$m^k\ m^{-3}$
N	total number concentration of particles	m^{-3}
n_{ph}	number of eruption phases	–
$Nu_{0,l}$	nucleation rate of mass specific number concentration	$kg^{-1}s^{-1}$
$Nu_{3,l}$	nucleation rate of mass mixing ratio	$kg\ kg^{-1}s^{-1}$
ν	radiation frequency	s^{-1}
Ω_l	coefficient to divide condensable mass	–
ω	single scattering albedo	–
p	scattering phase function	–
p_A	partial pressure of species A	atm
p_{00}	reference pressure	hPa
P_l	chemical production rate of gas g	$kg\ s^{-1}$
Φ_{in}	flux of gas phase species into droplet	molecules $cm^{-3}\ s^{-1}$
Φ_{out}	flux of aqueous phase species out of droplet	molecules $cm^{-3}\ s^{-1}$
Π	Exner function	–
$\hat{\Psi}_{0,l}$	mass specific number concentration of mode l	kg^{-1}
$\hat{\Psi}_{0,l}$	mass specific number concentration of mode l with diameter d_p	kg^{-1}
$\hat{\Psi}_{3,l}$	mass mixing ratio of mode l	$kg\ kg^{-1}$
$\hat{\Psi}_{3,l}$	mass mixing ratio of mode l with diameter d_p	–
$\hat{\Psi}_g$	mass mixing ratio of gas g	$kg\ kg^{-1}$
\tilde{Q}	adiabatic heat source terms	s^{-1}
Q_e	extinction efficiency	–
R^*	universal gas constant	$J\ mol^{-1}\ K^{-1}$
r	droplet or particle radius	m
r_v	radius of the vent	m
R_{ad}	rate of gas adsorption	s^{-1}
R_d	gas constant of dry air	$J\ kg^{-1}\ K^{-1}$
RH	relative humidity	%
$\hat{\rho}$	plume mixture density	$kg\ m^{-3}$

ρ_a	air density	kg m^{-3}
ρ_g	density of gas g	kg m^{-3}
ρ_p	particle density	kg m^{-3}
S	Suzuki distribution function	kg s^{-1}
S^*	normalized Suzuki distribution function	–
S_p	total surface area per unit volume of air	m^2m^{-3}
σ_e	extinction cross section	m^2
σ_l	standard deviation of mode l	–
T	temperature	K
t	time	s
T^0	reference temperature	K
t_{ph}	phase duration	s
Δt	model time step	s^{-1}
τ	optical depth or optical thickness	–
θ	scattering angle	°
θ_v	virtual potential temperature	K
$\mathbf{v} = (v_t, v_n, w)$	three-dimensional wind vector	m s^{-1}
$v_{e,ph}$	exit velocity of phase ph	m s^{-1}
v_n	horizontal wind component normal to the triangle edges	m s^{-1}
$v_{sed,k,l}$	sedimentation velocity for k -th moment of mode l	m s^{-1}
v_t	horizontal wind velocity tangential to the triangle edges	m s^{-1}
w	vertical wind component	m s^{-1}
$W_{0,l}$	wet deposition rate of zeroth moment	$\text{kg}^{-1} \text{s}^{-1}$
$W_{3,l}$	wet deposition rate of third moment	$\text{kg kg}^{-1} \text{s}^{-1}$
x	effective particle size	–
z	geometric altitude (vertical coordinate)	m
z^*	normalized plume height	–
Δz_i	thickness of vertical model level i	m
ζ	vertical component of the relative vorticity	s^{-1}

E. Bibliography

- Abdelkader, M., S. Metzger, B. Steil, K. Klingmüller, H. Tost, A. Pozzer, G. Stenchikov, L. Barrie, and J. Lelieveld, 2017: Sensitivity of transatlantic dust transport to chemical aging and related atmospheric processes. *Atmospheric Chemistry and Physics*, **17** (6), 3799–3821, doi:10.5194/acp-17-3799-2017.
- Abdelkader, M., G. Stenchikov, A. Pozzer, H. Tost, and J. Lelieveld, 2023: The effect of ash, water vapor, and heterogeneous chemistry on the evolution of a Pinatubo-size volcanic cloud. *Atmospheric Chemistry and Physics*, **23** (1), 471–500, doi:10.5194/acp-23-471-2023.
- Arrhenius, S., 1889: Über die Reaktionsgeschwindigkeit bei der Inversion von Rohrzucker durch Säuren. *Zeitschrift für Physikalische Chemie*, **4U** (1), 226–248, doi:doi:10.1515/zpch-1889-0416, URL <https://doi.org/10.1515/zpch-1889-0416>.
- Babu, R., L. S. P. Nguyen, G.-R. Sheu, S. M. Griffith, S. K. Pani, H.-Y. Huang, and N.-H. Lin, 2022: Long-range transport of La Soufrière volcanic plume to the western North Pacific: Influence on atmospheric mercury and aerosol properties. *Atmospheric Environment*, **268**, 118 806, doi:<https://doi.org/10.1016/j.atmosenv.2021.118806>.
- Bagheri, G. and C. Bonadonna, 2016: Chapter 2 - Aerodynamics of Volcanic Particles: Characterization of Size, Shape, and Settling Velocity. *Volcanic Ash*, Elsevier, 39–52.
- Bagnato, E., A. Aiuppa, A. Bertagnini, C. Bonadonna, R. Cioni, M. Pistolesi, M. Pedone, and A. Hoskuldsson, 2013: Scavenging of sulphur, halogens and trace metals by volcanic ash: The 2010 Eyjafjallajökull eruption. *Geochimica et Cosmochimica Acta*, **103**, 138–160, doi:10.1016/j.gca.2012.10.048.
- Bechtold, P., M. Koehler, T. Jung, M. Leutbecher, F. Doblas-Reyes, M. J. Rodwell, F. Vitart, and G. Balsamo, 2008: Advances in simulating atmospheric variability with the ECMWF model: From synoptic to decadal time-scales. *Quarterly Journal of the Royal Meteorological Society*, **134**, 1337–1351.
- Beckett, F. M., C. S. Witham, S. J. Leadbetter, R. Crocker, H. N. Webster, M. C. Hort, A. R. Jones, B. J. Devenish, and D. J. Thomson, 2020: Atmospheric Dispersion Modelling at the London VAAC: A Review of Developments since the 2010 Eyjafjallajökull Volcano Ash Cloud. *Atmosphere*, **11** (4), doi:10.3390/atmos11040352.
- Bekki, S., 1995: Oxidation of volcanic SO₂: A sink for stratospheric OH and H₂O. *Geophysical Research Letters*, **22** (8), 913–916, doi:<https://doi.org/10.1029/95GL00534>, URL <https://agupubs.onlinelibrary.wiley.com/doi/abs/10.1029/95GL00534>.
- Boucher, O., 2015: *Atmospheric Aerosol*. Springer Netherlands.
- Brown, R., C. Bonadonna, and A. Durant, 2012: A review of volcanic ash aggregation. *Physics and Chemistry of the Earth, Parts A/B/C*, **45-46**, 65–78, doi:<https://doi.org/10.1016/j.pce.2011.11.001>.

- Bruckert, J., L. Hirsch, A. Horváth, R. A. Kahn, T. Kölling, L. O. Muser, C. Timmreck, H. Vogel, S. Wallis, and G. A. Hoshyaripour, 2023: Dispersion and Aging of Volcanic Aerosols After the La Soufrière Eruption in April 2021. *Journal of Geophysical Research: Atmospheres*, **128** (8), e2022JD037694, doi:<https://doi.org/10.1029/2022JD037694>.
- Bruckert, J., G. A. Hoshyaripour, A. Horváth, L. O. Muser, F. J. Prata, C. Hoose, and B. Vogel, 2022: Online treatment of eruption dynamics improves the volcanic ash and SO₂ dispersion forecast: case of the 2019 Raikoke eruption. *Atmospheric Chemistry and Physics*, **22** (5), 3535–3552, doi:10.5194/acp-22-3535-2022.
- Bursik, M., 2001: Effect of wind on the rise height of volcanic plumes. *Geophysical Research Letters*, **28** (18), 3621–3624, doi:<https://doi.org/10.1029/2001GL013393>.
- CAM-chem, 2019: CAM-chem initial data for chemical species from the National Center for Atmospheric Research (NCAR). URL <https://www.acom.ucar.edu/cam-chem/cam-chem.shtml>, last access: 2023/03/04.
- Carazzo, G., E. Kaminski, and S. Tait, 2008: On the dynamics of volcanic columns: A comparison of field data with a new model of negatively buoyant jets. *Journal of Volcanology and Geothermal Research*, **178** (1), 94–103, doi:<https://doi.org/10.1016/j.jvolgeores.2008.01.002>.
- Carazzo, G., E. Kaminsky, and S. Tait, 2006: The route to self-similarity in turbulent jets and plumes. *Journal of Fluid Mechanics*, **547**, 137–148, doi:10.1017/S002211200500683X.
- Casadevall, T. J., 1994: Volcanic ash and aviation safety: Proceedings of the first international symposium on volcanic ash and aviation safety. *U.S. Geological Survey*, doi:10.3133/b2047.
- Chouza, F., T. Leblanc, J. Barnes, M. Brewer, P. Wang, and D. Koon, 2020: Long-term (1999–2019) variability of stratospheric aerosol over Mauna Loa, Hawaii, as seen by two co-located lidars and satellite measurements. *Atmospheric Chemistry and Physics*, **20** (11), 6821–6839, doi:10.5194/acp-20-6821-2020.
- Collini, E., M. S. Osoreo, A. Folch, J. Viramonte, G. Villaosa, and G. Salmuni, 2013: Volcanic ash forecast during the June 2011 Cordón Caulle eruption. *Natural Hazards*, **66** (2), 389–412, doi:10.1007/s11069-012-0492-y.
- Costa, A., A. Folch, and G. Macedonio, 2013: Density-driven transport in the umbrella region of volcanic clouds: Implications for tephra dispersion models. *Geophysical Research Letters*, **40** (18), 4823–4827, doi:<https://doi.org/10.1002/grl.50942>.
- de Leeuw, J., A. Schmidt, C. S. Witham, N. Theys, I. A. Taylor, R. G. Grainger, R. J. Pope, J. Haywood, M. Osborne, and N. I. Kristiansen, 2021: The 2019 Raikoke volcanic eruption – Part 1: Dispersion model simulations and satellite retrievals of volcanic sulfur dioxide. *Atmospheric Chemistry and Physics*, **21** (14), 10 851–10 879, doi:10.5194/acp-21-10851-2021.
- Degruyter, W. and C. Bonadonna, 2012: Improving on mass flow rate estimates of volcanic eruptions. *Geophysical Research Letters*, **39** (16), doi:10.1029/2012GL052566.
- Dhomse, S. S., K. M. Emmerson, G. W. Mann, N. Bellouin, K. S. Carslaw, M. P. Chipperfield, R. Hommel, N. L. Abraham, P. Telford, P. Braesicke, M. Dalvi, C. E. Johnson, F. O’Connor, O. Morgenstern, J. A. Pyle, T. Deshler,

- J. M. Zawodny, and L. W. Thomason, 2014: Aerosol microphysics simulations of the Mt. Pinatubo eruption with the UM-UKCA composition-climate model. *Atmospheric Chemistry and Physics*, **14** (20), 11 221–11 246, doi:10.5194/acp-14-11221-2014.
- Dhomse, S. S., G. W. Mann, J. C. Antuña Marrero, S. E. Shallcross, M. P. Chipperfield, K. S. Carslaw, L. Marshall, N. L. Abraham, and C. E. Johnson, 2020: Evaluating the simulated radiative forcings, aerosol properties, and stratospheric warmings from the 1963 Mt Agung, 1982 El Chichón, and 1991 Mt Pinatubo volcanic aerosol clouds. *Atmospheric Chemistry and Physics*, **20** (21), 13 627–13 654, doi:10.5194/acp-20-13627-2020.
- Emmons, L. K., S. Walters, P. G. Hess, J.-F. Lamarque, G. G. Pfister, D. Fillmore, C. Granier, A. Guenther, D. Kinnison, T. Laepple, J. Orlando, X. Tie, G. Tyndall, C. Wiedinmyer, S. L. Baughcum, and S. Kloster, 2010: Description and evaluation of the Model for Ozone and Related chemical Tracers, version 4 (MOZART-4). *Geoscientific Model Development*, **3** (1), 43–67, doi:10.5194/gmd-3-43-2010.
- Eriksson, A. C., C. Wittbom, P. Roldin, M. Sporre, E. Öström, P. Nilsson, J. Martinsson, J. Rissler, E. Z. Nordin, B. Svenningsson, J. Pagels, and E. Swietlicki, 2017: Diesel soot aging in urban plumes within hours under cold dark and humid conditions. *Scientific Reports*, **7** (1), doi:10.1038/s41598-017-12433-0.
- Ernst, G. G. J., R. S. J. Sparks, S. N. Carey, and M. I. Bursik, 1996: Sedimentation from turbulent jets and plumes. *Journal of Geophysical Research: Solid Earth*, **101** (B3), 5575–5589, doi:https://doi.org/10.1029/95JB01900.
- Feinberg, A., T. Sukhodolov, B.-P. Luo, E. Rozanov, L. H. E. Winkel, T. Peter, and A. Stenke, 2019: Improved tropospheric and stratospheric sulfur cycle in the aerosol–chemistry–climate model SOCOL-AERv2. *Geoscientific Model Development*, **12** (9), 3863–3887, doi:10.5194/gmd-12-3863-2019.
- Flower, V. J. B. and R. A. Kahn, 2020: The Evolution of Icelandic Volcano Emissions, as Observed From Space in the Era of NASA's Earth Observing System (EOS). *Journal of Geophysical Research: Atmospheres*, **125** (19), e2019JD031 625, doi:https://doi.org/10.1029/2019JD031625.
- Folch, A., A. Costa, and G. Macedonio, 2016: FPLUME-1.0: An integral volcanic plume model accounting for ash aggregation. *Geoscientific Model Development*, **9** (1), 431–450, doi:10.5194/gmd-9-431-2016.
- Fountoukis, C. and A. Nenes, 2007: ISORROPIA II: a computationally efficient thermodynamic equilibrium model for K^+ – Ca^{2+} – Mg^{2+} – NH_4^+ – Na^+ – SO_4^{2-} – NO_3^- – Cl^- – H_2O aerosols. *Atmospheric Chemistry and Physics*, **7** (17), 4639–4659, doi:10.5194/acp-7-4639-2007.
- Fuchs, N. and A. Sutugin, 1971: High-dispersed aerosols. *Topics in Current Aerosol Research*, HIDY, G. and J. BROCK, Eds., Pergamon, International Reviews in Aerosol Physics and Chemistry, 1.
- Galeazzo, T., S. Bekki, E. Martin, J. Savarino, and S. R. Arnold, 2018: Photochemical box modelling of volcanic SO_2 oxidation: isotopic constraints. *Atmospheric Chemistry and Physics*, **18** (24), 17 909–17 931, doi:10.5194/acp-18-17909-2018.
- Gasch, P., 2016: Numerische Simulation eines außergewöhnlichen Staubereignisses im östlichen Mittelmeerraum unter Berücksichtigung der Mineralstaub-Strahlungswechselwirkung. Master's thesis, Karlsruher Institut für Technologie (KIT).

- Gasch, P., D. Rieger, C. Walter, P. Khain, Y. Levi, P. Knippertz, and B. Vogel, 2017: Revealing the meteorological drivers of the September 2015 severe dust event in the Eastern Mediterranean. *Atmospheric Chemistry and Physics*, **17** (22), 13 573–13 604, doi:10.5194/acp-17-13573-2017, URL <https://acp.copernicus.org/articles/17/13573/2017/>.
- Gassmann, A. and H.-J. Herzog, 2008: Towards a consistent numerical compressible non-hydrostatic model using generalized Hamiltonian tools. *Quarterly Journal of the Royal Meteorological Society*, **134** (635), 1597–1613, doi:<https://doi.org/10.1002/qj.297>.
- Giorgetta, M. A., R. Brokopf, T. Crueger, M. Esch, S. Fiedler, J. Helmert, C. Hohenegger, L. Kornblueh, M. Köhler, E. Manzini, T. Mauritsen, C. Nam, T. Raddatz, S. Rast, D. Reinert, M. Sakradzija, H. Schmidt, R. Schneck, R. Schnur, L. Silvers, H. Wan, G. Zängl, and B. Stevens, 2018: ICON-A, the Atmosphere Component of the ICON Earth System Model: I. Model Description. *Journal of Advances in Modeling Earth Systems*, **10** (7), 1613–1637, doi:<https://doi.org/10.1029/2017MS001242>.
- Gordon, I., L. Rothman, C. Hill, R. Kochanov, Y. Tan, P. Bernath, M. Birk, V. Boudon, A. Campargue, K. Chance, B. Drouin, J.-M. Flaud, R. Gamache, J. Hodges, D. Jacquemart, V. Perevalov, A. Perrin, K. Shine, M.-A. Smith, J. Tennyson, G. Toon, H. Tran, V. Tyuterev, A. Barbe, A. Császár, V. Devi, T. Furtenbacher, J. Harrison, J.-M. Hartmann, A. Jolly, T. Johnson, T.J. and Karman, I. Kleiner, A. Kyuberis, J. Loos, O. Lyulin, S. Massie, S. Mikhailenko, N. Moazzen-Ahmadi, H. Müller, O. Naumenko, A. Nikitin, O. Polyansky, M. Rey, M. Rotger, S. Sharpe, K. Sung, E. Starikova, S. Tashkun, J. Vander Auwera, G. Wagner, J. Wilzewski, P. Wcislo, S. Yu, and E. Zak, 2017: The HITRAN2016 molecular spectroscopic database. *Journal of Quantitative Spectroscopy and Radiative Transfer*, **203**, 3–69, doi:<https://doi.org/10.1016/j.jqsrt.2017.06.038>, HITRAN2016 Special Issue.
- Gouhier, M., J. Eycheenne, N. Azzaoui, A. Guillin, M. Deslandes, M. Poret, A. Costa, and P. Husson, 2019: Low efficiency of large volcanic eruptions in transporting very fine ash into the atmosphere. *Scientific Reports*, **9** (1), 1449, doi:10.1038/s41598-019-38595-7.
- Haghighatnasab, M., J. Kretzschmar, K. Block, and J. Quaas, 2022: Impact of Holuhraun volcano aerosols on clouds in cloud-system-resolving simulations. *Atmospheric Chemistry and Physics*, **22** (13), 8457–8472, doi:10.5194/acp-22-8457-2022, URL <https://acp.copernicus.org/articles/22/8457/2022/>.
- Harris, E., B. Sinha, D. van Pinxteren, A. Tilgner, K. W. Fomba, J. Schneider, A. Roth, T. Gnauk, B. Fahlbusch, S. Mertes, T. Lee, J. Collett, S. Foley, S. Borrmann, P. Hoppe, and H. Herrmann, 2013: Enhanced role of transition metal ion catalysis during in-cloud oxidation of SO₂. *Science*, **340** (6133), 727–730, doi:10.1126/science.1230911.
- Harvey, N. J., N. Huntley, H. F. Dacre, M. Goldstein, D. Thomson, and H. Webster, 2018: Multi-level emulation of a volcanic ash transport and dispersion model to quantify sensitivity to uncertain parameters. *Natural Hazards and Earth System Sciences*, **18** (1), 41–43, doi:10.5194/nhess-18-41-2018.
- Heinze, R., A. Dipankar, C. C. Henken, C. Moseley, O. Sourdeval, S. Trömel, X. Xie, P. Adamidis, F. Ament, H. Baars, C. Barthlott, A. Behrendt, U. Blahak, S. Bley, S. Brdar, M. Brueck, S. Crewell, H. Deneke, P. Di Girolamo, R. Evaristo, J. Fischer, C. Frank, P. Friederichs, T. Göcke, K. Gorges, L. Hande, M. Hanke, A. Hansen, H.-C. Hege, C. Hoose, T. Jahns, N. Kalthoff, D. Klocke, S. Kneifel, P. Knippertz, A. Kuhn, T. van Laar, A. Macke, V. Maurer, B. Mayer, C. I. Meyer, S. K. Muppa, R. A. J. Neggers, E. Orlandi, F. Pantillon, B. Pospichal,

- N. Röber, L. Scheck, A. Seifert, P. Seifert, F. Senf, P. Siligam, C. Simmer, S. Steinke, B. Stevens, K. Wapler, M. Weniger, V. Wulfmeyer, G. Zängl, D. Zhang, and J. Quaas, 2017: Large-eddy simulations over Germany using ICON: a comprehensive evaluation. *Quarterly Journal of the Royal Meteorological Society*, **143** (702), 69–100, doi:<https://doi.org/10.1002/qj.2947>.
- Hogan, R. J. and A. Bozzo, 2018: A Flexible and Efficient Radiation Scheme for the ECMWF Model. *Journal of Advances in Modeling Earth Systems*, **10** (8), 1990–2008, doi:<https://doi.org/10.1029/2018MS001364>.
- Horváth, A., J. L. Carr, D. L. Girina, O. A. and Wu, A. A. Bril, A. A. Mazurov, D. V. Melnikov, G. A. Hoshyaripour, and B. S. A., 2021a: Geometric estimation of volcanic eruption column height from GOES-R near-limb imagery – Part 1: Methodology. *Atmospheric Chemistry and Physics*, **21** (16), 12 189–12 206, doi:10.5194/acp-21-12189-2021.
- Horváth, A., J. L. Carr, D. L. Wu, J. Bruckert, G. A. Hoshyaripour, and S. A. Buehler, 2022: Measurement report: Plume heights of the April 2021 La Soufrière eruptions from GOES-17 side views and GOES-16–MODIS stereo views. *Atmospheric Chemistry and Physics Discussions*, **2022**, 1–24, doi:10.5194/acp-2022-253.
- Horváth, A., O. A. Girina, J. L. Carr, D. L. Wu, A. A. Bril, A. A. Mazurov, D. V. Melnikov, G. A. Hoshyaripour, and B. S. A., 2021b: Geometric estimation of volcanic eruption column height from GOES-R near-limb imagery – Part 2: Case studies. *Atmospheric Chemistry and Physics*, **21** (16), 12 207–12 226, doi:10.5194/acp-21-12207-2021.
- Horwell, C. J. and P. J. Baxter, 2006: The respiratory health hazards of volcanic ash: A review for volcanic risk mitigation. *Bulletin of Volcanology*, **69** (1), 1–24, doi:10.1007/s00445-006-0052-y.
- Hoshyaripour, G. A., V. Bachmann, J. Förstner, A. Steiner, H. Vogel, F. Wagner, C. Walter, and B. Vogel, 2019: Effects of Particle Nonsphericity on Dust Optical Properties in a Forecast System: Implications for Model-Observation Comparison. *Journal of Geophysical Research: Atmospheres*, **124** (13), 7164–7178, doi:<https://doi.org/10.1029/2018JD030228>.
- Hoshyaripour, G. A., M. Hort, and B. Langmann, 2015: Ash iron mobilization through physicochemical processing in volcanic eruption plumes: a numerical modeling approach. *Atmospheric Chemistry and Physics*, **15** (16), 9361–9379, doi:10.5194/acp-15-9361-2015.
- Hoyle, C. R., V. Pinti, A. Welti, B. Zobrist, C. Marcolli, B. Luo, A. Höskuldsson, H. B. Mattsson, O. Stetzer, T. Thorsteinsson, G. Larsen, and T. Peter, 2011: Ice nucleation properties of volcanic ash from Eyjafjallajökull. *Atmospheric Chemistry and Physics*, **11** (18), 9911–9926, doi:10.5194/acp-11-9911-2011, URL <https://acp.copernicus.org/articles/11/9911/2011/>.
- Isono, K., M. Komabayasi, and A. Ono, 1959a: The Nature and the Origin of Ice Nuclei in the Atmosphere. *Journal of the Meteorological Society of Japan. Ser. II*, **37** (6), 211–233, doi:10.2151/jmsj1923.37.6_211.
- , 1959b: Volcanoes as a Source of Atmospheric Ice Nuclei. *Nature*, **183** (4657), 317–318, doi:10.1038/183317a0.
- Jacob, D. J., 1986: Chemistry of OH in remote clouds and its role in the production of formic acid and peroxymonosulfate. *Journal of Geophysical Research: Atmospheres*, **91** (D9), 9807–9826, doi:<https://doi.org/10.1029/JD091iD09p09807>.

- , 1999: *Introduction to Atmospheric Chemistry*. Princeton University Press.
- Jain, S., 2014: *Fundamentals of Physical Geology*. Springer Verlag.
- Jensen, E. J., S. Woods, R. P. Lawson, T. P. Bui, L. Pfister, T. D. Thornberry, A. W. Rollins, J.-P. Vernier, L. L. Pan, S. Honomichl, and O. B. Toon, 2018: Ash Particles Detected in the Tropical Lower Stratosphere. *Geophysical Research Letters*, **45** (20), 11,483–11,489, doi:<https://doi.org/10.1029/2018GL079605>.
- Johnson, B., K. Turnbull, P. Brown, R. Burgess, J. Dorsey, A. J. Baran, H. Webster, J. Haywood, R. Cotton, Z. Ulanowski, E. Hesse, A. Woolley, and P. Rosenberg, 2012: In situ observations of volcanic ash clouds from the FAAM aircraft during the eruption of Eyjafjallajökull in 2010. *Journal of Geophysical Research: Atmospheres*, **117** (D20), doi:<https://doi.org/10.1029/2011JD016760>.
- Joseph, E. P., M. Camejo-Harry, T. Christopher, R. Contreras-Arratia, S. Edwards, O. Graham, M. Johnson, A. Juman, J. L. Latchman, L. Lynch, V. L. Miller, I. Papadopoulos, K. Pascal, R. Robertson, G. A. Ryan, A. Stinton, R. Grandin, I. Hamling, M.-J. Jo, J. Barclay, P. Cole, B. V. Davies, and R. S. J. Sparks, 2022: Responding to eruptive transitions during the 2020–2021 eruption of La Soufrière volcano, St. Vincent. *Nature Communications*, **13** (1), 4129, doi:[10.1038/s41467-022-31901-4](https://doi.org/10.1038/s41467-022-31901-4).
- Jourdain, L., T. J. Roberts, M. Pirre, and B. Josse, 2016: Modeling the reactive halogen plume from Ambrym and its impact on the troposphere with the CCATT-BRAMS mesoscale model. *Atmospheric Chemistry and Physics*, **16** (18), 12 099–12 125, doi:[10.5194/acp-16-12099-2016](https://doi.org/10.5194/acp-16-12099-2016).
- Ka-Band Cloud Radar, 2022: Ka-Band Cloud Radar. URL <https://wiki.mpimet.mpg.de/doku.php?id=observations:bco:cloudradars:coralradar>.
- Kahn, R. A., P. Banerjee, and D. McDonald, 2001: Sensitivity of multiangle imaging to natural mixtures of aerosols over ocean. *Journal of Geophysical Research: Atmospheres*, **106** (D16), 18 219–18 238.
- Kahn, R. A. and B. J. Gaitley, 2015: An analysis of global aerosol type as retrieved by MISR. *Journal of Geophysical Research: Atmospheres*, **120** (9), 4248–4281, doi:<https://doi.org/10.1002/2015JD023322>.
- Kahn, R. A. and J. Limbacher, 2012: Eyjafjallajökull volcano plume particle-type characterization from space-based multi-angle imaging. *Atmospheric Chemistry and Physics*, **12** (20), 9459–9477, doi:[10.5194/acp-12-9459-2012](https://doi.org/10.5194/acp-12-9459-2012).
- Kerminen, V.-M. and A. S. Wexler, 1995: The interdependence of aerosol processes and mixing in point source plumes. *Atmospheric Environment*, **29** (3), 361–375, doi:[https://doi.org/10.1016/1352-2310\(94\)00262-J](https://doi.org/10.1016/1352-2310(94)00262-J).
- Klingebiel, M., V. P. Ghate, A. K. Naumann, F. Ditas, M. L. Pöhlker, C. Pöhlker, K. Kandler, H. Konow, and B. Stevens, 2019: Remote Sensing of Sea Salt Aerosol below Trade Wind Clouds. *Journal of the Atmospheric Sciences*, **76** (5), 1189 – 1202, doi:[10.1175/JAS-D-18-0139.1](https://doi.org/10.1175/JAS-D-18-0139.1).
- Kloss, C., G. Berthet, P. Sellitto, F. Ploeger, G. Taha, M. Tidiga, M. Eremenko, A. Bossolasco, F. Jégou, J.-B. Renard, and B. Legras, 2021: Stratospheric aerosol layer perturbation caused by the 2019 Raikoke and Ulawun eruptions and their radiative forcing. *Atmospheric Chemistry and Physics*, **21** (1), 535–560, doi:[10.5194/acp-21-535-2021](https://doi.org/10.5194/acp-21-535-2021).

- Koyaguchi, T. and A. W. Woods, 1996: On the formation of eruption columns following explosive mixing of magma and surface-water. *Journal of Geophysical Research: Solid Earth*, **101 (B3)**, 5561–5574, doi:<https://doi.org/10.1029/95JB01687>.
- Kraus, H., 2004: *Die Atmosphäre der Erde*. 3d ed., Springer Berlin, Heidelberg.
- Lachatre, M., S. Mailler, L. Menut, A. Cholakian, P. Sellitto, G. Siour, H. Guermazi, G. Salerno, and S. Giammanco, 2022: Modelling SO₂ conversion into sulphates in the mid-troposphere with a 3D chemistry-transport model: the case of Mount Etna's eruption on April 12, 2012. *Atmospheric Chemistry and Physics Discussions*, **2022**, 1–27, doi:10.5194/acp-2021-1025, URL <https://acp.copernicus.org/preprints/acp-2021-1025/>, in review.
- Lamarque, J.-F., L. K. Emmons, P. G. Hess, D. E. Kinnison, S. Tilmes, F. Vitt, C. L. Heald, E. A. Holland, P. H. Lauritzen, J. Neu, J. J. Orlando, P. J. Rasch, and G. K. Tyndall, 2012: CAM-chem: description and evaluation of interactive atmospheric chemistry in the Community Earth System Model. *Geoscientific Model Development*, **5 (2)**, 369–411, doi:10.5194/gmd-5-369-2012.
- Lasne, J., D. Urupina, E. C. Maters, P. Delmelle, M. N. Romanias, and F. Thevenet, 2022: Photo-enhanced uptake of SO₂ on Icelandic volcanic dusts. *Environ. Sci.: Atmos.*, **2**, 375–387, doi:10.1039/D1EA00094B.
- LeGrande, A. N., K. Tsigaridis, and S. E. Bauer, 2016: Role of atmospheric chemistry in the climate impacts of stratospheric volcanic injections. *Nature Geoscience*, **9 (9)**, 652–655, doi:10.1038/ngeo2771, URL <https://doi.org/10.1038/ngeo2771>.
- Li, L., Z. M. Chen, Y. H. Zhang, T. Zhu, J. L. Li, and J. Ding, 2006: Kinetics and mechanism of heterogeneous oxidation of sulfur dioxide by ozone on surface of calcium carbonate. *Atmospheric Chemistry and Physics*, **6 (9)**, 2453–2464, doi:10.5194/acp-6-2453-2006.
- Liang, J. and M. Z. Jacobson, 1999: A study of sulfur dioxide oxidation pathways over a range of liquid water contents, pH values, and temperatures. *Journal of Geophysical Research: Atmospheres*, **104 (D11)**, 13 749–13 769, doi:<https://doi.org/10.1029/1999JD900097>.
- Limbacher, J. A. and R. A. Kahn, 2014: MISR research-aerosol-algorithm refinements for dark water retrievals. *Atmospheric Measurement Techniques*, **7 (11)**, 3989–4007, doi:10.5194/amt-7-3989-2014, URL <https://amt.copernicus.org/articles/7/3989/2014/>.
- Liou, K. N., 2002: *An Introduction to Atmospheric Radiation*. 2d ed., Academic Press.
- Lohmann, U., F. Lüönd, and F. Mahrt, 2016: *An Introduction to Clouds: From the Microscale to Climate*. Cambridge University Press.
- Luterbacher, J. and C. Pfister, 2015: The year without a summer. *Nature Geoscience*, **8 (4)**, 246–248, doi:10.1038/ngeo2004.
- Malavelle, F. F., J. M. Haywood, A. Jones, A. Gettelman, L. Clarisse, S. Bauduin, J. E. Allan, L. Oreopoulos, N. Cho, D. Lee, N. Bellouin, O. Boucher, D. P. Grosvenor, K. S. Carslaw, S. Dhomse, G. W. Mann, A. Schmidt, H. Coe, M. E. Hartley, M. Dalvi, A. A. Hill, B. T. Johnson, C. E. Johnson, J. R. Knight, F. M. O'Connor,

- D. G. Partridge, P. Stier, G. Myhre, S. Platnick, G. L. Stephens, H. Takahashi, and T. Thordarson, 2017: Strong constraints on aerosol-cloud interactions from volcanic eruptions. *Nature*, **546 (7659)**, 485–491.
- Marshall, L. R., E. C. Maters, A. Schmidt, C. Timmreck, A. Robock, and M. Toohey, 2022: Volcanic effects on climate: recent advances and future avenues. *Bulletin of Volcanology*, **84 (5)**, 54, doi:10.1007/s00445-022-01559-3.
- Marti, A., A. Folch, O. Jorba, and Z. Janjic, 2017: Volcanic ash modeling with the online NMMB-MONARCH-ASH v1.0 model: model description, case simulation, and evaluation. *Atmospheric Chemistry and Physics*, **17 (6)**, 4005–4030, doi:10.5194/acp-17-4005-2017.
- Mastin, L. G., 2007: A user-friendly one-dimensional model for wet volcanic plumes. *Geochemistry, Geophysics, Geosystems*, **8 (3)**, doi:https://doi.org/10.1029/2006GC001455.
- Mastin, L. G., M. Guffanti, R. Servranckx, P. Webley, S. Barsotti, K. Dean, A. Durant, J. W. Ewert, A. Neri, W. I. Rose, D. Schneider, L. Siebert, B. Stunder, G. Swanson, A. Tupper, A. Volentik, and C. F. Waythomas, 2009: A multidisciplinary effort to assign realistic source parameters to models of volcanic ash-cloud transport and dispersion during eruptions. *Journal of Volcanology and Geothermal Research*, **186 (1-2)**, 10–21, doi:10.1016/j.jvolgeores.2009.01.008.
- Maters, E. C., P. Delmelle, M. J. Rossi, and P. M. Ayriss, 2017: Reactive Uptake of Sulfur Dioxide and Ozone on Volcanic Glass and Ash at Ambient Temperature. *Journal of Geophysical Research: Atmospheres*, **122 (18)**, 10,077–10,088, doi:https://doi.org/10.1002/2017JD026993.
- McKee, K., C. M. Smith, K. Reath, E. Snee, S. Maher, R. S. Matoza, S. Carn, L. Mastin, K. Anderson, D. Damby, D. C. Roman, A. Degterev, A. Rybin, M. Chibisova, J. D. Assink, R. de Neri Leiva, and A. Perttu, 2021: Evaluating the state-of-the-art in remote volcanic eruption characterization Part I: Raikoke volcano, Kuril Islands. *Journal of Volcanology and Geothermal Research*, **419**, 107354, doi:https://doi.org/10.1016/j.jvolgeores.2021.107354.
- Mie, G., 1908: Beiträge zur Optik trüber Medien, speziell kolloidaler Metallösungen. *Annalen der Physik*, **330 (3)**, 377–445, doi:https://doi.org/10.1002/andp.19083300302.
- Mills, M. J., J. H. Richter, S. Tilmes, B. Kravitz, D. G. MacMartin, A. A. Glanville, J. J. Tribbia, J.-F. Lamarque, F. Vitt, A. Schmidt, A. Gettelman, C. Hannay, J. T. Bacmeister, and D. E. Kinnison, 2017: Radiative and Chemical Response to Interactive Stratospheric Sulfate Aerosols in Fully Coupled CESM1(WACCM). *Journal of Geophysical Research: Atmospheres*, **122 (23)**, 13,061–13,078, doi:https://doi.org/10.1002/2017JD027006.
- Mishchenko, M. I., A. A. Lacis, B. E. Carlson, and L. D. Travis, 1995: Nonsphericity of dust-like tropospheric aerosols: Implications for aerosol remote sensing and climate modeling. *Geophysical Research Letters*, **22 (9)**, 1077–1080, doi:https://doi.org/10.1029/95GL00798.
- Mishchenko, M. I., L. D. Travis, R. A. Kahn, and R. A. West, 1997: Modeling phase functions for dustlike tropospheric aerosols using a shape mixture of randomly oriented polydisperse spheroids. *Journal of Geophysical Research: Atmospheres*, **102 (D14)**, 16 831–16 847, doi:https://doi.org/10.1029/96JD02110.

- Mitra, A., L. Di Girolamo, Y. Hong, Y. Zhan, and K. J. Mueller, 2021: Assessment and Error Analysis of Terra-MODIS and MISR Cloud-Top Heights Through Comparison With ISS-CATS Lidar. *Journal of Geophysical Research: Atmospheres*, **126** (9), e2020JD034281, doi:<https://doi.org/10.1029/2020JD034281>.
- Mlawer, E. J., S. J. Taubman, P. D. Brown, M. J. Iacono, and S. A. Clough, 1997: Radiative transfer for inhomogeneous atmospheres: RRTM, a validated correlated-k model for the longwave. *Journal of Geophysical Research: Atmospheres*, **102** (D14), 16 663–16 682, doi:<https://doi.org/10.1029/97JD00237>.
- Morton, B. R., G. Taylor, and J. S. Turner, 1956: Turbulent Gravitational Convection from Maintained and Instantaneous Sources. *Proceedings of the Royal Society of London Series A*, **234** (1196), 1–23, doi:[10.1098/rspa.1956.0011](https://doi.org/10.1098/rspa.1956.0011).
- MPI-M, 2021: Data from the BCO during the time-period of the Soufrière eruption. URL <https://observations.mpimet.mpg.de/repository/entry/show?entryid=656dc652-e02f-43c9-9378-7307a5143377>, last access: 2022/10/27.
- Muser, L. O., 2022: Combining Aerosol Aging and Data Assimilation for Improving Volcanic Aerosol Forecast. Ph.D. thesis, Karlsruher Institut für Technologie (KIT).
- Muser, L. O., G. A. Hoshyaripour, J. Bruckert, A. Horváth, E. Malinina, S. Wallis, F. J. Prata, A. Rozanov, C. von Savigny, H. Vogel, and B. Vogel, 2020: Particle aging and aerosol–radiation interaction affect volcanic plume dispersion: evidence from the Raikoke 2019 eruption. *Atmospheric Chemistry and Physics*, **20** (23), 15 015–15 036, doi:[10.5194/acp-20-15015-2020](https://doi.org/10.5194/acp-20-15015-2020).
- Muth, L. J., 2019: Simulation of primary and secondary aerosols of the Mt. Pinatubo eruption 1991 and their radiative effects. Master’s thesis, Karlsruher Institut für Technologie (KIT).
- Nelson, D. L., Y. Chen, R. A. Kahn, D. J. Diner, and D. Mazzoni, 2008: Example applications of the MISR INteractive eXplorer (MINX) software tool to wildfire smoke plume analyses. *Remote Sensing of Fire: Science and Application*, Hao, W. M., Ed., International Society for Optics and Photonics, SPIE, Vol. 7089, 65 – 75.
- Nelson, D. L., M. J. Garay, R. A. Kahn, and B. A. Dunst, 2013: Stereoscopic Height and Wind Retrievals for Aerosol Plumes with the MISR INteractive eXplorer (MINX). *Remote Sensing*, **5** (9), 4593–4628, doi:[10.3390/rs5094593](https://doi.org/10.3390/rs5094593).
- Nenes, A., S. N. Pandis, and C. Pilinis, 1998: ISORROPIA: A New Thermodynamic Equilibrium Model for Multiphase Multicomponent Inorganic Aerosols. *Aquatic Geochemistry*, **4** (1), 123–152, doi:[10.1023/A:1009604003981](https://doi.org/10.1023/A:1009604003981).
- Niemeier, U., F. Riede, and C. Timmreck, 2021: Simulation of ash clouds after a Laacher See-type eruption. *Climate of the Past*, **17** (2), 633–652, doi:[10.5194/cp-17-633-2021](https://doi.org/10.5194/cp-17-633-2021).
- Niemeier, U., C. Timmreck, H.-F. Graf, S. Kinne, S. Rast, and S. Self, 2009: Initial fate of fine ash and sulfur from large volcanic eruptions. *Atmospheric Chemistry and Physics*, **9** (22), 9043–9057, doi:[10.5194/acp-9-9043-2009](https://doi.org/10.5194/acp-9-9043-2009).

- Oberhuber, J. M., M. Herzog, H.-F. Graf, and K. Schwanke, 1998: Volcanic plume simulation on large scales. *Journal of Volcanology and Geothermal Research*, **87** (1), 29–53, doi:https://doi.org/10.1016/S0377-0273(98)00099-7.
- Pattantyus, A. K., S. Businger, and S. G. Howell, 2018: Review of sulfur dioxide to sulfate aerosol chemistry at Kīlauea Volcano, Hawai‘i. *Atmospheric Environment*, **185**, 262–271, doi:https://doi.org/10.1016/j.atmosenv.2018.04.055.
- Petty, G. W., 2004: *A First Course in Atmospheric Radiation*. Sundog Publishing.
- Plu, M., G. Bigeard, B. Sič, E. Emili, L. Bugliaro, L. El Amraoui, J. Guth, B. Josse, L. Mona, and D. Piontek, 2021: Modelling the volcanic ash plume from Eyjafjallajökull eruption (May 2010) over Europe: evaluation of the benefit of source term improvements and of the assimilation of aerosol measurements. *Natural Hazards and Earth System Sciences*, **21** (12), 3731–3747, doi:10.5194/nhess-21-3731-2021.
- Pollack, J. B., O. B. Toon, and B. N. Khare, 1973: Optical properties of some terrestrial rocks and glasses. *Icarus*, **19** (3), 372–389, doi:https://doi.org/10.1016/0019-1035(73)90115-2.
- Prata, A., W. Rose, S. Self, and D. O’Brien, 2004: *Global, Long-Term Sulphur Dioxide Measurements from TOVS Data: A New Tool for Studying Explosive Volcanism and Climate*, 75–92. American Geophysical Union (AGU), doi:https://doi.org/10.1029/139GM05.
- Prata, F., M. Woodhouse, H. E. Huppert, A. Prata, T. Thordarson, and S. Carn, 2017: Atmospheric processes affecting the separation of volcanic ash and SO₂ in volcanic eruptions: Inferences from the May 2011 Grímsvötn eruption. *Atmospheric Chemistry and Physics*, **17** (17), 10 709–10 732, doi:10.5194/acp-17-10709-2017.
- Rieger, D., 2016: Der Einfluss von natürlichem Aerosol auf Wolken über Mitteleuropa. Ph.D. thesis, Karlsruher Institut für Technologie (KIT).
- Rieger, D., M. Bangert, I. Bischoff-Gauss, J. Förstner, K. Lundgren, D. Reinert, J. Schröter, H. Vogel, G. Zängl, R. Ruhnke, and B. Vogel, 2015: ICON–ART 1.0 – a new online-coupled model system from the global to regional scale. *Geoscientific Model Development*, **8** (6), 1659–1676, doi:10.5194/gmd-8-1659-2015.
- Rieger, D., M. Köhler, R. J. Hogan, S. A. K. Schäfer, A. Seifert, A. de Lozar, and G. Zängl, 2019: ecRad in ICON - Details on the Implementation and First Results. *Reports on ICON*, **4**, doi:10.5676/DWD_pub/nwv/icon_004.
- Riemer, N., 2002: Numerische Simulationen zur Wirkung des Aerosols auf die troposphärische Chemie und die Sichtweite. Ph.D. thesis, Universität Karlsruhe (TH).
- Riemer, N., H. Vogel, B. Vogel, and F. Fiedler, 2003: Modeling aerosols on the mesoscale- γ : Treatment of soot aerosol and its radiative effects. *Journal of Geophysical Research: Atmospheres*, **108** (D19), doi:https://doi.org/10.1029/2003JD003448.
- Riley, C. M., W. I. Rose, and G. J. S. Bluth, 2003: Quantitative shape measurements of distal volcanic ash. *Journal of Geophysical Research: Solid Earth*, **108** (B10).
- Robock, A., 2000: Volcanic eruptions and climate. *Reviews of Geophysics*, **38** (2), 191–219, doi:https://doi.org/10.1029/1998RG000054.

- Rose, W. and A. Durant, 2009: Fine ash content of explosive eruptions. *Journal of Volcanology and Geothermal Research*, **186** (1), 32–39, doi:<https://doi.org/10.1016/j.jvolgeores.2009.01.010>, improved Prediction and Tracking of Volcanic Ash Clouds.
- Rosen, J. M., 1971: The Boiling Point of Stratospheric Aerosols. *Journal of Applied Meteorology and Climatology*, **10** (5), 1044 – 1046, doi:[10.1175/1520-0450\(1971\)010<1044:TBPOSA>2.0.CO;2](https://doi.org/10.1175/1520-0450(1971)010<1044:TBPOSA>2.0.CO;2).
- Sander, R., A. Baumgaertner, S. Gromov, H. Harder, P. Jöckel, A. Kerkweg, D. Kubistin, E. Regelin, H. Riede, A. Sandu, D. Taraborrelli, H. Tost, and Z.-Q. Xie, 2011: The atmospheric chemistry box model CAABA/MECCA-3.0. *Geoscientific Model Development*, **4** (2), 373–380, doi:[10.5194/gmd-4-373-2011](https://doi.org/10.5194/gmd-4-373-2011).
- Sandu, A. and R. Sander, 2006: Technical note: Simulating chemical systems in Fortran90 and Matlab with the Kinetic PreProcessor KPP-2.1. *Atmospheric Chemistry and Physics*, **6** (1), 187–195, doi:[10.5194/acp-6-187-2006](https://doi.org/10.5194/acp-6-187-2006).
- Sandu, A., J. Verwer, J. G. Blom, E. J. Spee, G. R. Carmichael, and F. A. Potra, 1997: Benchmarking stiff ode solvers for atmospheric chemistry problems II: Rosenbrock solvers. *Atmospheric Environment*, **31** (20), 3459–3472, doi:[https://doi.org/10.1016/S1352-2310\(97\)83212-8](https://doi.org/10.1016/S1352-2310(97)83212-8).
- Schmauss, D. and H. Keppler, 2014: Adsorption of sulfur dioxide on volcanic ashes. *American Mineralogist*, **99** (5-6), 1085–1094, doi:[doi:10.2138/am.2014.4656](https://doi.org/10.2138/am.2014.4656).
- Schmincke, H.-U., 2004: *Volcanism*. Springer Verlag.
- Schneider, D. J., W. I. Rose, L. R. Coke, G. J. S. Bluth, I. E. Sprod, and A. J. Krueger, 1999: Early evolution of a stratospheric volcanic eruption cloud as observed with TOMS and AVHRR. *Journal of Geophysical Research: Atmospheres*, **104** (D4), 4037–4050, doi:<https://doi.org/10.1029/1998JD200073>.
- Schröter, J., D. Rieger, C. Stassen, H. Vogel, M. Weimer, S. Werchner, J. Förstner, F. Prill, D. Reinert, G. Zängl, M. Giorgetta, R. Ruhnke, B. Vogel, and P. Braesicke, 2018: ICON-ART 2.1: a flexible tracer framework and its application for composition studies in numerical weather forecasting and climate simulations. *Geoscientific Model Development*, **11** (10), 4043–4068, doi:[10.5194/gmd-11-4043-2018](https://doi.org/10.5194/gmd-11-4043-2018).
- Schurer, A. P., G. C. Hegerl, J. Luterbacher, S. Brönnimann, T. Cowan, S. F. B. Tett, D. Zanchettin, and C. Timmermann, 2019: Disentangling the causes of the 1816 European year without a summer. *Environmental Research Letters*, **14** (9), 094019, doi:[10.1088/1748-9326/ab3a10](https://doi.org/10.1088/1748-9326/ab3a10).
- Schwartz, S. E., 1986: Mass-Transport Considerations Pertinent to Aqueous Phase Reactions of Gases in Liquid-Water Clouds. *Chemistry of Multiphase Atmospheric Systems*, Jaeschke, W., Ed., Springer Berlin Heidelberg, 415–471.
- Scollo, S., A. Folch, and A. Costa, 2008: A parametric and comparative study of different tephra fallout models. *Journal of Volcanology and Geothermal Research*, **176** (2), 199–211, doi:[10.1016/j.jvolgeores.2008.04.002](https://doi.org/10.1016/j.jvolgeores.2008.04.002).
- Scollo, S., R. A. Kahn, D. L. Nelson, M. Coltelli, D. J. Diner, M. J. Garay, and V. J. Realmuto, 2012: MISR observations of Etna volcanic plumes. *Journal of Geophysical Research: Atmospheres*, **117** (D6), doi:<https://doi.org/10.1029/2011JD016625>.

- Seinfeld, J. H. and S. N. Pandis, 2006: *Atmospheric Chemistry and Physics: From Air Pollution to Climate Change*. 2d ed., John Wiley & Sons.
- Sioris, C. E., A. Malo, C. A. McLinden, and R. D'Amours, 2016a: Direct injection of water vapor into the stratosphere by volcanic eruptions. *Geophysical Research Letters*, **43** (14), 7694–7700, doi:<https://doi.org/10.1002/2016GL069918>.
- Sioris, C. E., J. Zou, C. T. McElroy, C. D. Boone, P. E. Sheese, and P. F. Bernath, 2016b: Water vapour variability in the high-latitude upper troposphere – Part 2: Impact of volcanic eruptions. *Atmospheric Chemistry and Physics*, **16** (4), 2207–2219, doi:10.5194/acp-16-2207-2016.
- Solomon, S., 1999: Stratospheric ozone depletion: A review of concepts and history. *Reviews of Geophysics*, **37** (3), 275–316, doi:<https://doi.org/10.1029/1999RG900008>.
- Solomon, S., R. W. Portmann, R. R. Garcia, L. W. Thomason, L. R. Poole, and M. P. McCormick, 1996: The role of aerosol variations in anthropogenic ozone depletion at northern midlatitudes. *Journal of Geophysical Research: Atmospheres*, **101** (D3), 6713–6727, doi:<https://doi.org/10.1029/95JD03353>.
- Sparks, R., M. Burski, S. Carey, J. Gilbert, L. Glaze, H. Sigurdsson, and A. Woods, 1997: *Volcanic Plumes*. Wiley.
- Spence, R. J., I. Kelman, E. Calogero, G. Toyos, P. J. Baxter, and J. C. Komorowski, 2005: Modelling expected physical impacts and human casualties from explosive volcanic eruptions. *Natural Hazards and Earth System Science*, **5** (6), 1003–1015, doi:10.5194/nhess-5-1003-2005.
- Steinke, I., O. Möhler, A. Kiselev, M. Niemand, H. Saathoff, M. Schnaiter, J. Skrotzki, C. Hoose, and T. Leisner, 2011: Ice nucleation properties of fine ash particles from the Eyjafjallajökull eruption in April 2010. *Atmospheric Chemistry and Physics*, **11** (24), 12 945–12 958, doi:10.5194/acp-11-12945-2011.
- Stenchikov, G., A. Ukhov, S. Osipov, R. Ahmadov, G. Grell, K. Cady-Pereira, E. Mlawer, and M. Iacono, 2021: How Does a Pinatubo-Size Volcanic Cloud Reach the Middle Stratosphere? *Journal of Geophysical Research: Atmospheres*, **126** (10), e2020JD033 829, doi:<https://doi.org/10.1029/2020JD033829>.
- Stevens, B., D. Farrell, L. Hirsch, F. Jansen, L. Nuijens, I. Serikov, B. Brüggemann, M. Forde, H. Linne, K. Lonitz, and J. M. Prospero, 2016: The Barbados Cloud Observatory: Anchoring Investigations of Clouds and Circulation on the Edge of the ITCZ. *Bulletin of the American Meteorological Society*, **97** (5), 787 – 801, doi:10.1175/BAMS-D-14-00247.1.
- Stewart, C., D. Johnston, G. Leonard, C. Horwell, T. Thordarson, and S. Cronin, 2006: Contamination of water supplies by volcanic ashfall: A literature review and simple impact modelling. *Journal of Volcanology and Geothermal Research*, **158**, 296–306.
- Stockwell, W. R. and J. G. Calvert, 1983: The mechanism of the HO-SO₂ reaction. *Atmospheric Environment* (1967), **17** (11), 2231–2235, doi:[https://doi.org/10.1016/0004-6981\(83\)90220-2](https://doi.org/10.1016/0004-6981(83)90220-2).
- Stommel, H. and E. Stommel, 1979: The Year without a Summer. *Scientific American*, **240** (6), 176–187.
- Stothers, R. B., 1984: The Great Tambora Eruption in 1815 and its Aftermath. *Science*, **224** (4654), 1191–1198.

- Stuefer, M., S. R. Freitas, G. Grell, P. Webley, S. Peckham, and S. a. McKeen, 2012: Inclusion of Ash and SO₂ emissions from volcanic eruptions in WRF-CHEM: development and some applications. *Geoscientific Model Development Discussions*, **5** (3), 2571–2597, doi:10.5194/gmdd-5-2571-2012.
- Suzuki, T., 1983: A Theoretical Model for Dispersion of Tephra. *Arc Volcanism: Physics and Tectonics*, 95–113.
- Tabazadeh, A. and R. P. Turco, 1993: Stratospheric Chlorine Injection by Volcanic Eruptions: HCl Scavenging and Implications for Ozone. *Science*, **260** (5111), 1082–1086, doi:10.1126/science.260.5111.1082.
- Tarcea, N., 2004: Light as a universal tool : Microcapsule sizing by elastic light scattering and mineral investigation by in situ Raman spectroscopy. doctoralthesis, Universität Würzburg.
- Tate, P. M. and J. H. Middleton, 2000: Unification Of Non-Dimensional Solutions To Asymptotic Equations For Plumes Of Different Shape. *Boundary-Layer Meteorology*, **94** (2), 225–251, doi:10.1023/A:1002431928523.
- Textor, C., H.-F. Graf, M. Herzog, and J. M. Oberhuber, 2003: Injection of gases into the stratosphere by explosive volcanic eruptions. *Journal of Geophysical Research: Atmospheres*, **108** (D19), doi:https://doi.org/10.1029/2002JD002987.
- Textor, C., H. F. Graf, A. Longo, A. Neri, T. E. Ongaro, P. Papale, C. Timmreck, and G. Ernst, 2005: Numerical simulation of explosive volcanic eruptions from the conduit flow to global atmospheric scales. *Annals of Geophysics*, **48**, 817–842.
- Thomas, H. E. and A. J. Prata, 2011: Sulphur dioxide as a volcanic ash proxy during the April–May 2010 eruption of Eyjafjallajökull Volcano, Iceland. *Atmospheric Chemistry and Physics*, **11** (14), 6871–6880, doi:10.5194/acp-11-6871-2011.
- Tiedtke, M., 1989: A Comprehensive Mass Flux Scheme for Cumulus Parameterization in Large-Scale Models. *Monthly Weather Review*, **117** (8), 1779 – 1800, doi:10.1175/1520-0493(1989)117<1779:ACMFSF>2.0.CO;2.
- Timmreck, C., 2012: Modeling the climatic effects of large explosive volcanic eruptions. *WIREs Climate Change*, **3** (6), 545–564, doi:https://doi.org/10.1002/wcc.192.
- Toon, O. B. and T. P. Ackerman, 1981: Algorithms for the calculation of scattering by stratified spheres. *Appl. Opt.*, **20** (20), 3657–3660, doi:10.1364/AO.20.003657.
- Troe, J., 1983: Specific rate constants k(E, J) for unimolecular bond fissions. *The Journal of Chemical Physics*, **79** (12), 6017–6029, doi:10.1063/1.445784, URL <https://doi.org/10.1063/1.445784>, <https://doi.org/10.1063/1.445784>.
- Twomey, S., 1974: Pollution and the planetary albedo. *Atmospheric Environment (1967)*, **8** (12), 1251–1256, doi:https://doi.org/10.1016/0004-6981(74)90004-3.
- Urupina, D., J. Lasne, M. Romanias, V. Thiery, P. Dagsson-Waldhauserova, and F. Thevenet, 2019: Uptake and surface chemistry of SO₂ on natural volcanic dusts. *Atmospheric Environment*, **217**, 116942, doi:https://doi.org/10.1016/j.atmosenv.2019.116942.

- Usher, C. R., H. Al-Hosney, S. Carlos-Cuellar, and V. H. Grassian, 2002: A laboratory study of the heterogeneous uptake and oxidation of sulfur dioxide on mineral dust particles. *Journal of Geophysical Research: Atmospheres*, **107** (D23), ACH 16–1–ACH 16–9, doi:https://doi.org/10.1029/2002JD002051.
- van Eaton, A. R., J. D. Muirhead, C. J. Wilson, and C. Cimarelli, 2012: Growth of volcanic ash aggregates in the presence of liquid water and ice: An experimental approach. *Bulletin of Volcanology*, **74** (9), 1963–1984, doi:10.1007/s00445-012-0634-9.
- von Savigny, C., C. Timmreck, S. A. Buehler, J. P. Burrows, M. Giorgetta, G. Hegerl, A. Horvath, G. A. Hoshyaripour, C. Hoose, J. Quaas, E. Malinina, A. Rozanov, H. Schmidt, L. Thomason, M. Toohey, and B. Vogel, 2020: The Research Unit VolImpact: Revisiting the volcanic impact on atmosphere and climate ? preparations for the next big volcanic eruption. *Meteorologische Zeitschrift*, **29** (1), 3–18, doi:10.1127/metz/2019/0999.
- Walter, C., 2019: Simulationen der Ausbreitung von Vulkanasche unter expliziter Berücksichtigung der optischen Eigenschaften der Aschepartikel. Ph.D. thesis, Karlsruher Institut für Technologie (KIT).
- Wardman, J. B., T. M. Wilson, P. S. Bodger, J. W. Cole, and C. Stewart, 2012: Potential impacts from tephra fall to electric power systems: A review and mitigation strategies. *Bulletin of Volcanology*, **74** (10), 2221–2241, doi:10.1007/s00445-012-0664-3.
- Webster, H. N., D. J. Thomson, B. T. Johnson, I. P. C. Heard, K. Turnbull, F. Marengo, N. I. Kristiansen, J. Dorsey, A. Minikin, B. Weinzierl, U. Schumann, R. S. J. Sparks, S. C. Loughlin, M. C. Hort, S. J. Leadbetter, B. J. Devenish, A. J. Manning, C. S. Witham, J. M. Haywood, and B. W. Golding, 2012: Operational prediction of ash concentrations in the distal volcanic cloud from the 2010 Eyjafjallajökull eruption. *Journal of Geophysical Research: Atmospheres*, **117** (D20), doi:https://doi.org/10.1029/2011JD016790.
- Weimer, M., J. Schröter, J. Eckstein, K. Deetz, M. Neumaier, G. Fischbeck, L. Hu, D. B. Millet, D. Rieger, H. Vogel, B. Vogel, T. Reddmann, O. Kirner, R. Ruhnke, and P. Braesicke, 2017: An emission module for ICON-ART 2.0: implementation and simulations of acetone. *Geoscientific Model Development*, **10** (6), 2471–2494, doi:10.5194/gmd-10-2471-2017.
- Weingartner, E., H. Burtscher, and U. Baltensperger, 1997: Hygroscopic properties of carbon and diesel soot particles. *Atmospheric Environment*, **31** (15), 2311–2327, doi:https://doi.org/10.1016/S1352-2310(97)00023-X.
- Wernli, H., C. Hofmann, and M. Zimmer, 2009: Spatial Forecast Verification Methods Intercomparison Project: Application of the SAL Technique. *Weather and Forecasting*, **24** (6), 1472 – 1484, doi:10.1175/2009WAF2222271.1.
- Wernli, H., M. Paulat, M. Hagen, and C. Frei, 2008: SAL—A Novel Quality Measure for the Verification of Quantitative Precipitation Forecasts. *Monthly Weather Review*, **136** (11), 4470 – 4487, doi:10.1175/2008MWR2415.1.
- Whitby, E., P. McMurry, U. Shankar, and F. Binkowski, 1991: Modal Aerosol Dynamics Modeling. *Aerosol Science and Technology*.
- Whitby, K. T., 1978: The physical characteristics of sulfur aerosols. *Atmospheric Environment (1967)*, **12** (1), 135–159, doi:https://doi.org/10.1016/0004-6981(78)90196-8, proceedings of the International Symposium.

- Winker, D. M., M. A. Vaughan, A. Omar, Y. Hu, K. A. Powell, Z. Liu, W. H. Hunt, and S. A. Young, 2009: Overview of the CALIPSO Mission and CALIOP Data Processing Algorithms. *Journal of Atmospheric and Oceanic Technology*, **26** (11), 2310 – 2323, doi:10.1175/2009JTECHA1281.1.
- Woodhouse, M. J., A. J. Hogg, J. C. Phillips, and R. S. J. Sparks, 2013: Interaction between volcanic plumes and wind during the 2010 Eyjafjallajökull eruption, Iceland. *Journal of Geophysical Research: Solid Earth*, **118** (1), 92–109, doi:10.1029/2012JB009592.
- Woods, A. W., 1993: Moist convection and the injection of volcanic ash into the atmosphere. *Journal of Geophysical Research: Solid Earth*, **98** (B10), 17 627–17 636, doi:https://doi.org/10.1029/93JB00718.
- Zängl, G., D. Reinert, P. Rípodas, and M. Baldauf, 2015: The ICON (ICOsahedral Non-hydrostatic) modelling framework of DWD and MPI-M: Description of the non-hydrostatic dynamical core. *Quarterly Journal of the Royal Meteorological Society*, **141** (687), 563–579, doi:10.1002/qj.2378.
- Zhu, Y., O. B. Toon, E. J. Jensen, C. G. Bardeen, M. J. Mills, M. A. Tolbert, P. Yu, and S. Woods, 2020: Persisting volcanic ash particles impact stratospheric SO₂ lifetime and aerosol optical properties. *Nature Communications*, **11** (1), 1–11, doi:10.1038/s41467-020-18352-5.

F. List of figures

1.1	Schematic illustration of important processes in volcanic plumes and the impact on the atmosphere.	1
1.2	Schematic illustration of the chemical processes in tropospheric volcanic plumes. Taken from Galeazzo et al. (2018).	7
2.1	Schematic illustration displaying the processes relevant for volcanic aerosols.	9
2.2	Plume regions for large volcanic eruptions and related dynamic processes.	11
2.3	Vertical profiles of temperature, velocity, plume and air density, and fraction of air for the 2019 Raikoke eruption.	12
2.4	Scattering regimes as a function of particle size and wavelength adapted from Petty (2004).	24
3.1	Schematic illustration explaining the coupling between the ICON-ART model and the 1-D plume rise model FPlume.	30
3.2	Optical properties of volcanic ash modes at different wavelengths from Muser et al. (2020).	38
5.1	Raikoke plume height and MER of very fine ash.	52
5.2	Raikoke emission profiles for different phases and assumptions in other studies.	53
5.3	Raikoke daily mean column loadings for ash and SO ₂ .	54
5.4	Raikoke temporal evolution of the very fine ash amount in different experiments and observations from Himawari-8.	55
5.5	Ash and SO ₂ SAL values for the FPlume-rad experiment.	56
5.6	Effects of aerosol–radiation interaction on the plume top height and mass-averaged height for ash, SO ₂ , and sulfate.	58
5.7	Temporal evolution of the vertical distribution of ash and SO ₂ and the characteristic ash radius in FPlume-rad and FPlume-norad.	60
6.1	La Soufrière simulation setup with a global R3B07 domain and two nests around the volcano.	63
6.2	La Soufrière plume heights and MERs of very fine ash.	64
6.3	Comparison of BCO equivalent radar reflectivity and ICON-ART ash concentration.	65
6.4	La Soufrière 24 h-averages for ash, coated ash, SO ₂ , and sulfate column loadings.	67
6.5	La Soufrière temporal evolution of the very fine ash, SO ₂ , and sulfate mass.	67
6.6	Comparison of ICON-ART plume heights and MISR MINX retrieval heights.	68
6.7	Comparison between MISR RA and ICON-ART aerosol properties (AOD, fraction of spherical particles, SSA).	70
6.8	Comparison of CALIPSO and ICON-ART total attenuated backscatter and aerosol aging on 13 April 2021 at 5 UTC.	73

6.9	ICON-ART height-longitude cross-section for spherical mass fraction, mixed mass fraction, accumulation and coarse mode mass fractions.	75
7.1	R2B10 LAM area for the Raikoke chemistry experiment.	77
7.2	Temporal development of the mass burden for different chemical species and ash in different experiments after the 2019 Raikoke eruption.	79
7.3	12 h-averaged column loadings of gaseous SO ₂ , S(VI), S(IV), and liquid water on coated aerosols in different experiments.	80
7.4	Time–height cross-sections of horizontally-integrated concentration of SO ₂ (g), S(VI), S(IV), and liquid water on coated aerosols in different experiments with and without aqueous-phase chemistry. 81	
7.5	Time–height cross-section of the horizontally-averaged aerosol shell pH value and the ambient temperature.	82
7.6	Time–height cross-section of horizontally-integrated gaseous SO ₂ (g), S(VI), S(IV), and liquid water on coated aerosols in different experiments with and without adsorption as SO ₂ by ash particles.	83
7.7	As Figure 7.2, but only for the ADSORPTION experiment (solid) and an experiment with gas-phase chemistry and SO ₂ -adsorption on ash assuming the uptake coefficient from Zhu et al. (2020) (dashed).	85
7.8	Time–height cross-section of horizontally-averaged OH, O ₃ , and CH ₄ concentrations	86
C.1	Meteorological conditions above the vent in the first 20 h after simulation start to explain variations in the FPlume-derived MER.	105
C.2	Comparison plots for ash and SO ₂ 6 h-averaged column loadings in order to explain the discrepancy between simulated ICON-ART data and Himawari-8 observed data in the SAL analysis. . .	106
C.3	Horizontally-averaged ash particle characteristic radius and horizontal sum of the particle number of the different ash modes.	107
C.4	Height-dependent settling velocity and settling distance for the accumulation, coarse, and giant modes to explain the vertical lines in the BCO radar reflectivity and ICON-ART ash concentrations.108	
C.5	Ash concentration above Barbados split into the different modes.	109
C.6	Additional plots to explain the derivation of the ash-cloud combined heights from ICON-ART. . .	110
C.7	As Figure 6.8, but for 6 UTC on 10 April 2021.	111
C.8	As Figure 6.8, but for 17 UTC on 10 April 2021.	112
C.9	As Figure 6.8, but for 5 UTC on 11 April 2021.	113
C.10	As Figure 6.8, but for 16 UTC on 11 April 2021.	114
C.11	As Figure 6.8, but for 18 UTC on 11 April 2021.	115
C.12	As Figure 6.8, but for 4 UTC on 12 April 2021.	116
C.13	As Figure 6.8, but for 6 UTC on 12 April 2021.	117
C.14	As Figure 6.8, but for 15 UTC on 12 April 2021.	118
C.15	As Figure 6.8, but for 18 UTC on 12 April 2021.	119
C.16	As Figure 6.8, but for 3 UTC on 13 April 2021.	120
C.17	As Figure 6.8, but for 7 UTC on 13 April 2021.	121

G. List of tables

2.1	Changes in the number concentration, mass concentration, and median diameter due to aerosol dynamical processes.	21
3.1	Empirical relationships for the fraction of very fine ash derived by Gouhier et al. (2019).	31
3.2	Soluble and insoluble components available in the different mixing states of the Aitken, accumulation, coarse, and giant modes as considered in this work.	32
7.1	Raikoke chemistry experiments.	78
A.1	Eruption phase and exit conditions as assumed in FPlume for the 2019 Raikoke eruption.	93
A.2	Eruption phase and exit conditions as assumed in FPlume for the 2021 La Soufrière eruption.	95
B.1	Chemical reactions considered in chapter 6	103

Danksagung

An dieser Stelle möchte ich mich bei allen ganz herzlich bedanken die zum Gelingen dieser Arbeit beigetragen haben.

Zuerst gebührt mein Dank Prof. Dr. Corinna Hoose für die Betreuung und Begutachtung dieser Arbeit. Danke für Deine konstruktiven Anmerkungen, Anregungen und Ratschläge während der gesamten Zeit meiner Doktorarbeit. Diese waren mir immer eine große Hilfe. Des Weiteren danke ich Prof. Dr. Christian von Savigny für die Übernahme des Korreferats und das Interesse an dieser Arbeit.

Ein besonderer Dank geht an Dr. Ali Hoshyaripour, der mir die Möglichkeit gegeben hat an diesem spannendem Thema arbeiten zu dürfen. Danke, dass Du mir von Beginn an das nötige Vertrauen entgegengebracht hast meine eigenen Ideen umzusetzen und mich immer motiviert und mir weitergeholfen hast, wenn mal nicht alles geklappt hat. Vielen Dank, für die zahlreichen Gespräche und Diskussionen auf wissenschaftlicher sowie persönlicher Ebene und, dass Du jederzeit für Fragen zur Verfügung standest.

Dr. Bernhard Vogel danke ich für die Möglichkeit in seiner damaligen Arbeitsgruppe anzufangen. Dein Vertrauen in meine Arbeit, Deine motivierenden Worte und fachlichen Ratschläge haben mir immer weitergeholfen und haben besonders in den ersten zwei Jahren maßgeblich zum Fortschritt dieser Arbeit beigetragen.

Weiterhin möchte ich der gesamten Arbeitsgruppe 'Spurenstoffmodellierung und Klimaprozesse' für die wissenschaftlichen Diskussionen, das Anhören von Probenvorträgen, den Zusammenhalt innerhalb der Gruppe und die gemeinsamen Mittagspausen danken. Insbesondere danke ich Dir, Dr. Heike Vogel, für Deine Unterstützungen bei ICON-ART Simulationen, Deine hilfreichen Ideen und Ratschläge bei der Fehlersuche sowie jegliche Aufmunterungen zwischendurch. Ich danke Dir, Dr. Lukas Muser, für Deine Hilfe bei meinen ersten ICON-ART Simulationen, dass ich immer mit Fragen auf Dich zukommen konnte, sowie das Bereitstellen Deines Raikoke Setups und der Eingabedaten. Dir, Dr. Sven Werchner, danke ich für Deine Unterstützung bei jeglichen technischen Fragen zu ICON-ART und Deiner Hilfe bei der Veröffentlichung meiner Simulationsdaten.

Ich danke allen Koautoren meiner beiden Paper. Insbesondere danke ich Dr. Ákos Horváth für das schnelle Bereitstellen der Eruptionshöhen, die wissenschaftliche Zusammenarbeit im VolPlume Projekt und die vielen wertvollen Kommentare und Hilfestellungen beim Vorbereiten und Schreiben der Paper.

Diese Arbeit wurde von der Deutschen Forschungsgemeinschaft (DFG) im Rahmen der Forschergruppe VolImpact (FOR2820) gefördert. Ich danke dem gesamten VolImpact-Team für die gute Zusammenarbeit und den Austausch über unsere Forschungsergebnisse. Die Diskussionen bei jeglichen Treffen und besonders auch die Summerschool haben mich sehr motiviert und mir viele neue Ideen gegeben.

Ein herzliches 'Dankeschön' geht auch an Marisa Roch, Dr. Tim Tobaben und Marius Take für die Zeit und Mühen als Korrekturleser*innen dieser Arbeit.

Abschließend bedanke ich mich bei meinen Eltern, Michael und Stephanie, und meinem Bruder Dennis. Danke, dass Ihr jederzeit für mich da wart, an mich geglaubt habt und mir meinen bisherigen Lebensweg ermöglicht habt. Ein besonderer Dank gilt auch meinem Freund Marius, der mir besonders in der finalen Phase den Rücken freigehalten und mir einen starken emotionalen Rückhalt gegeben hat.